

Newcastle
University

FUNDAMENTAL AND APPLIED STUDIES
OF
NON-THERMAL PLASMA

Thesis submitted by:

ABDULLAH JUBRAN AL-ABDULY

For the degree of Doctor of Philosophy

Newcastle University

School of Chemical Engineering and Advanced Materials

January 2016

Preface

Declaration

I hereby declare that this thesis entitled “Fundamental and applied studies of non-thermal plasma” is the result of experiments carried out in the School of Chemical Engineering and Advanced Materials at Newcastle University. No part of this thesis has been submitted for a degree or any other qualification at Newcastle University or any other institution.

Abdullah Al-Abduly

November 2015

Acknowledgements

First and foremost I would like to thank my supervisor Prof. Paul A. Christensen for his supervision, knowledge, Friendship, guidance and support throughout my project, without which this work would not have been possible.

I would like to thank my secondary supervisor Prof. Adam Harvey for the regular discussions and support during my project. This thanks extended to my third supervisor Dr. Kui Zhang for his help and support.

I would like to thank all of the members of Christensen Research Group, Steven Jones, Khalid Zakaria, Pierrot Attidekou, Supandee Manelok, Halim Bin Md Ali, Zeinab Mashhadni, Panos Moussas, David Molyneaux, Daniel Lawrence, Douglas Linares-Moya and Nutchapon Chiarasumran for their friendship throughout my studies. This thanks extended to my friends in process intensification group (PIG).

Thanks also must go to Neville Dickman for his support during the DBD-PBR fabrication, Simon Daley for electronic work, William McCormack & Robyn Hare for their excellent glass blowing, David Dunbar & Christopher Burrow for the training and support received during the HPLC and the ESI-MS analyses and David Race for his support during the ion chromatography and TOC analyses.

A very special thanks must go to my parents, my wife, my kids, my brothers and sisters for their love, support and encouragement that helped me to reach the end of this work.

Finally, I would like to thank King Abdulaziz City for Science and Technology (KACS) and Newcastle University for the financial and technical supports received during this research.

List of Publications

Work published

1. Al-Abduly, A., Christensen, P., Harvey, A. and Zahng, K. (2014) 'Characterization and optimization of an oscillatory baffled reactor (OBR) for ozone-water mass transfer', *Chemical Engineering and Processing: Process Intensification*, 84, pp. 82-89.
2. Al-Abduly, A., and Christensen, P., (2015) 'An in situ and downstream study of non-thermal plasma chemistry in an air fed dielectric barrier discharge (DBD)', *Plasma Sources Science and Technology*, 24(6), p. 065006.

To be published

1. Characterization and optimization of a novel dielectric barrier discharge packed bed reactor (DBD-PBR) for ozone generation.
2. The remediation of water containing Cu(II)-EDTA or Fe(III)-EDTA by ozonation, and ozonation followed by UV irradiation using oscillatory baffled reactor (OBR).

Oral presentations

1. Ozone-water mass transfer using an OBR, CEAM PG research conference 2013.
2. A preliminary study on the application of non-thermal plasma (NTP) to air treatment, CEAM PG research conference 2014.

Award

Second best presentation at the PG chemical engineering CEAM conference 2014.

Abstract

This thesis reports a pure and applied study on non-thermal plasmas (NTPs) produced using Dielectric Barrier Discharge (DBD) generators of various forms. The main aim of the pure aspect of the study was to obtain a better understanding of the chemistry taking place within the NTP in an air-fed DBD and to what extent the plasma output varies from the glow to the downstream regions under various operational conditions. Thus, a DBD plasma jet generator was designed and employed for the investigations of these regions. The analyses of the plasma glow region and the downstream exhaust were carried out using Fourier Transform InfraRed (FTIR) and UV–Vis absorption spectroscopies. The applied studies focussed on the development of a novel, dielectric barrier discharge-packed bed reactor (DBD-PBR) for effective ozone generation from oxygen or air, and its application to the remediation of Cu(II)-EDTA and Fe(III)-EDTA containing water in combination with an oscillatory baffled reactor (OBR) and a UV irradiation reactor (UVR).

In-situ analysis of the plasma glow region of the plasma jet identified: O₃, N₂O₅, N₂O, NO₂, HNO₃, CO₂, CO and, for the first time, a vibrationally excited form of CO₂ (i.e. CO₂^{*}(ν)), while O₃, N₂O₅, HNO₃ and N₂O were detected in the downstream exhaust. The behaviour of these species was monitored as a function of a range of experimental conditions including: input power, gas flow rate, relative humidity, gas temperature and feed gas composition, and mechanisms postulated based on literature precedent. It is clear from this work that the feed gas composition, input power, gas temperature and relative humidity have a significant effect upon the NTP chemistry in the glow and post glow regions. Unexpectedly, the spectroscopic analyses of O₃, NO₂ and N₂O in the plasma glow region and in the downstream exhaust suggested the occurrence of chemical reactions in the afterglow region rather than simple diffusion. This behaviour rules out the general assumption that reactive chemistry is confined to the glow region.

The DBD-PBR was designed, fabricated, characterized and optimized for ozone generation from oxygen and air. The effects of reactor arrangement, feed gas flow rate, coolant temperature, input power and dielectric material on ozone generation were investigated. The highest ozone concentration of 152 g m⁻³ was obtained using 2.0 mm glass beads and an oxygen feed at 5 °C, and 0.06 dm³ min⁻¹, while the highest ozone yield efficiency was 210 g kW⁻¹ h⁻¹ at an oxygen feed rate of 15 dm³ min⁻¹ this compares to 173 g kW⁻¹h⁻¹ reported in the literature. The highest ozone concentration produced from air was 15.5 g m⁻³ at flow rate

of $0.06 \text{ dm}^3 \text{ min}^{-1}$ with Al_2O_3 beads as the dielectric. It was found that the dielectric employed in the DBD-PBR had a significant effect upon the selectivity towards ozone at low feed gas flow rates. Different NO_x by-products were formed along with ozone when the DBD-PBR was fed with air depending on the coolant temperature and the dielectric material. The efficiency of ozone generation via DBR-PBRs was significantly enhanced reducing the discharge current during the generation of NTP by decreasing the capacitance of the dielectric and by effective heat removal. Finally, a MnO_2 -based catalyst (CARULIT 200) tested for DBD-PBR exhaust control, and was found to be effective for simultaneous ozone and NO_x removal at room temperature.

The DBD-PBR was coupled to an OBR to intensify ozone-to-water mass transfer. The OBR was operated as a semi-batch and as a co-current, up-flow continuous reactor. The effect of input ozone concentration, input gas & water flow rates, and oscillation amplitude and frequency on gas hold up, volumetric mass transfer coefficient and mass transfer efficiency were determined. The same reactor was operated as a bubble column (i.e. without baffles or oscillation) and as a baffled column (without oscillation) to assess the effect of the reactor arrangement on the mass transfer. The results show that the OBR was 5 and 3 times more efficient for ozone-water mass transfer than the baffled and bubble columns, respectively. The enhancement obtained with the OBR over the baffled column reactor was found to decrease with gas flow rate due to changes in bubble flow pattern from homogenous to heterogeneous. Under continuous flow conditions, the performance of the baffled reactor and the OBR were found to be twice as efficient for ozone-water mass transfer than when operating under semi-batch conditions. The mass transfer efficiency (MTE, %) was found to increase from 57 % using the baffled reactor to 92 % with OBR under continuous flow at water and gas superficial velocities of 0.3 and 3.4 cm s^{-1} , respectively. From these results it is clear that the OBR and baffled reactor are promising approaches for enhancing ozone-water mass transfer and its application in water treatment.

One of the targeted fields of the DBD-PBR/OBR/UVR system is in water treatment, and hence it was important to evaluate its performance in such application. Therefore, the system was employed for the treatment of water samples contaminated with Cu(II)-EDTA and Fe(III)-EDTA . These compounds were chosen because they are difficult to remove from water using conventional methods. The effects of reactor arrangement, ozonation time and ozonation plus UV irradiation on remediation of the complexes were investigated under

continuous flow conditions. The results suggest that Cu(II)-EDTA was decomposed completely by ozonation within 17 minutes using the OBR, with no significant enhancement by UV irradiation. However, the Fe(III)-EDTA was converted to other stable complexes (i.e. Fe(III)-ED3A and Fe(III)-IDA) by ozonation, and hence following the ozonation by UV irradiation was essential to ensure complete degradation. The total organic carbon (TOC) of the Fe(III)-EDTA and Cu(II)-EDTA solutions was reduced by 50% after 17 minutes of O₃/UV treatment using the OBR. Some of the final products were identified using Ion Chromatography and included: oxalic acid, formic acid, acetic acid, glycolic acid, nitrate and nitrite ions. From these results, it is clear that the enhancement in ozone-water mass transfer using the OBR or the baffled reactor was essential for reducing the treatment time and ozone dosage required for the remediation of Cu(II)-EDTA and Fe(III)-EDTA over conventional bubble column reactors.

Table of Contents

Declaration.....	i
Acknowledgements.....	ii
List of Publications	iii
Abstract.....	iv
Table of Contents.....	ivii
List of Figures.....	xi
List of Tables	xxi
List of Abbreviations	xxiii
1. Introduction.....	1
1.1. Non-thermal plasma definition, principles and applications	1
1.2. NTP and ozone generation.....	3
1.2.1. Ozone	3
1.2.2. Ozone generation methods.....	3
1.2.3. Mechanism of NTP formation by electric discharge	5
1.2.4. Ozone generation in DBD.....	7
1.2.5. NTP chemistry of air and ozone generation	9
1.2.6. Types of DBD.....	11
1.3. Factors affecting ozone generation in DBD-PBRs	13
1.3.1. Discharge power characteristics	13
1.3.2. Temperature effect.....	15
1.4. Ozone catalytic destruction.....	20
1.5. Ozone –water mass transfer	20
1.5.1. Overview.....	20
1.5.2. Principles of gas-liquid mass transfer process	21
1.5.2.1. Two Films Theory	23
1.5.2.2. Surface Penetration Theory	24
1.5.2.3. Thin Film Renewal Theory.....	25
1.5.3. Ozone-water volumetric mass transfer coefficient ($k_L a$).....	25
1.5.4. Factors affecting ozone-water dissolution	26
1.5.5. Types of ozone-water contactors	29
1.5.6. Oscillatory baffled reactors (OBR).....	32
1.5.7. An overview of the OBRs as gas-liquid contactors.....	34

1.6. The remediation of M-EDTA complexes	35
1.7. Project aim and objectives	37
1.8. Thesis structure	38
1.9. References.....	39
2. Experimental.....	56
2.1. Materials, Chemicals and gases	56
2.1.1. Materials	56
2.1.2. Chemicals & gases.....	56
2.2. An in-situ and downstream analysis of air fed Non-thermal plasma (NTP)	57
2.2.1. Non-thermal plasma jet generator.....	57
2.2.2. Relative humidity control	57
2.2.3. Experimental procedures	57
2.2.4. FTIR analysis	60
2.2.5. N ₂ O calibration	62
2.2.6. UV analyses of ozone	62
2.2.7. Gas temperature measurement.....	63
2.3. Ozone generation via a dielectric barrier discharge packed bed reactor (DBD-PBR) .	63
2.3.1. Novel DBD-PBR structure and fabrication steps	63
2.3.2. DBD-PBR operation procedures	67
2.3.3. Discharge voltage and frequency measurements.....	67
2.3.4. Ozone destruction in the effluent gas	69
2.4. Ozone - water mass transfer.....	69
2.4.1. The Oscillatory Baffled Reactor (OBR)	69
2.5. EDTA complexes treatments using ozone, ozone and UV irradiation	72
2.5.1. EDTA samples preparation.....	72
2.5.2. UV reactor.....	73
2.5.3. EDTA complexes sampling and ion chromatography analysis	74
2.5.4. Total organic carbon (TOC) analysis.....	75
2.5.5. Mass spectroscopy analysis	76
2.6. References.....	77
3. An <i>in-situ</i> and downstream study of non-thermal plasma chemistry in an air fed dielectric barrier discharge (DBD)	79
3.1. Introduction.....	79
3.2. Non-thermal plasma In-situ analyses.....	79

3.2.1. The effect of feed gas composition.....	79
3.2.2. N ₂ O calibration	85
3.2.3. Non-thermal plasma & CO ₂	86
3.2.4. The effects of input power and gas flow rate.....	89
3.2.5. Relative humidity and gas temperature effects	94
3.3. Downstream analyses	101
3.3.1. FTIR analysis	101
3.3.2. Ozone analyses	102
3.3.3. N ₂ O analyses.....	104
3.3.4. The uncertainty associated with downstream UV analyses of ozone	105
3.4. Conclusions.....	107
3.5. References.....	108
4. A characteristic study of a novel dielectric barrier discharge packed bed reactor (DBD-PBR) for ozone generation	115
4.1. Introduction.....	115
4.2. Results and discussion	118
4.2.1. The effect of the discharge cell arrangement.....	118
4.2.2. The effect of cell separator thickness	119
4.2.3. The effect of dielectric packing gap width on ozone generation	120
4.2.4. The effect of dielectric material on ozone generation	124
4.2.5. Input power effect.....	126
4.2.6. Ozone yield efficiency	127
4.2.7. Cell arrangement and discharge power characteristics.....	132
4.2.8. Ozone generation from air	134
4.2.9. Coolant temperature effect.....	138
4.2.10. Ozone and NO _x control	142
4.3. Conclusions.....	145
4.4. References.....	146
5. Characterization and optimization of an oscillatory baffled reactor (OBR) for ozone-water mass transfer	150
5.1. Introduction.....	150
5.2. Ozone-water mass transfer under semi-batch conditions	151
5.2.1. The effect of ozone concentration on ozone-water solubility.....	151
5.2.2. The effect of oscillation conditions on ozone-water mass transfer	154

5.2.3 The effect of the reactor arrangement on ozone-water mass transfer	157
5.2.4. Gas hold-up and k_{La}	163
5.3. Ozone-water mass transfer under continuous flow conditions	165
5.3.1. The effect of the input gas and water flow rates on k_{La}	165
5.3.2 The effect of the input gas and liquid flow rates on mass transfer efficiency (MTE)	167
5.4. Conclusions.....	170
5.5. References.....	171
6. The remediation of water containing Cu(II)-EDTA or Fe(III)-EDTA by ozonation, and ozonation followed by UV irradiation	173
6.1. Introduction.....	173
6.2. Cu(II)-EDTA analysis and treatment.....	174
6.2.1. Cu(II)-EDTA analysis by ion chromatography	174
6.2.2. Cu(II)-EDTA treatment by ozone	176
6.2.3. Cu(II)-EDTA treatment by ozonation followed by UV irradiation.....	179
6.2.4. TOC analysis of Cu(II)-samples after treatments	180
6.3. Fe(III)-EDTA analysis and treatment	181
6.3.1. Fe(III)-EDTA analysis by ion chromatography.....	181
6.3.2. TOC analyses of Fe(III)-EDTA after treatments	182
6.4. Conclusions.....	190
6.5. References.....	190
7. Conclusions and future work	194

List of Figures

Figure 1.1. Examples of natural plasma: (i) the solar wind, (ii) Aurora Borealis and (iii) lightning. Photos were reproduced with permission from the NASA website: www.nasa.gov.....2

Figure 1.2. Schematic representation of cold corona discharge (CCD) (i), and dielectric barrier discharge (DBD) (ii); (1) High voltage cathode, (2) anode, (3) dielectric layer, (4) plasma discharge, (5) NTP streamers and (6) AC power supply. Redrawn from Tendero et al. [6].....4

Figure 1.3. Photos of micro-discharge development with time using DBD fed with dry air, discharge voltage and gap width were 28 kV and 5.0 mm, respectively. The photos were taken using an intensified charge-coupled device (ICCD) camera [48].....6

Figure 1.4. Schematic of the different types of DBD: volume discharge (VD), surface discharge (SD) and packed bed discharge (PBD). Each consists of: (1) power supply, (2) cathode, (3) NTP active region, (4) dielectric layer or beads, and (5) anode..... 12

Figure 1.5. Schematic representation of the heat transfer mechanisms in packed bed reactors [82, 83]. The red and blue arrows indicate the directions of heat flux for the independent and dependent mechanisms re gas flow, respectively. See text for details. 17

Figure 1.6. Schematic of the gas-liquid interface and the concentration profiles of the component in the gas and liquid phases. The arrows indicate the direction of mass transfer, P_G and P_{Gi} (atm) are the partial pressures in gas bulk and at the interface, C_{Li} and C_L (kmol m^{-3}) are the liquid side concentrations of the species at the interface and in the bulk liquid. Redrawn with modifications from [96]. 21

Figure 1.7. A plot of the gas-liquid concentrations and the driving force distribution in gas and liquid phases under equilibrium conditions. P_G , P_{Gi} and P_G^* (atm) are the partial pressures in gas bulk, at the interface and at equilibrium between the interface and the bulk, respectively. C_L , C_{Li} and C_L^* (kmol m^{-3}) are the liquid side concentrations of the absorbent in liquid bulk, at the interface and at equilibrium between the interface and at the bulk liquid. Redrawn with amendments from [97]. See text for further details. 22

Figure 1.8. Schematic of the gas-liquid interface as described by the two film theory [99]. δ_L (m) and δ_G (m) are the thicknesses of the stagnant liquid and gas films, respectively. Other components are the same as those shown in fig.1.6. 24

Figure 1.9. A diagram of the factors affecting gas-to-liquid mass transfer and their relationships. 27

Figure 1.10. Schematics showing ozone concentration profiles for slow and fast kinetic regimes [98]. 28

Figure 1.11. Schematic showing the different flow regimes observed using bubble columns redrawn after Bouaifi et al. [114]. 30

Figure 1.12. A plot of the different flow regimes in bubble column reactors as a function of feed gas velocity and column diameter [118]. 31

Figure 1.13. Photo of vortex formation during the operation of an oscillatory baffled reactor. The white arrows indicate eddy development within the reactor [124]. 33

Figure 2.1. A schematic of Non-thermal plasma jet transmission cell: (1) CaF₂ windows, (2) exhaust gas outlet, (3) Pyrex glass tube with a nozzle, (4) feed gas flow gap, (5) and (6) high voltage electrodes and (7) in-situ sampling zone of the NTP glow. 58

Figure 2.2. A schematic sketch of the experimental setup employed for in-situ and downstream analysis of NTP. The system consists of: (1) feed gases, (2) flow meters, (3) mixing cylinder, (4) relative humidity regulator, (5) relative humidity meter, (6) non-thermal plasma jet transmission cell, (7) in-situ FTIR, (8) downstream FTIR and (9) Ocean Optics spectrometer flow cell. Channels I and II were employed for in-situ and downstream monitoring, respectively. 59

Figure 2.3. An example of FTIR spectra processing: (i) a reference spectrum (S_R) collected from ambient air, (ii) a sample spectrum collected after powering the NTP generator (S_S) and (iii) $A = \text{Log}_{10}(S_S/S_R)$ 61

Figure 2.4. A photo showing the top view of the DBD-PBR system employed for ozone generation: (1) safety power regulator, (2) variac transformer, (3) high voltage power supply, (4) DBD-PBR discharge cell, (5) feed gas inlet, (6) exhaust gas outlet, (7) coolant inlet, (8) earthed metallic ring and (9) coolant outlet. 64

Figure 2.5. (a) A schematic of the DBD-PBR cell employed for ozone generation: (1) high voltage power supply, (2) cell lid, (3) 1.0 mm thick soft PTFE sheet, (4) 10.0

mm thick PTFE disk, (5) stainless steel mesh electrodes, (6) $10.0 \times 52.0 \times 60.0$ mm perforated PTFE plate, (7) dielectric beads filling gap, (8) feed gas inlet, (9) exhaust gas outlet, (10) coolant liquid inlet and (11) coolant outlet. (b) Cross-section view of the DBD-PBR cell shows the electrodes arrangement: (12) high voltage electrode and (13) stainless steel supporting electrodes. 65

Figure 2.6. Photographs of the electrode shapes and arrangement in the DBD-PBR discharge cell: Arrangement (a): the cell consists of two sets of planar electrodes with two supporting PTFE plates to maintain the electrode positions and the electrodes dimensions were: $6.0 \text{ cm} \times 0.1 \text{ cm} \times$ widths of: 5.0, 4.7 and 4.5 cm for the electrodes 1, 2 and 3, respectively. Arrangement (b): the cell consists of two sets of semi-cylindrical shaped mesh stainless steel electrodes $6.0 \text{ cm} \times 0.1 \text{ cm} \times$ widths of 7.0, 6.7 and 6.5 cm for the electrodes 3, 2 and 1, respectively, giving a gap of 2.0 mm between the two electrodes of each set. 66

Figure 2.7. Schematic of the setup employed for monitoring the discharge power: (1) HV power supply, (2) simultaneous polarity of the HV electrodes, (3) NDBD-PBR discharge cell, (4) coolant inlet, (5) inlet gas tube, (6) outlet gas tube, (7) HV probe, (8) grounded electrode, (9) oscilloscope and (10) a side view of the discharge cell during the operation. 68

Figure 2.8. Typical example of discharge power measurement carried out using the Philips oscilloscope. The oscilloscope voltage division was set at 2.0 kV and time division was 20 μs . The peak height was used to estimate the output voltage either as (i) kV RMS, (ii) kV or (iii) kV peak-peak. The frequency was determined by dividing the number of complete voltage cycles by time (iv). . 68

Figure 2.9. The Oscillatory Baffled Reactor system: (1) gas flow meter, (2) ozone generator (NDBD-PBR), (3) ozone distribution cell, (4) Ocean Optics flow cells, (5) oscillation supplying motor, (7) bubble removing cell, (8) peristaltic tubing pumps, (9) return port, (10) outlet port, (11) data collection station and (12) ozone destruction cells. 70

Figure 2.10. A schematic of the UV-photolysis reactor employed for water treatment: (1) feed water inlet, (2) borosilicate column, (3) UV lamp and (4) outlet port. 73

Figure 2.11. A photograph of the ion chromatography system employed for monitoring water samples after treatments. The system consists of: (1) mobile phase, (2) auto-sampler, (3) separation and detection unit and (4) data collection software. ... 75

Figure 2.12. A photograph of the TOC analyser. 76

- Figure 3.1. In-situ FTIR spectra collected as a function of running time. The input power was 36W, pure oxygen feed at a flow rate of $0.5 \text{ dm}^3 \text{ min}^{-1}$ 80
- Figure 3.2. In-situ FTIR Spectra collected after 1 minute at 36 W input power as a function of the feed gas composition: (i) ambient air, (ii) artificial air + 40% relative humidity and (iii) dry artificial air. The gas flow rate was $0.5 \text{ dm}^3 \text{ min}^{-1}$ 81
- Figure 3.3. A calibration curve of N_2O obtained using the FTIR spectroscopy setup shown in fig.2.2. The N_2O partial pressures employed for the calibration were obtained by admixing pure N_2O at $0.05 \text{ dm}^3 \text{ min}^{-1}$ with N_2 at 2.0, 3.0, 4.0 $\text{dm}^3 \text{ min}^{-1}$. ..86
- Figure 3.4. (a) In-situ FTIR Spectra collected from the NTP glow region after running the DBD for 10 minutes as a function of feed gas composition. Each spectrum was ratioed to its reference spectrum collected with no input power with the gas flowing at the specified rate. (b) The spectra in (a) replotted to show the gain features more clearly. The input power was 36 W. 87
- Figure 3.5. Plots of the partial pressures of: N_2O (a), O_3 (b), NO_2 (c) and (d) CO_2^* (v) absorbance at 2326 cm^{-1} as a function of discharge energy density and feed gas composition monitored using in-situ FTIR spectroscopy 1 minute after the plasma was turned on. The input power and feed gas flow rates ranged from 27-36W and $0.2\text{-}0.5 \text{ dm}^3 \text{ min}^{-1}$, respectively. 93
- Figure 3.6. In-situ FTIR spectra collected after 1 minute of DBD operation at 36W using: dry artificial air and artificial air + 20 % RH. The input power was 36W and gas flow rate $0.5 \text{ dm}^3 \text{ min}^{-1}$ 94
- Figure 3.7. Plots of NO_2 partial pressure monitored in-situ using FTIR spectroscopy as a function of running time and relative humidity using artificial air. The input power was 36 W at $0.5 \text{ dm}^3 \text{ min}^{-1}$. Maximum N_2O partial pressure = $P^*_{\text{NO}_2} = 7.7 \pm 0.62 \times 10^{-5} \text{ atm}$ 96
- Figure 3.8. Plot of plasma jet temperature 5.0 mm from the DBD nozzle as a function of running time using ambient air. The input power was 36 W at $0.5 \text{ dm}^3 \text{ min}^{-1}$. 97
- Figure 3.9. Plots of NO_2 partial pressure as a function of relative humidity and plasma jet temperature monitored in-situ using FTIR. The feed gas was artificial air. The input power was 36 W at $0.5 \text{ dm}^3 \text{ min}^{-1}$. Maximum NO_2 partial pressure = $P^*_{\text{NO}_2} = 7.7 \pm 0.62 \times 10^{-5} \text{ atm}$ 98
- Figure 3.10. Plots of O_3 partial pressure monitored using in-situ FTIR spectroscopy as a function of relative humidity vs.: (a) running time, (b) plasma jet temperature

	using artificial air. The input power was 36 W at 0.5 dm ³ min ⁻¹ . Maximum ozone partial pressure = $P^*_{O_3} = 8.9 \pm 0.08 \times 10^{-4}$ atm.....	99
Figure 3.11.	Plots of N ₂ O partial pressure monitored using in-situ FTIR spectroscopy as a function of relative humidity vs.: (a) running time, (b) plasma jet temperature using artificial air. The input power was 36 W at 0.5 dm ³ min ⁻¹ . Maximum N ₂ O partial pressure = $P^*_{N_2O} = 2.07 \pm 0.1 \times 10^{-5}$ atm.....	101
Figure 3.12.	FTIR Spectra collected in downstream after 1 minute of DBD operation as a function of the feed gas composition. The input power was 36W and gas flow rate 0.5 dm ³ min ⁻¹	102
Figure 3.13.	Plots of ozone partial pressure as a function of running time and feed gas composition, monitored using in-situ (i) + (iii) and downstream FTIR spectroscopy (ii) + (iv). The input power was 36 W at 0.5 dm ³ min ⁻¹	104
Figure 3.14.	Plots of ozone partial pressure as a function of running time and feed gas composition, monitored in-situ (ii) + (iv) and downstream (ii) + (iv) using FTIR spectroscopy. The input power was 36 W at 0.5 dm ³ min ⁻¹	105
Figure 3.15.	Plots of ozone partial pressure as a function of running time and feed gas composition monitored downstream using FTIR spectroscopy (i) + (iii), and UV-Vis spectroscopy (ii) + (iv). The input power was 36 W at 0.5 dm ³ min ⁻¹ . Plots (ii) and (iv) were obtained from fig. 3.13.	106
Figure 4.1.	Schematic of the DBD-PBR discharge cell arrangements employed for ozone generation: (1) support electrode, (2) high voltage electrode, (3) perforated PTFE supports, (4) perforated PTFE sheet (i.e. the cell separator), (5) feed gas inlet, (6) exhaust gas outlet, (7) coolant liquid inlet and (8) coolant outlet. The cell names indicate the shape and number of electrodes in each half: planer electrodes in A and semi-cylindrical in B.	116
Figure 4.2.	Schematic of the DBD-PBR discharge cell shows the corross-sections of arrangements shown in fig.4.1: (1) support electrode, (2) high voltage electrode, (3) perforated PTFE supports, (4) perforated PTFE sheet (i.e. the cell separator), (5) feed gas inlet, (6) exhaust gas outlet, (7) coolant liquid inlet and (8) coolant outlet.	117
Figure 4.3.	Plots of ozone concentration as a function of oxygen flow rate and discharge cell arrangement. The dielectric was 1.0 mm thick perforated sheets of PTFE (D6).	

The input power and the coolant temperature were 17W and 5.0 °C, respectively. 119

Figure 4.4. Plots of ozone concentration as a function of input power and the discharge B2 cell divider thickness. Oxygen flow rate 1.0 dm³ min⁻¹ and coolant temperature 5.0 °C using 1.0 mm thick perforated sheets of PTFE (D6) as the dielectric. 120

Figure 4.5. Ozone concentrations as a function of the dielectric type and packing gap width. The dielectrics employed were (D1) 2 mm alumina pellets (D2) 2 mm borosilicate glass beads, (D3) 2 mm A3 molecular sieve, (D4) 3 mm Soda-Lime glass beads and (D5) 3 mm alumina pellets. Using the B2 arrangement at an input power of 35W, coolant temperature of 5 °C and oxygen flow rate of 1.0 dm³ min⁻¹. 121

Figure 4.6. Plots of ozone concentrations as a function of oxygen flow rate and dielectric packing gap width. The dielectric employed was 2 mm borosilicate glass beads (D2), using the cell B2 at an input power of 35W and coolant temperature of 5 °C. 123

Figure 4.7. Plots of ozone concentrations as a function of oxygen flow rate and the packing gap width of the dielectric (PGWD). The dielectric employed was 3 mm alumina pellets (D5), using cell B2 at an input power of 35W and coolant temperature of 5 °C. 123

Figure 4.8. Ozone concentration as a function of oxygen flow rate using cell B2 packed with: 2 mm alumina pellets (D1), 2 mm borosilicate glass beads (D2), 2 mm A3 molecular sieve (D3), 3 mm Soda-Lime glass beads (D4) and 3 mm alumina pellets (D5). The packing gap width of the dielectric (PGWD) were 2 mm for D1, 3 mm for D2, D3 and D5, and 4 mm for D4. Using the cell B2; input power was 35W at a coolant temperature of 5.0 °C. 124

Figure 4.9. Plots of ozone concentration as a function of input power using cell B2 packed with: 2 mm alumina pellets (D1), 2 mm borosilicate glass beads (D2), 2 mm A3 molecular sieve (D3), 3 mm Soda-Lime glass beads (D4) and 3 mm alumina pellets (D5). The packing gap widths of the dielectric (PGWD) were same as those in fig. 4.8. The cell was fed with oxygen at 1.0 dm³ min⁻¹, and the coolant temperature was 5.0 °C. 127

Figure 4.10. Plot of ozone yield efficiency as a function of input power and dielectric from the data in fig. 4.9. Cell B2 was packed with: 2 mm alumina pellets (D1), 2 mm borosilicate glass beads (D2), 2 mm A3 molecular sieve (D3), 3 mm Soda-Lime

	glass beads (D4) and 3 mm alumina pellets (D5). The packing gap widths of the dielectric were same as those in fig. 4.8. The cell was fed with oxygen at $1.0 \text{ dm}^3 \text{ min}^{-1}$, and the coolant temperature was $5.0 \text{ }^\circ\text{C}$	128
Figure 4.11.	Plots of ozone yield efficiency as a function of oxygen flow rate and dielectric material using cell B with 2 electrode configuration and a dielectric thickness of 3.0 mm. The input power was 35W and coolant temperature was $5.0 \text{ }^\circ\text{C}$	129
Figure 4.12.	Plots of ozone concentration as a function of specific energy density, cell arrangement and oxygen flow rate. All experiments were carried out using 2 mm glass beads (D2) and a fixed packing gap width of 2 mm. The coolant temperature was $5.0 \text{ }^\circ\text{C}$. The dashed red lines were added for comparison purposes, see text for more details.	130
Figure 4.13.	Plots of ozone yield efficiency as a function of specific energy density, cell arrangement and oxygen flow rate. Using 2 mm glass beads (D2). The coolant temperature was $5.0 \text{ }^\circ\text{C}$	132
Figure 4.14.	Plots of discharge voltage as a function of input power and cell arrangement. The oxygen flow rate was $1.0 \text{ dm}^3 \text{ min}^{-1}$, using 2 mm glass beads for packing with PGWD of 2.0 mm, and coolant temperature $5.0 \text{ }^\circ\text{C}$. The uncertainty in the discharge voltage measurement was $\pm 0.2 \text{ kV}$	133
Figure 4.15.	(a) FTIR spectra collected of the exhaust from cell B2 after running the DBD-PBR for 30 minutes as a function of dielectric type. (b) The spectra in (a) replotted to show the gain features more clearly. Each spectrum was ratioed to its reference spectrum collected with no input power. The feed gas was dried ambient air at $\text{RH} \leq 0.6\%$, input power 35W, gas flow rate $0.06 \text{ dm}^3 \text{ min}^{-1}$ and coolant temperature $5.0 \text{ }^\circ\text{C}$	136
Figure 4.16.	Ozone concentration as a function of air flow rate using the dielectrics: 2 mm alumina pellets (D1), 2 mm borosilicate glass beads (D2), 2 mm A3 molecular sieve (D3), 3 mm Soda-Lime glass beads (D4) and 3 mm alumina pellets. The packing gap width of the dielectric (PGWD) were 2 mm for D1, 3 mm for D2, D3 and D5, and 4 mm for D4, input power of 35W at coolant temperature of $5.0 \text{ }^\circ\text{C}$, monitored using FTIR spectroscopy.	137
Figure 4.17.	Plots of ozone concentration as a function of coolant temperature using dielectrics: 2 mm alumina pellets (D1), 2 mm borosilicate glass beads (D2), 2 mm A3 molecular sieve (D3), 3 mm Soda-Lime glass beads (D4) and 3 mm	

alumina pellets (D5). The PGWDs were the same as in fig.4.16. The input power was 35W and oxygen flow rate was 1.0 dm ³ min ⁻¹	139
Figure 4.18. FTIR spectra collected from the exhaust of cell B after running the DBD-PBR for 30 minutes at different temperatures: (a) 50, (b) 30, (c) 10 and (d) 5 °C. Using dried ambient air at different flow rate. RH ≤ 0.6%, input power 35W, using 2.0 mm glass beads (D2).....	141
Figure 4.19. FTIR spectra collected from cell B exhaust after running the DBD-PBR for 30 minutes monitored (a) before and (b) after the interaction with the MnO ₂ catalyst. Using the cell B at 50 °C, 2.0 mm glass beads (D2) and fed with dried ambient air.	144
Figure 5.1. Plots of dissolved ozone concentration with time as a function of the input gas phase ozone concentration using the baffled reactor. The input gas flow rate (Q _G) was 1.0 dm ³ min ⁻¹	153
Figure 5.2. Plots of ozone volumetric mass transfer coefficient (k _{LA}) as a function of (a) oscillation amplitude at 5.0 Hz and (b) oscillation frequency at 6.0 mm, using the OBR. The ozone concentration in oxygen was 62.0 mg dm ⁻³ at a flow rate of 1.0 dm ³ min ⁻¹	155
Figure 5.3. Plot of ozone-water mass transfer coefficient as a function of Re _o for the data in figs. 5.2 (a) and (b).....	157
Figure 5.4. Plots of ozone-water dissolution as a function of running time and reactor arrangement. [O ₃] _G was 65 mg dm ⁻³ at an input gas flow rate (Q _G) of 0.1 dm ³ min ⁻¹ . Re _o was fixed at 4600 in the case of the OBR. The inset plots of Ln ([O ₃] _S - [O ₃] _t) vs. time used for the determination of k _{LA} (see text for further details).	158
Figure 5.5. Chart of ozone-water mass transfer coefficients as a function of the reactor arrangement and input gas flow rate. Re _o was kept at 4600 in the case of the OBR.	160
Figure 5.6. Images of various gas flow patterns observed using the baffled reactor at an input gas flow rate of 0.4 dm ³ min ⁻¹ (a) and the OBR at 0.4 dm ³ min ⁻¹ (b) and 1.6 dm ³ min ⁻¹ (c). The Re _o was fixed at 4600 in both (b) and (c).	162
Figure 5.7. Plot of gas hold-up as a function of the gas superficial velocity obtained using gas diffusers A and B in the baffled reactor. See text for details.....	164

- Figure 5.8. Plot of k_{LA} as a function of gas superficial velocity obtained using gas diffusers A and B in the baffled reactor. 164
- Figure 5.9. Plot of ozone-water mass transfer coefficients as a function of gas hold-up obtained using the three reactor arrangements, under various input gas flow rates and oscillation conditions. 165
- Figure 5.10. A surface plot of the variation in ozone-water mass transfer coefficient as a function of the input gas (Q_G) and water flow rates (Q_L) using the baffled reactor. 166
- Figure 5.11. Plots of ozone-water mass transfer coefficient (k_{LA}) obtained using the baffled reactor without oscillation and the OBR at Re_o of 4600 as a function of input water flow rate. At $Q_G = 0.2 \text{ dm}^3 \text{ min}^{-1}$ and $[O_3]_G = 29.8 \text{ mg dm}^{-3}$ 167
- Figure 5.12. A surface plot of ozone-water mass transfer efficiency as a function of the input gas and water flow rates obtained using the baffled reactor. 168
- Figure 5.13. Plots of MTE obtained using the baffled reactor and the OBR as a function of input water flow rate; the conditions as for fig. 5.11. 169
-
- Figure 6.1. A typical chromatogram of 50 mg dm^{-3} of Cu(II)-EDTA in water obtained using ion chromatography. 175
- Figure 6.2. Calibration curve of Cu(II)-EDTA in water obtained using ion chromatography for the peak observed at the retention time of 13.4 minutes. $R^2 = 0.999$ 175
- Figure 6.3. Plots of % removal of Cu(II)-EDTA by ozonation as a function of the reactor arrangement and water residence time. The input water flow rate was varied from 0.02 to $0.1 \text{ dm}^3 \text{ min}^{-1}$. The experiments were carried out at room temperature with no pH adjustment. The Cu(II)-EDTA initial concentration was 250 mg dm^{-3} . Ozone flow rate and concentration were $0.4 \text{ dm}^3 \text{ min}^{-1}$ and $60.4 \pm 0.7 \text{ g m}^{-3}$, respectively. The oscillatory Reynolds number (Re_o) was fixed at 4600 in the case of the OBR. The inset shows plots of $\ln ([\text{Cu(II)-EDTA}]_t / [\text{Cu(II)-EDTA}]_0)$ vs. time. 176
- Figure 6.4. Photographs of Cu(II)-EDTA solution before and after ozonation treatment using the baffled reactor (a), and (b) the effluent collected from the baffled reactor and OBR after treatment. The input ozone concentration was $60.4 \pm 0.7 \text{ g m}^{-3}$ at $0.4 \text{ dm}^3 \text{ min}^{-1}$. The Cu(II)-EDTA initial concentration was 250 mg dm^{-3} and the water flow rate was $0.02 \text{ dm}^3 \text{ min}^{-1}$ 178

Figure 6.5. Plots of % reduction in the total organic carbon (TOC) content of the Cu(II)-EDTA solutions as a function of total residence time and reactor arrangement. The initial TOC concentration was $86.0 \pm 1.0 \text{ mg dm}^{-3}$. The experimental conditions were the same as those in fig. 6.3..... 181

Figure 6.6. A typical IC chromatogram of 50 mg dm^{-3} of Fe(III)- EDTA in water. 182

Figure 6.7. Plots of the reduction in total organic carbon (TOC) of the Fe(III)-EDTA solutions as a function of total residence time, treatment type and reactor arrangement. TOC at 0% reduction = $45.0 \pm 1.0 \text{ mg dm}^{-3}$. The experimental conditions were the same as in fig. 6.3. 183

Figure 6.8. Photos of Fe(III)-EDTA solution after ozonation and UV treatment (i) and (ii), and after ozonation (iii) and (iv) using baffled reactor (i) and (iii) and OBR (ii) and (iv) treatment (a) and (b) the effluents characteristic collected from baffled reactor and OBR after treatment. The experimental conditions were the same as in 6.9. 184

Figure 6.9. Electrospray Ionization Mass Spectroscopy (ESI-MS) spectra of Fe(III) EDTA samples after ozonation for: (a) 8 and (b) 17 minutes using the OBR. The experimental conditions were the same as in fig. 6.7. 185

Figure 6.10. Electrospray Ionization Mass Spectroscopy (ESI-MS) spectra of Fe(III) EDTA samples after ozonation for: (a) 8 and (b) 17 minutes using the OBR followed by UV irradiation. The experimental conditions were the same as in fig. 6.7. 187

Figure 6.11. Typical IC chromatogram of Cu(II)-EDTA degradation by-products after ozonation and UV irradiation. The input ozone concentration was $60.4 \pm 0.7 \text{ mg dm}^{-3}$ at $0.4 \text{ dm}^3 \text{ min}^{-1}$. The initial concentration of Cu(II)-EDTA was 250 mg dm^3 , and the input water flow rate was $0.2 \text{ dm}^3 \text{ min}^{-1}$ using the baffled reactor for ozonation. 188

Figure 6.12. Degradation pathways of EDTA: A, B and C by ozonation, A and B by UV irradiation. Reproduced after Gilbert and Hoffmann-Glewe [9] and Sorensen et al. [23]. (*) identified during this work..... 189

Figure 6.13. Possible mechanism for the formation and decomposition of N-MED3A. .. 189

List of Tables

Table 1.1. A summary of NTP reactions induced by electron collisions [7, 43-45].5

Table 1.2. Typical ozone generating and destroying reactions in NTPs and their rate coefficients. T is the temperature in K.8

Table 1.3. Ozone concentration and yield efficiency generated by different types of DBD. 13

Table 2.1. Physical properties of the dielectrics employed for ozone generation using novel dielectric barrier discharge-packed beads reactor (DBD-PBR).56

Table 2.2 Summary of the experimental conditions employed in FTIR experiments reported in this thesis.60

Table 2.3. Summary of the experimental conditions employed for ozone- water mass transfer study.72

Table 2.4. The oscillation conditions employed for the work reported in this thesis.72

Table 2.5 Summary of the operational conditions employed for M-EDTA treatment.74

Table 3.1. Assignments of the various features observed in the spectra shown in figure 3.282

Table 3.2. List of initiating reactions induced by electron collisions with different molecules within ambient air [11-13].82

Table 3.3. List of chemical reactions taking place in humid artificial air non-thermal plasma and their rate coefficients. N_2^* and O_2^* correspond to the electronically excited states $N_2(A)$ and $O_2(^1\Delta)$, respectively. * T is the temperature in K. ...85

Table 3.4. Input power and feed gas flow rates and their corresponding specific energy densities employed for the in-situ FTIR experiments.90

Table 2.1. Physical properties of the dielectrics employed for ozone generation using the novel dielectric barrier discharge-packed beads reactor (DBD-PBR). 117

Table 4.2. R^2 coefficients and slopes of the plots in fig. 4.12. 131

Table 4.3. The concentrations of O_3 , N_2O and NO_2 as a function of dielectric calculated from the data shown in figs. 4.15(a) and (b). BDL = below detection limit... 136

Table 4.4. The concentrations of NO ₂ , O ₃ and N ₂ O as a function of dielectric calculated from the data shown in figs. 4.18(a), (b), (c) and (d). DBL = below detection limit.	142
Table 2.3. Summary of the experimental conditions employed in the ozone- water mass transfer study.....	151
Table 2.4. The oscillation conditions employed for the work reported in this chapter.	151
Table 5.1. Summary of k _{LA} values, Henry's law constant and steady state dissolved ozone concentrations at different input ozone concentrations from the data in fig.5.1.	153
Table 5.2. A comparison of ozone-water mass transfer coefficient (k _{LA} , s ⁻¹) determined in this work using the bubble column with the correlation proposed by Watanabe et al. [16] for bubble columns.	160
Table 5.2. The effect of the reactor arrangement and input gas (Q _G) and liquid flow rates (Q _L) on the dissolved ozone concentration and MTE. The Re _o was 4600 in the case of the OBR.	170
Table 2.5. Summary of the operational conditions employed for water remediation.	174
Table 6.1. A comparison of the experimental conditions and results of Cu(II)-EDTA treatment with ozone obtained in this work to those obtained by Yang et al. [7] using a bubble column reactor. * Estimated using the decomposition rates $2.22 \times 10^{-1} \pm 4.8 \times 10^{-3}$ and $2.64 \times 10^{-1} \pm 5.4 \times 10^{-3} \text{ min}^{-1}$ obtained from fig. 6.3 using the baffled reactor and the OBR, respectively.	178
Table 6.2. A comparison of Cu(II)-EDTA % removal by ozonation and ozonation followed by UV irradiation as a function of reactor arrangement and total residence time. The experimental conditions were similar to those showed in figure 6.3.	179

List of Abbreviations

Nomenclature

C_d	Dielectric capacitance (F)
P	Discharge power (W)
V_o	Discharge onset voltage (kV)
V	Discharge voltage (kV)
C_g	Gas capacitance (F)
C	Total capacitance of the dielectric and gas (F)
A	Dielectric surface area (m^2)
d	Discharge gap thickness (m)
q	The overall heat transfer rate ($kJ\ m^{-2}\ hr^{-1}$)
k_e	Heat transfer coefficient ($kJ\ m^{-1}\ hr^{-1}\ K^{-1}$)
Re	Reynolds number
Δx	The pathlength of heat transfer (m)
ΔT	Change in temperature (K)
C_p	Specific heat of the gas ($kJ\ kg^{-1}\ ^\circ C^{-1}$)
G	Gas mass flow rate ($kg\ m^2\ hr^{-1}$)
L_p	Average length between the centres of two neighbouring particles (m)
D_p	Average diameter of packing particles (m)
k_s	Thermal conductivities of the packing material ($kJ\ m^{-1}\ hr^{-1}\ K^{-1}$)
k_g	Thermal conductivities of the feed gas ($kJ\ m^{-1}\ hr^{-1}\ K^{-1}$)
L_s	The length of solid affected by thermal conductivity (m)
L_v	The gas film thickness adjacent to the contact of two solid particles (m)
h_{rs}	Heat transfer coefficient for solid-to-solid ($kJ\ m^{-1}\ hr^{-1}\ K^{-1}$)
h_{rv}	Heat transfer coefficient for void-to-void radiations ($kJ\ m^{-1}\ hr^{-1}\ K^{-1}$)
P_G	Partial pressure of the substance in the gas phase (atm)
P_{Gi}	Partial pressure of the substance in gas at the gas-liquid interface (atm)

Preface

C_L	Concentration of the substance in Liquid bulk (mol dm^{-3})
C_{Li}	Concentration of the substance in liquid at the at interface (mol dm^{-3})
NA	Overall rate of gas-to-liquid mass transfer ($\text{kmol m}^{-2} \text{s}^{-1}$)
k_G	Mass transfer coefficient in gas phase ($\text{kmol m}^{-2} \text{s}^{-1} \text{atm}^{-1}$)
k_L	Mass transfer coefficient in liquid phase (m s^{-1})
K_G	Overall mass transfer coefficient in gas phase ($\text{kmol m}^{-2} \text{s}^{-1} \text{atm}^{-1}$)
K_L	Liquid overall mass transfer coefficients (m s^{-1})
m	Equilibrium coefficient between two phases ($\text{atm m}^3 \text{kmol}^{-1}$).
D_L	Diffusivity coefficient in liquid phase ($\text{m}^2 \text{s}^{-1}$)
D_G	Diffusivity coefficient in gas phase ($\text{m}^2 \text{s}^{-1}$)
d_b	Sauter mean bubble diameter (m)
U_b	Rising velocity of the bubble (m s^{-1})
t	Time (s)
S	Liquid film renewal rate (s^{-1})
C^*	Steady state dissolved gas concentration (mg dm^{-3})
C	The dissolved ozone concentration (mg dm^{-3})
D_A	Gas diffusivity coefficient ($\text{m}^2 \text{s}^{-1}$)
Ha	Hatta number
Re_o	Oscillatory Reynolds number
St	Strouhal number
x_o	Oscillation amplitude centre to peak (m)
A	Absorbance
S_R	Reference spectrum
S_S	Sample spectra
IBI	Integrated band intensity coefficient (cm molecule^{-1})
b	The transmission cell pathlength (cm)
U_G	Superficial gas velocity (cm s^{-1})

Preface

Q_G	Gas flow rate ($\text{cm}^3 \text{s}^{-1}$)
r	Cylinder radius (cm)
H	The height of the catalyst (cm)
D_o	Internal diameter of column (mm)
Q_L	Liquid flow rate ($\text{cm}^3 \text{min}^{-1}$)
U_L	Superficial liquid velocity (cm s^{-1})
TOC	Total organic carbon (mg dm^{-3})
TC	Total carbon (mg dm^{-3})
IC	Inorganic carbon (mg dm^{-3})
ESI	Electrospray Ionization
MS	Mass Spectroscopy
SED	The specific energy density (J cm^{-3})
T	Temperature (K)
R	Ideal gas constant ($\text{dm}^3 \text{atm K}^{-1} \text{mol}^{-1}$)
H_o	Henry's Law constant ($\text{atm dm}^3 \text{mol}^{-1}$)
h	The liquid height in the column during the aeration (cm)
h_o	The liquid height in the column before the aeration (cm)
D1	2.0 mm Alumina pellets
D2	Borosilicate glass beads
D3	A ₃ molecular sieve
D4	Soda-Lime glass beads
D5	3.0 mm Alumina pellets
D6	Perforated PTFE sheets

Greek Symbols

ϵ_r	The dielectric constant (F m^{-1})
ϵ_o	The vacuum permittivity ($8.854 \times 10^{-12} \text{F m}^{-1}$)

Preface

α	The ratio of the feed gas mass velocity in packed bed to the empty bed
η	Ozone yield efficiency (g/kWh)
ρ	The liquid density (kg m^{-3})
μ	The liquid viscosity ($\text{kg m}^{-1} \text{s}^{-1}$)
ϵ_G	Gas hold-up
δ_L	Liquid film thickness at the gas-liquid interface (m)
δ_G	Gas film thickness at the gas-liquid interface (m)
β	The ratio of L_p to D_p
ρ_g	Gas density (kg m^{-3})
μ_g	Gas viscosity ($\text{kg m}^{-1} \text{s}^{-1}$)
δ	The ratio of the area between two particles to the total cross-sectional area of the particles
γ	The ratio of L_s to the D_p
ϕ	The ratio of L_v to D_p
ϵ	Fractional void

Acronyms

NTP	Non-thermal Plasma
TP	Thermal Plasma
DBD	Dielectric Barrier Discharge
SDBD	surface dielectric barrier discharge
CCD	Cold Corona Discharge
DC	Direct current
AC	Alternating current
E	Electric field strength
FTIR	Fourier Transform InfraRed spectroscopy
APPJ	Argon-fed atmospheric pressure plasma jet

Preface

VD	Volume discharge
SD	Surface discharge
PBD	Packed bed discharge
DBD-PBR	Dielectric barrier discharge packed bed reactor
E	Enhancement factor caused by chemical reaction
ST	Stirred tank
OBR	Oscillatory baffled reactors
PGWD	The packing gap width for the dielectric (cm)
DBL	Below Detection Limit
MTE	The mass transfer efficiency (%)

1. Introduction

The main focus of this thesis is twofold: (i) understanding the chemistry taking place in an air-fed non-thermal plasma (NTP) as a fundamental step in the (ii) application of NTP in ozone production from oxygen or air and the application of ozone in combination with UV irradiation for water treatment. Thus, the main aim of this chapter is to introduce the concepts, background, challenges and the hypothesis of the research. The research aims & objectives and the overall structure of the thesis are presented towards the end of this chapter.

1.1. Non-thermal plasma definition, principles and applications

Plasma is normally referred to as the fourth state of matter due to its distinctive physical and chemical properties. Plasma is an ionized gas that consists of free electrons, ions, radicals, excited and neutral molecules or atoms. Hence, it is electrically conductive and sensitive to magnetic fields [1, 2]. Plasma can occur naturally or be produced artificially. Solar corona, the solar wind, lightning and the Aurora Borealis are forms of natural plasma, and these are shown in fig. 1.1. The Aurora Borealis (fig. 1.1 (ii)) occurs because of the trapping of charged particles formed outside the Earth's atmosphere by solar irradiation by the magnetic field of the Earth [1]. This phenomenon may be taken as an example of the plasma sensitivity toward magnetic fields. On the other hand, plasma can be produced artificially through the injection of a sufficient amount of energy to cause gas excitation [2]. This energy may be delivered in different forms: by heating (e.g. radiofrequency [3] and microwave plasma [4]), photoionization (e.g. laser-plasma [2, 5]), by exposing neutral gas to beams of charged ions or electrons or by electrical discharge [2].

Atmospheric pressure plasma can be classified as either thermal (TP) or non-thermal (NTP) depending on the temperature of the electrons and heavier components (i.e. atoms, molecules, radicals and ions) [6]. In the case of TP, the electrons and the other species have similar temperatures ($\approx 10,000$ K), and hence it is termed an equilibrium plasma [6, 7]. The formation of TP requires high power densities, e.g. from 100 W cm^{-3} to 10 kW cm^{-3} [8]. This type of plasma has found wide application in industry including: materials processing, plasma cutting, spray coating, vapour deposition, solid waste treatment, welding and powder disinfection [9]. In Non Thermal Plasma, the electron temperature (i.e. $10000 - 100000$ K) is much higher than that of the heavier components which remain between 300 to 1000 K [6]. The energy of NTP electrons lies between 1 and 10 eV [6, 7, 10], and when these

electrons collide with neutral gas molecules, the latter undergo reactions including excitation, ionization and dissociation, and hence free radicals, ions, photons and excited molecules are produced.

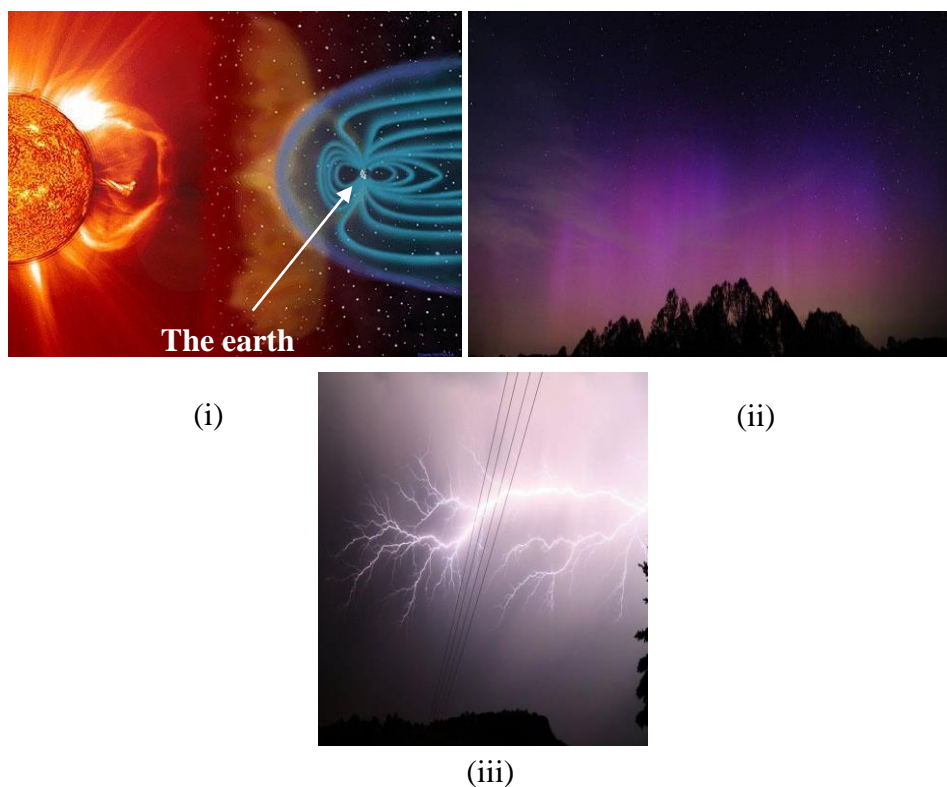


Figure 1.1. Examples of natural plasma: (i) the solar wind, (ii) Aurora Borealis and (iii) lightning. Photos were reproduced with permission from the NASA website: www.nasa.gov.

The high activity of NTP and low temperature of the gas molecules has led to a wide range of applications in the industrial, environmental and medical fields. Some of the NTP applications are: ozone generation, polymer processing [11-13], the removal of air contaminants such as SO₂, NO_x, VOC [14-17], the hydrogenation of CO₂ [18], and the sterilization and disinfection of contaminated surfaces [19-22] including living tissues [23, 24].

1.2. NTP and ozone generation

1.2.1. Ozone

Ozone is a triatomic oxygen molecule (O_3) that was first discovered by Martinus Van Marum in 1785 and accepted as a new chemical compound in 1839 [25]. The first reliable method for ozone generation from air or oxygen was proposed by Werner Siemens (1887), and was based on passing oxygen through an alternating electric field between two electrodes separated by a glass tube and with a narrow gap [7, 25]. This method is known today as dielectric barrier discharge (DBD), and is recognised as an effective method of generating NTP and finds wide applications in different fields including ozone generation [26].

Ozone is a strong oxidant with a redox potential of up to 2.07 V in acidic media [27], which generates nontoxic by-products (i.e. O_2) compared to other oxidants (e.g. Cl_2 or $KMnO_4$). In addition, ozone is produced on-site and hence does not require storage or transportation to the point of use. Ozone is employed in water and wastewater treatment due to its high oxidation potential and ability to remove a wide range of chemical [28, 29] and biological contaminants [30]. Ozone can be used alone or in combination with other approaches such as UV irradiation to induce the formation of free radicals such as $\cdot OH$ (i.e. stronger oxidizing agent than ozone) [31, 32]. Some other applications of ozone include: flue gas treatment, food preservation, indoor air cleaning, and semiconductor processing [33].

1.2.2. Ozone generation methods

There are a number of established methods for ozone generation including: photo-dissociation of oxygen by UV irradiation at 172 nm [34], catalytic electrolysis of water [35] and by electrical discharge [36]. Among these methods, electrical discharge is considered to be the most effective technique for generating high concentrations of ozone [37]. Cold Corona Discharge (CCD) and Dielectric Barrier Discharge (DBD) are the most common electrical discharge-based ozone generators available to date. Both CCD and DBD are based on the same principle of ozone generation, varying only in the arrangement of the electrodes and the inclusion of a dielectric layer (e.g. glass or ceramic) in the case of DBD system as can be seen in figure 1.2.

In CCD systems, the NTP is induced by an alternating or pulsing low current (ca. $10^{-10} - 10^{-5}$ A) power supply [6] to prevent arcing [38]. The electrodes commonly employed in CCD

generators are wire and plate, see fig. 1.2 (i); this arrangement increases the homogeneity of the discharge and gives rise to higher electric fields [7]. Accordingly, the NTP produced in a CCD generator is primarily limited to the area surrounding the tip of the wire electrode [6, 7, 39].

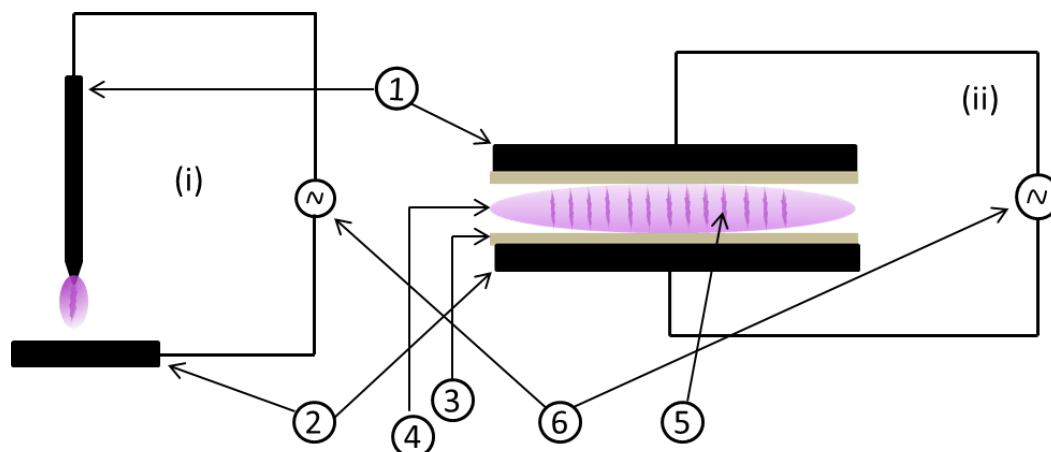


Figure 1.2. Schematic representation of cold corona discharge (CCD) (i), and dielectric barrier discharge (DBD) (ii); (1) High voltage cathode, (2) anode, (3) dielectric layer, (4) plasma discharge, (5) NTP streamers and (6) AC power supply. Redrawn from Tendero et al. [6].

In contrast to CCDs, DBD systems consist of two parallel metal electrodes at least one of which is covered by a layer of dielectric material. The dielectric between the DBD electrodes plays an important role in enhancing the efficiency of NTP generation. One of the ways in which this is achieved is that the dielectric decreases the discharge gap volume between the DBD electrodes, and hence increases the field strength according to:

$$E = V/d \quad (1.1)$$

Where E is the field strength ($V\ m^{-1}$), V is the discharge voltage (V) and d is the gap width between electrodes (m). Another benefit of the dielectric layer is the accumulation of charge on its surface (i.e. dielectric capacitance) which causes a homogenous distribution of the micro-discharges across the entire discharge gap [6, 7, 40]. This increases the active area of

the NTP along the system. In addition, the dielectric layer prevents arcing by lowering the discharge current which can be continuous (DC) or pulsing (AC), with the latter being preferred for ozone generation to limit heat formation [6]. Hence, DBD is generally found to be more efficient for ozone production than CCD.

1.2.3. Mechanism of NTP formation by electric discharge

In both CCD and DBD, an electrical field is generated between two electrodes, one of which is connected to a high voltage power supply (cathode) while the other is grounded (anode). The electric field strength between the electrodes increases with the input power until the gas starts to breakdown, e.g. at an electric field of 30 - 37 kV cm⁻¹ in oxygen and 47 - 57 kV cm⁻¹ in air depending on the electrode arrangement [37, 41]. Above the threshold of gas breakdown, highly energetic electrons (initiators) having energies of 1-10 eV [10] accumulate on the surface of the cathode [37, 43]. Consequently, electronegative molecules within the gap migrate towards the cathode side and undergo a series of reactions including excitation, dissociation, ionization and recombination which are summarized in table 1.1 [43 - 45, 7]. Within a few nanoseconds, the area near the cathode becomes more conductive and facilitates the movement of electrons and ions towards the anode. The high energy electrons move first, followed by the lower energetic electrons (i.e. secondary electrons) and heavier particles forming micro-discharging channels (i.e. streamers) through the discharge gap with a typical width of 100 - 400 μm [42]. Secondary electrons are those with energies insufficient

Types of NTP initiative reactions		
<i>Excitation</i>	$e + O_2 \longrightarrow O_2^* + e$	(1.1)
<i>Dissociation</i>	$e + O_2 \longrightarrow O + O + e$	(1.2)
<i>Attachment</i>	$e + O_2 + M \longrightarrow O_2^- + M$	(1.3)
<i>Dissociative attachment</i>	$e + O_2 \longrightarrow O^- + O$	(1.4)
<i>Ionization</i>	$e + O_2 \longrightarrow O_2^+ + e + e$	(1.5)
<i>Recombination</i>	$e + O_2^+ \longrightarrow O_2$	(1.6)
<i>Detachment</i>	$e + O_2^- \longrightarrow O_2 + e + e$	(1.7)
<i>Dissociative ionization</i>	$e + O_2 \longrightarrow O^+ + O + e$	(1.8)

Table 1.1. A summary of NTP reactions induced by electron collisions [7, 43-45].

for changing the electronic structure of the neutral molecules [46], and hence these electrons tend to increase the temperature of the gas by increasing the rates of elastic collisions [6, 46, 47].

Figure 1.3 shows photos of the development and propagation of a single micro-discharge within a DBD fed with dry artificial air (i.e. 20 % O₂ in N₂), each of these photos was obtained for a separate micro-discharge by Ryo et al. [48] using an intensified charge-coupled device (ICCD) camera. It should be noted that the DBD system in their work was operated in positive discharge mode (i.e. the working electrode was the anode), and hence the main streamer propagation occurred from the anode side toward the cathode. The length

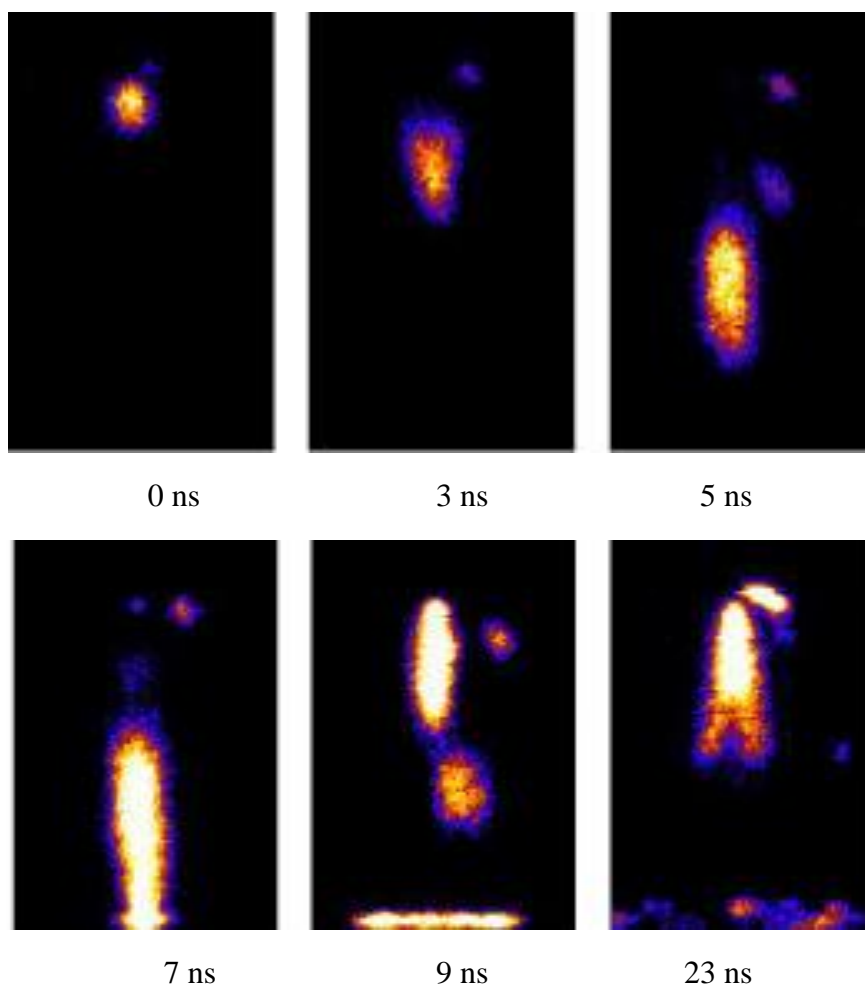


Figure 1.3. Photos of micro-discharge development with time using DBD fed with dry air, discharge voltage and gap width were 28 kV and 5.0 mm, respectively. The photos were taken using an intensified charge-coupled device (ICCD) camera [48].

of a micro-discharge channel across the discharge gap (i.e. 5.0 mm) increases as the input voltage increases, and hence the plasma volume increases until it reaches an optimal level [48]. Exceeding the optimal input power leads to arc formation between both electrodes causing the electric field to breakdown [38]. As can be seen from fig. 1.3, during the streamer propagation from the cathode toward the dielectric they lose some of their brightness (i.e. their energy). As the micro-discharge reaches the dielectric, it spreads on its surface and reduce the electric field on the covered areas of the dielectric [26], while allowing new micro-discharges to arrive at uncovered parts of the surface depending on the dielectric surface area and dielectric constant. This effect regulates the amount of current delivered by each micro-discharge which is one of the advantages of dielectric materials in DBDs. The number and thickness of these micro-discharges increase with the discharge power, frequency, electric field strength (E), surface area and dielectric constant of the dielectric material [26, 40]. The unionized gas surrounding the micro-discharges absorbs the energy released and collect products (e.g. ozone) from the micro-discharges [26].

Ryo et al. [48] observed the highest ozone concentrations in the brightest regions of the micro-discharge, see fig. 1.3. In addition, the concentration of ozone was observed to increase with the width of the micro-discharges during their propagation within the DBD [48]; this suggested that ozone generation is not limited to the preliminary stages of NTP formation, but can occur through interaction between the NTP with oxygen molecules [48]. Similar behaviour was observed by Schmidt-Bleker et al. [49] who investigated the formation of chemically and biologically active species through the interaction of a plasma jet with the surrounding air during the application of an argon-fed atmospheric pressure plasma jet (APPJ). In their system, the plasma jet device was mounted in a chamber in which humidified mixtures of oxygen and nitrogen were introduced to the jet. The exhaust was then monitored downstream of the plasma using Fourier Transform InfraRed (FTIR) spectroscopy. Their results showed that ozone and nitrogen dioxide were the main products, with small amounts of H_2O_2 and HNO_3 .

1.2.4. Ozone generation in DBD

The generation of ozone is initiated within 10^{-8} s of the formation of a NTP [7] through the interaction of atomic oxygen radicals (i.e. produced from reaction 1.2) with oxygen molecules to form ozone through reaction (1.9) as can be seen in table 1.2. Table 1.2 shows some examples of the chemical reactions responsible for ozone generation and destruction

in a dry mixture of oxygen and nitrogen, along with their rate coefficients. In reaction (1.9), M represents a third body (e.g. oxygen or nitrogen) which absorbs the energy released from the ozone generating reaction. According to Haacke and co-workers [41], electrons with energies ≥ 6 eV can split oxygen molecules into atoms, while electrons with lower energies accelerate ozone dissociation. Thus, the rate of reactions (1.2) and, consequently, (1.9) are determined primarily by the energy and number of the colliding electrons. These are determined by the discharge field strength and current, respectively [40].

From table 1.2, it can be seen that reactions (1.10), (1.11) and (1.12) are the main routes for ozone dissociation within the DBD when pure oxygen is employed as a feed gas. As can be seen from the table, the rate coefficient of reaction (1.9) is increased by decreasing temperature, and the opposite is true in the case of reactions (1.10), (1.11) and (1.12); hence ozone generation is highly temperature-dependent. Furthermore, even though atomic oxygen is necessary for ozone generation via (1.9) the ratio of $[O]/[O_2]$ should not exceed ca. 10^{-4} to minimize the loss of ozone via reaction (1.11) [36].

(R#)	Reaction	Rate coefficient (k)	Ref
(1.9)	$O + O_2 + M \rightarrow O_3 + O_2$	$5.6 \times 10^{-34} (T/300)^{-2.8} \text{ cm}^6 \text{ s}^{-1}$ (M = O ₂)	[50]
(1.10)	$O_3 + M \rightarrow O + O_2 + M$	$3.92 \times 10^{-16} \exp(-11400/T) \text{ cm}^3 \text{ s}^{-1}$	[51]
(1.11)	$O + O_3 \rightarrow O_2 + O_2$	$8.0 \times 10^{-12} \exp(-2060/T) \text{ cm}^3 \text{ s}^{-1}$	[52]
(1.12)	$O_2^* + O_3 \rightarrow O + O_2 + O_2$	$5.2 \times 10^{-11} \exp(-2840/T) \text{ cm}^3 \text{ s}^{-1}$	[53]
(1.13)	$O + O + O_2 \rightarrow O_2 + O_2$	$2.45 \times 10^{-31} (T)^{-0.63} \text{ cm}^3 \text{ s}^{-1}$	[25]
(1.14)	$N + O + M \rightarrow NO + M$	$6.3 \times 10^{-33} \exp(140/T) \text{ cm}^6 \text{ s}^{-1}$	[54]
(1.15)	$N + O_2 \rightarrow NO + O$	$4.4 \times 10^{-12} \exp(-3220/T) \text{ cm}^3 \text{ s}^{-1}$	[52]
(1.16)	$O_3 + N \rightarrow NO + O_2$	$6.3 \times 10^{-33} \exp(140/T) \text{ cm}^6 \text{ s}^{-1}$	[55]
(1.17)	$O_3 + NO \rightarrow NO_2 + O_2$	$4.3 \times 10^{-12} \exp(-1560/T) \text{ cm}^3 \text{ s}^{-1}$	[55]
(1.18)	$O_3 + NO_2 \rightarrow NO_3 + O_2$	$1.03 \times 10^{-16} \exp(-2628/T) \text{ cm}^3 \text{ s}^{-1}$	[55]

Table 1.2. Typical ozone generating and destroying reactions in NTPs and their rate coefficients. T is the temperature in K.

When the feed gas contains nitrogen in addition to oxygen, the number of direct ozone destructive reactions increases to include the reactions with atomic nitrogen (1.16), NO (1.17) and NO₂ (1.18). In simple terms, the contribution of these species to ozone decomposition would be expected to increase with their concentration. Furthermore, the presence of N₂ molecules can depress the generation of ozone indirectly through: (i) consumption of energetic electrons by the dissociation and/or ionization of N₂; and (ii) consumption of atomic oxygen through, for instance, reaction (1.14). However, as was the case for (1.10), (1.11) and (1.12), almost all of the direct and indirect ozone-destroying reactions induced by the presence of N₂ are temperature-dependant, and their effect may be minimized by efficient cooling of the DBD. On the other hand, some N₂ excited species and radicals can assist ozone formation via splitting oxygen molecules, e.g. reaction (1.15). It should be noted that, besides the reactions listed in table 1.2, there are other reactions that can affect ozone generation such as those including other NO_x species and excited molecules. In addition, the presence of water vapour and CO₂ within the feed gas (i.e. ambient air) play additional roles in ozone decomposition. Therefore, the mechanism of ozone generation is affected significantly by the chemical composition of the NTP.

1.2.5. NTP chemistry of air and ozone generation

From the above discussion it may be concluded that the ozone generation mechanism is very complex when NTP is produced from ambient air due to the significant increase in the number of reactions that can occur within the NTP by different air constituents in contrast, for instance, to pure oxygen. The concentrations of neutral species and other intermediates such as ions, excited components and radicals within the NTP have been estimated by numerical modelling based on schemes consisting a number of elementary reactions that are expected to take place in the plasma. Interestingly, the number of these elementary reactions varies from tens [56, 57] to hundreds [58] or even to thousands [43] depending on the species considered. Furthermore, most of these models assume that the gas temperature during the discharge remains unchanged [57, 58]. In fact, this assumption is invalid considering the fact that one of the properties associated with DBD is the continuous change in the temperature of the dielectric during operation [24, 59, 60]. Hence, not only the output of the plasma will be affected by the plasma temperature but also the rates of diffusion of the constituents of the plasma from the plasma to the post-discharge regions [61].

Recently, monitoring the composition of the NTP has received more attention in some fields such as biomedical applications [49, 62] to identify the possible formation of bioactive species during the interaction of argon plasma with air during treatment of, for example, living tissues. For instance, Pipa & Ropcke [62] have shown that Fourier Transform InfraRed spectroscopy (FTIR) can be employed to identify the species within the exhaust stream of an argon-fed atmospheric pressure plasma jet (APPJ) which was contaminated with 1.0% ambient air. The authors identified: NO_2 , NO , N_2O , HNO_2 , HNO_3 , CO_2 and CO in the exhaust, and suggested that the formation of the latter two may be due to the interaction of the plasma jet with plastic components of the APPJ. The study carried out by Reuter et al. [63] showed that the ozone formed by feeding a mixture of pure oxygen and argon to an APPJ can be monitored in and after the plasma glow region using mid-infrared quantum cascade laser absorption spectroscopy. Thus, in contrast to the work of Pipa and Ropcke [62], it may be concluded that the chemical composition of the exhaust of NTP depends on the method of introducing air to the plasma jet (i.e. in the feed gas, or by interaction of the air surrounding the plasma jet). In addition, these results suggest that the composition of the plasma effluent changes as it moves downstream from the discharge [43]. This change may be due to continuous internal chemical reactions within the NTP, and/or to the latter interaction with the surrounding molecules as discussed in section 1.2.3.

Despite the wide application of DBD, there are few studies in which the output of these reactors post the glow region is monitored, and no papers report the analysis of the plasma glow itself. The only study in which the near discharge region of a DBD was investigated (i.e. ca. 2 cm post the plasma glow) was that by Sakiyama et al. using FTIR spectroscopy [64]. In their work, a numerical model including 600 chemical reactions was proposed to simulate the changes in the exhaust of a surface dielectric barrier discharge (SDBD) with time. Their model was based on the assumption that the concentrations of the neutral species in post plasma region are mainly determined by the rate of their diffusion from the discharge region. In their experimental work, FTIR analysis was carried out to identify the neutral species in the exhaust of a SDBD ca. 2.0 cm after the plasma glow in a closed system using a fixed volume of humidified artificial air (i.e. 80% N_2 + 20% O_2). The authors detected a number of neutral species, i.e. O_3 , N_2O , N_2O_5 and HNO_3 . However, no quantitative analysis was conducted to compare the experimental data with those predicted by their model.

From the work discussed in this section it is clear that direct NTP monitoring may be achievable by extending the plasma glow to out of DBD reactor to facilitate direct spectroscopic analysis. Hence, this can be attained by modifying the DBD to obtain a similar configuration to that proposed by Koinuma et al. [65] to produce a plasma jet with sufficient length for monitoring. This would be expected to allow better understand of the NTP dynamics specially if it was combined with the analysis of the downstream region (i.e. post the plasma glow region).

1.2.6. Types of DBD

Dielectric barrier discharge has been classified into three different types based on the electrode arrangement i.e.: volume discharge (VD), surface discharge (SD) and packed bed discharge (PBD) [40, 66, 67]. These three types are shown in fig. 1.4. In the case of VD, the active region of NTP is within the gap between the cathode and the dielectric layer, while in case of SD the discharge takes place only on the surface of the dielectric material. In both SD and VD the NTP concentrates near the high voltage electrode as can be seen in fig.1.4.

In the case of packed bed reactors (PBD), dielectric pellets or beads are placed between the electrodes, and the configuration can be plate to plate or cylinder to cylinder [10]. As a result, the simultaneous occurrence of volume discharge and surface discharge is more likely in a PBD. The volume discharge occurs within the voids between the beads, while the surface discharge takes place on the surface of the beads as well as at the points of contact between the beads and discharge electrodes [68, 69]. Another advantage of the packed bed configuration is the numerous contact points between the electrodes and the dielectric which increases the electric field strength and lowers the required onset voltage by reducing the discharge gap [37], see equation 1.1. Table 1.3 shows a comparison between the three types of DBD based on the highest ozone concentration and yield efficiency. The ozone yield efficiency (g/kWh) is determined according to [42, 70]:

$$\eta = C Q / P \quad (1.2)$$

where C is the ozone concentration (g dm^{-3}), Q is flow rate ($\text{dm}^3 \text{ h}^{-1}$), and P is input power (kW).

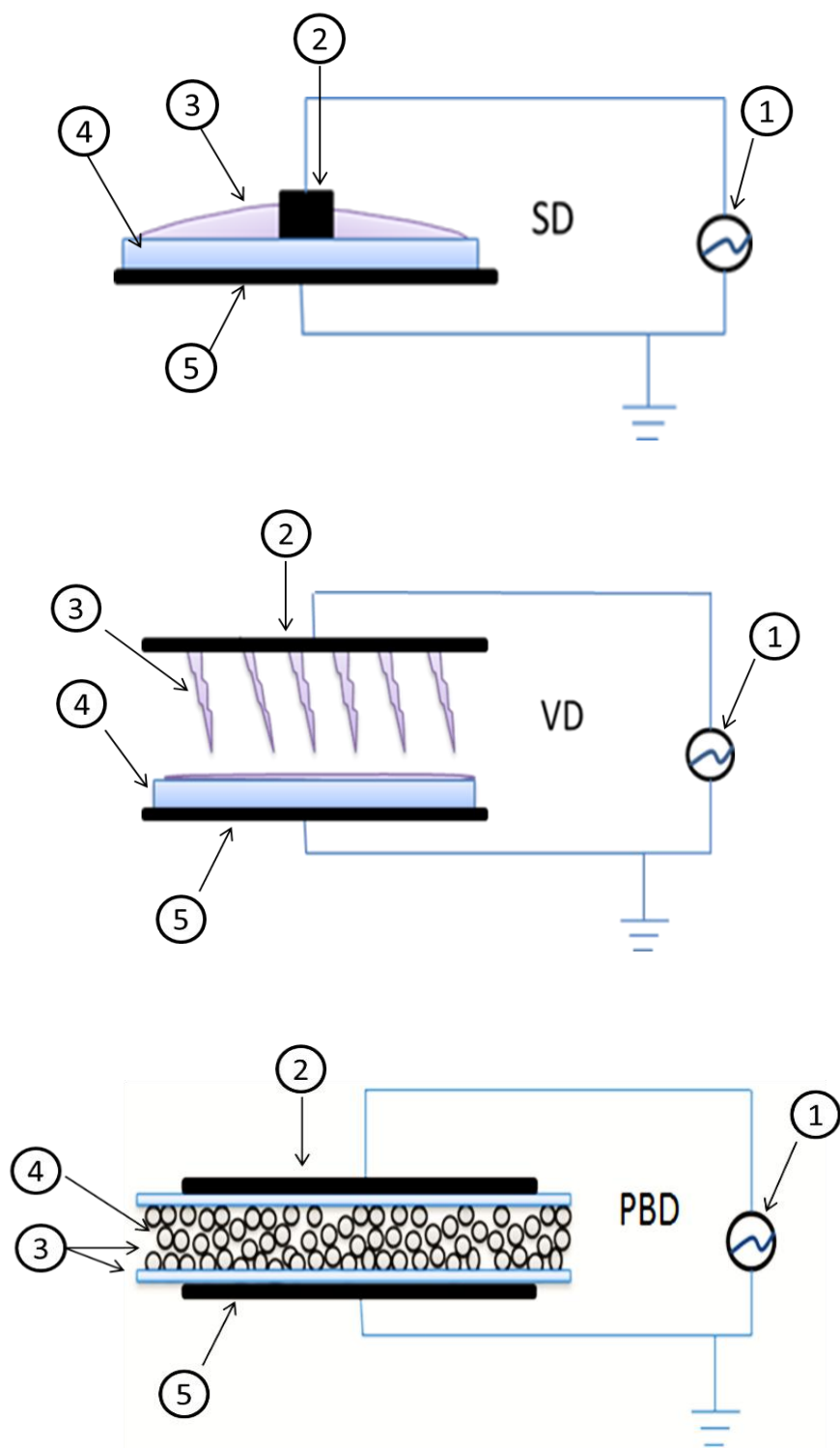


Figure 1.4. Schematic of the different types of DBD: volume discharge (VD), surface discharge (SD) and packed bed discharge (PBD). Each consists of: (1) power supply, (2) cathode, (3) NTP active region, (4) dielectric layer or beads, and (5) anode.

<i>DBD type</i>	<i>Feed gas</i>	<i>Ozone concentration/ g m⁻³</i>	<i>Ozone yield efficiency/ g kW⁻¹ h⁻¹</i>	<i>Coolant temperature/ °C</i>	<i>Reference</i>
<i>PBD</i>	Oxygen	61	173	No cooling	[70]
<i>PBD</i>	Oxygen	130	83.3	Water/ 25 °C	[67]
<i>SD</i>	Oxygen	4	173	Air/ 21 °C	[73]
<i>SD</i>	Oxygen	2	170	No cooling	[66]
<i>VD</i>	Oxygen	4	210	No cooling	[66]
<i>VD</i>	Oxygen	20	202	No cooling	[74]
<i>VD</i>	Oxygen	31	425	Water/ -5 °C	[75]
<i>VD</i>	Air	11	175	Water/ -5 °C	[75]

Table 1.3. Ozone concentration and yield efficiency generated by different types of DBD.

As can be seen from table 1.3, SD-DBD exhibit the lowest concentration of ozone compared with other DBDs; this may be related to its low plasma density and high temperature of the dielectric surface [41, 66]. Among the DBD reactor types, Packed Bed Reactors (DBD-PBRs) have shown promise for generating high concentrations of ozone. However, DBD-PBRs have shown lower yield efficiency than the VD-DBD, and this was found to be mainly due to continuous heat formation in this type of reactor [71]. From the table, it is clear that higher ozone concentrations have been obtained when DBD-PBRs were cooled [67]. Therefore, it can be concluded that employing DBD-PBRs with efficient cooling systems is required for maintaining high concentrations of ozone [70, 72].

1.3. Factors affecting ozone generation in DBD-PBRs

1.3.1. Discharge power characteristics

Discharge power is one of the most important factors that determine the performance and efficiency of any ozone generator. From the discussions in sections 1.2.2 and 1.2.3 it is clear

that NTP is initiated and sustained only when a sufficient power was supplied to the DBD reactors. In addition, the number and energy of the discharge electrons are determined by the discharge current and voltage, respectively [40, 76]. However, at a constant input power, the discharge voltage and current are determined by a number of parameters including: electric field strength (E , kV cm^{-1}), discharge frequency (f , Hz), feed gas composition, and the dielectric capacitance (C_d , F) [6, 7, 40, 41, 77, 26]. The effects of these parameters on the discharge power may be understood on the basis of Manley's equation [78]:

$$P = 4 f C_d V_o (V - V_o C_g/C) \quad (1.3)$$

and C can be determined according to:

$$1/C = 1/C_g + 1/C_d \quad (1.4)$$

$$C_{d,g} = \epsilon_r \times \epsilon_o A/d \quad (1.5)$$

where P is the discharge power (W), V_o is the discharge onset voltage (kV), V is the discharge voltage (kV), C_g is the capacitance of the background gas within the discharge gap (F), C is the total capacitance of the dielectric and gas (F), ϵ_r is the dielectric constant, ϵ_o is vacuum permittivity ($8.854 \times 10^{-12} \text{ F m}^{-1}$), A and d are the dielectric surface area (m^2) and thickness (m), respectively. From the discussion in section 1.2.3, it is clear that the value of V_o is mainly determined by the feed gas composition and the discharge gap width (d), while the discharge frequency (f , Hz) is determined by the input power supply. From equations 1.4 and 1.5, C_d is determined by the dielectric material properties and C_g is determined by the background gas composition, the width and the cross-sectional area of discharge gap.

Given that the discharge power (P , W) is voltage times current, the average discharge current (I , coulomb s^{-1}) can be estimated from equation 1.3 according to [78]:

$$I = 4 f C_d (V - V_o C_g/C) = P/V_o \quad (1.6)$$

From equation 1.3, it is clear that at a constant input power and frequency the discharge voltage is determined mainly by the capacitances of the dielectric and the background gas. In other words, increasing the capacitance of the dielectric increases the current and lowers the voltage of the discharge [77, 79].

Meiners and co-workers [77] have investigated the effect of varying the dielectric capacitance on the discharge power using a conventional VD-DBD, similar to that shown in fig. 1.4(ii). Their reactor was made of two parallel copper electrodes separated from each by two Al_2O_3 plates $10 \text{ mm} \times 10 \text{ mm} \times$ thicknesses of 0.5, 1.0 and 2.0 mm, and the discharge gap was maintained at 1.0 mm. The system was fed with air at a flow rate of $1.2 \text{ dm}^3 \text{ min}^{-1}$, and the discharge power was delivered to the system via a 12 kV and 14-16 kHz power supply. According to their results, reducing the dielectric thickness from 2.0 to 0.5 mm caused a significant increase in the discharge current (i.e. electron density increased), which was associated with the generation of strong micro-discharges and significant heat formation. For instance, at an input power of 5.0 W the gas temperatures observed at dielectric thicknesses of 0.5, 1.0 and 2.0 mm were 450, 375 and 320 K, respectively. In addition, the discharge current was observed to increase exponentially with the discharge voltage as the thickness of the dielectric decreased from 2.0 to 0.5 mm. The authors have attributed the increase in gas temperature with reduction in the dielectric thickness to an increase in secondary (weak) electron emission. Similar behaviour was observed by Chen and co-workers [79] who investigated the effect of the dielectric size on the removal of NO_x from air using a conventional DBD-PBR filled with dielectric beads with diameters of: 6.0, 4.8, 3.8, 3.0 or 1.1 mm (the dielectric type was not mentioned). According to their results, at a constant input power, the discharge voltage decreased with the size of the dielectric beads.

Haverkamp et al. [80] have investigated the effect of varying the discharge frequency from 19 to 72 kHz on ozone yield efficiency using a VD-DBD. The DBD employed in their study was made of 2 plates of silicon-mica separated by 1.86 mm gap in which a zigzag-shaped high voltage alumina mesh electrode $6 \times 10 \text{ mm}$ was placed to contact periodically the dielectric layers. The external surfaces of the silicon-mica plates were grounded. According to their results, the productivity of ozone from oxygen at a flow rate of $6.0 \text{ dm}^3 \text{ min}^{-1}$ decreased from $110 \text{ g kW}^{-1} \text{ h}^{-1}$ to ca. $60 \text{ g kW}^{-1} \text{ h}^{-1}$ as the discharge frequency was increased from 19 to 72 kHz, at a fixed input power of 40 W.

1.3.2. Temperature effect

One of the most common and undesirable side effects of NTP generation in a DBD is heat formation which reduces the efficiency of ozone generation. This effect has been found to be more pronounced in the case of DBD-PBRs due to a gradual increase in the temperature of the beads [71, 81]. The only study in which the temperature of the beads and background

gas in a DBD-PBR were monitored was that carried out under non-forced convection conditions (i.e. no feed gas was passed through the reactor) by Li and co-workers [81]. Their reactor was made of a quartz glass tube filled with Al_2O_3 pellets 3 mm in diameter with a 1.5 mm stainless steel rod HV electrode passed along the axis of the tube, and a grounded aluminum sheet wrapped around the external wall of the tube. The HV and the grounded electrode were connected to a 10 kV, 30 kHz, 40 mA power supply. The dielectric pellets were divided into 5 layers along the axial direction of the tube by using thermoelectric pairs to monitor the change in the temperature of the background gas. The change in the temperature of the alumina pellets was monitored 5, 15, 30, 45 and 55 cm along the axial direction of the reactor using an infrared thermometer. According to their results, the temperatures of the dielectric pellets and the background gas increased with discharge time, input power and the height of the reactor [81]. For instance, by increasing the input power from 0 to 0.72 W and to 1.0 W the pellets temperature increased from 20 to 30 and 45 °C and the gas temperature increased from 20 to 32 and to 47 °C, respectively, after 35 minutes of plasma initiation. In addition, by maintaining the input power at 2.0 W, the temperature of the background gas was found to increase from 50 to 55 °C over time from 25 to 35 minutes. The major limitation of this work was the operation under non-forced convection which is a completely atypical mode of operation. Another limitation was the small range of input power which was 10 to 20× lower than that normally employed in ozone production (ca. 13-33W [70]), or for air remediation (ca. 50 W [17]).

Due to the structural similarity between the DBD-PBRs and conventional packed beds (i.e. which are normally employed for heat or mass transfer) it was not unreasonable to postulate that the mechanisms of heat transfer within these reactors are similar. For the purpose of simplicity, the NTP would be treated as a source of heat only. According to Yagi and Kunii [82] there are 7 mechanisms by which heat can be transferred within packed bed reactors, and they were classified as dependent on, and independent of, the feed gas flow. The independent mechanisms are:

- (1) Thermal conduction within a solid particle.
- (2) Thermal conduction through the contact points between solid particles and particles to the bed wall.
- (3) Radiative heat transfer between particles.
- (4) Radiative heat transfer between neighbouring voids.

The dependent mechanisms are:

- (5) Thermal conduction through thin stagnant films of gas near the contact points between particles.
- (6) Convective heat transfer from solid particles and/or the bed wall to the gas.
- (7) Heat transfer induced by lateral mixing.

These mechanisms are shown in fig. 1.5 [82, 83]; the arrows indicate the direction of heat flux, while the colours distinguish the dependent (blue) from the independent (red) mechanisms.

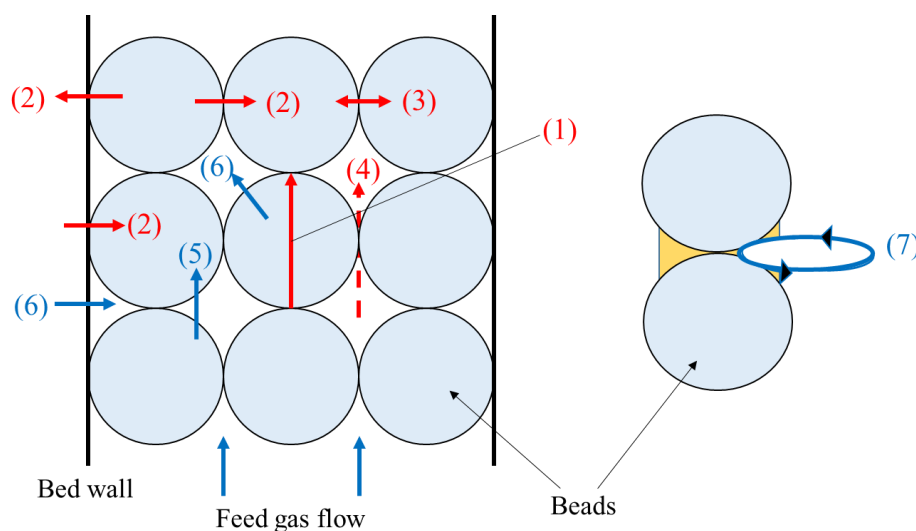


Figure 1.5. Schematic representation of the heat transfer mechanisms in packed bed reactors [82, 83]. The red and blue arrows indicate the directions of heat flux for the independent and dependent mechanisms re gas flow, respectively. See text for details.

According to Yagi and Kunii [82], the importance of each mechanism of heat transfer is determined by several factors including: the working temperature, gas flow rate, the packing particles size, shape and thermal conductivity. For instance, mechanisms 1, 3, 4 and 5 are the most important in the case of low gas flow rates, while at high flow rates heat transfer

via mechanism 7 dominates. Hence, the overall heat transfer rate (q , $\text{kJ m}^{-2} \text{hr}^{-1}$) in packed beds:

$$q = \frac{k_e}{\Delta x} \Delta T \quad (1.7)$$

the heat transfer coefficient (k_e , $\text{kJ m}^{-1} \text{hr}^{-1} \text{K}^{-1}$) varies depending on the gas flow conditions. In the case of flow rates that are sufficiently high to induce lateral mixing, i.e. characterised by a Reynolds number (Re) > 200 [84], the k_e is determined by [85]:

$$k_e = \alpha C_p G \beta D_p \quad (1.8)$$

$$\beta = L_p / D_p \quad (1.9)$$

$$\text{Re} = u_g D_p \rho_g / \mu_g \quad (1.10)$$

where Δx is the pathlength of heat transfer (m), ΔT is the change in temperature (K), α is the ratio of the feed gas mass velocity in packed bed to that of empty tube in the direction of gas flow, C_p is the specific heat of the gas ($\text{kJ kg}^{-1} \text{K}^{-1}$), G is the gas mass flow rate ($\text{kg m}^2 \text{hr}^{-1}$), β is the ratio of average length between the centres of two neighbouring particles (L_p , m) to the average diameter of packing particles (D_p , m), u_g , ρ_g and μ_g are the feed gas superficial velocity (m s^{-1}), density (kg m^{-3}) and viscosity ($\text{kg m}^{-1} \text{s}^{-1}$), respectively. In contrast, if there is no gas flow, the overall heat transfer rate (q) is determined by the heat transferred through mechanisms (1), (2), (3) and (4) [82]:

$$q = \delta \frac{k_s}{\Delta x} \Delta T + U_s (1 - \epsilon - \delta) \Delta T + U_v \epsilon \Delta T \quad (1.11)$$

$$1/U_s = \Delta x / L_p (\gamma D_p / k_s + 1 / ((k_g / \phi D_p) + h_{rs})) \quad (1.12)$$

$$1/U_v = \Delta x (1 / h_{rv} L_p) \quad (1.13)$$

where δ is the ratio of the area between two particles to the total cross-sectional area of the particles, k_s and k_g are the thermal conductivities of the packing material and the feed gas, respectively ($\text{kJ m}^{-1} \text{hr}^{-1} \text{K}^{-1}$), ϵ is the fractional void, γ is the ratio of the length of solid

affected by thermal conductivity (L_s , m) to the D_p , ϕ is the ratio of the effective gas film thickness adjacent to the contact of two solid particles (L_v , m) to the D_p , h_{rs} and h_{rv} are the heat transfer coefficient for solid-to-solid and void-to-void radiations, respectively, ($\text{kJ m}^{-1} \text{hr}^{-1} \text{K}^{-1}$).

From equations 1.7 and 1.8 it is clear that the rate of heat transfer in packed beds increase with feed gas flow rate, the temperature difference between the packing particles and the feed gas and the specific heat capacity of the gas. On the other hand, the heat transfer rate under non-forced convection or at low gas flow rate increased with the thermal conductivity and contact areas of the packing particles and decreased with the void size between them. In addition, the rate of heat transfer decreased with increasing length of the packed bed regardless of the feed gas flow rate, and this may be the reason for the gradual increase in temperature with the length of DBD-PBR observed by Li and co-workers [81], discussed above.

Sung and Sakoda [75] have shown that cooling both anode and cathode in a DBD-VD reactor increased ozone efficiency, with a maximum efficiency of 425 g/kWh being achieved at -5.0 °C and oxygen flow rate of $3.0 \text{ dm}^3 \text{ min}^{-1}$, which is the highest observed among all DBD reactors. Their reactor was made of two Rogowski-shaped electrodes made of stainless steel with a diameter of 6 cm, and the cooling water was passed continuously through each electrode. The dielectric was a 1.0 mm thick quartz disk, and the discharge gap was maintained at 0.2 mm. In contrast, the highest ozone concentration obtained was 30 g m^{-3} at an efficiency of 100 g/kWh, which is lower than that observed using non-cooled DBD-PBD reactors [70] as shown in table 1.3.

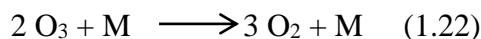
On the basis of the discussions in sections 1.3.1 and 1.3.2, the negative effect of heat formation within the DBD-PBRs on ozone generation would be expected to be reduced by: (i) reducing the amount of discharge current during the generation of NTP by decreasing the discharge frequency and the capacitance of the dielectric; (ii) minimizing the heat localization in the system via enhancing conductive and convective heat transfer through optimizing the length of the DBD-PBR, size and thermal conductivity of the dielectric material, and feed gas flow rate and (iii) supplying the DBD-PBR with a cooling system to operate with the improvements in (ii) for effective heat removal.

1.4. Ozone catalytic destruction

Despite the wide range of environmental applications of ozone, it is a pollutant when present in the troposphere [86]. Thus, the effective destruction of ozone to oxygen is required before it can be released to the atmosphere. Manganese oxides are well known for their high activity towards the degradation of ozone to oxygen. Li and co-workers [87] have shown that the mechanism of ozone conversion to oxygen at MnO₂ is initiated as soon as ozone is in contact with the MnO₂ surface via adsorption, and a layer of atomic oxygen formed on the surface of the catalyst. This layer of atomic oxygen reacts further with new ozone molecules to produce oxygen according to:



The overall reaction is:



where M is the surface of MnO₂. This mechanism is supported by the work of Radhakrishnan and Oyama, who confirmed the formation of the peroxide layer (MO₂) using *in-situ* laser Raman spectroscopy [88].

1.5. Ozone –water mass transfer

1.5.1. Overview

The main shortcoming of ozone in water and wastewater treatment is its low solubility in water as this increases the capital and operational costs of the treatment. Hence, enhancing the solubility of ozone in water has been the focus of a significant number of studies, and several techniques have been employed to achieve this, including: bubble columns, stirred tanks, and packed bed columns [32, 89-95].

1.5.2. Principles of gas-liquid mass transfer process

Gas-to-liquid mass transfer is the transfer of molecules from the gas to liquid phase through their interfacial layer caused by difference in concentrations (i.e. the driving force) [96]. Figure 1.6 shows a schematic of the gas-liquid interface and concentration profiles in each phase [96]. From the figure, P_G , P_{Gi} , C_L and C_{Li} are the concentrations of the substance subject to mass transfer in the gas bulk (atm), in gas at the interface (atm), in liquid at the interface (kmol m^{-3}) and in liquid bulk (kmol m^{-3}), respectively. Thus, the overall rate of gas-liquid mass transfer is determined, fundamentally, by the rates of: (i) mass transfer from the gas bulk to the interface, (ii) the rate of mass transfer through the interface and (iii) the rate of mass transfer from the interface to the liquid bulk.

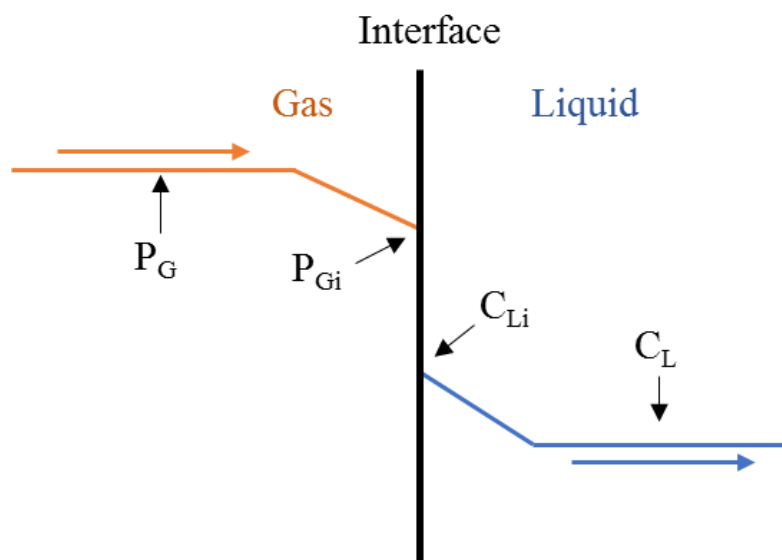


Figure 1.6. Schematic of the gas-liquid interface and the concentration profiles of the component in the gas and liquid phases. The arrows indicate the direction of mass transfer, P_G and P_{Gi} (atm) are the partial pressures in gas bulk and at the interface, C_{Li} and C_L (kmol m^{-3}) are the liquid side concentrations of the species at the interface and in the bulk liquid. Redrawn with modifications from [96].

The rate at which mass is transferred from the gas bulk to the interface (N_A , $\text{kmol m}^{-2} \text{ s}^{-1}$) is given by:

$$N_A = k_G (P_G - P_{Gi}) \quad (1.14)$$

where k_G is the mass transfer coefficient in gas phase ($\text{kmol m}^{-2} \text{s}^{-1} \text{atm}^{-1}$). Similarly, the rate of mass transfer from the interface to the liquid bulk is:

$$N_A = k_L (C_{Li} - C_L) \quad (1.15)$$

where k_L is the mass transfer coefficient in liquid phase (m s^{-1}). Since the mass transfer coefficients k_G and k_L are associated only with the mass transfer in gas or in liquid phase, respectively, they are normally referred to as "partial mass transfer coefficients". In fact, there is no means of determining concentrations at the interface [96, 97]. Thus, to allow the calculation of the N_A without knowing the concentrations at the interface, the gas and liquid phases are normally assumed to be in equilibrium. Figure 1.7 shows a plot of the gas and liquid concentration profiles under equilibrium conditions [97]. From the figure, P_G^* and C_L^* are the equilibrium partial pressure and concentration of the absorbent in the region between the interface and the gas and liquid bulks, respectively. The slope of the equilibrium line (i.e.

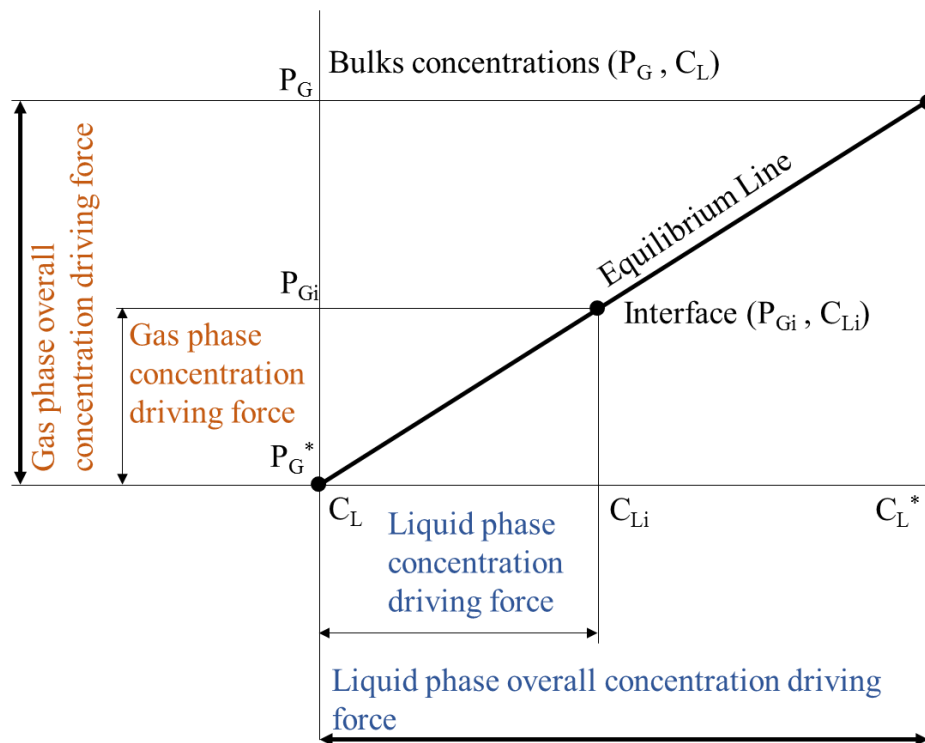


Figure 1.7. A plot of the gas-liquid concentrations and the driving force distribution in gas and liquid phases under equilibrium conditions. P_G , P_{Gi} and P_G^* (atm) are the partial pressures in gas bulk, at the interface and at equilibrium between the interface and the bulk, respectively. C_L , C_{Li} and C_L^* (kmol m^{-3}) are the liquid side concentrations of the absorbent in liquid bulk, at the interface and at equilibrium between the interface and at the bulk liquid. Redrawn with amendments from [97]. See text for further details.

equilibrium coefficient, m , $\text{atm m}^3 \text{ kmol}^{-1}$, see equation (1.17)) is then employed to correlate the partial mass transfer rates in equations 1.14 and 1.15 to the overall mass transfer rates:

$$N_A = k_G (P_G - P_{Gi}) = k_L (C_{Li} - C_L) = K_G (P_G - P_G^*) = K_L (C_L^* - C_L) \quad (1.16)$$

where K_G ($\text{kmol m}^{-2} \text{ s}^{-1} \text{ atm}^{-1}$) and K_L (m s^{-1}) are the gas and liquid overall mass transfer coefficients.

Unlike the partial mass transfer coefficients, the overall mass transfer coefficients include the mass transfer resistance in gas and liquid phases. For instance, from equation 1.16 the overall mass transfer rate is:

$$N_A = K_L (C_L^* - C_L) = k_G 1/m (P_G - P_{Gi}) + k_L (C_{Li} - C_L) \quad (1.17)$$

where m is the equilibrium coefficient ($\text{atm m}^3 \text{ kmol}^{-1}$). Taking into account the fact that the resistive forces towards the mass transfer in each phase are the reverse of the mass transfer coefficients [96, 97] the following correlation can be obtained from equation 1.17:

$$1/K_L = 1/k_L + 1/k_G m \quad (1.18)$$

In the case of the gases that are sparingly soluble in liquids (e.g. oxygen or ozone in water) m in equation 1.18 is very high, and the overall mass transfer coefficient is then:

$$K_L \approx k_L \quad (1.19)$$

Under the conditions of equation 1.19, the main resistive forces are considered to be concentrated in the liquid phase. [93, 94, 98].

Several theories have been proposed to allow the determination of the partial mass transfer coefficients in the gas (k_G) and liquid phases (k_L), and these are discussed below.

1.5.2.1. Two Films Theory

The Two Film Theory (TFT) was proposed in 1923 by Lewis and Whitman et al. [99], and it assumes the presence of two stagnant films separating the gas and liquid bulks from the interface. Figure 1.8 shows a schematic representation of the two film theory. According to

the theory, mass transfer is only determined by molecular diffusion in the gas and liquid phases. Thus, the liquid and gas partial mass transfer coefficients in equations 1.14 and 1.15 can be written as [100]:

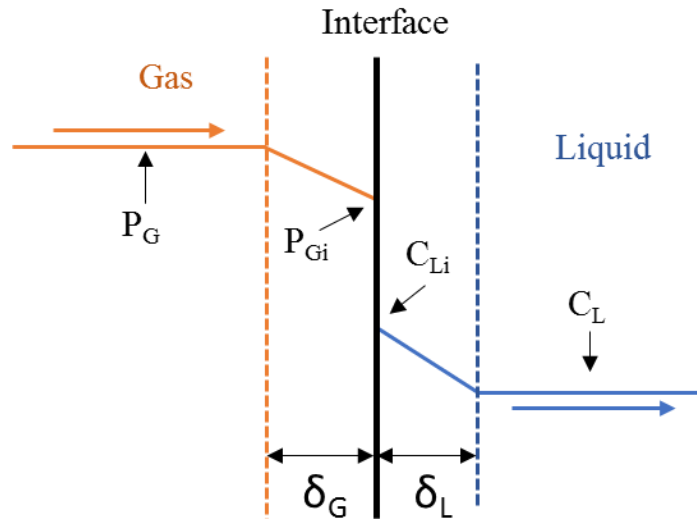


Figure 1.8. Schematic of the gas-liquid interface as described by the two film theory [99]. δ_L (m) and δ_G (m) are the thicknesses of the stagnant liquid and gas films, respectively. Other components are the same as those shown in fig.1.6.

$$k_L = D_L / \delta_L \quad (1.20)$$

$$k_G = D_G / \delta_G \quad (1.21)$$

where D_L , D_G , δ_L and δ_G are the diffusivity in liquid and gas phase ($\text{m}^2 \text{s}^{-1}$), and the liquid and gas films thickness (m), respectively. The main limitations of this theory are: that the values of δ_L and δ_G cannot be determined, it does not take into account the effect of the contact time between gas and liquid phases, or the effect of fluid turbulence caused by gas bubble movement on the partial mass transfer coefficients.

1.5.2.2. Surface Penetration Theory

The effect of the contact time between the gas and the liquid phases on mass transfer was incorporated in the Surface Penetration Theory (SPT), proposed by Higbie in 1935 [101].

This theory deals primarily with the liquid side mass transfer coefficient and it assumes that the contact time at the interface between the gas and liquid is short (e.g. in bubble columns) and the liquid components are mixed before and after contact with the gas phase. Hence, the concentration at the interface is similar to that in the bulk liquid [100]. From this theory the contact time of a rising bubble into a liquid phase is:

$$t = d_b / U_b \quad (1.22)$$

where d_b and U_b are the Sauter mean bubble diameter (m) and the rising velocity of the bubble (m s^{-1}), respectively. Accordingly, the liquid phase mass transfer coefficient is given by:

$$k_L = (4 D_L / \pi t)^{1/2} \quad (1.23)$$

where t is the gas-liquid contact time (s) & D_L is the diffusivity in the liquid phase ($\text{m}^2 \text{s}^{-1}$).

1.5.2.3. Thin Film Renewal Theory

As may be inferred from the name, the Thin Film Renewal Theory (TFRT) postulates that the liquid film at the interface layer, shown in fig. 1.8, is renewed continuously at a constant rate as a result of liquid turbulence. This theory was proposed by Danckwerts in 1951 [102], and was considered to be an extension of SPT, discussed above, [100]. TFRT predicts that the liquid phase mass transfer coefficient is proportional to the square root of the rate of the liquid film renewal:

$$k_L = (D_L S)^{1/2} \quad (1.24)$$

where S is the liquid film renewal rate (s^{-1}).

1.5.3. Ozone-water volumetric mass transfer coefficient (k_{LA})

The volumetric mass transfer coefficient (k_{LA} , s^{-1}) is the most common term employed to determine the rate of gas-to-liquid mass transfer. This term includes the liquid phase mass transfer coefficient (k_L , m s^{-1}) and the interfacial area per unit volume (a , $\text{m}^2 \text{m}^{-3}$), and is given by [92, 103]:

$$N_{O_3} = dC/dt = k_{LA} (C^* - C) \quad (1.25)$$

which can be integrated and rearranged to give [103]:

$$\ln (C^* - C) = - k_L a t + \text{constant} \quad (1.26)$$

where C^* is the steady state dissolved ozone concentration (mg dm^{-3}), C is the dissolved ozone concentration (mg dm^{-3}) at time t (s). Thus, by plotting the values of $\ln (C^* - C)$ versus t (s) for each experiment a straight line with slope equal to $k_L a$ (s^{-1}) should be obtained.

1.5.4. Factors affecting ozone-water dissolution

The rate and amount of ozone transferred to water is determined by several external and internal factors. The external factors are those associated with the operational conditions such as the reactor geometry, mixing conditions and the input gas and liquid flow rates [91, 104, 105]. These factors affect, significantly, parameters including the gas-liquid interfacial area, and the bubble size and residence time of the gas within the liquid. Figure 1.9 shows a diagram of the relationships between various factors that can affect ozone-water mass transfer [104, 105].

Gas hold-up (ϵ_G) is one of the most important hydrodynamic factors that determine the fraction of gas within the liquid at any time of the gas dissolution process. This factor is used with the volumetric mass transfer coefficient ($k_L a$) as an indicator of the performance of any reactor toward gas-liquid dissolution [90, 105-108].

From fig. 1.9, the physical and chemical properties of the liquid phase is one of the important factors that can significantly affect the rate of gas-liquid mass transfer. These properties include the surface tension, ionic strength, temperature, pH and chemical composition. Wilkinson and co-workers [106] investigated the effect of replacing deionised water with a 0.8 M solution of sodium sulphite on the air-to-water volumetric mass transfer coefficient using a bubble column 1.5 m length and 15.8 cm internal diameter. According to their results, a significant reduction in bubble size and increase in gas hold-up was observed using the sodium sulphite solution over that obtained with deionised water. The authors interpreted their data in terms of the reduction in bubble coalescence rate caused by electrolyte addition. Zieminski and Whittemore [109] have shown that the overall volumetric mass transfer coefficient ($K_L a$) of oxygen-to-water increased linearly with ionic over the range from 0 to $0.45 \text{ mole dm}^{-3}$. Their experiments were carried out using a bubble column 0.5 m height and

13 cm internal diameter. The feed gas was air, and the ionic strength of water was varied using different inorganic salts, namely: NaCl, NaBr, NaI, LiCl, Na₂SO₄, AlCl₃, Al₂(SO₄)₃, MgSO₄, Na₃PO₄, MgCl₂ and CaCl₂. In addition, the authors observed that at a fixed ionic strength, the most effective electrolytes for preventing bubble coalescence and increasing the gas-liquid interfacial area were those containing trivalent cations.

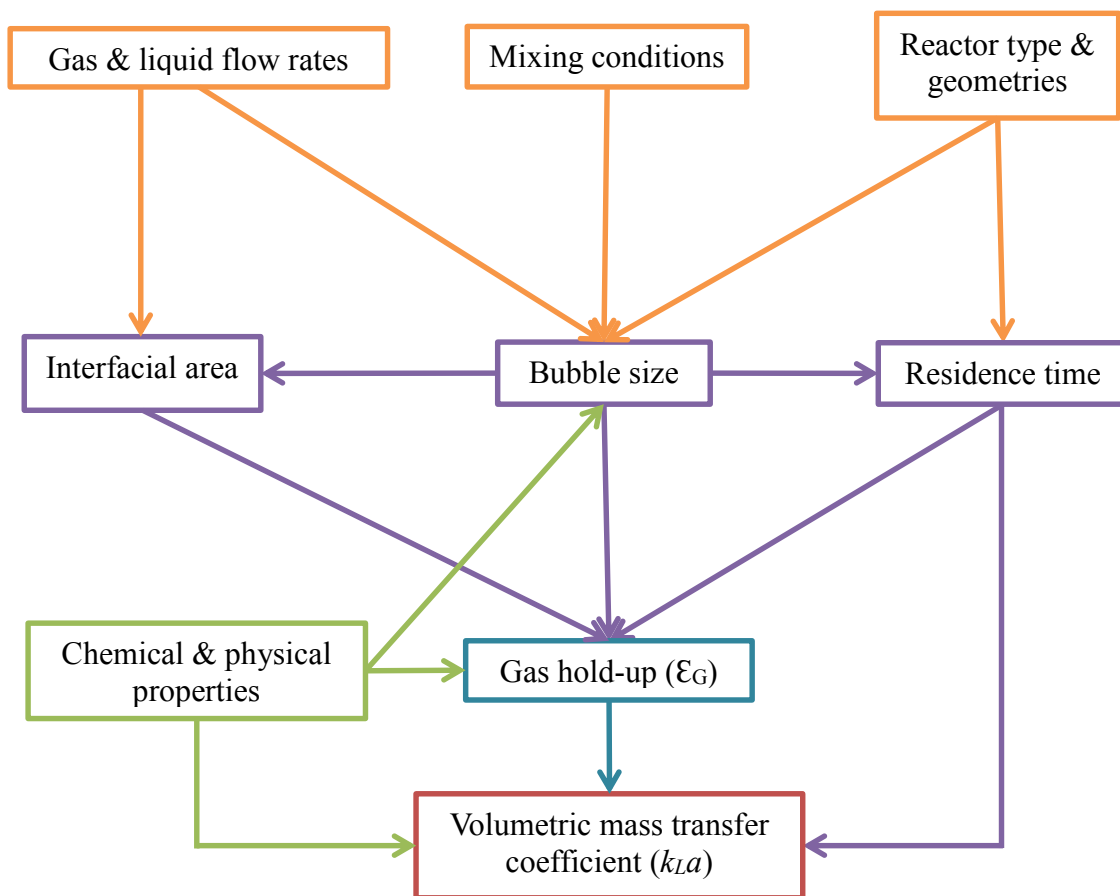


Figure 1.9. A diagram of the factors affecting gas-to-liquid mass transfer and their relationships.

The presence of one or more of the chemical species that can react with a dissolved gas can dramatically change the rate of mass transfer depending on the reaction kinetics. According to Charpentier et al. [110], the effect of chemical reactions taking place in the liquid phase on the overall gas-liquid mass transfer can be classified either as slow or fast kinetic regimes. Figure 1.10 shows schematics of ozone concentration profiles postulated to take place in fast

and slow kinetic regimes by Zhou and Smith [98]. As can be seen from the figure, the slow kinetic regimes lower the concentration of the dissolved gas (e.g. ozone) within the liquid bulk only, and hence the driving force behind mass transfer increases. In the case of fast kinetic regimes, the rate of gas consumption is significantly high and causes a complete depletion of the gas from the liquid film next to the gas-liquid interface. Hence, the overall rate of gas-to-liquid mass transfer become independent of physical absorption (see below) [98].

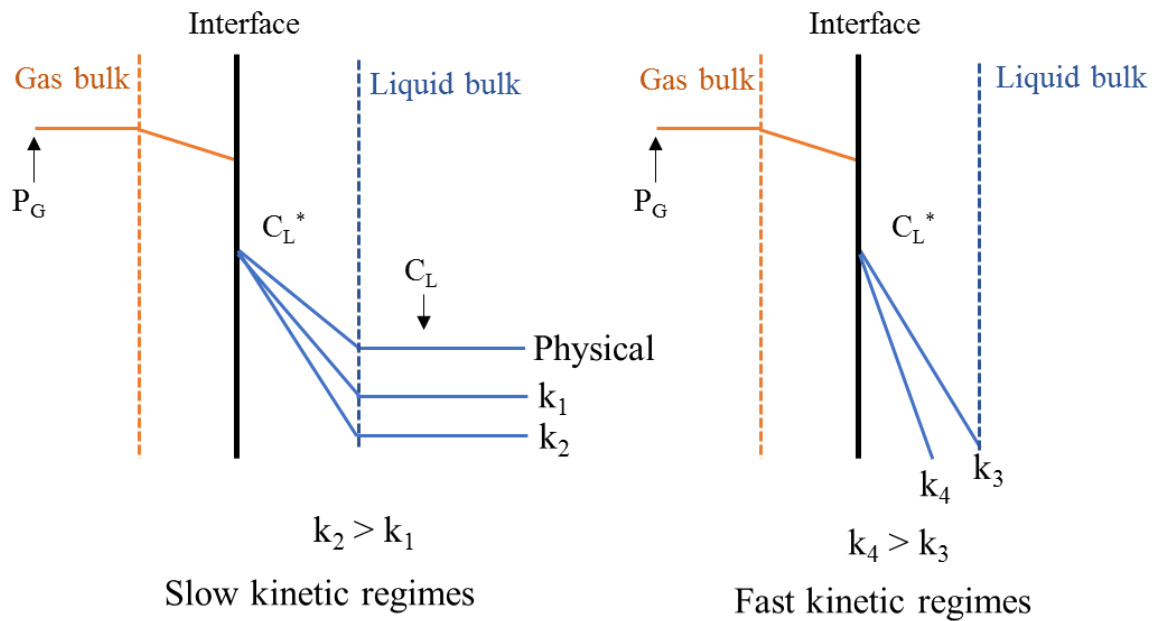


Figure 1.10. Schematics showing ozone concentration profiles for slow and fast kinetic regimes [98].

According to Charpentier et al. [110], the type of the chemical regime can be identified by determining the ratio of the chemical reaction rate constant (k , $\text{m}^3 \text{mol}^{-1} \text{s}^{-1}$) to the liquid phase mass transfer coefficient (k_L , m s^{-1}) to obtain the Hatta number (Ha, a dimensionless parameter) [111]:

$$\text{Ha} = \sqrt{\frac{(\frac{2}{m} + 1) D_A k [C^*]^{m-1}}{k_L}} \quad (1.27)$$

where m is the reaction order for the gas, D_A is the gas diffusivity ($\text{m}^2 \text{s}^{-1}$) and C^* is the steady state dissolved gas concentration (mole m^{-3}). Slow regimes are those with Ha values ≤ 0.3 and the overall rate of gas-to-liquid mass transfer (N_{Aa} , $\text{mole m}^{-3} \text{s}^{-1}$) in these regimes is determined by the physical absorption of the gas [110]:

$$N_{Aa} = k_{La} (C_L^* - C_L) \quad (1.28)$$

where k_{La} is the volumetric mass transfer coefficient (s^{-1}) and C_L is the dissolved gas concentration in liquid bulk (mole m^{-3}). At Ha values higher than 3.0, the reaction regime is fast [110] and N_{Aa} is significantly affected by chemical reaction [93]:

$$N_{Aa} = k_{La} C_L^* E \quad (1.29)$$

Where E is the enhancement factor caused by chemical reaction.

1.5.5. Types of ozone-water contactors

Several types of gas-liquid contactors have been investigated for ozone-water dissolution including: bubble column [32, 89-91], stirred tank [92-94] and packed bed reactors [95]. Among these types, bubble columns are the most common due to their simplicity in construction and operation. Bubble column reactors essentially consist of a column with a gas diffuser at the base. The efficiency of these reactors towards ozone dissolution is normally improved by increasing the column length and the feed gas flow rate using fine bubble diffusers [90, 98, 112]. Reducing the bubble size increases the interfacial area and slows the bubble rise velocity within the column [113], while increasing the column height increases the contact time [90] both which increase mass transfer. However, the volumetric ozone-water mass transfer coefficient (k_{La} , s^{-1}) has been found to increase with feed gas superficial velocity, regardless of the column length or bubble size [89-91, 98]. In all of these studies, this behaviour was associated with an increase in the gas hold-up (ϵ_G) as a result of increasing the gas/liquid volumetric ratio.

Depending on the feed gas superficial velocity and the internal diameter of the bubble column, four different flow regimes are commonly observed which are: perfect bubbly, imperfect bubbly, churn-turbulent and slug [114]. These flow regimes are shown schematically in fig. 1.11. As can be seen from the figure, the perfect bubbly (sometimes called homogeneous flow) can be distinguished by the homogenous size and distribution of

small bubbles over the entire column, and this is associated with slow rising velocities and no coalescence or break-up of the bubbles [115]. This type of flow is normally attained at low superficial gas velocities typically within the range from 0.02 to 0.05 cm s⁻¹; above this range the flow passes through the imperfect bubbly regime (also known as heterogeneous bubbly) which comprises a mixture of bubbles with different sizes, followed by the formation of churn-turbulent or a slug flow depending on the column diameter [112, 116, 117]. Figure 1.12 shows a plot of the different flow regimes in bubble columns as a function of feed gas velocity and column diameter as proposed by Shah et al. [118] From the figure, the regions between the flow regimes represent transitional states in which the bubble size and rising velocities increases gradually [117].

As can be seen from fig. 1.11, the main characteristics of the churn turbulent flow are the wide range of bubble sizes distribution (i.e. from a few mm to a few cm [112]), high rising velocities and liquid circulation. This flow regime normally results from bubble coalescence [112] at high flow rates of the feed gas, and is observed in bubble columns with diameters larger than 15 - 20 cm, as can be seen from fig. 1.12 [112, 114, 119]. As a consequence, the gas-to-liquid mass transfer attained under the churn-turbulent regime is normally lower than that from the perfect bubbly flow regime [112]. The slug flow regime normally occurs under

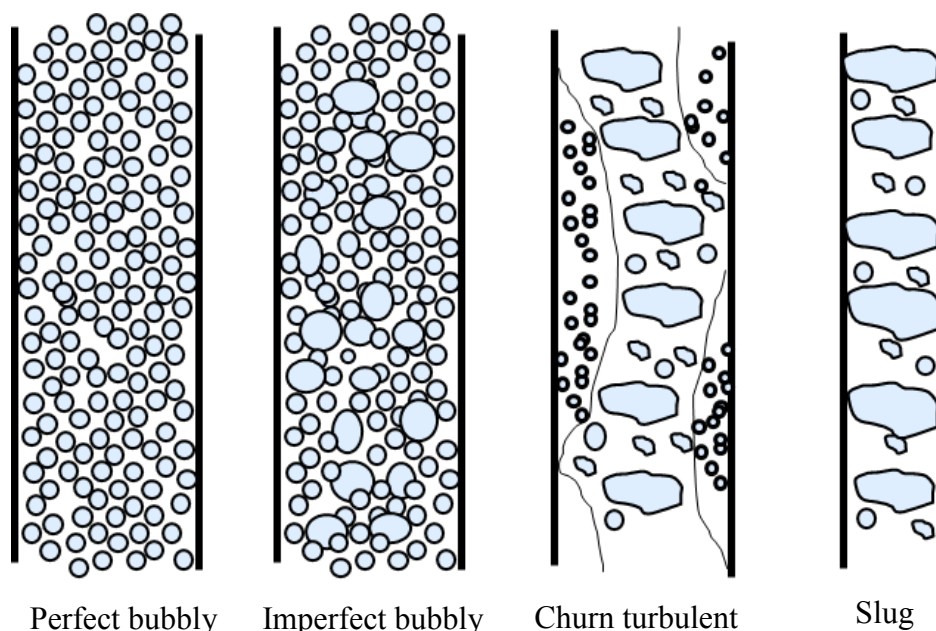


Figure 1.11. Schematic showing the different flow regimes observed using bubble columns redrawn after Bouaifi et al. [114].

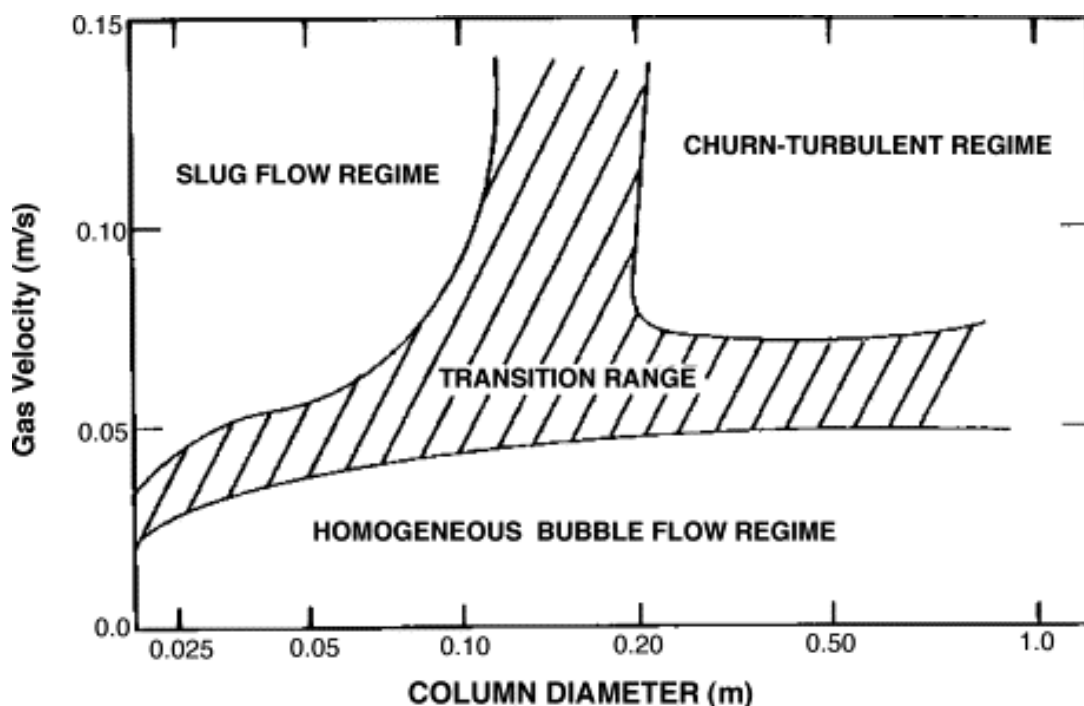


Figure 1.12. A plot of the different flow regimes in bubble column reactors as a function of feed gas velocity and column diameter [118].

similar or even lower superficial gas velocities than the churn-turbulent but in columns with smaller diameters [119]. As can be seen from fig. 1.11, the main characteristic of the latter flow is the formation of large bubbles that span entire column diameter.

The ozone-water volumetric mass transfer coefficients for bubble columns have been found to fall in a range given by two equations describe the two extremes [90, 120, 121]:

$$k_{LA} = 0.67 U_G^{1.15} \quad (1.30)$$

$$k_{LA} = 1.89 U_G^{0.932} \quad (1.31)$$

where U_G is the feed gas superficial velocity (m s^{-1}). According to the work carried out by Bin et al. [90], the k_{LA} of ozone dissolution in water can reach 0.02 s^{-1} using a bubble column that is 5.0 m in length and 0.15 m internal diameter and supplied with a diffuser with pore diameter 0.1 - 0.15 mm at gas superficial velocity of 0.02 m s^{-1} .

Bubble columns are not effective for the dissolution of ozone in water due to several limitations: (i) the requirement of high flow rates of the feed gas which decrease the effectiveness of the method due to the cost of ozone and of gas pumping, (ii) they are operated under semi-batch conditions (i.e. no water throughput) due to low mass transfer rates and (iii) the slowness of the process increases ozone loss through self-decomposition [90, 93].

Carrying out ozone-to-water dissolution in stirred tanks (ST) was investigated by several authors under semi-batch conditions using deionised water [92] or in the presence of species that can react with ozone such as sodium phosphate [93] or dichlorophenol [94]. In all of these studies the rate of ozone-water dissolution increased with the speed of agitation and feed gas flow rate. Wu and Masten [92] investigated the mass transfer coefficient of ozone-water using a stirred tank 1.5 dm³ in size with a fine bubble diffuser to form bubbles with diameters < 1.0 mm placed above a magnetic stirrer at the base of the reactor (the dimensions of the reactor were not reported). According to their results, the ozone-water volumetric mass transfer coefficient (k_{LA}) observed at a gas flow rate of 0.4 dm³ min⁻¹ increased from 0.006 to 0.008 s⁻¹ when the speed of agitation was increased from 0 to 600 rpm, respectively. However, by increasing the feed gas flow rate from 0.1 to 0.5 dm³ min⁻¹, k_{LA} increased from 0.005 to 0.009 s⁻¹, respectively, without mixing. Thus, it can be concluded that the enhancement caused by agitation was unimportant compared to the effect of the feed gas flow rate. The low values of k_{LA} limits the application of STs to semi-batch operation.

Oscillatory Baffled Reactors (OBR's) have shown promise with respect to the dissolution of oxygen in water [103, 122, 123]. OBRs were found to enhance the dissolution of oxygen in water 6 times faster than bubble columns [103], and to be 75% more power efficient than stirred vessels [122]. Unlike most gas-liquid contactors the type of gas diffuser employed had no effect on OBR efficiency [123], and this may be considered as a unique feature of this type of reactor.

1.5.6. Oscillatory baffled reactors (OBR)

Oscillatory baffled reactors consist of a column within which are mounted a series of equally spaced baffles dividing the column into cells. The oscillation of the liquid within the OBR is generated by a piston or bellows mounted at one end. Gas-liquid mixing in OBRs takes place via the formation of vortices or eddies between each pair of baffles. Figure 1.13 shows

an example of eddy formation during the operation of an OBR [124]. Normally the internal diameter of the baffles and the spacing between them are kept at $0.5\times$ and $1.5 - 1.8\times$ the column diameter to maintain optimal mixing [125]. The oscillating fluid is accelerated as it passes through the baffles and forms eddies near the wall of the column next to the baffle surface as indicated by the white arrows in fig. 1.13. By reversing the flow direction during the second half of the oscillating pulse, these eddies withdraw to the centre of each cell and new vortices are produced on the other side of the baffle. The size and intensity of these eddies depend on the baffle geometries and the oscillation frequency and amplitude [103, 125, 126].

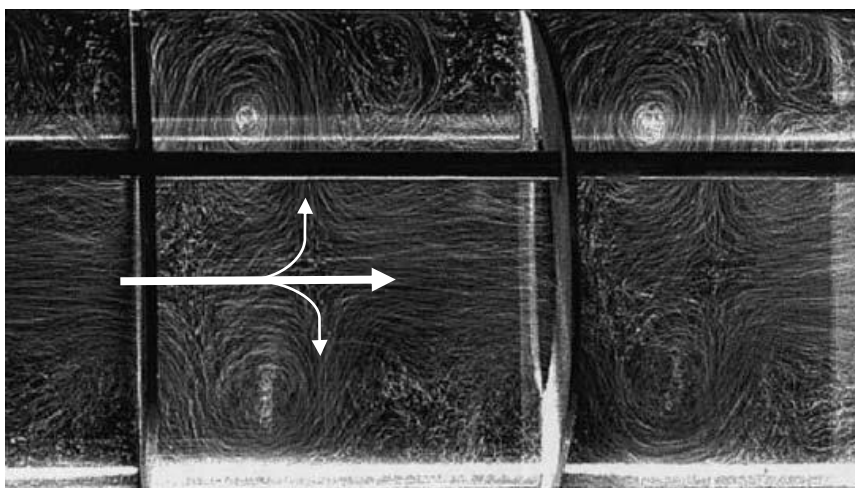


Figure 1.13. Photo of vortex formation during the operation of an oscillatory baffled reactor. The white arrows indicate eddy development within the reactor [124].

The oscillatory Reynolds number (Re_o) is normally used to describe mixing in OBRs, while the Strouhal number (St) measures the efficiency of eddy propagation [103]. These parameters are important characteristics of OBRs, and are calculated using equations 1.32 and 1.33, respectively [103, 126, 127]:

$$Re_o = \frac{2\pi f X_0 \rho D}{\mu} \quad (1.32)$$

$$\text{St} = \frac{D}{4\pi x_0} \quad (1.33)$$

where f is the oscillation frequency (Hz), x_0 the oscillation amplitude centre to peak (m), ρ is the liquid density (kg m^{-3}), μ is the liquid viscosity ($\text{kg m}^{-1} \text{s}^{-1}$) and D is the column inner diameter (m).

1.5.7. An overview of the OBRs as gas-liquid contactors

Hewgill et al. [103] investigated the efficiency of an OBR (1 m in height and 2.6 cm internal diameter) for oxygen-to-water mass transfer under semi-batch conditions. The authors studied the effects of the feed gas superficial velocity, reactor arrangement and the oscillation amplitude on the volumetric oxygen-water mass transfer coefficient. The effect of the reactor arrangement was carried out using the same column as a bubble column (i.e. without baffles or oscillation), baffled reactor (i.e. without oscillation) and as an OBR. According to their results, the oxygen-water volumetric mass transfer coefficient (k_{LA} , s^{-1}) obtained using the baffled reactor was the lowest among other arrangements. In the case of the OBR the k_{LA} increased from 0.003 to 0.017 s^{-1} as the oscillation amplitude was increased from 0 to 4 mm at a fixed frequency at 8 Hz and superficial gas velocity at $7.4 \times 10^{-4} \text{ m s}^{-1}$. Interestingly, the highest k_{LA} (i.e. 0.017 s^{-1}) attained using the OBR was 6 times higher than that obtained using the bubble column at the same superficial gas velocity (i.e. $7.4 \times 10^{-4} \text{ m s}^{-1}$).

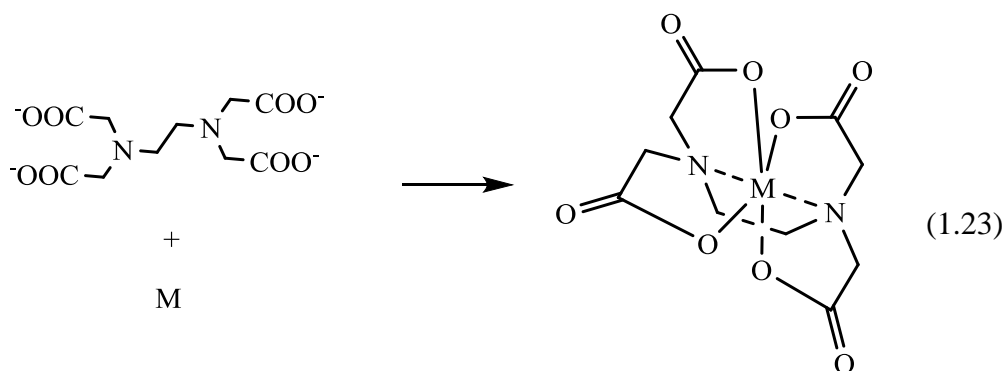
Oliveira et al. [105] investigated the effects of bubble size, gas holdup, superficial gas velocity, oscillation frequency and amplitude on the oxygen-water volumetric mass transfer coefficient using an OBR 1.5 m in height and 5 cm internal diameter. The OBR was operated under semi-batch conditions at superficial gas velocities from 1×10^{-3} to $4.24 \times 10^{-3} \text{ m s}^{-1}$, and the oscillation conditions were varied from 0 to 8 mm for the amplitude and from 1 to 8 Hz for the frequency. According to the authors, the oxygen-water k_{LA} increased linearly with the superficial gas velocity regardless of the oscillation conditions. Interestingly, at a constant amplitude at 2 or 4 or 8 mm and increasing oscillation frequency, the k_{LA} increased in almost an exponential pattern. At the most intensive conditions of oscillations ($x_0 = 4 \text{ mm}$ and $f = 8 \text{ Hz}$) the k_{LA} was ca. 4× higher than that attained using the same reactor without oscillation. The authors attributed the enhancement on oxygen-water mass transfer using the OBR to the reduction in bubble size by high fluid turbulence caused by oscillation and the

increase in gas hold up through bubble circulation within high speed eddies formed in the reactor.

In both the studies discussed above, the OBRs were operated under semi-batch conditions, and the effect of liquid phase flow on the performance of OBRs towards gas-liquid mass transfer was not investigated. This may be interesting for understanding the feasibility of operating the OBRs under continuous flow conditions that is more pontifical in some applications such as water and waste water treatments. Furthermore, in both studies the oxygen-water volumetric mass transfer coefficient increased linearly with the superficial gas velocity, but no change in the flow regime was reported which is an important factor to consider during the design of any gas-liquid contactor, as discussed in section 1.5.5. This may due to the small ranges of superficial gas velocities covered in both studies.

1.6. The remediation of M-EDTA complexes

Ethylenediaminetetraacetate (EDTA) is well known for its ability to chelate most of the alkaline earth and heavy metals [128] to form stable complexes. The stability of EDTA complexes is mainly due to the formation of multi-coordinating bonds with the metal cation centre as can be seen from reaction (1.23). Thus, EDTA has been employed in a wide range of applications that required the prevention of insoluble metal salt occurrence such as: food preservation, the production of pharmaceuticals, and for cleaning precipitated metal salts from tubes or tanks [128, 129]. Also, EDTA can be used for the remediation of land contaminated by heavy metals or radioactive nuclides [128-133]. Hence, the subsequent remediation of such metal-EDTA complexes is essential.



Most EDTA complexes are highly resistant to remediation via conventional biological and thermal approaches [128, 129, 134, 135]. For instance, the work carried out by Belly et al.

[129] has shown that 89% of Fe(III)-EDTA can be removed after 5 days of treatment using a mixed population of microorganisms. Satroutdinov and co-workers [134] compared the biodegradability of uncomplexed EDTA to its complexes with Ca^{2+} , Mg^{2+} , Mn^{2+} , Co^{2+} , Cu^{2+} , Pb^{2+} , Zn^{2+} , Fe^{3+} and Cd^{2+} using the bacterial strain DSM 9103. According to their results, the complete biodegradation of EDTA, Ca(II)-EDTA, Mg(II)-EDTA and Mn(II)-EDTA was attained within 10 hours of the treatment. However, after 48 hours the removal of only 55 - 85% was observed in the cases of Pb(II)-EDTA, Co(II)-EDTA, Zn(II)-EDTA, and no more than 30% of Cu(II)-EDTA. Fe(III)-EDTA and Cd(II)-EDTA, were which the most resistant compounds towards bio-degradation. According to the same authors, the limited biodegradability of EDTA complexes was attributed to: (i) high thermodynamic stability and (ii) the harmful impact of the metal ions released during the treatment on the microorganisms.

Several approaches have been suggested to facilitate the decomposition of uncomplexed EDTA in water such as: ozonation [136-139], combined ozone and gamma irradiation [137], ozone and UV irradiation [137] and H_2O_2 + UV irradiation [140]. However, there are only a few studies on the treatment of metal-EDTA complexes. Gilbert and Hoffmann-Glewe [136] investigated the degradation of 1.0 mM EDTA using a vessel 1 dm³ in size equipped with a gas diffuser to allow bubbling of 10 g m⁻³ of ozone at 0.4 dm³ min⁻¹ for 80 minutes. According to their results, the degradation of free EDTA by ozone is slower in the presence of free metal ions such as Ca^{2+} , Cd^{2+} and Fe^{3+} , and the slowest rate of degradation was observed in the presence of Fe^{3+} . This behaviour was attributed to the formation of stable complexes such as Fe(III)-EDTA. Interestingly, the same authors tested the biodegradability of the treated EDTA solution, and observed that, unlike the parent molecule, the ozonation by-products were readily biodegradable. A similar observation was made by Munoz and von Sonntag [139] during their kinetic study of ozone reactivity with various molecules including: EDTA, Ca(II)-EDTA and Fe(III)-EDTA. According to their results the rate constant of ozone reaction with EDTA (i.e. $3.2 \times 10^6 \text{ M}^{-1} \text{ s}^{-1}$) was ca. $13 \times$ higher than that observed with Ca(II)-EDTA (i.e. $10^5 \text{ M}^{-1} \text{ s}^{-1}$) and 4 orders of magnitude higher than that with Fe(III)-EDTA (i.e. $3.3 \times 10^2 \text{ M}^{-1} \text{ s}^{-1}$) at a pH of 6.

It is interesting to note that the majority of the published work on EDTA treatment by ozone or ozone combined with UV irradiation did not consider the effect of the ozone-water mass transfer rate on performance. Hence, it is not clear to what extent the ozone dissolution rate

can affect the treatment of EDTA complexes. Yang and co-workers [141] investigated the efficiency of combining ozonation with UV irradiation using a reactor supplied with an agitator, UV lamp (i.e. photolysis reactor) and a gas diffuser at the base on removing different EDTA complexes. According to their results, the rate of mineralization (i.e. complete oxidation to CO₂ and H₂O) after 30 minutes of ozonation and UV irradiation decreased in the order: Fe(III)-EDTA > Fe(II)-EDTA > Al(III)-EDTA > Pb(II)-EDTA > Na-EDTA > Zn(II)-EDTA > Cu(II)-EDTA [141]. Their experiments were carried out under semi-batch conditions by passing 20.0 mg dm⁻³ of ozone at 1.71 dm³ min⁻¹ and 1.0 kW UV lamp (200-650 nm). The authors showed that the synergetic effect of ozonation and UV irradiation was more significant than the individual treatments. In addition, by placing a 2 m in length and 3.0 cm internal diameter bubble column reactor prior to the photolysis reactor, the degradation of Na-EDTA by ozone only increased from 20% after 30 minutes to 97% after 5 minutes. Nevertheless, the authors have not studied other M-EDTA compounds using their reactor, particularly those presenting higher resistivity towards ozone such as Fe(III)-EDTA [139] and Cu(II)-EDTA [142]. The authors attributed the enhancement observed by adding the bubble column reactor to the increase in the contact time between ozone and water samples [141]. Therefore, it can be concluded that ozone-water mass transfer can significantly affect the M-EDTA degradation, and enhancing this process would be expected to reduce the time required for the treatment.

1.7. Project aim and objectives

The main aim of this thesis was two-fold:

1. To obtain a better understanding of the chemistry taking place within the NTP of an air-fed DBD and to determine to what extent the plasma outputs vary from the glow to the downstream regions under a range of operational conditions.
2. To develop a novel dielectric barrier discharge-packed bed reactor (DBD-PBR) for effective ozone generation from oxygen or air, and its application to wastewater treatment in combination with an oscillatory baffled reactor (OBR) and a UV irradiation reactor (UVR).

The objectives were to:

1. Carry out an *in-situ* analysis (i.e. the analysis of the plasma glow) and downstream (i.e. post plasma region) analyses of a NTP produced using air-fed dielectric barrier discharge (DBD) jet generator using Fourier Transform InfraRed (FTIR) and UV-Vis spectroscopies as a function of input power, relative humidity, feed gas composition, temperature and flow rate.
2. Design, commission, characterize and optimize a novel DBD-PBR with an effective cooling system for ozone production from oxygen or air.
3. Couple the DBD-PBR to an oscillatory baffled reactor (OBR) to investigate the performance of the latter towards ozone-to-water mass transfer under semi-batch and continuous flow conditions as a function of input ozone concentration, mixing conditions, type of gas diffuser, feed gas and water flow rates.
4. Commission the system DBD-PBR/ OBR coupled to a UV irradiation reactor (UVR) for water treatment using the most recalcitrant complexes Cu(II)-EDTA and Fe(III)-EDTA as an example to evaluate the performance of the system.

1.8. Thesis structure

Chapter two discuss chemicals, materials, analytical approaches, set-ups and experimental procedures employed during this project.

Chapter three presents the results of the *in-situ* analysis of the plasma glow and downstream regions of a NTP produced using an air-fed dielectric barrier discharge (DBD)-plasma jet. These analyses were performed using Fourier Transform InfraRed (FTIR) and UV-Vis spectroscopies. The behaviour of the species present in these regions was monitored as a function of: input power, gas flow rate, relative humidity, feed gas composition and temperature.

Chapter four discusses the performance of a novel DBD-PBR supplied with an efficient cooling system towards ozone generation from oxygen and air. The effects of reactor arrangement, feed gas flow rate, input power and coolant temperature, dielectric material properties on ozone generation are described.

Chapter five reports an investigation of the performance of an oscillatory baffled reactor (OBR) coupled to the DBD-PBR towards ozone-water mass transfer under semi-batch and continuous flow conditions. The effects of the reactor arrangement, input ozone concentration, mixing conditions, type of gas diffuser, feed gas and water flow rates on ozone-to-water volumetric mass transfer coefficient (k_{La}) and mass transfer efficiency (MTE) are presented.

Chapter six presents the results of employing the DBD-PBR and OBR coupled to a UV irradiation reactor (UVR) on the remediation of water containing Cu(II)-EDTA and Fe(III)-EDTA. The effect of input water flow rate, reactor arrangement and UV irradiation was investigated.

Chapter seven presents the conclusions of the research and proposed future work.

1.9. References

- [1] Fridman, A.A. (2012) 'Plasma Chemistry', (Cambridge: Cambridge University Press), pp. 1-11.

- [2] Conrads, H. and Schmidt, M. (2000) 'Plasma generation and plasma sources', *Plasma Sources Science and Technology*, 9(4), p. 441.

- [3] Fauchais, P. and Vardelle, A. (1997) 'Thermal plasmas', *Plasma Science, IEEE Transactions on*, 25(6), pp. 1258-1280.

- [4] Uhm, H.S., Hong, Y.C. and Shin, D.H. (2006) 'A microwave plasma torch and its applications', *Plasma Sources Science and Technology*, 15(2), p. S26.

- [5] Carman, R.L., Forslund, D.W. and Kindel, J.M. (1981) 'Visible Harmonic Emission as a Way of Measuring Profile Steepening', *Physical Review Letters*, 46(1), pp. 29-32.

- [6] Tendero, C., Tixier, C., Tristant, P., Desmaison, J. and Leprince, P. (2006) 'Atmospheric pressure plasmas: A review', *Spectrochimica Acta Part B: Atomic Spectroscopy*, 61(1), pp. 2-30.

- [7] Eliasson, B. and Kogelschatz, U. (1991) 'Nonequilibrium volume plasma chemical processing', *Plasma Science, IEEE Transactions on*, 19(6), pp. 1063-1077.
- [8] Roth, J.R. (2001) 'Industrial Plasma Engineering: Volume 2 - Applications to Nonthermal Plasma Processing', (London: Institute Of Physics Ltd.), pp. 1-2.
- [9] Pfender, E. (1999) 'Thermal Plasma Technology: Where Do We Stand and Where Are We Going?', *Plasma Chemistry and Plasma Processing*, 19(1), pp. 1-31.
- [10] Chen, H.L., Lee, H.M. and Chen, S.H. (2008) 'Review of Packed-Bed Plasma Reactor for Ozone Generation and Air Pollution Control', *Industrial & Engineering Chemistry Research*, 47(7), pp. 2122-2130.
- [11] Borcia, G., Anderson, C.A. and Brown, N.M.D. (2003) 'Dielectric barrier discharge for surface treatment: application to selected polymers in film and fibre form', *Plasma Sources Science and Technology*, 12(3), p. 335.
- [12] Borcia, G. and Brown, N.M.D. (2007) 'Hydrophobic coatings on selected polymers in an atmospheric pressure dielectric barrier discharge', *Journal of Physics D: Applied Physics*, 40(7), p. 1927.
- [13] Kostov, K.G., dos Santos, A.L.R., Honda, R.Y., Nascente, P.A.P., Kayama, M.E., Algatti, M.A. and Mota, R.P. (2010) 'Treatment of PET and PU polymers by atmospheric pressure plasma generated in dielectric barrier discharge in air', *Surface and Coatings Technology*, 204(18-19), pp. 3064-3068.
- [14] Chen, Z. and Mathur, V.K. (2002) 'Nonthermal plasma for gaseous pollution control', *Industrial & Engineering Chemistry Research*, 41(9), pp. 2082-2089.
- [15] Gentile, A.C. and Kushner, M.J. (1995) 'Reaction chemistry and optimization of plasma remediation of N_xO_y from gas streams', *Journal of Applied Physics*, 78(3), pp. 2074-2085.

- [16] Liang, P., Jiang, W., Zhang, L., Wu, J., Zhang, J. and Yang, D. (2015) 'Experimental studies of removing typical VOCs by dielectric barrier discharge reactor of different sizes', *Process Safety and Environmental Protection*, 94, pp. 380-384.
- [17] b Abd Allah, Z., Whitehead, J.C. and Martin, P. (2014) 'Remediation of Dichloromethane (CH₂Cl₂) Using Non-thermal, Atmospheric Pressure Plasma Generated in a Packed-Bed Reactor', *Environmental Science & Technology*, 48(1), pp. 558-565.
- [18] Eliasson, B., Kogelschatz, U., Xue, B. and Zhou, L.-M. (1998) 'Hydrogenation of Carbon Dioxide to Methanol with a Discharge-Activated Catalyst', *Industrial & Engineering Chemistry Research*, 37(8), pp. 3350-3357.
- [19] Kostov, K.G., Rocha, V., Koga-Ito, C.Y., Matos, B.M., Algatti, M.A., Honda, R.Y., Kayama, M.E. and Mota, R.P. (2010) 'Bacterial sterilization by a dielectric barrier discharge (DBD) in air', *Surface and Coatings Technology*, 204(18–19), pp. 2954-2959.
- [20] Colagar, A.H., Sohbatzadeh, F., Mirzanejhad, S. and Omran, A.V. (2010) 'Sterilization of Streptococcus pyogenes by afterglow dielectric barrier discharge using O₂ and CO₂ working gases', *Biochemical Engineering Journal*, 51(3), pp. 189-193.
- [21] Pavlovich, M.J., Chen, Z., Sakiyama, Y., Clark, D.S. and Graves, D.B. (2013) 'Effect of Discharge Parameters and Surface Characteristics on Ambient-Gas Plasma Disinfection', *Plasma Processes and Polymers*, 10(1), pp. 69-76.
- [22] Akitsu, T., Ohkawa, H., Tsuji, M., Kimura, H. and Kogoma, M. (2005) 'Plasma sterilization using glow discharge at atmospheric pressure', *Surface and Coatings Technology*, 193(1–3), pp. 29-34.
- [23] Fridman, G., Peddinghaus, M., Balasubramanian, M., Ayan, H., Fridman, A., Gutsol, A. and Brooks, A. (2006) 'Blood Coagulation and Living Tissue Sterilization by Floating-Electrode Dielectric Barrier Discharge in Air', *Plasma Chemistry and Plasma Processing*, 26(4), pp. 425-442.

- [24] Sladek, R.E.J., Stoffels, E., Walraven, R., Tielbeek, P.J.A. and Koolhoven, R. (2004) 'Plasma treatment of dental cavities: a feasibility study', *Plasma Science, IEEE Transactions on*, 32(4), pp. 1540-1543.
- [25] Fridman, A.A. (2012) 'Plasma Chemistry', (Cambridge: Cambridge University Press), pp. 383-397.
- [26] Kogelschatz, U. (2003) 'Dielectric-Barrier Discharges: Their History, Discharge Physics, and Industrial Applications', *Plasma Chemistry and Plasma Processing*, 23(1), pp. 1-46.
- [27] Peleg, M. (1976) 'The chemistry of ozone in the treatment of water', *Water Research*, 10(5), pp. 361-365.
- [28] Hoigné, J., Bader, H., Haag, W.R. and Staehelin, J. (1985) 'Rate constants of reactions of ozone with organic and inorganic compounds in water—III. Inorganic compounds and radicals', *Water Research*, 19(8), pp. 993-1004.
- [29] Ikehata, K. and El-Din, M.G. (2004) 'Degradation of Recalcitrant Surfactants in Wastewater by Ozonation and Advanced Oxidation Processes: A Review', *Ozone: Science & Engineering*, 26(4), pp. 327-343.
- [30] Paraskeva, P. and Graham, N.J.D. (2002) 'Ozonation of Municipal Wastewater Effluents', *Water Environment Research*, 74(6), pp. 569-581.
- [31] Agustina, T.E., Ang, H.M. and Vareek, V.K. (2005) 'A review of synergistic effect of photocatalysis and ozonation on wastewater treatment', *Journal of Photochemistry and Photobiology C: Photochemistry Reviews*, 6(4), pp. 264-273.
- [32] Beltran, F.J., Garcia-Araya, J.F. and Encinar, J.M. (1997) 'Henry and mass transfer coefficients in the ozonation of wastewaters'.
- [33] Rice, R.G. (2002) 'Century 21 - Pregnant with Ozone', *Ozone: Science & Engineering*, 24(1), pp. 1-15.

[34] Eliasson, B. and Kogelschatz, U. (1991) 'Ozone Generation with Narrow-Band UV Radiation', *Ozone: Science & Engineering*, 13(3), pp. 365-373.

[35] Christensen, P.A., Yonar, T. and Zakaria, K. (2013) 'The Electrochemical Generation of Ozone: A Review', *Ozone: Science & Engineering*, 35(3), pp. 149-167.

[36] Eliasson, B., Hirth, M. and Kogelschatz, U. (1987) 'Ozone synthesis from oxygen in dielectric barrier discharges', *Journal of Physics D: Applied Physics*, 20(11), p. 1421.

[37] Fang, Z., Qiu, Y., Sun, Y., Wang, H. and Edmund, K. (2008) 'Experimental study on discharge characteristics and ozone generation of dielectric barrier discharge in a cylinder-cylinder reactor and a wire-cylinder reactor', *Journal of Electrostatics*, 66(7-8), pp. 421-426.

[38] Fridman, A., Chirokov, A. and Gutsol, A. (2005) 'Non-thermal atmospheric pressure discharges', *Journal of Physics D: Applied Physics*, 38(2), p. R1.

[39] Chang, J., x, Shih, Lawless, P.A. and Yamamoto, T. (1991) 'Corona discharge processes', *Plasma Science, IEEE Transactions on*, 19(6), pp. 1152-1166.

[40] Pietsch, G.J. and Gibalov, V.I. (1998) 'Dielectric barrier discharges and ozone synthesis', *Pure and Applied Chemistry*, 70(6), pp. 1169-1174.

[41] Haacke, M., Humpert, C. and Pietsch, G.J. (2002) 'Influence of Field Strength and Energy Distribution of Different Barrier Discharge Arrangements on Ozone Generation', *Ozone: Science & Engineering*, 24(3), pp. 193-201.

[42] Gibalov, V.I. and Pietsch, G.J. (2006) 'On the Performance of Ozone Generators Working with Dielectric Barrier Discharges', *Ozone: Science & Engineering*, 28(2), pp. 119-124.

[43] Gaens, W.V. and Bogaerts, A. (2013) 'Kinetic modelling for an atmospheric pressure argon plasma jet in humid air', *Journal of Physics D: Applied Physics*, 46(27), p. 275201.

[44] Lowke, J.J. and Morrow, R. (1995) 'Theoretical analysis of removal of oxides of sulphur and nitrogen in pulsed operation of electrostatic precipitators', *Plasma Science, IEEE Transactions on*, 23(4), pp. 661-671.

[45] Cravens, T.E., Kozyra, J.U., Nagy, A.F., Gombosi, T.I. and Kurtz, M. (1987) 'Electron impact ionization in the vicinity of comets', *Journal of Geophysical Research: Space Physics (1978–2012)*, 92(A7), pp. 7341-7353.

[46] Braithwaite, N.S.J. (2000) 'Introduction to gas discharges', *Plasma Sources Science and Technology*, 9(4), p. 517.

[47] Spyrou, N., Held, B., Peyrous, R., Manassis, C. and Pignolet, P. (1992) 'Gas temperature in a secondary streamer discharge: an approach to the electric wind', *Journal of Physics D: Applied Physics*, 25(2), p. 211.

[48] Ryo, O. and Tetsuji, O. (2007) 'Ozone production process in pulsed positive dielectric barrier discharge', *Journal of Physics D: Applied Physics*, 40(1), p. 176.

[49] Schmidt-Bleker, A., Winter, J., Iseni, S., Dünnbier, M., Weltmann, K.D. and Reuter, S. (2014) 'Reactive species output of a plasma jet with a shielding gas device—combination of FTIR absorption spectroscopy and gas phase modelling', *Journal of Physics D: Applied Physics*, 47(14), p. 145201.

[50] Atkinson, R., Baulch, D.L., Cox, R.A., Hampson, R.F., Kerr, J.A., Rossi, M.J. and Troe, J. (1997) 'Evaluated Kinetic and Photochemical Data for Atmospheric Chemistry: Supplement VI. IUPAC Subcommittee on Gas Kinetic Data Evaluation for Atmospheric Chemistry', *Journal of Physical and Chemical Reference Data*, 26(6), pp. 1329-1499.

[51] Jeong, J.Y., Park, J., Henins, I., Babayan, S.E., Tu, V.J., Selwyn, G.S., Ding, G. and Hicks, R.F. (2000) 'Reaction Chemistry in the Afterglow of an Oxygen–Helium, Atmospheric-Pressure Plasma', *The Journal of Physical Chemistry A*, 104(34), pp. 8027-8032.

[52] Atkinson, R., Baulch, D.L., Cox, R.A., Hampson, R.F., Kerr, J.A. and Troe, J. (1989) 'Evaluated Kinetic and Photochemical Data for Atmospheric Chemistry: Supplement III. IUPAC Subcommittee on Gas Kinetic Data Evaluation for Atmospheric Chemistry', *Journal of Physical and Chemical Reference Data*, 18(2), pp. 881-1097.

[53] Atkinson, R., Baulch, D.L., Cox, R.A., Hampson Jr, R.F., Kerr, J.A., Rossi, M.J. and Troe, J. (1997) 'Evaluated kinetic, photochemical and heterogeneous data for atmospheric chemistry: Supplement V. IUPAC Subcommittee on Gas Kinetic Data Evaluation for Atmospheric Chemistry', *Journal of Physical and Chemical Reference Data*, 26(3), pp. 521-1011.

[54] Herron, J. and Green, D. (2001) 'Chemical Kinetics Database and Predictive Schemes for Nonthermal Humid Air Plasma Chemistry. Part II. Neutral Species Reactions', *Plasma Chemistry and Plasma Processing*, 21(3), pp. 459-481.

[55] Kossyi, I.A., Kostinsky, A.Y., Matveyev, A.A. and Silakov, V.P. (1992) 'Kinetic scheme of the non-equilibrium discharge in nitrogen-oxygen mixtures', *Plasma Sources Science and Technology*, 1(3), p. 207.

[56] Kogelschatz, U., Eliasson, B. and Hirth, M. (1988) 'Ozone Generation from Oxygen and Air: Discharge Physics and Reaction Mechanisms', *Ozone: Science & Engineering*, 10(4), pp. 367-377.

[57] Eliasson, B. and Kogelschatz, U. (1987) 'Nitrogen oxide formation in ozonizers. In: *Proc. 8th Int. Symp. on Plasma Chemistry (ISPC-8), Tokyo*, pp 736-41.

[58] Yukinori, S., David, B.G., Hung-Wen, C., Tetsuji, S. and Gregor, E.M. (2012) 'Plasma chemistry model of surface microdischarge in humid air and dynamics of reactive neutral species', *Journal of Physics D: Applied Physics*, 45(42), p. 425201.

[59] Akitsu, T., Ohkawa, H., Tsuji, M., Kimura, H. and Kogoma, M. (2005) 'Plasma sterilization using glow discharge at atmospheric pressure', *Surface and Coatings Technology*, 193(1-3), pp. 29-34.

[60] Visser, R.J. (1989) 'Determination of the power and current densities in argon and oxygen plasmas by insitu temperature measurements', *Journal of Vacuum Science & Technology A*, 7(2), pp. 189-194.

[61] Chen, N.H. and Othmer, D.F. (1962) 'New Generalized Equation for Gas Diffusion Coefficient', *Journal of Chemical & Engineering Data*, 7(1), pp. 37-41.

[62] Pipa, A.V. and Ropcke, J. (2009) 'Analysis of the Mid-Infrared Spectrum of the Exhaust Gas From an Atmospheric Pressure Plasma Jet (APPJ) Working With an Argon-Air Mixture', *Plasma Science, IEEE Transactions on*, 37(6), pp. 1000-1003.

[63] Reuter, S., Winter, J., Iseni, S., Peters, S., Schmidt-Bleker, A., Dünnbier, M., Schäfer, J., Foest, R. and Weltmann, K.D. (2012) 'Detection of ozone in a MHz argon plasma bullet jet', *Plasma Sources Science and Technology*, 21(3), p. 034015.

[64] Yukinori, S., David, B.G., Hung-Wen, C., Tetsuji, S. and Gregor, E.M. (2012) 'Plasma chemistry model of surface microdischarge in humid air and dynamics of reactive neutral species', *Journal of Physics D: Applied Physics*, 45(42), p. 425201.

[65] Koinuma, H., Ohkubo, H., Hashimoto, T., Inomata, K., Shiraishi, T., Miyanaga, A. and Hayashi, S. (1992) 'Development and application of a microbeam plasma generator', *Applied Physics Letters*, 60(7), pp. 816-817.

[66] Nomoto, Y., Ohkubo, T., Kanazawa, S. and Adachi, T. (1995) 'Improvement of ozone yield by a silent-surface hybrid discharge ozonizer', *Industry Applications, IEEE Transactions on*, 31(6), pp. 1458-1462.

[67] Schmidt-Szałowski, K., Borucka, A. and Jodzis, S. (1990) 'Catalytic activity of silica in ozone formation in electrical discharges', *Plasma Chemistry and Plasma Processing*, 10(3), pp. 443-450.

[68] Jung, J.-S. and Moon, J.-D. (2008) 'Corona discharge and ozone generation characteristics of a wire-plate discharge system with a glass-fiber layer', *Journal of Electrostatics*, 66(5–6), pp. 335-341.

[69] Chang, J., x, Shih, Kostov, K.G., Urashima, K., Yamamoto, T., Okayasu, Y., Kato, T., Iwaizumi, T. and Yoshimura, K. (2000) 'Removal of NF_3 from semiconductor-process flue gases by tandem packed-bed plasma and adsorbent hybrid systems', *Industry Applications, IEEE Transactions on*, 36(5), pp. 1251-1259.

[70] Liang Chen, H., Ming Lee, H. and Been Chang, M. (2006) 'Enhancement of Energy Yield for Ozone Production via Packed-Bed Reactors', *Ozone: Science & Engineering*, 28(2), pp. 111-118.

[71] Li, S., Tang, Z. and Gu, F. (2010) 'Experimental study on temperature characteristics and energy conversion in packed bed reactor with dielectric barrier discharge', *Heat and Mass Transfer*, 46(8-9), pp. 851-857.

[72] Moon, J.D. and Geum, S.T. (1998) 'Discharge and ozone generation characteristics of a ferroelectric-ball/mica-sheet barrier', *Ieee Transactions on Industry Applications*, 34(6), pp. 1206-1211.

[73] Šimek, M., Pekárek, S. and Prukner, V. (2010) 'Influence of Power Modulation on Ozone Production Using an AC Surface Dielectric Barrier Discharge in Oxygen', *Plasma Chemistry and Plasma Processing*, 30(5), pp. 607-617.

[74] Samaranayake, W.J.M., Miyahara, Y., Namihira, T., Katsuki, S., Hackam, R. and Akiyama, H. (2000) 'Ozone production using pulsed dielectric barrier discharge in oxygen', *Dielectrics and Electrical Insulation, IEEE Transactions on*, 7(6), pp. 849-854.

[75] Sung, Y.-M. and Sakoda, T. (2005) 'Optimum conditions for ozone formation in a micro dielectric barrier discharge', *Surface and Coatings Technology*, 197(2-3), pp. 148-153.

[76] Morent, R. and Leys, C. (2005) 'Ozone Generation in Air by a DC-Excited Multi-Pin-to-Plane Plasma Source', *Ozone: Science & Engineering*, 27(3), pp. 239-245.

[77] Meiners, A., Leck, M. and Abel, B. (2010) 'Efficiency enhancement of a dielectric barrier plasma discharge by dielectric barrier optimization', *Review of Scientific Instruments*, 81(11), p. 113507.

- [78] Manley, T.C. (1943) 'The Electric Characteristics of the Ozonator Discharge', *Transactions of The Electrochemical Society*, 84(1), pp. 83-96.
- [79] Chen, M.-G., Mihalcioiu, A., Takashima, K. and Mizuno, A. (2009) 'Catalyst Size Impact on Non-Thermal Plasma Catalyst Assisted deNO_x Reactors', in Yan, K. (ed.) *Electrostatic Precipitation*. Springer Berlin Heidelberg, pp. 681-684.
- [80] Haverkamp, R.G., Miller, B.B. and Free, K.W. (2002) 'Ozone Production in a High Frequency Dielectric Barrier Discharge Generator', *Ozone: Science & Engineering*, 24(5), pp. 321-328.
- [81] Li, S., Zheng, W., Tang, Z. and Gu, F. (2012) 'Plasma heating and temperature difference between gas pellets in packed bed with dielectric barrier discharge under natural convection condition', *Heat Transfer Engineering*, 33(7), pp. 609-617.
- [82] Yagi, S. and Kunii, D. (1957) 'Studies on effective thermal conductivities in packed beds', *AIChE Journal*, 3(3), pp. 373-381.
- [83] Smolec, W. and Thomas, A. (1993) 'Theoretical and experimental investigations of heat transfer in a Trombe wall', *Energy Conversion and Management*, 34(5), pp. 385-400.
- [84] Cong, T. N., He, Y., Chen, H., Ding, Y. and Wen, D. (2007) 'Heat transfer of gas–solid two-phase mixtures flowing through a packed bed under constant wall heat flux conditions', *Chemical Engineering Journal*, 130(1), pp. 1-10.
- [85] Ranz, W. E. (1952) 'Friction and transfer coefficients for single particles and packed beds', *Chemical Engineering Progress*, 48(5), pp. 247-253.
- [86] Finlayson-Pitts, B.J. and Pitts, J.N. (1997) 'Tropospheric air pollution: ozone, airborne toxics, polycyclic aromatic hydrocarbons, and particles', *Science*, 276(5315), pp. 1045-1051.
- [87] Li, W., Gibbs, G.V. and Oyama, S.T. (1998) 'Mechanism of ozone decomposition on a manganese oxide catalyst. 1. In situ Raman spectroscopy and ab initio molecular orbital calculations', *Journal of the American Chemical Society*, 120(35), pp. 9041-9046.

- [88] Radhakrishnan, R. and Oyama, S.T. (2001) 'Ozone decomposition over manganese oxide supported on ZrO₂ and TiO₂: A kinetic study using in situ laser Raman spectroscopy', *Journal of Catalysis*, 199(2), pp. 282-290.
- [89] Tiwari, G. and Bose, P. (2007) 'Determination of ozone mass transfer coefficient in a tall continuous flow counter-current bubble contactor', *Chemical Engineering Journal*, 132(1), pp. 215-225.
- [90] Biń, A.K., Duczmal, B. and Machniewski, P. (2001) 'Hydrodynamics and ozone mass transfer in a tall bubble column', *Chemical Engineering Science*, 56(21–22), pp. 6233-6240.
- [91] Mizuno, T. and Tsuno, H. (2010) 'Evaluation of solubility and the gas-liquid equilibrium coefficient of high concentration gaseous ozone to water', *Ozone: Science & Engineering*, 32(1), pp. 3-15.
- [92] Wu, J.J. and Masten, S.J. (2001) 'Mass transfer of ozone in semibatch stirred reactor', *Journal of Environmental Engineering*, 127(12), pp. 1089-1099.
- [93] Sotelo, J.L., Beltrán, F.J., Benitez, F.J. and Beltrán-Heredia, J. (1989) 'Henry's law constant for the ozone-water system', *Water Research*, 23(10), pp. 1239-1246.
- [94] Qiu, Y., Kuo, C.-H. and Zappi, M.E. (2001) 'Performance and simulation of ozone absorption and reactions in a stirred-tank reactor', *Environmental Science & Technology*, 35(1), pp. 209-215.
- [95] Farines, V., Baig, S., Albet, J., Molinier, J. and Legay, C. (2003) 'Ozone transfer from gas to water in a co-current up-flow packed bed reactor containing silica gel', *Chemical Engineering Journal*, 91(1), pp. 67-73.
- [96] Kolev, N. (2006) 'Chapter 1 - Basic information', in Kolev, N. (ed.) *Packed Bed Columns*. Amsterdam: Elsevier Science, pp. 40-94.

[97] Asano, K. (2006) 'Mass transfer: from fundamentals to modern industrial applications-diffusion and mass transfer', in *Mass Transfer*. Wiley-VCH Verlag GmbH & Co. KGaA, pp. 9-26.

[98] Zhou, H. and Smith, D.W. (2000) 'Ozone mass transfer in water and wastewater treatment: experimental observations using a 2D laser particle dynamics analyzer', *Water Research*, 34(3), pp. 909-921.

[99] Lewis, W.K. and Whitman, W.G. (1924) 'Principles of gas absorption', *Industrial & Engineering Chemistry*, 16(12), pp. 1215-1220.

[100] Baehr, H.D. and Stephan, K. (1998) 'Heat and mass transfer', (New York: Springer-Verlag Berlin Heidelberg), pp. 79-87.

[101] Higbie, R. (1935) 'The rate of absorption of a pure gas into a still liquid during short periods of exposure', *Trans. Am. Inst. Chem. Eng.*, 31(Copyright (C) 2015 American Chemical Society (ACS). All Rights Reserved.), pp. 365-89.

[102] Danckwerts, P.V. (1951) 'Significance of liquid-film coefficients in gas absorption', *Ind. Eng. Chem.*, 43(Copyright (C) 2015 American Chemical Society (ACS). All Rights Reserved.), pp. 1460-7.

[103] Hewgill, M.R., Mackley, M.R., Pandit, A.B. and Pannu, S.S. (1993) 'Enhancement of gas-liquid mass transfer using oscillatory flow in a baffled tube', *Chemical Engineering Science*, 48(4), pp. 799-809.

[104] Garcia-Ochoa, F. and Gomez, E. (2009) 'Bioreactor scale-up and oxygen transfer rate in microbial processes: An overview', *Biotechnology Advances*, 27(2), pp. 153-176.

[105] Oliveira, M.S.N. and Ni, X.-W. (2004) 'Effect of hydrodynamics on mass transfer in a gas-liquid oscillatory baffled column', *Chemical Engineering Journal*, 99(1), pp. 59-68.

[106] Wilkinson, P.M., Haringa, H. and Van Dierendonck, L.L. (1994) 'Mass transfer and bubble size in a bubble column under pressure', *Chemical Engineering Science*, 49(9), pp. 1417-1427.

[107] Alves, S.S., Maia, C.I. and Vasconcelos, J.M.T. (2004) 'Gas-liquid mass transfer coefficient in stirred tanks interpreted through bubble contamination kinetics', *Chemical Engineering and Processing: Process Intensification*, 43(7), pp. 823-830.

[108] Jamialahmadi, M. and Müller-Steinhagen, H. (1993) 'Effect of superficial gas velocity on bubble size, terminal bubble rise velocity and gas hold-up in bubble columns', *Developments in Chemical Engineering and Mineral Processing*, 1(1), pp. 16-31.

[109] Zieminski, S.A. and Whittemore, R.C. (1971) 'Behavior of gas bubbles in aqueous electrolyte solutions', *Chemical Engineering Science*, 26(4), pp. 509-520.

[110] Charpentier, J.-C. (1981) 'Mass-Transfer rates in gas-liquid absorbers and reactors', in Thomas B. Drew, G.R.C.J.W.H. and Theodore, V. (eds.) *Advances in Chemical Engineering*. Academic Press, pp. 1-133.

[111] Hatta, S. (1932) 'Absorption velocity of gases by liquids. II. Theoretical considerations of gas absorption due to chemical reactions', *Technol. Rep. Tohoku Imp. Univ.*, 10, pp. 119-35.

[112] Kantarci, N., Borak, F. and Ulgen, K.O. (2005) 'Bubble column reactors', *Process Biochemistry*, 40(7), pp. 2263-2283.

[113] Martin, W.W. and Chandler, G.M. (1982) 'The local measurement of the size and velocity of bubbles rising in liquids', *Applied Scientific Research*, 38(1), pp. 239-246.

[114] Bouaifi, M., Hebrard, G., Bastoul, D. and Roustan, M. (2001) 'A comparative study of gas hold-up, bubble size, interfacial area and mass transfer coefficients in stirred gas-liquid reactors and bubble columns', *Chemical Engineering and Processing: Process Intensification*, 40(2), pp. 97-111.

[115] Schumpe, A. and Grund, G. (1986) 'The gas disengagement technique for studying gas holdup structure in bubble columns', *The Canadian Journal of Chemical Engineering*, 64(6), pp. 891-896.

[116] Bukur, D.B. and Daly, J.G. (1987) 'Gas hold-up in bubble columns for Fischer-Tropsch synthesis', *Chemical Engineering Science*, 42(12), pp. 2967-2969.

[117] Hyndman, C.L., Larachi, F. and Guy, C. (1997) 'Understanding gas-phase hydrodynamics in bubble columns: a convective model based on kinetic theory', *Chemical Engineering Science*, 52(1), pp. 63-77.

[118] Shah, Y.T., Kelkar, B.G., Godbole, S.P. and Deckwer, W.D. (1982) 'Design parameters estimations for bubble column reactors', *AIChE Journal*, 28(3), pp. 353-379.

[119] Hyndman, C. L., Larachi, F. and Guy, C. (1997) 'Understanding gas-phase hydrodynamics in bubble columns: A convective model based on kinetic theory', *Chemical Engineering Science*, 52(1), pp. 63-77.

[120] Biń, A. K. and Roustan, M. (2000) 'Mass transfer in ozone reactors', *Proceedings of the international specialised symposium on IOA 2000, Fundamental and engineering concepts for ozone reactor design*, Toulouse, March 1–3, pp. 99-131.

[121] Watanab, K., Kinugasa, I. and Higaki, K. (1991) 'Ozone absorption in bubble column', *Memoir of Niihama College of Technology*, 27, pp. 48-52.

[122] Ni, X., Gao, S., Cumming, R.H. and Pritchard, D.W. (1995) 'A comparative study of mass transfer in yeast for a batch pulsed baffled bioreactor and a stirred tank fermenter', *Chemical Engineering Science*, 50(13), pp. 2127-2136.

[123] Oliveira, M.S.N. and Ni, X. (2001) 'Gas hold-up and bubble diameters in a gassed oscillatory baffled column', *Chemical Engineering Science*, 56(21–22), pp. 6143-6148.

[124] Stonestreet, P. and Van Der Veecken, P.M.J. (1999) 'The effects of oscillatory flow and bulk flow components on residence time distribution in baffled tube reactors', *Chemical Engineering Research and Design*, 77(8), pp. 671-684.

[125] Ni, X., Brogan, G., Struthers, A., Bennett, D.C. and Wilson, S.F. (1998) 'A systematic study of the effect of geometrical parameters on mixing time in oscillatory baffled columns', *Chemical Engineering Research and Design*, 76(5), pp. 635-642.

[126] Harvey, A.P., Mackley, M.R. and Stonestreet, P. (2001) 'Operation and optimization of an oscillatory flow continuous reactor', *Industrial & Engineering Chemistry Research*, 40(23), pp. 5371-5377.

[127] Ni, X. and Gough, P. (1997) 'On the discussion of the dimensionless groups governing oscillatory flow in a baffled tube', *Chemical Engineering Science*, 52(18), pp. 3209-3212.

[128] Nörtemann, B. (1999) 'Biodegradation of EDTA', *Applied Microbiology and Biotechnology*, 51(6), pp. 751-759.

[129] Belly, R.T., Lauff, J.J. and Goodhue, C.T. (1975) 'Degradation of ethylenediaminetetraacetic acid by microbial populations from an aerated lagoon', *Applied microbiology*, 29(6), pp. 78-794.

[130] Finžgar, N. and Leštan, D. (2006) 'Heap leaching of Pb and Zn contaminated soil using ozone/UV treatment of EDTA extractants', *Chemosphere*, 63(10), pp. 1736-1743.

[131] Toste, A.P. and Lechner-Fish, T.J. (1993) 'Chemo-degradation of chelating and complexing agents in a simulated, mixed nuclear waste', *Waste Management*, 13(3), pp. 237-244.

[132] Pocięcha, M. and Lestan, D. (2009) 'EDTA leaching of Cu contaminated soil using electrochemical treatment of the washing solution', *Journal of hazardous materials*, 165(1), pp. 533-539.

[133] Udovic, M. and Lestan, D. (2007) 'EDTA leaching of Cu contaminated soils using ozone/UV for treatment and reuse of washing solution in a closed loop', *Water, Air, and Soil Pollution*, 181(1-4), pp. 319-327.

[134] Satroutdinov, A.D., Dedyukhina, E.G., Chistyakova, T.y.I., Witschel, M., Minkevich, I.G., Eroshin, V.K. and Egli, T. (2000) 'Degradation of metal-EDTA complexes by resting cells of the bacterial strain DSM 9103', *Environmental science & technology*, 34(9), pp. 1715-1720.

[135] Motekaitis, R.J., Cox Iii, X.B., Taylor, P., Martell, A.E., Miles, B. and Tvedt Jr, T.J. (1982) 'Thermal degradation of EDTA chelates in aqueous solution', *Canadian Journal of Chemistry*, 60(10), pp. 1207-1213.

[136] Gilbert, E. and Hoffmann-Glewe, S. (1990) 'Ozonation of ethylenediaminetetraacetic acid (EDTA) in aqueous solution, influence of pH value and metal ions', *Water Research*, 24(1), pp. 39-44.

[137] Krapfenbauer, K. and Getoff, N. (1999) 'Comparative studies of photo- and radiation-induced degradation of aqueous EDTA. Synergistic effects of oxygen, ozone and TiO₂ (acronym: CoPhoRaDe/EDTA)', *Radiation Physics and Chemistry*, 55(4), pp. 385-393.

[138] Wang, J., Wang, X., Li, G., Guo, P. and Luo, Z. (2010) 'Degradation of EDTA in aqueous solution by using ozonolysis and ozonolysis combined with sonolysis', *Journal of hazardous materials*, 176(1-3), pp. 333-338.

[139] Munoz, F. and von Sonntag, C. (2000) 'The reactions of ozone with tertiary amines including the complexing agents nitrilotriacetic acid (NTA) and ethylenediaminetetraacetic acid (EDTA) in aqueous solution', *Journal of the Chemical Society, Perkin Transactions 2*, (10), pp. 2029-2033.

[140] Chitra, S., Paramasivan, K., Sinha, P.K. and Lal, K.B. (2003) 'Treatment of Liquid Waste Containing Ethylenediamine Tetraaceticacid by Advanced Oxidation Processes', *Journal of Advanced Oxidation Technologies*, 6(1), pp. 109-114.

[141] Yang, C., Xu, Y.R., Teo, K.C., Goh, N.K., Chia, L.S. and Xie, R.J. (2005) 'Destruction of organic pollutants in reusable wastewater using advanced oxidation technology', *Chemosphere*, 59(3), pp. 441-445.

[142] Morooka, S., Ikemizu, K., Kamano, H. and Kato, Y. (1986) 'Ozonation rate of water-soluble chelates and related compounds', *Journal of chemical engineering of Japan*, 19(4), pp. 294-299.

2. Experimental

2.1. Materials, Chemicals and gases

2.1.1. Materials

Al₂O₃ pellets with diameters of 2.0 mm and 3.0 mm were purchased from Pingxiang Xingfeng, Chemical Packing (China), and Alfa Aesar (USA), respectively. 2.0 mm Borosilicate and 3.0 mm Soda-Lime spherical glass beads and 2.0 mm molecular sieve UOP type 3A beads were purchased from Sigma Aldrich. Table 2.1 compares some of the physical properties of dielectrics employed for ozone generation. 1.0 and 10.0 mm thick PTFE sheets were obtained from Direct Plastics Limited (UK). Perforated stainless steel sheets 1.0 mm thick were purchased from John Staniar & Co Ltd (UK).

2.1.2. Chemicals & gases

Na₂[Cu(II)-EDTA] ($\geq 97\%$), Na[Fe(III)-EDTA] ($\geq 98\%$) and sodium thiosulfate pentahydrate Na₂S₂O₃·5H₂O ($\geq 99.5\%$) were obtained from Sigma Aldrich. MnO₂-containing catalyst, CARULIT 200, was obtained from Cara Corp (UK). All chemicals were used as received without further treatment. O₂ ($\geq 99.9\%$), N₂ ($> 99.99\%$), N₂O ($> 99.99\%$), 1.0% CO₂ in argon were obtained from BOC. "Artificial air" was formulated by mixing O₂ and N₂ (20% O₂ + 80% N₂), and ambient air were employed.

Dielectric	Type	Diameter /mm	Dielectric constant	Thermal conductivity /W m ⁻¹ K ⁻¹
D1	Alumina pellets (93%)	2	8.5 – 10	14.0 - 24.0
D2	Borosilicate glass beads	2	4 – 6	1.0 - 1.2
D3	A ₃ molecular sieve	2	N/A	0.12 - 0.14
D4	Soda-Lime glass beads	3	7.3	0.9 - 1.1
D5	Alumina pellets (93%)	3	8.5 – 10.0	14.0 - 24.0
PTFE	Perforated sheets	1	2.1	0.25 - 0.3

Table 2.1. Physical properties of the dielectrics employed for ozone generation using novel dielectric barrier discharge-packed beads reactor (DBD-PBR).

2.2. *An in-situ and downstream analysis of air fed Non-thermal plasma (NTP)*

2.2.1. *Non-thermal plasma jet generator*

A dielectric barrier discharge (DBD) jet generator was designed and fabricated in-house with a configuration similar to that reported by Koinuma et al. [1] to allow the formation of a jet of non-thermal plasma (NTP) of sufficient length for the direct *in-situ* analysis. A schematic of the NTP jet generator is shown in figure 2.1. As may be seen from the figure, the plasma was produced by passing the desired gas composition over a central, stainless steel rod, 1.5 mm thick, mounted in a borosilicate glass tube of 1.8 mm internal diameter, 1.0 mm thick and 6.3 cm in length. The external electrode was made of stainless steel foil 10 mm long and ca. 0.1 mm thick wrapped around the glass tube near the tip and covered with PTFE as an external insulator. The external and internal electrodes were connected to a sinusoidal type, high-voltage power supply NP-10000-30, (NeonPro, China) which was employed to provide a range of high voltage outputs up to 10 kV at a constant frequency of 24 kHz. A variable transformer (Y16HM, Zenith) was used to control the input power to the HV power supply. The input power was monitored using a power meter (2000 MU, Pro-digit Electronics), and was the total power consumed by the system after subtracting that consumed by the variable transformer.

2.2.2. *Relative humidity control*

The relative humidity of the feed gas was controlled using a humidity regulator which was a jacketed Dreschel bottle containing supersaturated aqueous solution of NaCl (400 cm³). The temperature of the Dreschel was maintained constant between 4.0 and 40.0 °C via a Grant LTC1 Water Recycler. The relative humidity of the gas exiting the Dreschel bottle was monitored using a calibrated Testo 605-H1 humidity meter.

2.2.3. *Experimental procedures*

The FTIR analyses of the plasma chemical composition was carried out directly (*in-situ*) by passing the infrared beam through the plasma, or through the exhaust gas ca. 2 m downstream, see figure 2.2. As can be seen from the figure, the feed gas was passed through a gas mixing cylinder at a fixed flow rate to allow homogeneity when more than one gas was used. The mixed gas was then passed, if needed, through a relative humidity regulator placed prior to the dielectric barrier discharge. Depending on the type of experiment, the feed gas was passed either through channel (I) or (II) for *in-situ* or downstream FTIR monitoring,

respectively. As may be seen in figures 2.1 and 2.2, the NTP jet generator was inserted into an in-house built infrared (IR) transmission cell, with a pathlength of 5.1 cm made of a Pyrex glass cylinder capped by two 2.5 cm dia., 3.0 mm thick CaF₂ windows (Crystran). The total volume of the transmission cell was ca. 47 cm³.

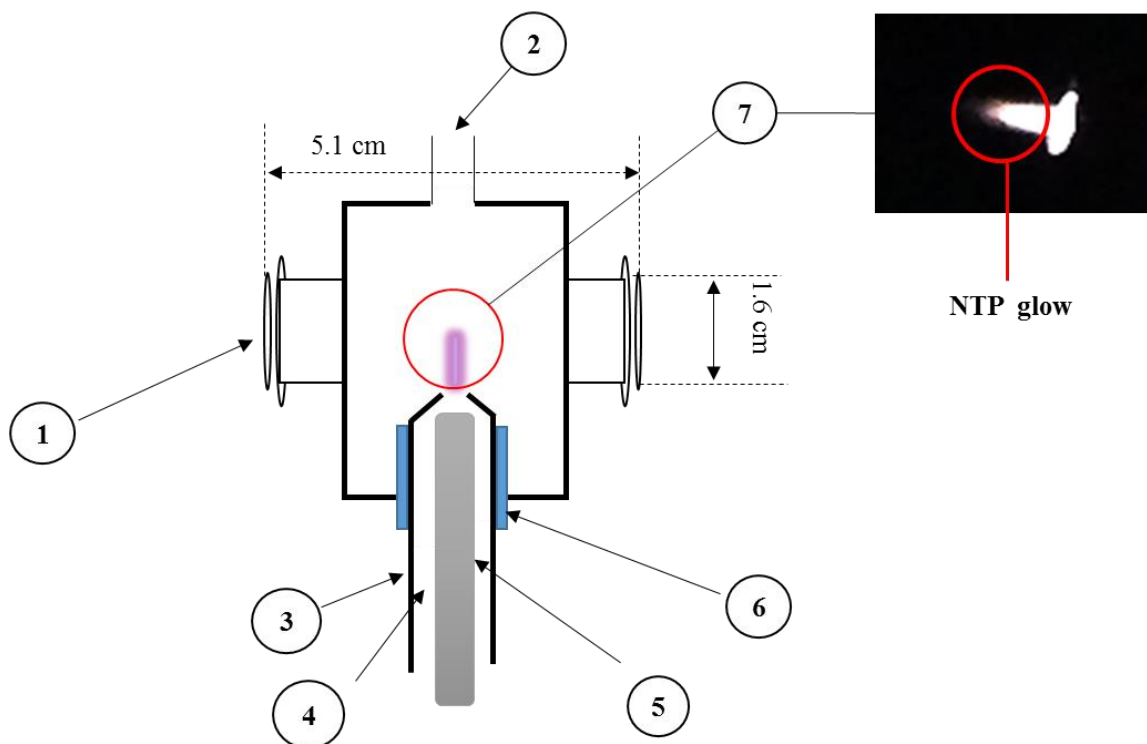


Figure 2.1. A schematic of Non-thermal plasma jet transmission cell: (1) CaF₂ windows, (2) exhaust gas outlet, (3) Pyrex glass tube with a nozzle, (4) feed gas flow gap, (5) and (6) high voltage electrodes and (7) in-situ sampling zone of the NTP glow.

For the *in-situ* experiments, the transmission cell was placed into the sample compartment of the Varian FTS 7000 FTIR spectrometer such that the IR beam passed through the non-thermal plasma jet, the length of which depended on the feed gas flow rate. The exhaust gases exited via a port opposite the NTP jet generator, as can be seen from figure 2.1. The concentration of ozone in the exhaust stream was monitored using a UV-Vis flow cell (1.0 cm pathlength, Ocean Optics Systems) positioned ca. 2.7 m after the transmission cell, connected via polyethylene tubing. The flow cell was connected via fibre optic cables to an Ocean Optics USB2000 spectrometer. The time required for ozone to pass from the transmission cell to the UV flow cell at flow rate of 0.5 dm³ min⁻¹ was ca. 9 seconds. For the

downstream FTIR analyses, channel (II) was employed, where the NTP jet generator was connected to an external transmission cell, similar to that used for the *in-situ* analysis, via 2.0 m and 6.0 mm internal diameter polyethylene tubing. The time required for the effluent gas to pass from the external to the internal transmission cell was ca. 7 seconds at $0.5 \text{ dm}^3 \text{ min}^{-1}$. Table 2.2 summarizes the ranges of the experimental conditions employed in this work.

It is important to note that, all of the *in-situ* and downstream experiments were carried out such that ambient air was not in contact with the plasma or the plasma exhaust to maintain the consistency of experimental conditions and accuracy of measurements.

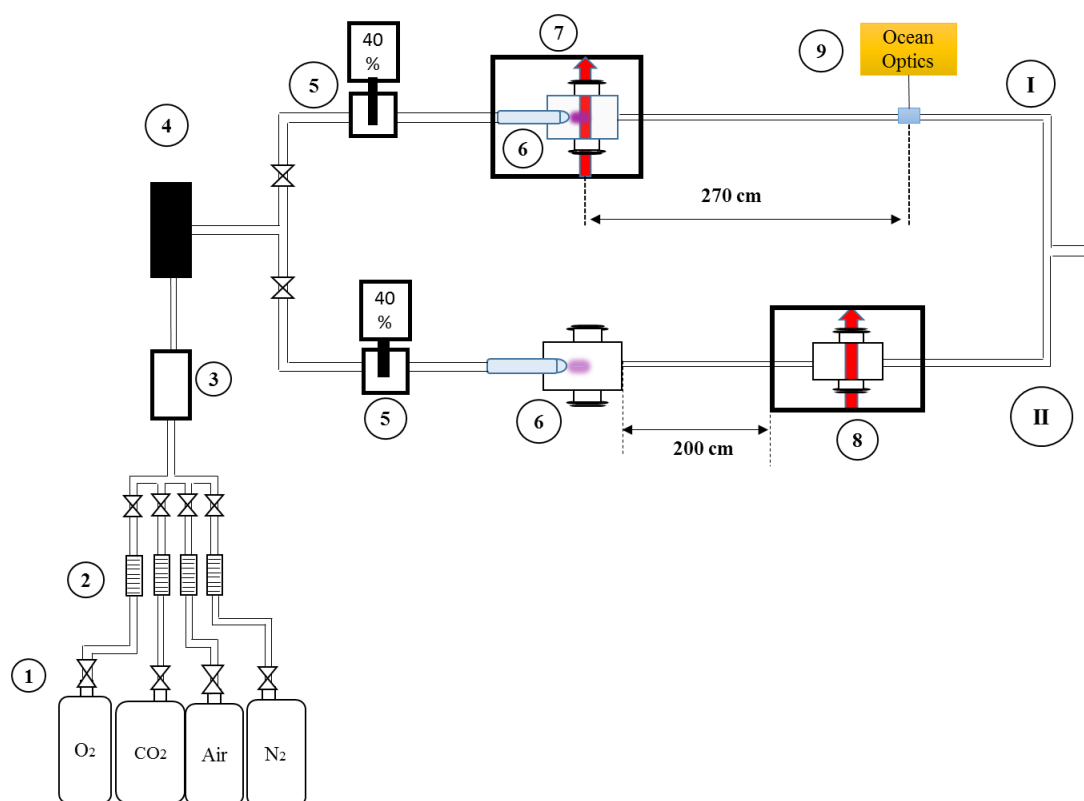


Figure 2.2. A schematic sketch of the experimental setup employed for *in-situ* and downstream analysis of NTP. The system consists of: (1) feed gases, (2) flow meters, (3) mixing cylinder, (4) relative humidity regulator, (5) relative humidity meter, (6) non-thermal plasma jet transmission cell, (7) *in-situ* FTIR, (8) downstream FTIR and (9) Ocean Optics spectrometer flow cell. Channels I and II were employed for *in-situ* and downstream monitoring, respectively.

Parameter	
Feed gas compositions	N ₂ , O ₂ , artificial air (80% N ₂ + 20% O ₂), ambient air and 1.0% of CO ₂ in Ar.
Input power/ W	27, 30, 33, 36
Discharge voltage/ kV (± 0.2)	8.8, 9.2, 9.6, 10
Gas flow rate/ dm ³ min ⁻¹	0.2 - 0.5
Gas velocity within the DBD/ cm s ⁻¹	1698 - 4244
Jet length/ cm	0.1 - 0.6
Relative humidity/ %	5.0 – 80

Table 2.2 Summary of the experimental conditions employed in FTIR experiments reported in this thesis.

2.2.4. FTIR analysis

FTIR experiments were carried out using a Varian FTS7000 spectrometer equipped with a ceramic, air cooled infrared source and a liquid nitrogen-cooled MCT detector. In each experiment, a reference spectrum (S_R , 8 cm⁻¹ resolution, 100 co-added and averaged scans) was obtained with the gas flowing but with no discharge. A sample spectrum was then collected, immediately after which the high voltage power supply was switched on, and further sample spectra (S_S) collected at regular intervals up to 10 minutes. The sample spectra were ratioed to the reference spectrum according to:

$$\text{Absorbance, } A = \text{Log}_{10}(S_S/S_R) \quad (2.1)$$

This data manipulation results in difference spectra in which peaks pointing up, to +(Absorbance), arise from the gain of absorbing species in S_S with respect to S_R , and peaks pointing down, to -(Absorbance), to the loss of absorbing species. Figure 2.3 shows an example of FTIR spectra processing for an air sample passed through the NTP and monitored downstream. From the same figure the reference spectrum (S_R) showed in (i) was collected before powering the plasma generator. The sample spectrum (S_S) showed in (ii) was collected after switching the plasma generator on, and the spectrum showed in (iii) was obtained by solving the equation (2.1). It should be pointed out that the FTIR resolution of 8.0 cm⁻¹ was chosen to maintain rapid scans, and the time required for each scan was 45 s.

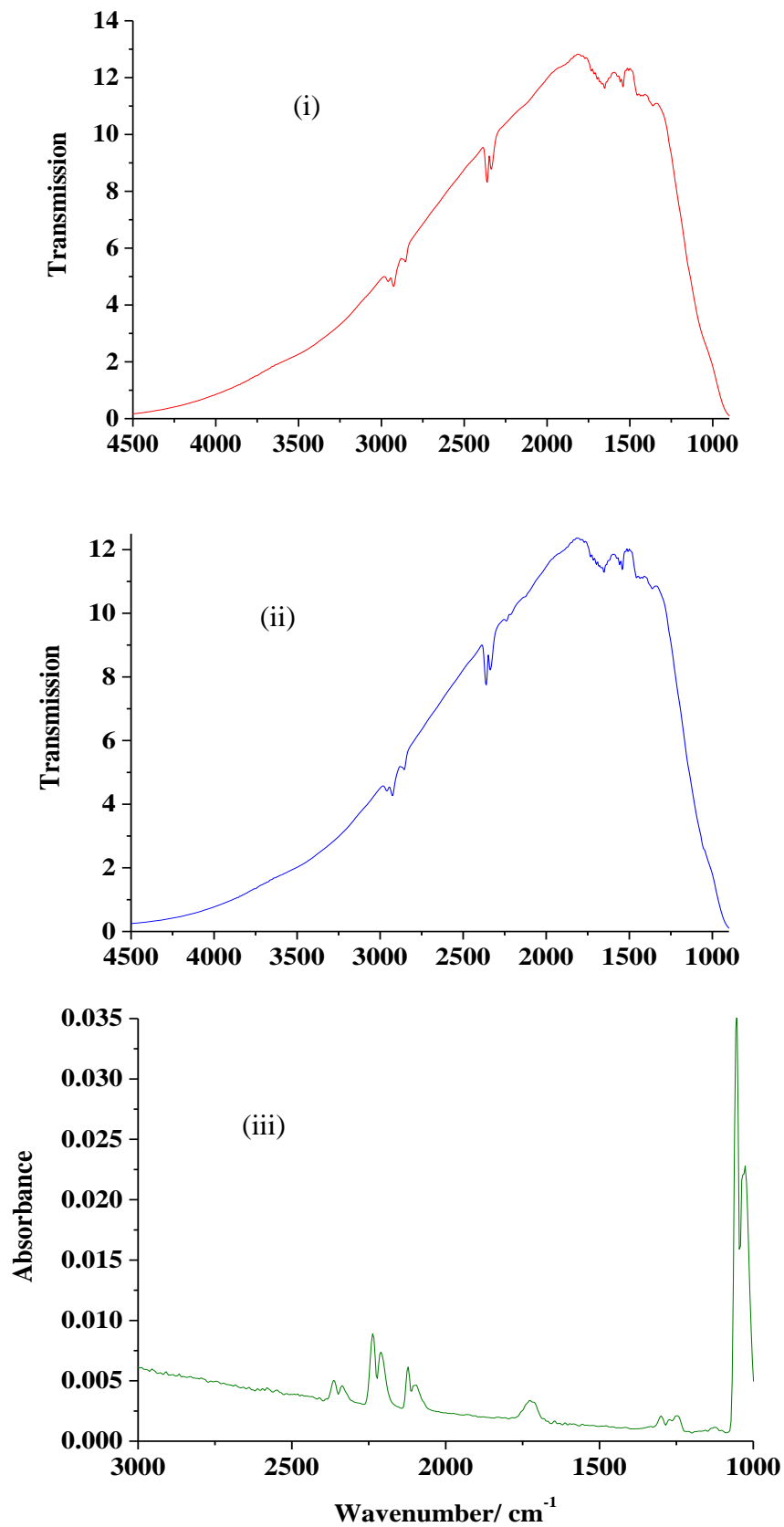


Figure 2.3. An example of FTIR spectra processing: (i) a reference spectrum (S_R) collected from ambient air, (ii) a sample spectrum collected after powering the NTP generator (S_S) and (iii) $A = \text{Log}_{10}(S_S/S_R)$.

The ozone concentration was monitored by integrating the FTIR absorbance band from 2070 to 2135 cm^{-1} using an integrated band intensity coefficient (IBI) of 6.04×10^{-19} cm molecule $^{-1}$, as reported by Perner et al. [2]. The NO_2 concentration was monitored at 1631 cm^{-1} employing an extinction coefficient of 1.81×10^{-19} cm^2 molecule $^{-1}$ [3], and the concentration of N_2O was quantified by integrating the band from 2167 to 2268 cm^{-1} using an integrated band intensity coefficient of 463 cm^{-2} atm $^{-1}$, determined during this work (see section 3.2.2). The bands integrations were carried out using OriginPro software.

2.2.5. N_2O calibration

In order to allow the estimation of N_2O partial pressure, the integrated band intensity coefficient (IBI) for the FTIR absorbance band from 2167 to 2268 cm^{-1} was determined by the means of a calibration curve. The calibration was carried out using the experimental setup shown in fig. 2.2 channel (I). Prior to each run, the reference spectrum (S_R) was collected using N_2 . The partial pressures of 1.23, 1.64 and 2.44×10^{-2} atm of N_2O were prepared by admixing pure N_2O at 0.05 dm^3 min $^{-1}$ with N_2 at 4.0, 3.0 and 2.0 dm^3 min $^{-1}$, respectively. The mixed gases were allowed to pass through the IR transmission cell for at least 5 minutes to ensure homogeneity, after which the sample spectrum (S_S) was collected. After each run, the transmission cell was purged with N_2 . The calibration curve was established by plotting the integrated band areas vs. the partial pressures of N_2O , and the IBI for the band from 2167 to 2268 cm^{-1} was estimated on the basis of the Beer Lambert Law:

$$A = \text{IBI} \times b \times c \quad (2.2)$$

where A is the integrated band area (cm^{-1}), IBI is integrated band intensity coefficient (cm^{-2} atm $^{-1}$), b is the transmission cell pathlength (cm) and c is the partial pressure (atm).

2.2.6. UV analyses of ozone

The concentration of ozone was monitored online UV-Vis spectroscopy by passing the gas through a 10 mm optical pathlength flow cell connected to an Ocean Optics spectrometer (USB2000, Ocean Optics), and the absorbance was monitored at 254 nm. Prior to the analysis, the cell was purged with pure carrier gas (i.e. air or oxygen) to calibrate the spectrometer background. The ozone concentration was calculated using a molar extinction coefficient of 3000 dm^3 mol $^{-1}$ cm^{-1} [4]. This approach was employed only when the feed gas was pure oxygen. However, when the feed gas was dried air, FTIR spectroscopic analyses

were carried out to avoid possible interferences of other by-products such as N_2O_5 and HNO_3 with ozone at 254 nm [5], see section 3.3.4. The concentration was then converted from atm to g m^{-3} using the Ideal Gas Law.

A similar flow cell was employed for monitoring the instantaneous change in dissolved ozone concentration at 258 nm using a molar extinction coefficient of $2900 \text{ dm}^3 \text{ mol}^{-1} \text{ cm}^{-1}$ [6] after adjusting the spectrometer background with deionised water.

2.2.7. Gas temperature measurement

Gas temperature within the discharge region is one of the most important factors that can have a significant effect on the physical and chemical properties of the NTP. Hence, in separate experiments, the change in the NTP jet generator exhaust gas temperature with time was monitored using a transmission cell similar to that employed for *in-situ* and downstream analyses, but with an additional port on the top of the cell. The port at the top was used to pass a thermometer (Fisherbrand, FB58555, UK) into the plasma jet 5 mm beyond the DBD nozzle. This procedure was taken to ensure direct monitoring of the gas temperature within the jet without interfering significantly with the jet flow.

2.3. Ozone generation via a dielectric barrier discharge packed bed reactor (DBD-PBR)

This section discusses the design, fabrication steps and the operation procedures of a novel dielectric barrier discharge packed bed reactor (DBD-PBR) produced during the work reported in this thesis and employed for ozone generation from oxygen and air.

2.3.1. Novel DBD-PBR structure and fabrication steps

Figure 2.4 shows the novel DBD-PBR system employed for ozone generation. As can be seen from the figure, the system consists of three main sections: the power supply, cooling system, and a discharge cell. The power supply was a high-voltage, sinusoidal type power transformer (NP-10000-30, NeonPro, China) with AC output voltages ranged from 0 to 10 kV peak-to-peak at a constant frequency of 24 kHz. The input power supplied to the high voltage power transformer was adjusted to the desired level using a voltage controller (Variac transformer) placed prior to the power supply, and the amount of power consumed by the system was monitored using a 2000 MU, Prodigit Electronics power meter. The discharge cell temperature was maintained at the desired level using a water recycler

(LTC1Grant, Cambridge Ltd) with a temperature controller. For safety purposes, the coolant inlet and outlet tubes of the discharge cell were passed through earthed metallic rings.

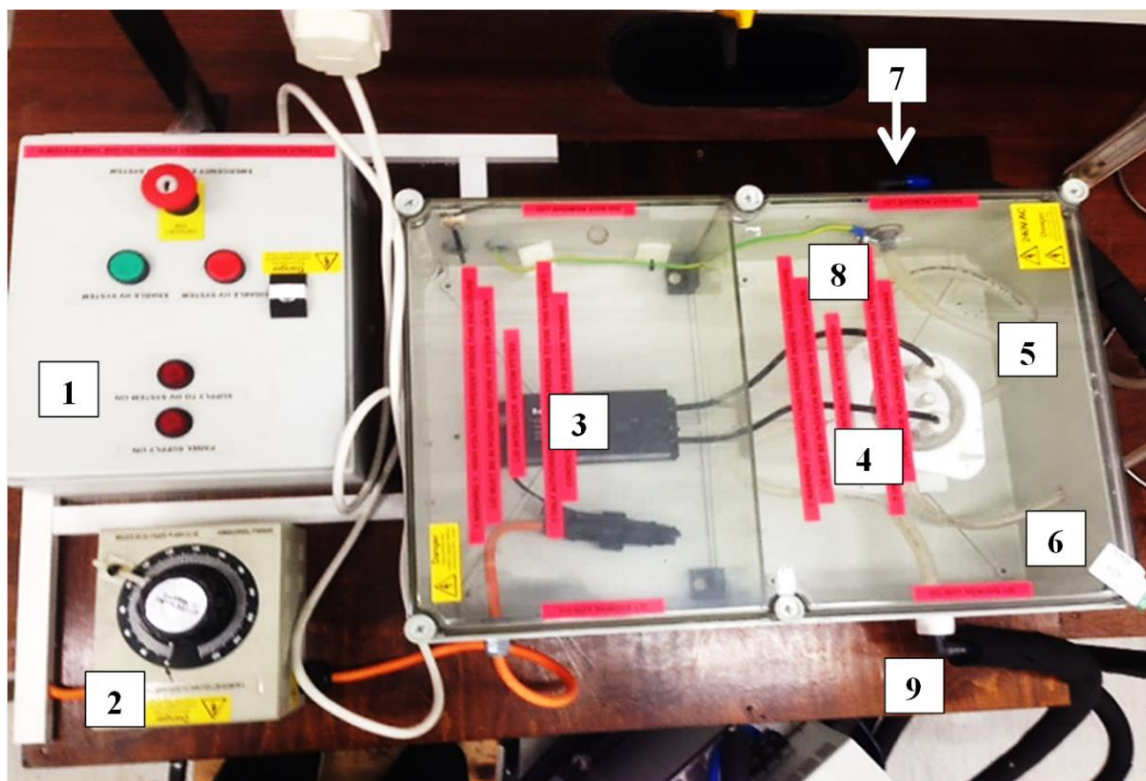


Figure 2.4. A photo showing the top view of the DBD-PBR system employed for ozone generation: (1) safety power regulator, (2) variac transformer, (3) high voltage power supply, (4) DBD-PBR discharge cell, (5) feed gas inlet, (6) exhaust gas outlet, (7) coolant inlet, (8) earthed metallic ring and (9) coolant outlet.

Figure 2.5 shows a schematic of the novel discharge cell employed for ozone generation. The cell consisted of a jacketed cylindrical base made of borosilicate glass with internal diameter of 5.2 cm and height of 7.0 cm. The cell was covered with a glass lid penetrated by 2 ports to allow access for the HV wires. A PTFE plate 1.0 cm thick, 6.0 cm high and 5.2 cm width was placed perpendicular to the input and outlet gas path in the centre of the jacketed base dividing the cell into two halves. Each half consisted of a set of 2 or 3 perforated stainless steel mesh electrodes separated from each another by a layer or more of dielectric. Each set of electrodes consists a high voltage electrode and one or two supporting

electrodes. The gap between the supporting and HV electrodes were varied from 2.0 to 4.0 mm to determine the effect of the dielectric packing gap width on the performance of the cell, and to enhance the distribution of heat along the dielectric layer.

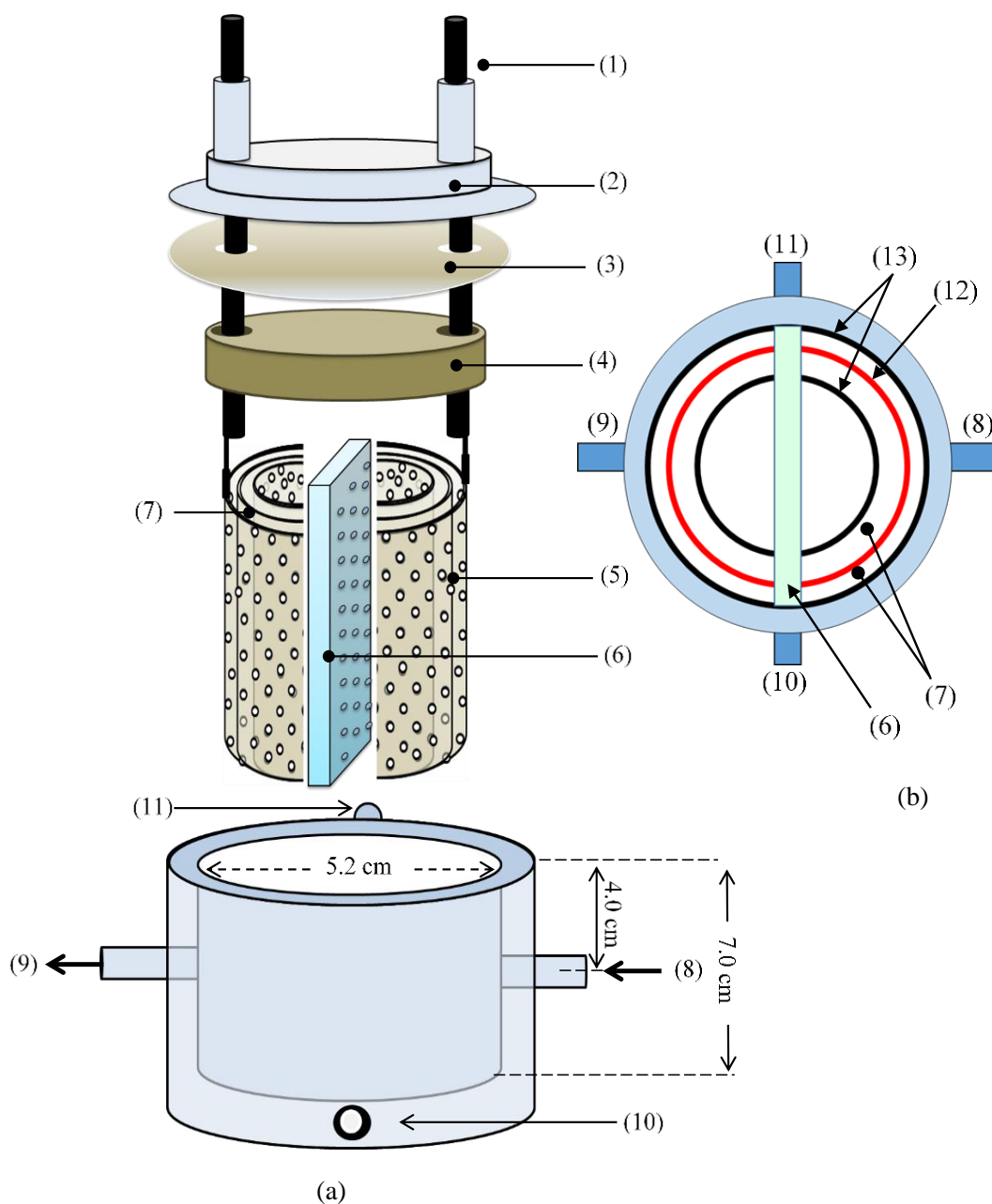


Figure 2.5. (a) A schematic of the DBD-PBR cell employed for ozone generation: (1) high voltage power supply, (2) cell lid, (3) 1.0 mm thick soft PTFE sheet, (4) 10.0 mm thick PTFE disk, (5) stainless steel mesh electrodes, (6) 10.0 × 52.0 × 60.0 mm perforated PTFE plate, (7) dielectric beads filling gap, (8) feed gas inlet, (9) exhaust gas outlet, (10) coolant liquid inlet and (11) coolant outlet. (b) Cross-section view of the DBD-PBR cell shows the electrodes arrangement: (12) high voltage electrode and (13) stainless steel supporting electrodes.

Two shapes of electrodes were employed, semi-cylindrical and planer, to assess the effect of electrode shape on ozone production as can be seen from fig. 2.6. From the figure it can be seen that the electrodes in each set were numbered starting from the cell centre, and electrode # 1 was added or removed from each half depending on the number of electrodes required. The dimensions of the HV and supporting electrodes were varied depending on the cell arrangement and the packing width of the dielectric layer. For instance, to maintain a dielectric packing gap width of 2.0 mm between the HV and the supporting electrodes using the cell (a) the electrodes dimensions were 6.0 cm × 0.1 cm × widths of: 5.0, 4.7 and 4.5 cm for the electrodes 1, 2 and 3, respectively. However, for the same packing gap width but using the cell (b) the electrodes dimensions were 6.0 cm × 0.1 cm × widths of 6.5, 6.7 and 7.0 cm for the electrodes 1, 2 and 3, respectively. After arranging electrodes and dielectric layers, the cell was then sealed using a soft gasket sheet of PTFE placed between the jacketed base and the cover, and both the base and the cover were assembled using silicon rubber glue. The sealed cell was left to dry for 24 hours with nitrogen gas passing through.

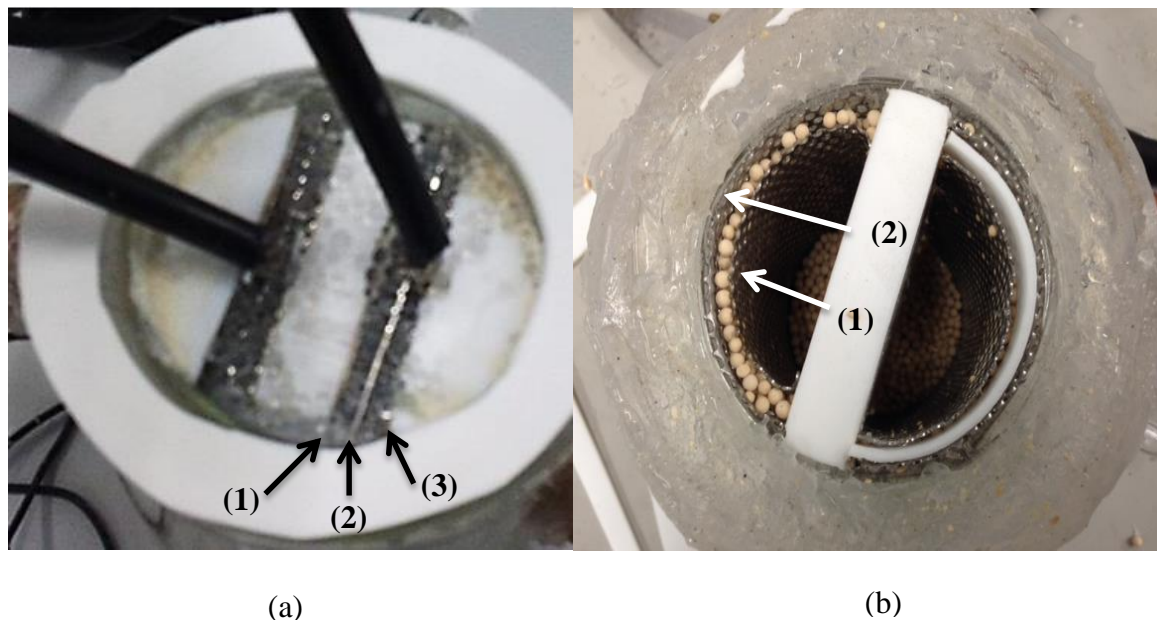


Figure 2.6. Photographs of the electrode shapes and arrangement in the DBD-PBR discharge cell: Arrangement (a): the cell consists of two sets of planar electrodes with two supporting PTFE plates to maintain the electrode positions and the electrodes dimensions were: 6.0 cm × 0.1 cm × widths of: 5.0, 4.7 and 4.5 cm for the electrodes 1, 2 and 3, respectively. Arrangement (b): the cell consists of two sets of semi-cylindrical shaped mesh stainless steel electrodes 6.0 cm × 0.1 cm × widths of 7.0, 6.7 and 6.5 cm for the electrodes 3, 2 and 1, respectively, giving a gap of 2.0 mm between the two electrodes of each set.

2.3.2. DBD-PBR operation procedures

The system was fed with pure oxygen or dried air depending on the experiment. The dried air was produced by pumping ambient air using a KOI AIR25 Blagdon air pump through a Dreschel bottle filled with a freshly activated silica gel to maintain the relative humidity at $\leq 0.6\%$. The relative humidity of the gas exiting the Dreschel bottle was monitored using a calibrated Testo 605-H1 humidity meter. The feed gas flow rate was adjusted using a needle valve and monitored with a calibrated gas flow meter (NGX, PLATON) placed prior to the DBD-PBR system. Before operating the DBD-PBR, water was recycled through the discharge cell and its temperature was adjusted to the desired level and allowed to stabilize. The feed gas was allowed to pass through the system at a fixed flow rate and used to set the background of the ozone analyzer. The voltage transformer was then adjusted to the desired level, and the ozone concentration was monitored. The DBD-PBR required ca. 30 minutes to reach a steady state and all the data presented in the results sections were obtained under steady state conditions.

2.3.3. Discharge voltage and frequency measurements

In order to characterize the discharge power, a 1.0 mm in diameter stainless steel rod was passed through the output gas pipe and connected to one of the HV electrodes within the sealed cell. Figure 2.7 shows a schematic of the setup employed for monitoring the discharge power. The discharge voltage and frequency were then monitored using a HV 1000:1 reducing probe (Testec, RS 366-9141) with a maximum load of 15 kV peak-to-peak coupled with an oscilloscope (Philips, PM3217). The HV probe passed the sampled power through a chain of resistors by which the input voltage was reduced 1000 \times before it passed to the oscilloscope. During the operation of the DBD-PBR using dried air, a bright glow (i.e. the NTP) was observed to cover the inner wall of the discharge cell as can be seen from fig. 2.7.

Figure 2.8 shows a typical example of the discharge power analysis. As can be seen from the figure, the amplitude of the trace is the discharge voltage, while the frequency is the number of the voltage cycles per second.

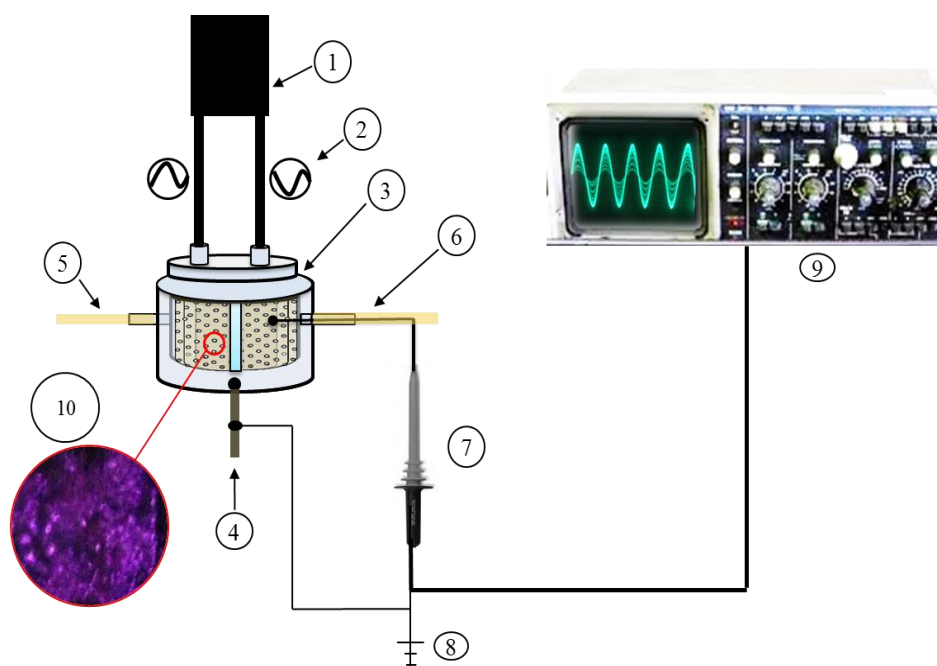


Figure 2.7. Schematic of the setup employed for monitoring the discharge power: (1) HV power supply, (2) simultaneous polarity of the HV electrodes, (3) NDBD-PBR discharge cell, (4) coolant inlet, (5) inlet gas tube, (6) outlet gas tube, (7) HV probe, (8) grounded electrode, (9) oscilloscope and (10) a side view of the discharge cell during the operation.

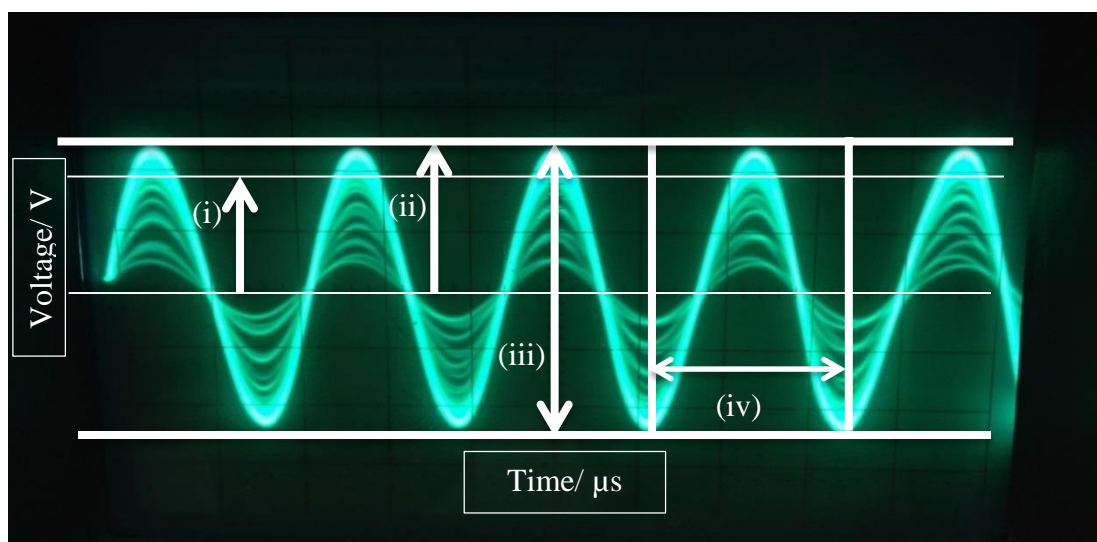


Figure 2.8. Typical example of discharge power measurement carried out using the Philips oscilloscope. The oscilloscope voltage division was set at 2.0 kV and time division was 20 μ s. The peak height was used to estimate the output voltage either as (i) kV RMS, (ii) kV or (iii) kV peak-peak. The frequency was determined by dividing the number of complete voltage cycles by time (iv).

2.3.4. Ozone destruction in the effluent gas

For safety purposes, the ozone-containing exhaust gas was passed through a Dreschel bottle filled with a MnO₂-based catalyst to convert the ozone to oxygen [7, 8]. The catalyst, (Carulit 200), was obtained from Cara Corp, UK, and used without further treatment. From the information provided by Cara Corp, the interaction time between ozone and the catalyst should be at least 0.72 seconds, while the gas velocity should not exceed 66 cm s⁻¹. From this information, the amount of catalyst placed into the Dreschel bottle (internal diameter 6.3 cm and height 15.0 cm) was calculated for the highest working flow rate of 20 dm³min⁻¹. The catalyst layer height within the bottle was determined according to:

$$U_G = Q_G / \pi \times r^2 \quad (2.3)$$

Where U_G is the gas velocity (cm s⁻¹), Q_G is the flow rate in cm³s⁻¹, and r is the cylinder radius (cm). From equation 2.2, the height of catalyst layer could be identified for any cylindrical cell by substituting the relative radius. Thus, the gas linear velocity at 20.0 dm³ min⁻¹ was determined using equation 2.3 as follows:

$$U_G = 333 \text{ cm}^3\text{s}^{-1} / \pi \times 9.92 \text{ cm}^2 = 10.7 \text{ cm s}^{-1}$$

The minimum height of the catalyst layer was calculated based on the gas velocity according to:

$$H = U_G \times T \quad (2.4)$$

In which H is the catalyst height (cm) and T is the interaction time (s) respectively. Therefore, the height of the catalyst layer should be at least 7.7 cm to obtain a contacting time of 0.72 s between the catalyst and ozone gas. The efficiency of the cell with respect to ozone destruction was confirmed by placing Ocean Optics flow cells before and after the destruction unit.

2.4. Ozone - water mass transfer

2.4.1. The Oscillatory Baffled Reactor (OBR)

The Oscillatory Baffled Reactor (OBR) system is shown in fig. 2.9 and consisted of a jacketed column, 190 cm in length and 2.5 cm in internal diameter (D), which was mounted

vertically on an oscillation-inducing motor. The column contained orifice-type baffles made of 2.0 mm thick stainless steel with an outer diameter of 24 mm and an inner diameter (D_o) 12.5 mm. The baffles were fixed along the column using two stainless steel rods of diameter 2.0 mm, and the distance separating each pair of baffles was 37.5 mm. These baffle geometries were chosen to maintain optimal mixing [9]. The fluid oscillation motion was provided by a motor connected to a piston fixed at the bottom of the column. The oscillation frequency and amplitude were adjusted using control units connected to the motor. As can be seen in fig. 2.9, the column had two inlets at the bottom for ozone and water, and a sampling port located 90 cm from the column bottom.

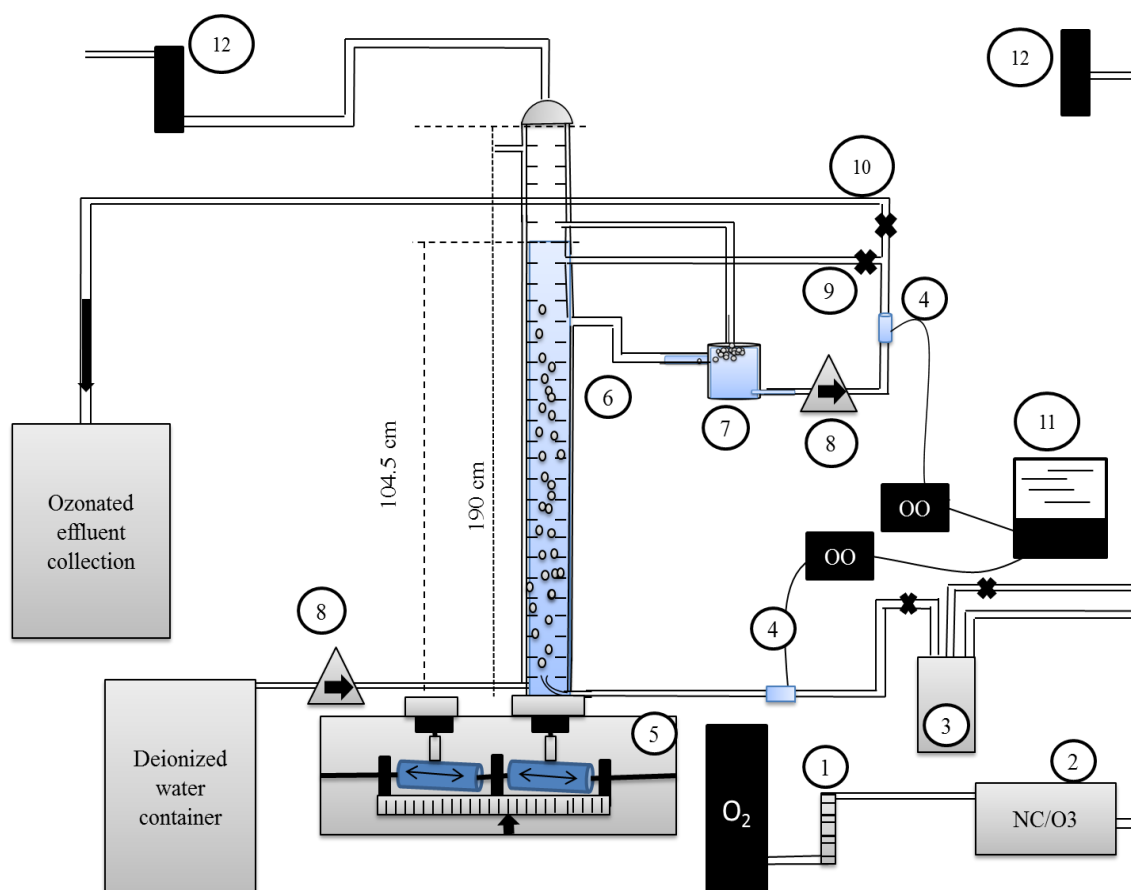


Figure 2.9. The Oscillatory Baffled Reactor system: (1) gas flow meter, (2) ozone generator (NDBD-PBR), (3) ozone distribution cell, (4) Ocean Optics flow cells, (5) oscillation supplying motor, (7) bubble removing cell, (8) peristaltic tubing pumps, (9) return port, (10) outlet port, (11) data collection station and (12) ozone destruction cells.

Ozone was passed through an ozone distribution cell placed prior to the reactor to control the direction of the input gas flow. The distribution cell consisted of one inlet channel for the ozone feed and two outputs each with a valve for gas release. As can be seen in fig. 2.9, one of the output channels was connected to the flow cell of an Ocean Optics Spectrometer positioned prior to the OBR while the other one was directed to an ozone catalytic destruction cell. The ozone distribution cell was included to allow the ozone generator to reach the steady state before ozone was introduced into the reactor through the bottom of the OBR.

The instantaneous change in the dissolved ozone concentration was monitored by passing the sampled water at a pre-set flow rate through an Ocean Optics spectrometer flow cell (10 mm optical pathlength). The water sampling rate was maintained using a calibrated peristaltic pump (520S/R, Watson-Marlow). A bubble-removing cell was placed prior to the flow cell to remove any remaining bubbles from the sample before analysis. The released gas was returned to the column through a gas returning port located 35 cm above the sampling port. The water was then passed either back to the column through a water return port located 15 cm above the sampling port, or to an external tank, depending on the type of experiment performed. The volume of water occupying the analytical cycle including the bubble-removing cell, was 57 cm^3 , and the actual volume within the column at any time during the analysis was 500 cm^3 , with a height of 104 cm with no aeration at room temperature. After each run, the feed gas was allowed to pass directly to the ozone destruction cell through the gas distribution cell. The system was purged with oxygen for 10 minutes to remove the dissolved ozone, after which the water was completely removed from the column, and the latter flushed with fresh, deionised water.

It should be highlighted that all these experiments were performed at room temperature under atmospheric pressure with no pH adjustment, using deionised water from a Millipore Milli-Q system ($18.3 \text{ M}\Omega \text{ cm}$). Hence, any complications arising from the presence of ozone-scavenging species were avoided [10, 11]. The range of experimental conditions in terms of the input gas and liquid flow rates, ozone concentrations and oscillation amplitude and frequency in the semi-batch and in continuous flow experiments are summarized in tables 2.3 and 2.4.

Parameter	Semi-bath	Continuous
$Q_G/\text{dm}^3 \text{ min}^{-1}$	0.1 - 2.0	0.1 - 1.0
$U_G/\text{cm s}^{-1}$	0.3 - 6.8	0.3 - 3.4
$Q_L/\text{dm}^3 \text{ min}^{-1}$	0.0	0.1 - 1.0
$U_L/\text{cm s}^{-1}$	0.0	0.3 - 3.4
$[\text{O}_3]_G/\text{mg dm}^{-3}$	11.3 - 64.5	11.3 - 64.5
Sampling rate $/\text{dm}^3 \text{ min}^{-1}$	0.18	= Q_L

Table 2.3. Summary of the experimental conditions employed for ozone- water mass transfer study.

Parameter	Semi-batch	Continuous
Frequency /Hz	1.2 - 5.0	5.0
Amplitude /mm	1.0 - 6.0	6.0
Re_o	178 - 4600	4600
St	1.99 - 0.33	0.33

Table 2.4. The oscillation conditions employed for the work reported in this thesis.

2.5. EDTA complexes treatments using ozone, ozone and UV irradiation

2.5.1. EDTA samples preparation

Aqueous solutions of $\text{Na}_2[\text{Cu(II)-EDTA}]$ and $\text{Na}[\text{Fe(III)-EDTA}]$ were prepared by placing the required mass of each salt into 5.0 dm^3 flask containing deionised water ($18.3 \text{ M}\Omega \text{ cm}$). The solution was left to mix overnight using magnetic stirrer to assure complete dissolution. These solutions were subjected to the ozonation and UV irradiation treatments. The Cu(II)-EDTA and Fe(III)-EDTA concentrations employed for water treatment experiments were 250 and 100 mg dm^{-3} .

2.5.2. UV reactor

Water treatment experiments were carried out under continuous flow conditions with and without oscillation using the setup shown in fig. 2.9. The ozonated sample was passed through a sampling cell similar to the one used for bubble removing shown in fig. 2.9 with three ports: inlet, outlet and a top one for sample collection. The top port of the sampling cell was capped with a rubber subbaseal to allow sampling using a 20 ml syringe. The outlet port of the sampling cell was connected to a UV-Photolysis reactor using Teflon tubing. Figure 2.10 shows a sketch of the UV photolysis reactor employed. The reactor consisted of a 320 mm long UV-light lamp (TUV 16 W, UP-SE-UNP, Philips, UK, $\lambda_{\text{max}} = 254 \text{ nm}$) mounted in a 30 mm internal diameter quartz glass tube positioned at the centre of a 70 mm internal diameter borosilicate column. Two ports were employed one at the bottom for feeding and the other at the top to facilitate continuous flow operation. As can be seen from figure 2.10, the effective irradiation area of the UV-reactor is that between the points A and B, and hence the time required for the water sample to pass from A to B was considered as the treatment residence time, determined primarily by the input water flow rate. Table 2.5 summarizes the experimental conditions employed during the EDTA solutions treatment.

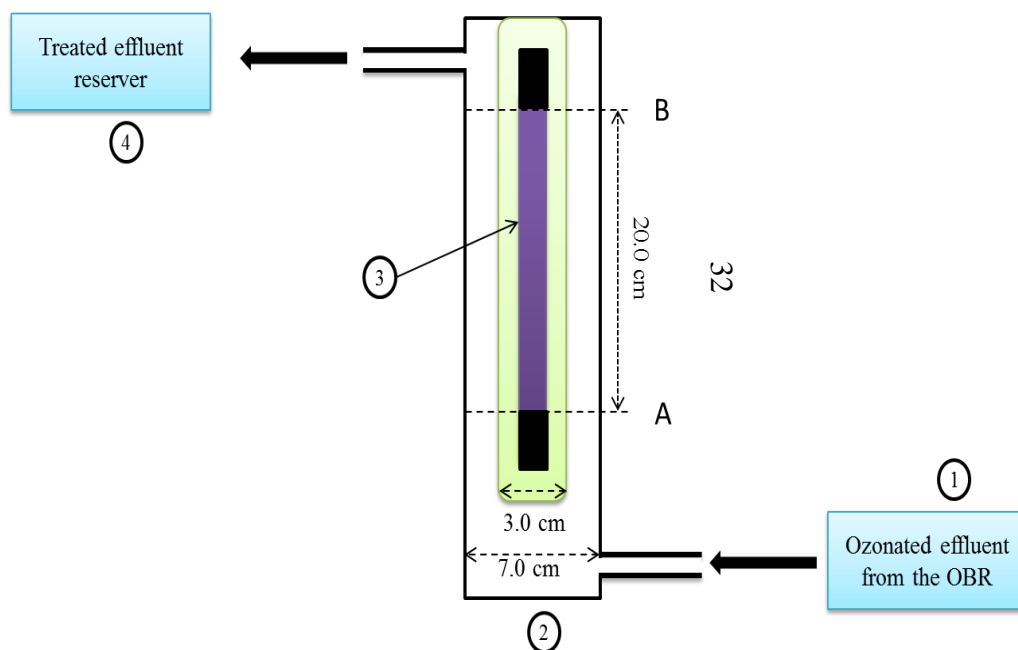


Figure 2.10. A schematic of the UV-photolysis reactor employed for water treatment: (1) feed water inlet, (2) borosilicate column, (3) UV lamp and (4) outlet port.

Water sample flow rate /cm ³ min ⁻¹	Baffled reactor residence time /min	OBR residence time /min	UVR-photolysis residence time /min
20.0	18.16	16.69	15.10
30.0	11.42	10.50	9.50
40.0	9.08	8.25	7.55
60.0	6.05	5.57	5.03
80.0	4.54	4.09	3.78
100.0	3.63	3.3	3.02

Table 2.5 Summary of the operational conditions employed for M-EDTA treatment.

2.5.3. EDTA complexes sampling and ion chromatography analysis

After conducting the required treatment, 10 ml of water sample was collected and placed into a vial consisting a 100 μl of $10 \times 10^3 \text{ mg dm}^{-3}$ sodium thiosulfate ($\text{Na}_2\text{S}_2\text{O}_3$) solution. The vial was capped with a plastic lid containing PTFE septum and shaken. Sodium thiosulfate solution was added to prevent any possible oxidation of M-EDTA beyond sample collection, and hence to allow accurate evaluation of the treatment performance [12, 13]. The dissolved Cu(II)-EDTA concentrations in water were monitored using an Ion Chromatography Dionex ICS-1000 system, shown in fig. 2.11. The system was equipped with an AS40 auto-sampler and a conductivity detector. The stationary phase was an Ionpac AS14A, 4 x 250 mm analytical column, and the carrier phase was 8.0 mM Na_2CO_3 /1.0 mM NaHCO_3 solution; the injection loop was 25.0 μl , and the eluent flow rate was 1.0 $\text{cm}^3 \text{ min}^{-1}$.

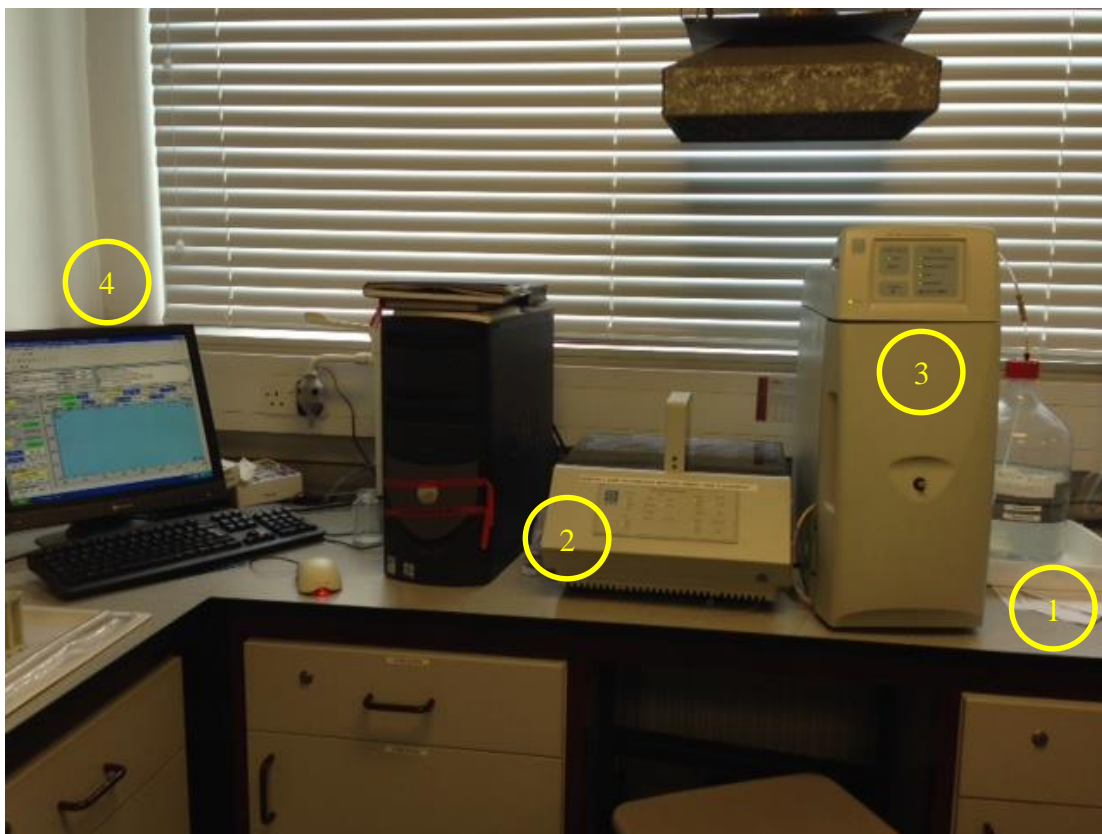


Figure 2.11. A photograph of the ion chromatography system employed for monitoring water samples after treatments. The system consists of: (1) mobile phase, (2) auto-sampler, (3) separation and detection unit and (4) data collection software.

2.5.4. Total organic carbon (TOC) analysis

Total organic carbon (TOC) analysis is normally employed for evaluating the efficiency of water treatment approaches towards the mineralization of organic compounds [14, 15]. The TOC analyses were carried out using a TOC analyser (Shimadzu TOC-5050A) equipped with ASI-5000A auto-sampler and a non-dispersive infrared detector (NDIR). Figure 2.12 shows a photograph of the system employed for monitoring the TOC of water samples. Prior to each experiment, the system was calibrated using standard solutions with TOC concentrations from 10 to 500 mg dm⁻³. The system monitors the total carbon (TC) and inorganic carbon (IC) (i.e. bicarbonate, carbonate and dissolved CO₂) in each sample, and the TOC analysis was obtained by subtracting IC from TC. In each run, 2.5 cm³ of the water sample was automatically injected into the system, and split for IC and TC analyses. For the IC analysis the sample was passed through an acidification vessel consisting of a

concentrated solution of H_3PO_4 to convert all inorganic carbon to CO_2 . The latter was then transferred to the NDIR for IC monitoring using a carrier gas (i.e. CO_2 free air) at $150 \text{ cm}^3 \text{ min}^{-1}$. The second portion of the water sample was passed through a $680 \text{ }^\circ\text{C}$ furnace using the carrier gas to convert all carbon containing molecules to CO_2 . The exhaust of the furnace passed through a dehumidifier and a halogen scrubber positioned prior to NDIR for TC analysis. The detection range of the TOC monitoring system (according to the manufacturer) was from 0.05 to 400 mg dm^{-3} .

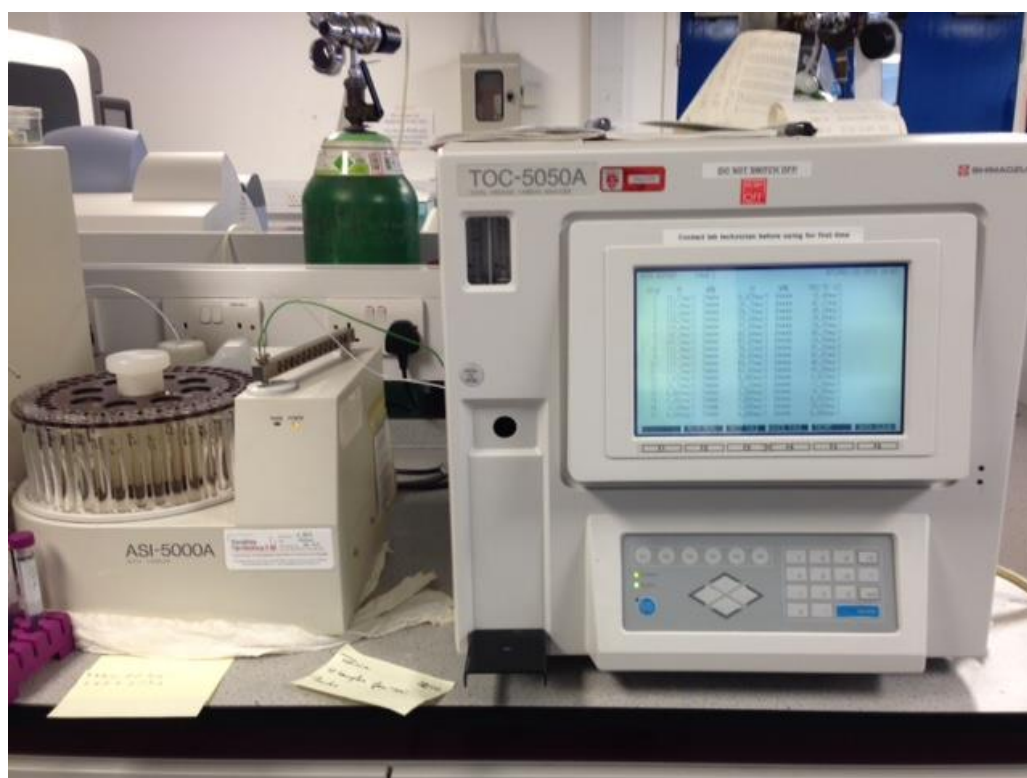


Figure 2.12. A photograph of the TOC analyser.

2.5.5. Mass spectroscopy analysis

Mass spectroscopy analyses were carried out to identify the by-products resulting from EDTA treatment using a Waters LCT Premier Micro-mass equipped with an electrospray ionization (ESI) source operated in negative ionization mode. The carrier solution was deionised water, with a sampling rate of $20.0 \text{ mm}^3 \text{ min}^{-1}$ using nitrogen gas for drying and

nebulizing. The source and the de-solvation temperatures were maintained at 120 and 250 °C, respectively.

2.6. References

[1] Koinuma, H., Ohkubo, H., Hashimoto, T., Inomata, K., Shiraishi, T., Miyanaga, A. and Hayashi, S. (1992) 'Development and application of a microbeam plasma generator', *Applied Physics Letters*, 60(7), pp. 816-817.

[2] Perner, D., Schmeltekopf, A., Winkler, R.H., Johnston, H.S., Calvert, J.G., Cantrell, C.A. and Stockwell, W.R. (1985) 'A laboratory and field study of the equilibrium N_2O_5 yields reversibly $\text{NO}_3 + \text{NO}_2$ ', *Journal of Geophysical Research*, 20, pp. 3807-3812.

[3] Tuazon, E.C., Sanhueza, E., Atkinson, R., Carter, W.P.L., Winer, A.M. and Pitts Jr, J.N. (1984) 'Direct determination of the equilibrium constant at 298 K for the nitrogen dioxide + nitrogen trioxide (NO_3). dblrw. nitrogen pentoxide (N_2O_5) reactions', *The Journal of Physical Chemistry*, 88(14), pp. 3095-3098.

[4] Rakness, K., Gordon, G., Langlais, B., Masschelein, W., Matsumoto, N., Richard, Y., Robson, C.M. and Somiya, I. (1996) 'Guideline for measurement of ozone concentration in the process gas from an ozone generator', *Ozone-Science & Engineering*, 18(3), pp. 209-229.

[5] Moiseev T, Misra N N, Patil S, Cullen P J, Bourke P, Keener K M and Mosnier J P 2014 Post-discharge gas composition of a large-gap DBD in humid air by UV-Vis absorption spectroscopy *Plasma Sources Science and Technology* **23** 065033

[6] Stucki, S., Baumann, H., Christen, H.J. and Kotz, R. (1987) 'Performance of a pressurized electrochemical ozone generator', *Journal of Applied Electrochemistry*, 17(4), pp. 773-778.

[7] Li, W., Gibbs, G.V. and Oyama, S.T. (1998) 'Mechanism of ozone decomposition on a manganese oxide catalyst. I. In situ Raman spectroscopy and ab initio molecular orbital calculations', *Journal of the American Chemical Society*, 120(35), pp. 9041-9046.

- [8] Radhakrishnan, R. and Oyama, S.T. (2001) 'Ozone decomposition over manganese oxide supported on ZrO₂ and TiO₂: A kinetic study using in situ laser Raman spectroscopy', *Journal of Catalysis*, 199(2), pp. 282-290.
- [9] Ni, X., Brogan, G., Struthers, A., Bennett, D.C. and Wilson, S.F. (1998) 'A systematic study of the effect of geometrical parameters on mixing time in oscillatory baffled columns', *Chemical Engineering Research and Design*, 76(5), pp. 635-642.
- [10] Hoigné, J., Bader, H., Haag, W.R. and Staehelin, J. (1985) 'Rate constants of reactions of ozone with organic and inorganic compounds in water-III. Inorganic compounds and radicals', *Water Research*, 19(8), pp. 993-1004.
- [11] Zhou, H. and Smith, D.W. (2000) 'Ozone mass transfer in water and wastewater treatment: experimental observations using a 2D laser particle dynamics analyzer', *Water Research*, 34(3), pp. 909-921.
- [12] Hureki, L., Croué, J.P., Legube, B. and Doré, M. (1998) 'Ozonation of amino acids: ozone demand and aldehyde formation', *Ozone: Science & Engineering*, 20(5), pp. 381-402.
- [13] Glaze, W.H. and Kang, J.W. (1989) 'Advanced oxidation processes. Description of a kinetic model for the oxidation of hazardous materials in aqueous media with ozone and hydrogen peroxide in a semi-batch reactor', *Industrial & Engineering Chemistry Research*, 28(11), pp. 1573-1580.
- [14] Faria, P.C.C., Órfão, J.J.M. and Pereira, M.F.R. (2005) 'Mineralisation of coloured aqueous solutions by ozonation in the presence of activated carbon', *Water Research*, 39(8), pp. 1461-1470.
- [15] Rosal, R., Rodríguez, A., Perdígón-Melón, J.A., Mezcua, M., Hernando, M.D., Letón, P., García-Calvo, E., Agüera, A. and Fernández-Alba, A.R. (2008) 'Removal of pharmaceuticals and kinetics of mineralization by O₃/H₂O₂ in a biotreated municipal wastewater', *Water Research*, 42(14), pp. 3719-3728.

3. An *in-situ* and downstream study of non-thermal plasma chemistry in an air fed dielectric barrier discharge (DBD)

3.1. Introduction

The aim of this chapter was to achieve a better understanding of how the chemistry of a non-thermal plasma (NTP) varies from the glow region to the downstream exhaust under a range of experimental conditions. To this end, a dielectric barrier discharge (DBD) plasma jet was employed to carry out *in-situ* (i.e. the analysis of the plasma glow) and downstream (i.e. post plasma region) analyses. These analyses were performed using Fourier Transform InfraRed (FTIR) and UV-Vis spectroscopies. A range of neutral and metastable species were identified and monitored in the plasma as they propagated from the plasma glow to downstream regions. The behaviour of these species was monitored as a function of experimental conditions including: input power, gas flow rate, relative humidity and feed gas composition. Because the temperature of the dielectric was expected to increase with time during the DBD operation [1-3], the gas temperature as well as its chemical composition were monitored in the work reported in this chapter. In addition, the uncertainty associated with UV-Vis detection of ozone in the presence of N_2O_5 and/or HNO_3 as interfering species was determined.

3.2. Non-thermal plasma *In-situ* analyses

3.2.1. The effect of feed gas composition

One of the most important parameters that determines the chemical composition of non-thermal plasma is the feed gas composition. Hence, the species formed within the glow and near glow regions were monitored as a function of the feed gas composition. Pure gases were tested first, and then gas mixtures. Figure 3.1 shows spectra collected as a function of time using pure oxygen. As can be seen from the figure, the spectra consist of two pairs of bands, at 2121 & 2098 cm^{-1} and 1055 & 1030 cm^{-1} , which may be unambiguously attributed to the 1st overtone and fundamental absorptions, respectively, of O_3 [5]. Apart from the distinctive bands due to ozone, no other bands were observed. When oxygen was replaced by pure nitrogen, no absorption bands were observed, in agreement with the work of Schmidt-Bleker

et al. [6]. In all cases, as soon as the DBD power supply was switched off, all absorptions disappeared.

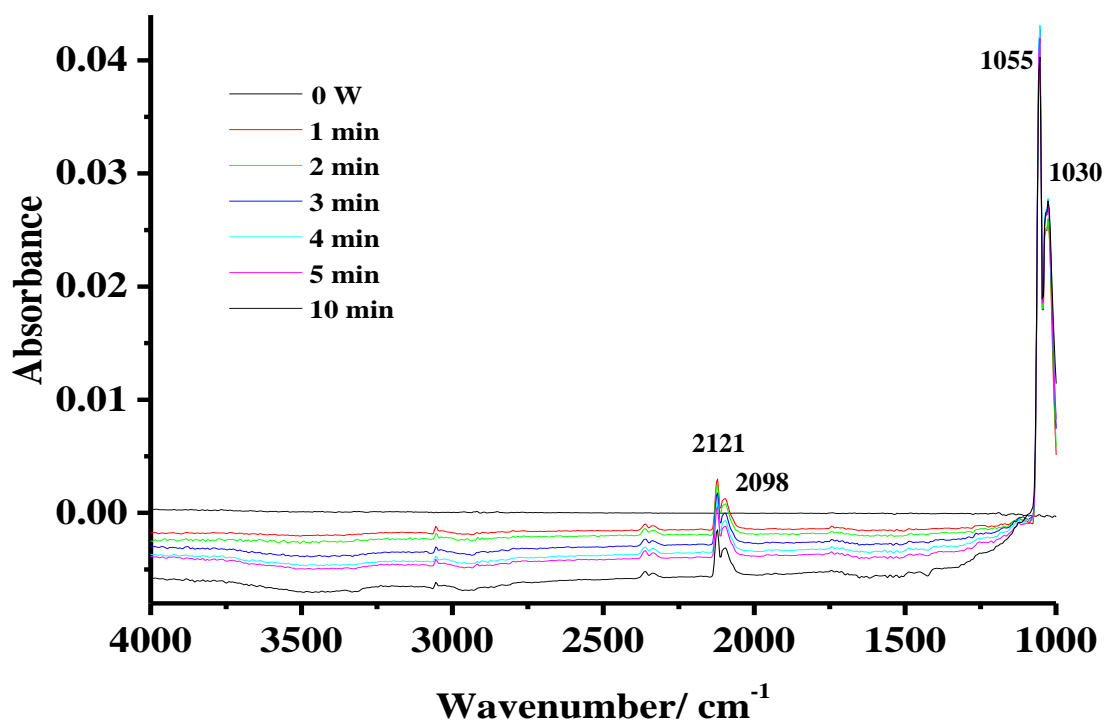


Figure 3.1. In-situ FTIR spectra collected as a function of running time. The input power was 36W, pure oxygen feed at a flow rate of $0.5 \text{ dm}^3 \text{ min}^{-1}$.

Figure 3.2 shows typical *in-situ* spectra collected after 1 minute using: ambient air, humidified artificial air at 40% RH and dry artificial air at a flow rate of $0.5 \text{ dm}^3 \text{ min}^{-1}$ and input power of 36W. The bands observed in the figure are summarized in table 3.1. The features at 2121 and 2098 cm^{-1} may be taken as indicative of ozone production, and hence the features at 1055 and 1030 cm^{-1} are not shown in the spectra presented below for clarity. From figure 3.2, it can be seen that bands due to N_2O , O_3 , N_2O_5 and NO_2 were observed when the feed gas contained N_2 and O_2 . An additional shoulder at 1700 cm^{-1} , and bands at 1341 and 1314 cm^{-1} were observed when the feed gas was ambient air or humidified artificial air, and may be attributed to HNO_3 [7]. The features at 2360 and 2340 cm^{-1} in spectra (ii) and (iii) may be unambiguously assigned to CO_2 [8], and are due to purge mismatch in the FTIR sample compartment. The two features in the same region as CO_2 in spectrum (i) may

be attributed to a vibrationally excited form of CO_2 , $\text{CO}_2^*(\nu)$, and this is discussed in detail below.

Table 3.2 shows the plasma initiating reactions induced by electron collisions with ambient air molecules. The reactions from (3.1) to (3.11) include electronic and vibrational excitation, ionization and dissociation. Table 3.3 lists the chemical reactions taking place in the plasma along with their rate coefficients involving free radicals, free radicals + neutral species and neutral + neutral species. Due to the fact that the concentrations of ions were expected to be significantly lower than those of the neutral species (i.e. 4 orders of magnitude [10]) and hence their effects would be limited to the NTP glow region, these reactions were not included.

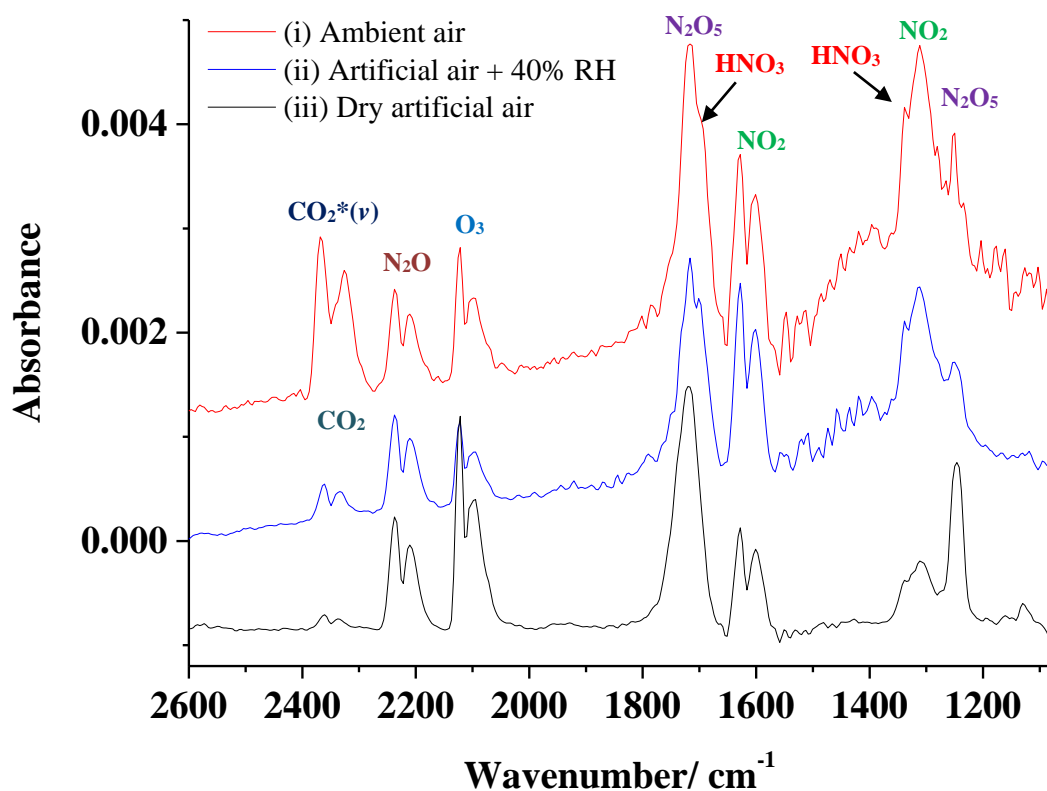


Figure 3.2. In-situ FTIR Spectra collected after 1 minute at 36 W input power as a function of the feed gas composition: (i) ambient air, (ii) artificial air + 40% relative humidity and (iii) dry artificial air. The gas flow rate was $0.5 \text{ dm}^3 \text{ min}^{-1}$.

Band/ cm ⁻¹	Assignment	Reference
2326, 2366	CO ₂ [*] (ν)	This work
1300, 2211, 2237	N ₂ O	[7]
1055, 1030, 2098, 2121	O ₃	[5]
1247, 1720	N ₂ O ₅	[7]
1313, 1341, 1700 (sh)	HNO ₃	[7]
1600, 1627	NO ₂	[7, 9]
2360, 2340	CO ₂	[8]
2176, 2121	CO	[8]

Table 3.1. Assignments of the various features observed in the spectra shown in figure 3.2

(R#)	Reaction
(3.1)	$e + N_2 \rightarrow N_2^* + e$
(3.2)	$e + O_2 \rightarrow O_2^* + e$
(3.3)	$e + CO_2 \rightarrow CO_2^* + e$
(3.4)	$e + N_2 \rightarrow N + N + e$
(3.5)	$e + O_2 \rightarrow O + O + e$
(3.6)	$e + CO_2 \rightarrow CO + O$
(3.7)	$e + H_2O \rightarrow OH + H + e$
(3.8)	$e + N_2 \rightarrow N_2^+ + e + e$
(3.9)	$e + O_2 \rightarrow O_2^+ + e + e$
(3.10)	$e + H_2O \rightarrow H_2O^+ + e + e$
(3.11)	$e + CO_2 \rightarrow CO_2^+ + e + e$

Table 3.2. List of initiating reactions induced by electron collisions with different molecules within ambient air [11-13].

(R#)	Reaction	Rate coefficient (k)	Ref
(3.12)	$\text{N}_2^* + \text{O}_2 \rightarrow \text{O} + \text{O} + \text{N}_2$	$1.5 \times 10^{-12} \text{ cm}^3 \text{ s}^{-1}$	[14]
(3.13)	$\text{N}_2^* + \text{N}_2\text{O} \rightarrow \text{NO} + \text{N} + \text{N}_2$	$8 \times 10^{-17} \text{ cm}^3 \text{ s}^{-1}$	[15]
(3.14)	$\text{N}_2^* + \text{O}_2 \rightarrow \text{N}_2\text{O} + \text{O}$	$7.8 \times 10^{-14} \text{ cm}^3 \text{ s}^{-1}$	[16]
(3.15)	$\text{O}_2^* + \text{O}_3 \rightarrow \text{O} + \text{O}_2 + \text{O}_2$	$5.2 \times 10^{-11} \exp(-2840/T^*) \text{ cm}^3 \text{ s}^{-1}$	[17]
(3.16)	$\text{O}_2^* + \text{N}_2 \rightarrow \text{O}_2 + \text{N}_2$	$3.0 \times 10^{-18} \exp(-200/T) \text{ cm}^3 \text{ s}^{-1}$	[18]
(3.17)	$\text{N} + \text{OH} \rightarrow \text{NO} + \text{H}$	$3.8 \times 10^{-11} \exp(-85/T) \text{ cm}^3 \text{ s}^{-1}$	[19]
(3.18)	$\text{N} + \text{O} + \text{M} \rightarrow \text{NO} + \text{M}$	$6.3 \times 10^{-33} \exp(140/T) \text{ cm}^6 \text{ s}^{-1}$	[20]
(3.19)	$\text{N} + \text{NO} \rightarrow \text{N}_{2(v)} + \text{O}$	$3.4 \times 10^{-11} \exp(-24/T) \text{ cm}^3 \text{ s}^{-1}$	[20]
(3.20)	$\text{N} + \text{O}_2 \rightarrow \text{NO} + \text{O}$	$4.4 \times 10^{-12} \exp(-3220/T) \text{ cm}^3 \text{ s}^{-1}$	[19]
(3.21)	$\text{N} + \text{O}_3 \rightarrow \text{NO} + \text{O}_2$	$2.0 \times 10^{-16} \text{ cm}^3 \text{ s}^{-1}$	[21]
(3.22)	$\text{N} + \text{NO}_2 \rightarrow \text{N}_2 + \text{O} + \text{O}$	$9.1 \times 10^{-13} \text{ cm}^3 \text{ s}^{-1}$	[21]
(3.23)	$\text{N} + \text{NO}_2 \rightarrow \text{NO} + \text{NO}$	$6 \times 10^{-19} \text{ cm}^3 \text{ s}^{-1}$	[22]
(3.24)	$\text{N} + \text{NO}_2 \rightarrow \text{N}_2\text{O} + \text{O}$	$5.8 \times 10^{-12} \exp(220/T) \text{ cm}^3 \text{ s}^{-1}$	[20]
(3.25)	$\text{N} + \text{HO}_2 \rightarrow \text{NO} + \text{OH}$	$1.7 \times 10^{-17} \exp(-1000/T) \text{ cm}^3 \text{ s}^{-1}$	[23]
(3.26)	$\text{N} + \text{HNO} \rightarrow \text{H} + \text{N}_2\text{O}$	$1.44 \times 10^{-12} \text{ cm}^3 \text{ s}^{-1}$	[24]
(3.27)	$\text{N} + \text{N}_2\text{O} \rightarrow \text{N}_2 + \text{NO}$	$1.5 \times 10^{-17} \exp(-570/T) \text{ cm}^3 \text{ s}^{-1}$	[20]
(3.28)	$\text{N} + \text{NO} \rightarrow \text{N}_2\text{O}$	$6 \times 10^{-17} \text{ cm}^3 \text{ s}^{-1}$	[21]
(3.29)	$\text{O} + \text{NO} + \text{M} \rightarrow \text{NO}_2 + \text{M}$	$1 \times 10^{-43} (300/T)^{1.6}$	[20]
(3.30)	$\text{O} + \text{O}_2 + \text{M} \rightarrow \text{O}_3 + \text{M}$	$5.6 \times 10^{-34} (T/300)^{-2.8} \text{ cm}^6 \text{ s}^{-1}$	[18]
(3.31)	$\text{O} + \text{HO}_2 \rightarrow \text{OH} + \text{O}_2$	$2.9 \times 10^{-11} \exp(-200/T) \text{ cm}^3 \text{ s}^{-1}$	[21]
(3.32)	$\text{O} + \text{OH} \rightarrow \text{H} + \text{O}_2$	$2.3 \times 10^{-11} \exp(110/T) \text{ cm}^3 \text{ s}^{-1}$	[18]
(3.33)	$\text{O} + \text{O}_3 \rightarrow \text{O}_2 + \text{O}_2$	$8.0 \times 10^{-12} \exp(-2060/T) \text{ cm}^3 \text{ s}^{-1}$	[19]
(3.34)	$\text{O} + \text{HO}_2 \rightarrow \text{OH} + \text{O}_2$	$2.7 \times 10^{-11} \exp(224/T) \text{ cm}^3 \text{ s}^{-1}$	[18]
(3.35)	$\text{O} + \text{NO}_2 \rightarrow \text{NO} + \text{O}_2$	$6.5 \times 10^{-12} \exp(120/T) \text{ cm}^3 \text{ s}^{-1}$	[19]
(3.36)	$\text{O} + \text{NO}_2 + \text{M} \rightarrow \text{NO}_3 + \text{M}$	$9.0 \times 10^{-32} (T/300)^{-2.0} \text{ cm}^6 \text{ s}^{-1}$	[18]
(3.37)	$\text{O} + \text{NO}_3 \rightarrow \text{O}_2 + \text{NO}_2$	$1.7 \times 10^{-11} \text{ cm}^3 \text{ s}^{-1}$	[21]
(3.38)	$\text{O} + \text{N}_2\text{O}_5 \rightarrow \text{products}$	$3 \times 10^{-16} \text{ cm}^3 \text{ s}^{-1}$	[21]
(3.39)	$\text{O} + \text{HNO} \rightarrow \text{OH} + \text{NO}$	$5.99 \times 10^{-17} \text{ cm}^3 \text{ s}^{-1}$	[15]
(3.40)	$\text{O} + \text{HNO}_2 \rightarrow \text{NO}_2 + \text{OH}$	$2 \times 10^{-11} \exp(-3000/T) \text{ cm}^3 \text{ s}^{-1}$	[20]
(3.41)	$\text{O} + \text{N}_2\text{O} \rightarrow \text{N}_2 + \text{O}_2$	$4.4 \times 10^{-17} \text{ cm}^3 \text{ s}^{-1}$	[20]
(3.42)	$\text{H} + \text{HNO}_2 \rightarrow \text{NO}_2 + \text{H}_2$	$2 \times 10^{-17} \exp(-3700/T) \text{ cm}^3 \text{ s}^{-1}$	[20]
(3.43)	$\text{H} + \text{HNO}_3 \rightarrow \text{NO}_2 + \text{H}_2\text{O}$	$1.39 \times 10^{-20} (T/298)^{3.29} \exp(-3160/T)$	[25]
(3.44)	$\text{H} + \text{O}_2 + \text{M} \rightarrow \text{HO}_2 + \text{M}$	$1.8 \times 10^{-32} (T/298)^{-0.8} \text{ cm}^6 \text{ s}^{-1}$	[26]
(3.45)	$\text{H} + \text{O}_3 \rightarrow \text{OH} + \text{O}_2$	$1.4 \times 10^{-10} \exp(-470/T) \text{ cm}^3 \text{ s}^{-1}$	[20]
(3.46)	$\text{H} + \text{H} + \text{M} \rightarrow \text{H}_2 + \text{M}$	$1.8 \times 10^{-42}/T$	[27]

(3.47)	$\text{H} + \text{OH} + \text{M} \rightarrow \text{H}_2\text{O} + \text{M}$	$6.1 \times 10^{-38}/\text{T}$	[27]
(3.48)	$\text{H} + \text{NO}_2 \rightarrow \text{OH} + \text{NO}$	$4.0 \times 10^{-10} \exp(-340/\text{T}) \text{ cm}^3 \text{ s}^{-1}$	[20]
(3.49)	$\text{H} + \text{NO}_3 \rightarrow \text{OH} + \text{NO}_2$	$5.8 \times 10^{-16} \exp(-750/\text{T}) \text{ cm}^3 \text{ s}^{-1}$	[23]
(3.50)	$\text{H} + \text{H}_2\text{O}_2 \rightarrow \text{OH} + \text{H}_2\text{O}$	$1.69 \times 10^{-17} \exp(-1800/\text{T}) \text{ cm}^3 \text{ s}^{-1}$	[25]
(3.51)	$\text{H} + \text{H}_2\text{O}_2 \rightarrow \text{HO}_2 + \text{H}_2$	$2.8 \times 10^{-18} \exp(-1900/\text{T}) \text{ cm}^3 \text{ s}^{-1}$	[23]
(3.52)	$\text{H} + \text{HO}_2 \rightarrow \text{H}_2 + \text{O}_2$	$5.6 \times 10^{-18} \text{ cm}^3 \text{ s}^{-1}$	[18]
(3.53)	$\text{H} + \text{HO}_2 \rightarrow \text{O} + \text{H}_2\text{O}$	$2.4 \times 10^{-18} \text{ cm}^3 \text{ s}^{-1}$	[18]
(3.54)	$\text{H} + \text{HO}_2 \rightarrow \text{OH} + \text{OH}$	$4.2 \times 10^{-16} \exp(-950/\text{T}) \text{ cm}^3 \text{ s}^{-1}$	[23]
(3.55)	$\text{H} + \text{HNO} \rightarrow \text{NO} + \text{H}_2$	$3 \times 10^{-17} \exp(-500/\text{T}) \text{ cm}^3 \text{ s}^{-1}$	[20]
(3.56)	$\text{OH} + \text{HO}_2 \rightarrow \text{H}_2\text{O} + \text{O}_2$	$4.8 \times 10^{-11} \exp(250/\text{T}) \text{ cm}^3 \text{ s}^{-1}$	[18]
(3.57)	$\text{OH} + \text{O}_3 \rightarrow \text{HO}_2 + \text{O}_2$	$1.9 \times 10^{-12} \exp(-1000/\text{T}) \text{ cm}^3 \text{ s}^{-1}$	[18]
(3.58)	$\text{OH} + \text{NO}_2 + \text{M} \rightarrow \text{HNO}_3 + \text{M}$	$2.6 \times 10^{-30} (\text{T}/300)^{-2.9} \text{ cm}^6 \text{ s}^{-1}$	[18]
(3.59)	$\text{OH} + \text{NO}_3 \rightarrow \text{HO}_2 + \text{NO}_2$	$2 \times 10^{-17} \text{ cm}^3 \text{ s}^{-1}$	[18]
(3.60)	$\text{OH} + \text{OH} + \text{M} \rightarrow \text{H}_2\text{O}_2 + \text{M}$	$6.9 \times 10^{-31} (\text{T}/298)^{-0.8} \text{ cm}^6 \text{ s}^{-1}$	[18]
(3.61)	$\text{OH} + \text{HNO}_3 \rightarrow \text{NO}_3 + \text{H}_2\text{O}$	$1.5 \times 10^{-14} \exp(650/\text{T}) \text{ cm}^3 \text{ s}^{-1}$	[28]
(3.62)	$\text{OH} + \text{H}_2\text{O}_2 \rightarrow \text{H}_2\text{O} + \text{HO}_2$	$2.9 \times 10^{-12} \exp(-160/\text{T}) \text{ cm}^6 \text{ s}^{-1}$	[18]
(3.63)	$\text{OH} + \text{H}_2 \rightarrow \text{H} + \text{H}_2\text{O}$	$3.2 \times 10^{-17} \exp(-2600/\text{T}) \text{ cm}^3 \text{ s}^{-1}$	[23]
(3.64)	$\text{OH} + \text{OH} \rightarrow \text{O} + \text{H}_2\text{O}$	$8.8 \times 10^{-18} \exp(-503/\text{T}) \text{ cm}^3 \text{ s}^{-1}$	[23]
(3.65)	$\text{OH} + \text{HNO} \rightarrow \text{NO} + \text{H}_2\text{O}$	$8 \times 10^{-17} \exp(-500/\text{T}) \text{ cm}^3 \text{ s}^{-1}$	[20]
(3.66)	$\text{OH} + \text{HNO}_2 \rightarrow \text{NO}_2 + \text{H}_2\text{O}$	$2.7 \times 10^{-12} \exp(260/\text{T}) \text{ cm}^3 \text{ s}^{-1}$	[18]
(3.67)	$\text{OH} + \text{N}_2\text{O} \rightarrow \text{HO}_2 + \text{N}_2$	3.69×10^{-13}	[29]
(3.68)	$\text{OH} + \text{N}_2\text{O} \rightarrow \text{HNO} + \text{NO}$	3.80×10^{-17}	[30]
(3.69)	$\text{OH} + \text{N}_2\text{O}_5 \rightarrow \text{HNO}_3 + \text{NO}_3$	2.85×10^{-15}	[20]
(3.70)	$\text{OH} + \text{N}_2\text{O}_5 \rightarrow \text{HO}_2 + 2\text{NO}_2$	2.85×10^{-15}	[20]
(3.71)	$\text{NO} + \text{OH} + \text{M} \rightarrow \text{HNO}_2 + \text{M}$	$7.4 \times 10^{-31} (\text{T}/300)^{-2.4} \text{ cm}^6 \text{ s}^{-1}$	[18]
(3.72)	$\text{NO} + \text{HO}_2 \rightarrow \text{NO}_2 + \text{OH}$	$3.4 \times 10^{-12} \exp(270/\text{T}) \text{ cm}^3 \text{ s}^{-1}$	[18]
(3.73)	$\text{NO} + \text{O}_3 \rightarrow \text{NO}_2 + \text{O}_2$	$4.3 \times 10^{-12} \exp(-1560/\text{T}) \text{ cm}^3 \text{ s}^{-1}$	[21]
(3.74)	$\text{NO} + \text{NO}_3 \rightarrow \text{NO}_2 + \text{NO}_2$	$1.7 \times 10^{-11} \text{ cm}^3 \text{ s}^{-1}$	[21]
(3.75)	$\text{NO} + \text{NO}_2 + \text{M} \rightarrow \text{N}_2\text{O}_3 + \text{M}$	$3.09 \times 10^{-46} (300/\text{T})^{7.7}$	[25]
(3.76)	$\text{NO} + \text{HO}_2 \rightarrow \text{O}_2 + \text{HNO}$	$3.3 \times 10^{-19} \exp(-1000/\text{T}) \text{ cm}^3 \text{ s}^{-1}$	[23]
(3.77)	$\text{NO}_2 + \text{NO}_3 \rightarrow \text{NO}_2 + \text{NO} + \text{O}_2$	$2.3 \times 10^{-13} \exp(-1600/\text{T})$	[21]
(3.78)	$\text{NO}_2 + \text{NO}_2 + \text{M} \rightarrow \text{N}_2\text{O}_4 + \text{M}$	$1.17 \times 10^{-45} (300/\text{T})^{3.8}$	[25]
(3.79)	$\text{NO}_2 + \text{NO}_3 + \text{M} \rightarrow \text{N}_2\text{O}_5 + \text{M}$	$2.8 \times 10^{-42} (300/\text{T})^{3.5}$	[18]
(3.80)	$\text{NO}_3 + \text{HO}_2 \rightarrow \text{NO}_2 + \text{OH} + \text{O}_2$	$4.0 \times 10^{-12} \text{ cm}^3 \text{ s}^{-1}$	[18]
(3.81)	$\text{NO}_3 + \text{HO}_2 \rightarrow \text{HNO}_3 + \text{O}_2$	$9.2 \times 10^{-13} \text{ cm}^3 \text{ s}^{-1}$	[25]
(3.82)	$\text{NO}_3 + \text{NO}_3 \rightarrow 2\text{NO}_2 + \text{O}_2$	$5 \times 10^{-12} \exp(-3000/\text{T}) \text{ cm}^3 \text{ s}^{-1}$	[21]

(3.83)	$O_3 + NO_2 \rightarrow NO_3 + O_2$	$1.2 \times 10^{-13} \exp(-2450/T) \text{ cm}^3 \text{ s}^{-1}$	[21]
(3.84)	$O_3 + M \rightarrow O + O_2 + M$	$3.92 \times 10^{-16} \exp(-11400/T) \text{ cm}^3 \text{ s}^{-1}$	[31]
(3.85)	$O_3 + HO_2 \rightarrow OH + O_2 + O_2$	$1.4 \times 10^{-20} \exp(-600/T) \text{ cm}^3 \text{ s}^{-1}$	[18]
(3.86)	$N_2O_3 + M \rightarrow NO + NO_2 + M$	$1.03 \times 10^{-16} \exp(-2628/T) \text{ cm}^3 \text{ s}^{-1}$	[25]
(3.87)	$N_2O_4 + M \rightarrow NO_2 + NO_2 + M$	$1.09 \times 10^{-13} \exp(-4952/T) \text{ cm}^3 \text{ s}^{-1}$	[25]
(3.88)	$N_2O_5 \rightarrow NO_3 + NO_2$	$9.7 \times 10^{14} (T/298)^{0.1} \exp(-11080/T) \text{ s}^{-1}$	[18]
(3.89)	$HNO + O_2 \rightarrow NO_2 + OH$	$1.7 \times 10^{-15} \text{ cm}^3 \text{ s}^{-1}$	[15]
(3.90)	$HNO + O_2 \rightarrow NO + HO_2$	$3.3 \times 10^{-14} \text{ cm}^3 \text{ s}^{-1}$	[15]
(3.91)	$HNO + HNO \rightarrow N_2O + H_2O$	$1.4 \times 10^{-21} \exp(-1600/T) \text{ cm}^3 \text{ s}^{-1}$	[15]
(3.92)	$HNO_2 + HNO_2 \rightarrow NO + NO_2 + H_2O$	$1 \times 10^{-26} \text{ cm}^3 \text{ s}^{-1}$	[15]
(3.93)	$HNO_2 + HNO_3 \rightarrow 2 NO_2 + H_2O$	$1.6 \times 10^{-23} \text{ cm}^3 \text{ s}^{-1}$	[15]
(3.94)	$HO_2 + HO_2 + M \rightarrow H_2O_2 + O_2 + M$	$1.9 \times 10^{-33} \exp(980/T) \text{ cm}^6 \text{ s}^{-1}$	[18]
(3.95)	$N_2O_5 + H_2O \rightarrow 2HNO_3$	$2.50 \times 10^{-22} \text{ cm}^3 \text{ s}^{-1}$	[20]
(3.96)	$N_2O_5 + M \rightarrow NO_2 + NO_3 + M$	$1 \times 10^{-9} (300/T)^{3.5} \exp(-11000/T) \text{ cm}^3 \text{ s}^{-1}$	[20]

Table 3.3. List of chemical reactions taking place in humid artificial air non-thermal plasma and their rate coefficients. N_2^* and O_2^* correspond to the electronically excited states $N_2(A)$ and $O_2(^1\Delta)$, respectively. * T is the temperature in K.

3.2.2. N_2O calibration

Figure 3.3 shows the calibration curve employed for determining the integrated band intensity coefficient (IBI, $\text{cm}^{-2} \text{ atm}^{-1}$) of N_2O for the band from 2167 to 2268 cm^{-1} as discussed in section 2.2.5. As can be seen from the figure, by plotting the N_2O partial pressure vs. the integrated band area a linear correlation was observed with a regression coefficient of 0.998. The plot was extended to the origin to cover the partial pressures below the range of calibration curve employed. The IBI was determined to be 463 $\text{cm}^{-2} \text{ atm}^{-1}$ from the slope of the plot according to:

$$A = \text{IBI} \times b \times c \quad (3.1)$$

where A is the absorbance band area (cm^{-1}), b is the transmission cell pathlength (5.1 cm) and c is the N_2O partial pressure (atm).

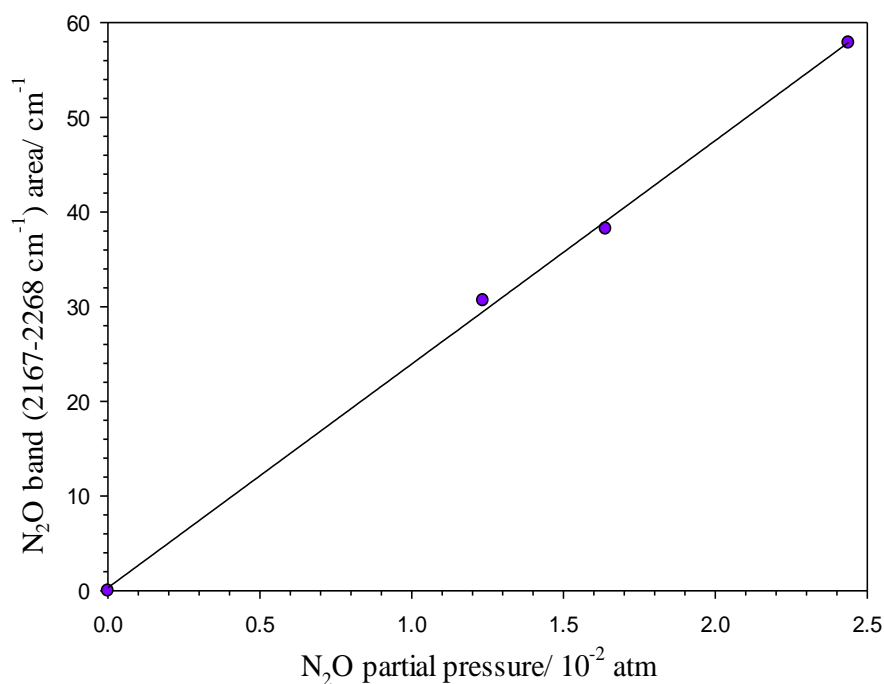


Figure 3.3. A calibration curve of N_2O obtained using the FTIR spectroscopy setup shown in fig.2.2. The N_2O partial pressures employed for the calibration were obtained by admixing pure N_2O at $0.05 \text{ dm}^3 \text{ min}^{-1}$ with N_2 at $2.0, 3.0, 4.0 \text{ dm}^3 \text{ min}^{-1}$.

3.2.3. Non-thermal plasma & CO_2

From figure 3.2 it may be seen that two distinctive gain features were observed at 2366 and 2326 cm^{-1} with air but not with artificial air, and hence these bands were assumed to be due to one or more forms of CO_2 . To test this hypothesis, experiments were conducted using CO_2 mixed with various feed gases, and the results are shown in figures 3.4(a) and (b). As can be seen from the figures, the gain features at 2366 and 2326 cm^{-1} were superimposed upon the CO_2 loss features; given the chemical simplicity of the system it does seem likely that these bands are due to some form of CO_2 . In addition, the intensities of these features were found to be greater in plasma than in the afterglow region, as will be shown below. Hence, the bands at 2366 and 2326 cm^{-1} may be attributed to a vibrationally excited (linear) form of CO_2 , (i.e. $CO_2^*(v)$). It is highly unlikely that the $CO_2^*(v)$ is electronically excited, as the first anti-bonding orbital of CO_2 ($2\pi_u$) is strongly stabilized by reducing the angle of the molecule from 180° , hence CO_2^- is bent [32]. Furthermore, the nature of the operation of a Fourier Transform spectrometer rules out the 2366 and 2326 cm^{-1} features as being due to emission, leaving only absorption by a high concentration of vibrationally excited CO_2 molecules.

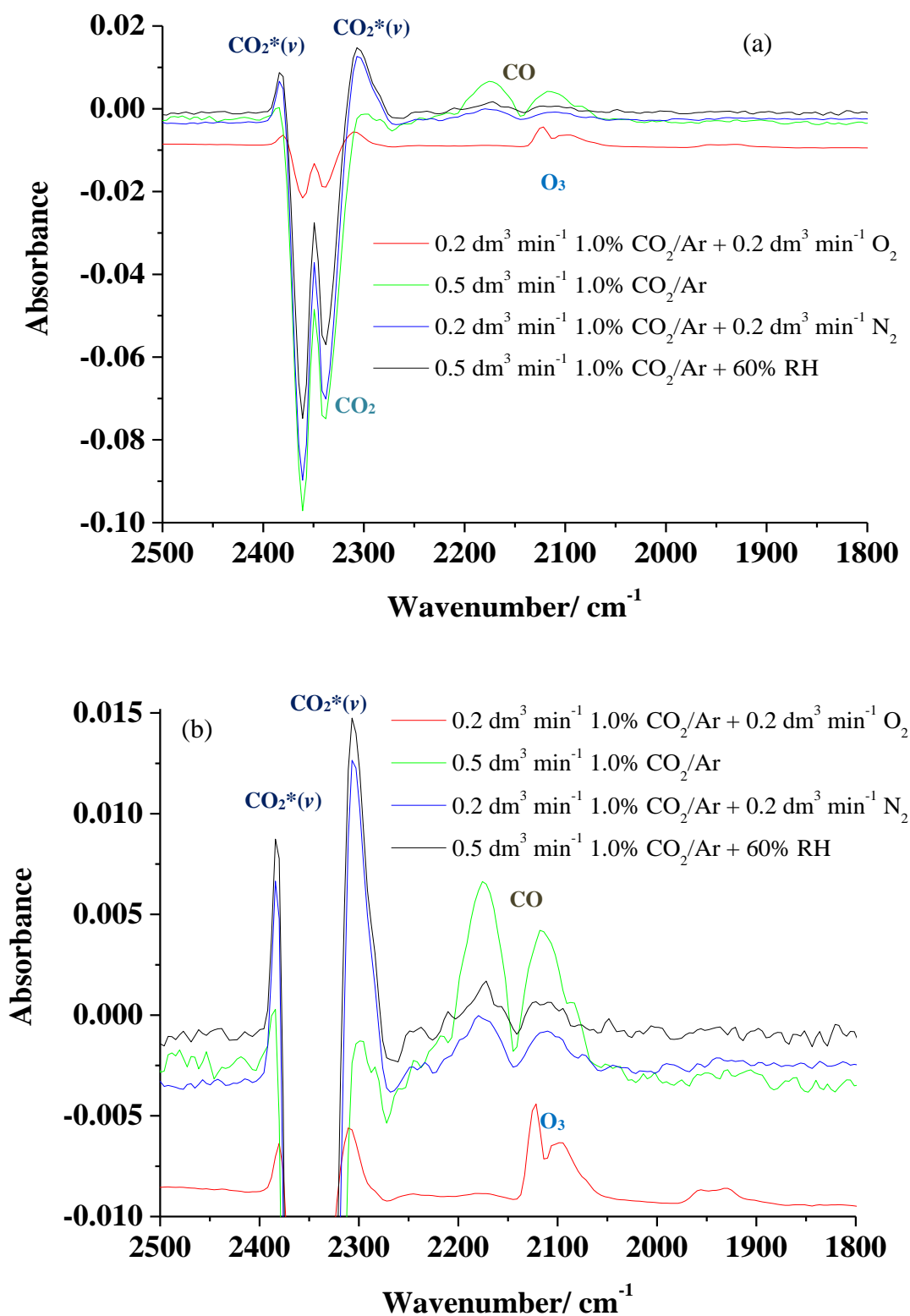


Figure 3.4. (a) In-situ FTIR Spectra collected from the NTP glow region after running the DBD for 10 minutes as a function of feed gas composition. Each spectrum was ratioed to its reference spectrum collected with no input power with the gas flowing at the specified rate. (b) The spectra in (a) replotted to show the gain features more clearly. The input power was 36 W.

Modest and Bharadwaj [33] reported transmission spectra of 1% CO₂ in dry N₂ at temperatures up to 1550 K using long pathlength cells. At temperatures ≥ 600 K they observed a highly asymmetric band around 4.3 μm (2325 cm^{-1}) with a tail to the low energy side, the band being broader than that of CO₂ at 298K. The band broadened significantly to the low energy side with increasing temperature. The identity of the species responsible for the 4.3 μm feature was not stated by the authors. Toselli and Barker [34] attributed emission at 4.3 μm as being from vibrationally excited levels of the asymmetric ν_3 O=C=O vibration, ie. $\nu_3 \geq 1$. Hence it does not seem unreasonable to attribute the absorptions at 2366 and 2326 cm^{-1} to vibrational excitation of the $\nu_3 = 1$ excited state of CO₂.

The formation of CO₂^{*}(ν) may take place through direct electron collision [29, 35], or through the interaction with vibrationally excited species such as molecular nitrogen N₂^{*}(ν) [29]:



CO₂^{*}(ν) decay may take place through relaxation to CO₂ or dissociation to CO and atomic oxygen [29, 35]:

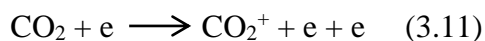


The dissociation of CO₂ to CO and O can take place via two possible direct routes depending on the level of excitation [36, 37]: (1) excitation to vibrational levels of the ground excited state with energies exceeding the dissociation threshold, this results in ground electronic state CO and singlet oxygen, O (¹D); (2) excitation to the first excited triplet state of CO₂ (³B₂) via intersystem crossing which dissociates to the ground electronic states CO and ground state, atomic oxygen (O (³P)). The latter is more efficient due to the non-adiabatic intersystem crossing between the ground electronic and triplet states of the CO₂. Singlet oxygen is 1.48 eV higher in energy than O (³P) [38], hence the energy required for dissociation is reduced from 6.94 eV to 5.46 eV [39].

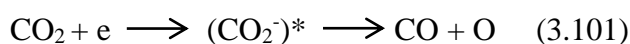
As can be seen in fig 3.4(a) (ii), the only gain features observed were due to CO₂^{*}(ν) and CO, suggesting that these were the only detectable metastable and neutral products,

respectively, from CO₂. The loss feature due to CO₂ at 2360 cm⁻¹ has an absorbance of ca. 0.095: given that the absorbance of this band in the absence of plasma is 0.65, this suggests ca. 15% conversion of CO₂ to CO₂^{*}(*v*) and CO, a significant amount. From figures 3.4(a) and (b) it can be seen that the amount of CO formed via CO₂ dissociation varies with the composition of the feed gas. When the feed gas contained water vapor or N₂ lower concentrations of CO were produced and higher amount of CO₂^{*}(*v*) was obtained, in contrast to that observed with pure CO₂/Ar. Thus, it is clear from figures 3.4(a) and (b) that, in the presence of molecules able to absorb vibrational energy, the dissociation route is disfavored with respect to vibrational relaxation to CO₂^{*}(*v*). Furthermore, in the presence of oxygen the absorbance due to CO was not observed, and the intensities of the CO₂ loss features were found to be the lowest of all the gases; this suggests that CO was oxidized, as soon as it was formed, back to CO₂ or to CO₂^{*}(*v*), most likely by ozone or atomic oxygen [40, 41].

In addition to the direct dissociation of CO₂^{*}(*v*), several pathways have been proposed for CO₂ dissociation to CO such as electron impact ionization [42, 43]:



or dissociative attachment [35, 43]:



Thus, it does not seem unreasonable to postulate that, in the presence of other species such as N₂, water vapour or oxygen within the feed gas, a lower number of electrons with sufficient energy will be available to induce CO₂ dissociation [44]. From figures 3.4(a) and (b) it may be seen that, in the absence of oxygen, the absorbance intensity of the CO₂^{*}(*v*) band correlate inversely with the formation of CO. This suggested that additional excitation may be required to facilitate the dissociation of CO₂^{*}(*v*) to CO.

3.2.4. The effects of input power and gas flow rate

The change in the plasma chemical composition was monitored as a function of the input power and gas flow rate using ambient air and dry artificial air as feed gases. The specific

energy density (SED, J cm⁻³) was employed to assess the combined effect of the input power and gas flow rate on the plasma composition:

$$\text{SED} = P / Q_G \quad (3.2)$$

where P is the input power (W) and Q_G is the gas flow rate (cm³ s⁻¹). Table 3.4 shows the range of specific energy densities at different input power and gas flow rates employed for the *in-situ* FTIR experiments. As can be seen from the table, energy densities from 2.8 to 4.3 J cm⁻³ were obtained at a constant gas flow rate of 0.5 dm³ min⁻¹ and varied input power, and the higher energy densities were at an input power of 36 W and varied gas flow rate. Figure 3.5 shows plots of the partial pressures of NO₂, O₃ and N₂O and the absorbance of CO₂^{*}(ν) at 2326 cm⁻¹ monitored *in-situ* as a function of energy density collected after 1 minute of the DBD being turned on. The partial pressures of these species were determined using the extinction coefficients discussed in sections 2.2.4 and 3.2.2. HNO₃ and N₂O₅ produced in ambient air were not monitored due to their interference with each other and with other species, as shown in figure 3.2.

Input power/ W	Gas flow rate/ dm ³ min ⁻¹	Specific energy density/ J cm ⁻³
23	0.5	2.8
24	0.5	2.9
27	0.5	3.2
30	0.5	3.6
33	0.5	4.0
36	0.5	4.3
36	0.4	5.4
36	0.3	7.2
36	0.2	10.8

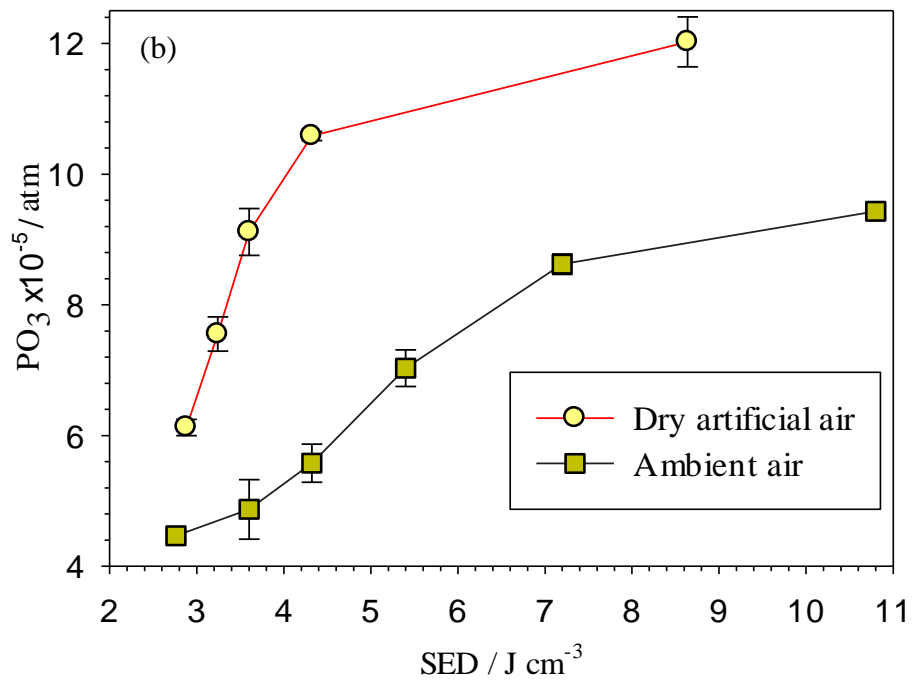
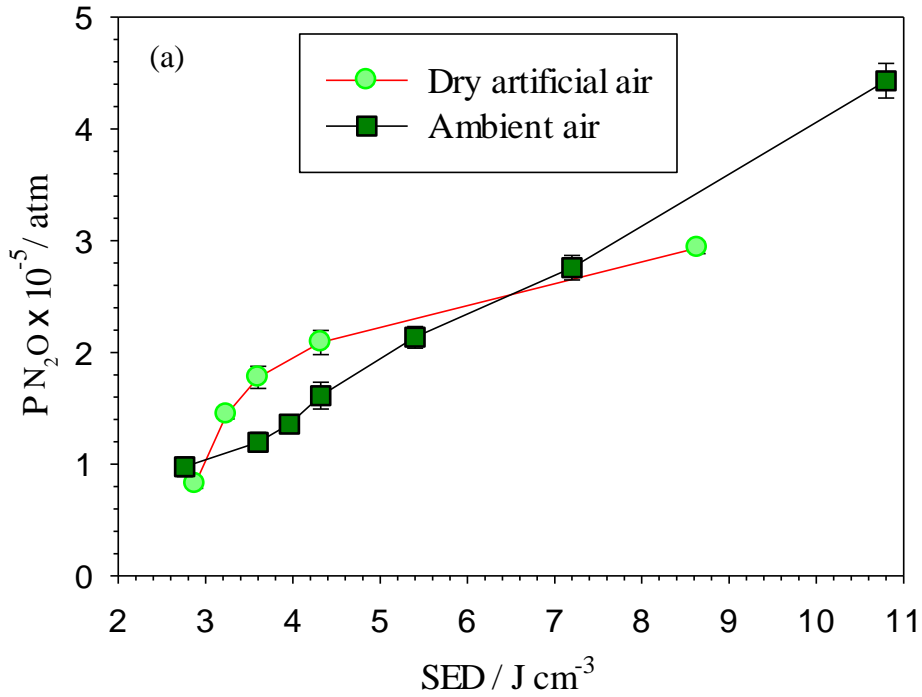
Table 3.4. Input power and feed gas flow rates and their corresponding specific energy densities employed for the in-situ FTIR experiments.

As can be seen from fig. 3.5(a), the partial pressure of N₂O was found to increase linearly with the specific energy density when ambient air was used. However, in dry artificial air the partial pressure of N₂O was found to increase rapidly with the energy density from 2.8 to 4.3 J cm⁻³, but the increase was much less pronounced at higher energy densities. In the case of ozone, similar behaviour was observed with ambient and dry artificial air; in both cases the ozone partial pressure increased more rapidly with energy density at lower energy than at higher energy densities, see fig. 3.5(b). At all power densities, the partial pressures of ozone were higher with the dry artificial air feed than with ambient air. No steady state was observed. This behaviour may be attributed to the combined effect of relative humidity and plasma temperature, as will be discussed below. The formation of NO₂ was found to vary with feed gas composition and flow rate: as can be seen from fig. 3.5(c), when ambient air was employed, two trends were observed: (I) from 2.8 to 4.3 J cm⁻³ and (II) from 5.4 to 10.8 J cm⁻³, with the slope of the plot in region (I) higher than in region (II).

The partial pressure of NO₂ at 5.4 J cm⁻³ was found to be 24% lower than that obtained at 4.3 J cm⁻³, corresponding to a reduction in flow rate from 0.5 to 0.4 dm³ min⁻¹. Considering the direct effect of the feed gas flow rate on the length of the plasma jet, it may be concluded that a significant fraction of the NO₂ was concentrated within the plasma region, in agreement with previous studies [10, 11]. Because the same amount of NO₂ was obtained at energy densities of 4.3 and 10.8 J cm⁻³, i.e. 9.44×10^{-5} atm \pm 1%, it does not seem unreasonable to postulate that the reduction of NO₂ partial pressure with increasing gas flow rate was compensated by increasing the energy density. However, by replacing the ambient air with artificial dry air, the NO₂ partial pressure declined with increasing energy density. Thus, it is clear that the presence of water vapour has a major effect upon the production of NO₂.

Unlike the case of N₂O, the formation of CO₂^{*}(*v*) from ambient air was found to be more sensitive to the input power and flow rate than the energy density itself. As can be seen from figure 3.5(d), the absorbance of CO₂^{*}(*v*) increased significantly with energy density from 3.2 to 4.3 J cm⁻³. Within the same range of input power densities using ambient air, it may be observed that the rate of CO₂^{*}(*v*) absorbance increase was the highest among other species shown in figure 3.5. But as the energy density increased from 4.3 to 10.8 J cm⁻³ by reducing the flow rate from 0.5 to 0.2 dm³ min⁻¹ at 36 W, the absorbance of CO₂^{*}(*v*) decreased. By determining the CO₂^{*}(*v*) absorbance at 10.8 J cm⁻³ it was found to be ca. 65% lower than

that at 4.3 J cm^{-3} , corresponding to a 60% reduction in the flow rate from 0.5 to $0.2 \text{ dm}^3 \text{ min}^{-1}$. Therefore, it can be concluded that the $\text{CO}_2^*(v)$ molecules were confined within the plasma glow region. It should be noted that heat generation and ionization would be expected to be additional routes of power dissipation.



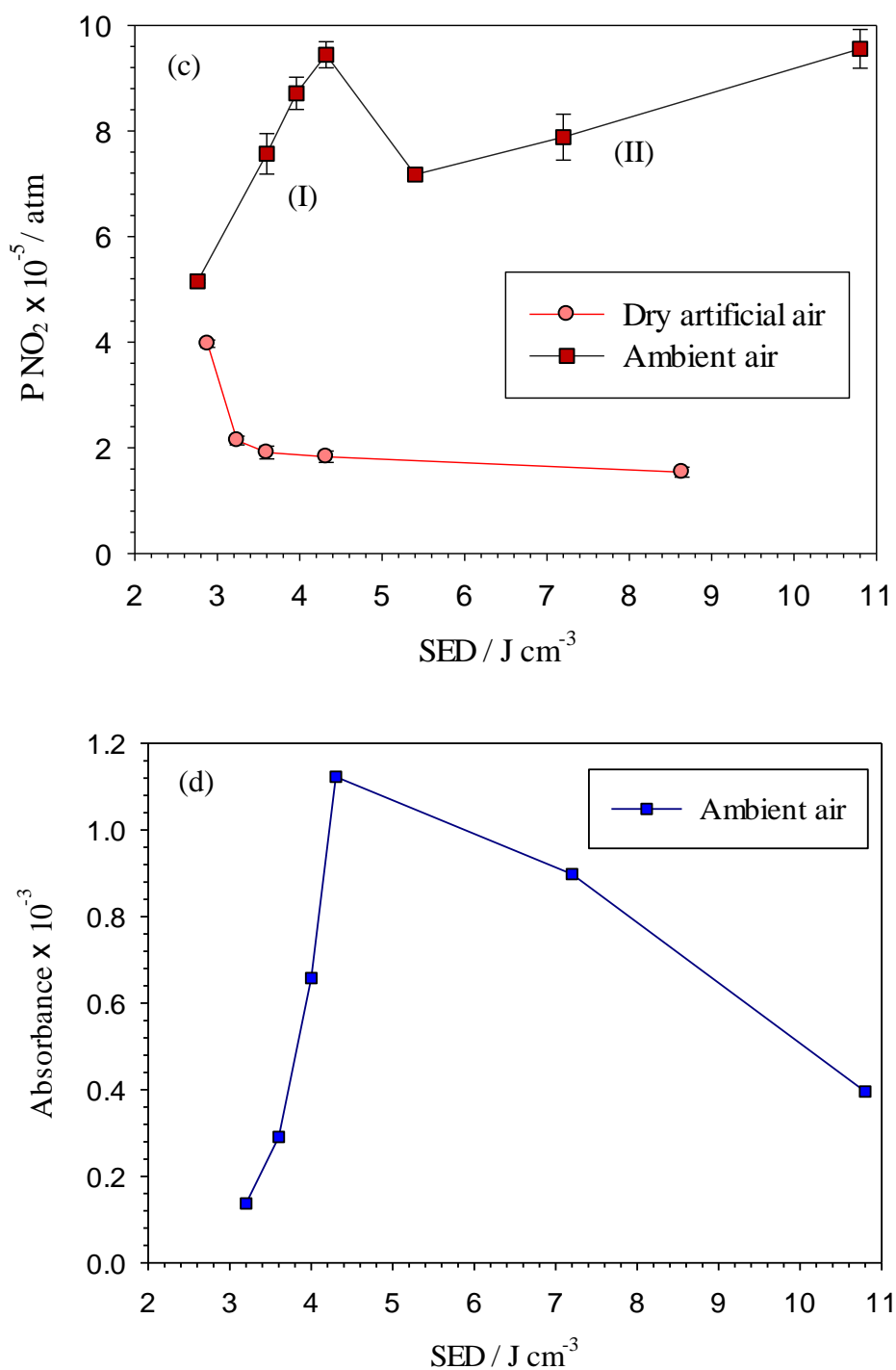


Figure 3.5. Plots of the partial pressures of: N_2O (a), O_3 (b), NO_2 (c) and (d) $\text{CO}_2^*(\nu)$ absorbance at 2326 cm^{-1} as a function of discharge energy density and feed gas composition monitored using in-situ FTIR spectroscopy 1 minute after the plasma was turned on. The input power and feed gas flow rates ranged from 27-36W and $0.2\text{-}0.5 \text{ dm}^3 \text{ min}^{-1}$, respectively.

3.2.5. Relative humidity and gas temperature effects

Due to the apparently significant effect of water vapor on the chemical composition of the NTP, it was decided to determine this in a more measured fashion. Figure 3.6 shows spectra collected after 1 minute of NTP using: (i) dry and (ii) humidified artificial air at 20% RH. Spectrum (iii) in figure 3.6 shows spectrum (i) subtracted from (ii). As can be seen from the same figure, the addition of water vapor to the feed gas led to a reduction in the concentrations of O_3 , N_2O_5 and N_2O , an increase in NO_2 and the appearance of HNO_3 .

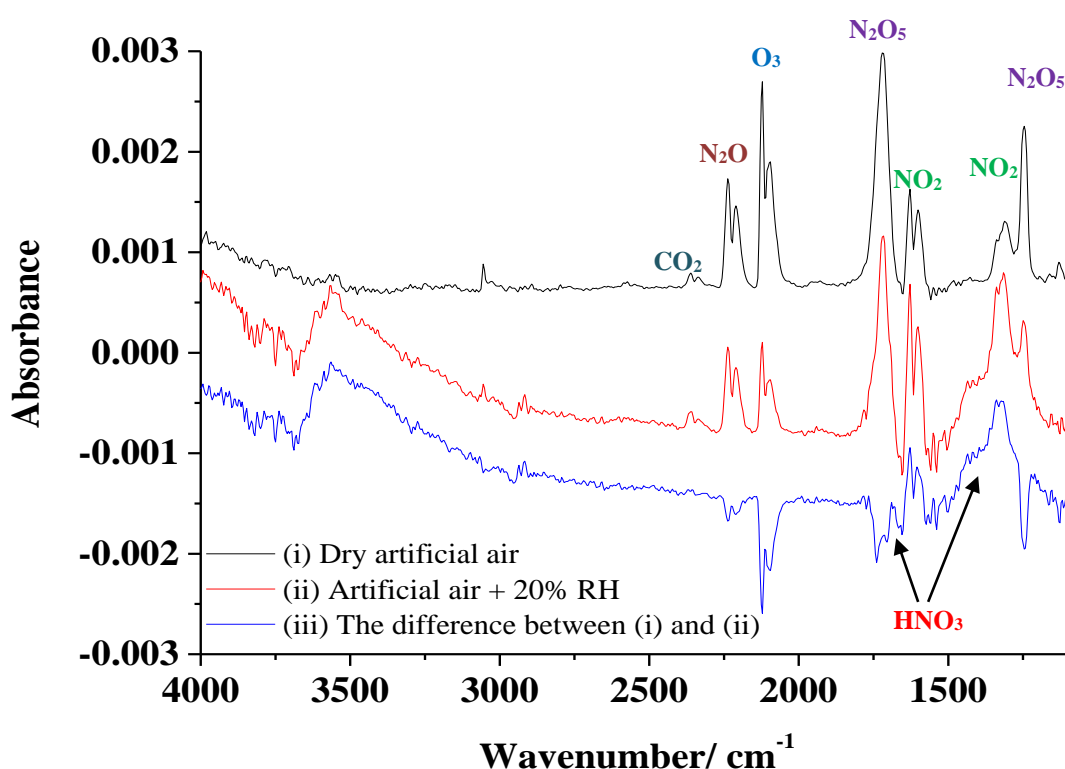


Figure 3.6. In-situ FTIR spectra collected after 1 minute of DBD operation at 36W using: dry artificial air and artificial air + 20 % RH. The input power was 36W and gas flow rate $0.5 \text{ dm}^3 \text{ min}^{-1}$.

Because of the interference between the bands of N_2O_5 and HNO_3 and other products bands, as shown in figures 3.2 and 3.6, it was difficult to monitor the variation of their concentrations with relative humidity. N_2O_5 formation was expected to occur via reaction (3.79), as well as being involved in several decomposition reactions in dry air such as (3.38), (3.88), and (3.96). However, the reduction of N_2O_5 observed with humidified air may be

attributed to the additional destructive reactions (3.69), (3.70) and (3.95). In addition to reactions (3.95) and (3.69), HNO_3 can be produced through the reactions (3.58) and (3.81). However, HNO_3 can decompose to NO_2 through the reactions (3.43) & (3.93), or to NO_3 through the reaction (3.61).

Figure 3.7 shows the change in NO_2 partial pressure as a function of operational time and relative humidity, measured using *in-situ* FTIR spectroscopy at 36 W and $0.5 \text{ dm}^3 \text{ min}^{-1}$. As can be seen from the figure, the partial pressure of NO_2 increased with relative humidity and running time. However, when using dry artificial air, the partial pressure of NO_2 was low and remained essentially constant with running time. After the first minute, the partial pressure of NO_2 using dry air increased by ca. 50, 82 and $109 \pm 2\%$ as the relative humidity was increased to 20, 40 and 60%, respectively. In humidified artificial air the partial pressure of NO_2 after 10 minutes was ca. 2.2 times higher than that obtained after the first minute, and this was observed at all humidity levels studied.

Taking into account the continuity of gas flow in these experiments, it may be postulated that the gradual increase in NO_2 concentration with time is mainly due to a change in dielectric temperature [1-3]. As a result, the gas temperature may change due to heat transfer from the dielectric by convection and thermal radiation [3, 45]. The amount of heat that can be transferred to the plasma background gas is determined by several factors including: the feed gas composition, discharge current, the proximity to the discharge centre and the shape and configuration of the discharge electrodes [45-48]. The gas temperature would be expected to be the highest near the discharge electrodes and to decrease with the length of the plasma jet [11, 45, 47, 49]. Thus, it can be assumed that the gas temperature profile along the jet is determined by the temperature near the discharge electrodes. Based on this assumption and because of the small discharge gap width of the DBD employed in these experiments, and the limited length of the jet (i.e. 6.0 mm) it was found to be difficult to monitor the change in the gas temperature at different points along the jet axis. Instead, the change in gas temperature with time was monitored at a single point ca. 5.0 mm beyond the DBD nozzle and correlated with the changes in concentration of different species observed with time. This point was chosen to ensure direct monitoring of the gas temperature within the jet without interfering significantly with the jet flow.

Figure 3.8 shows the gas temperature monitored using the thermometer 5.0 mm beyond the DBD nozzle as a function of running time. As can be seen from the figure, the gas temperature increased rapidly during the first five minutes and less significantly at longer times. In general, this behaviour was found to agree with the work reported by Akitsu et al. [1] and Visser et al. [3]. In addition, it can be seen from figure 3.8 that the change in gas temperature showed the same basic profile as the plots of NO_2 partial pressure showed in figure 3.7.

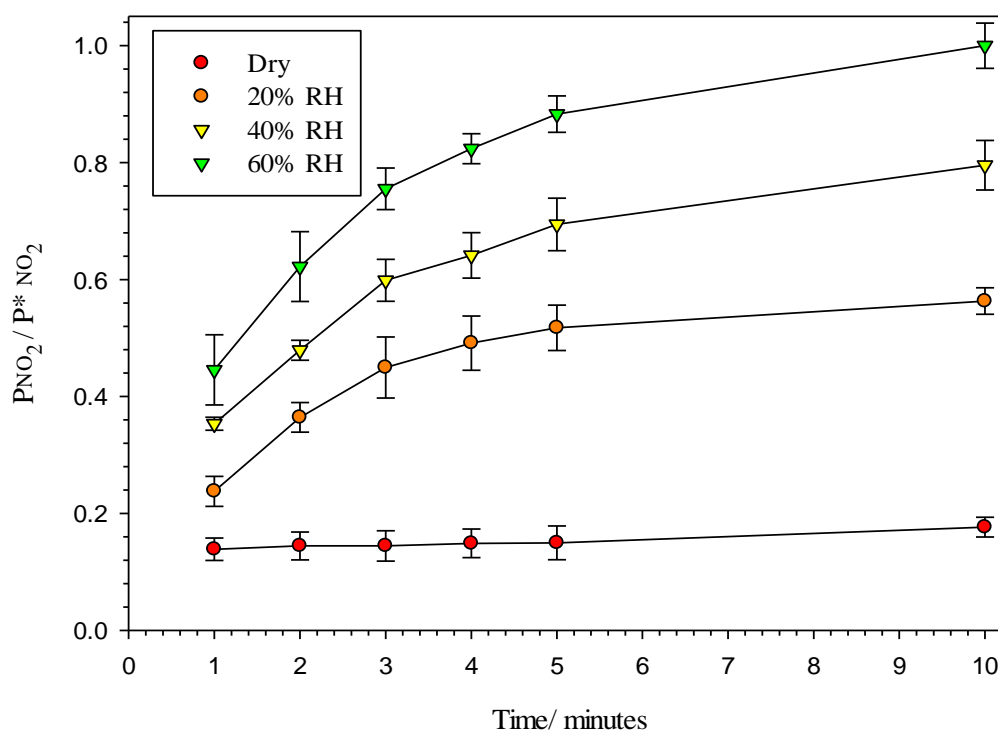


Figure 3.7. Plots of NO_2 partial pressure monitored in-situ using FTIR spectroscopy as a function of running time and relative humidity using artificial air. The input power was 36 W at $0.5 \text{ dm}^3 \text{ min}^{-1}$. Maximum N_2O partial pressure = $P^*_{\text{NO}_2} = 7.7 \pm 0.62 \times 10^{-5} \text{ atm}$.

Figure 3.9 shows the change in NO_2 partial pressure as a function of relative humidity and plasma temperature; the data points were extracted from figures 3.7 and 3.8. As can be seen from the figure, the concentration of NO_2 was found to increase linearly with the gas temperature with the exception of dry air, where it varied very little. This suggests that the change in NO_2 with time using humid air was primarily due to the increase in plasma

temperature. Furthermore, it can be seen from the same figure that the effect of humidity on the formation of NO_2 was more pronounced at high temperatures. Hence, it can be concluded that there is a synergic effect of humidity and temperature.

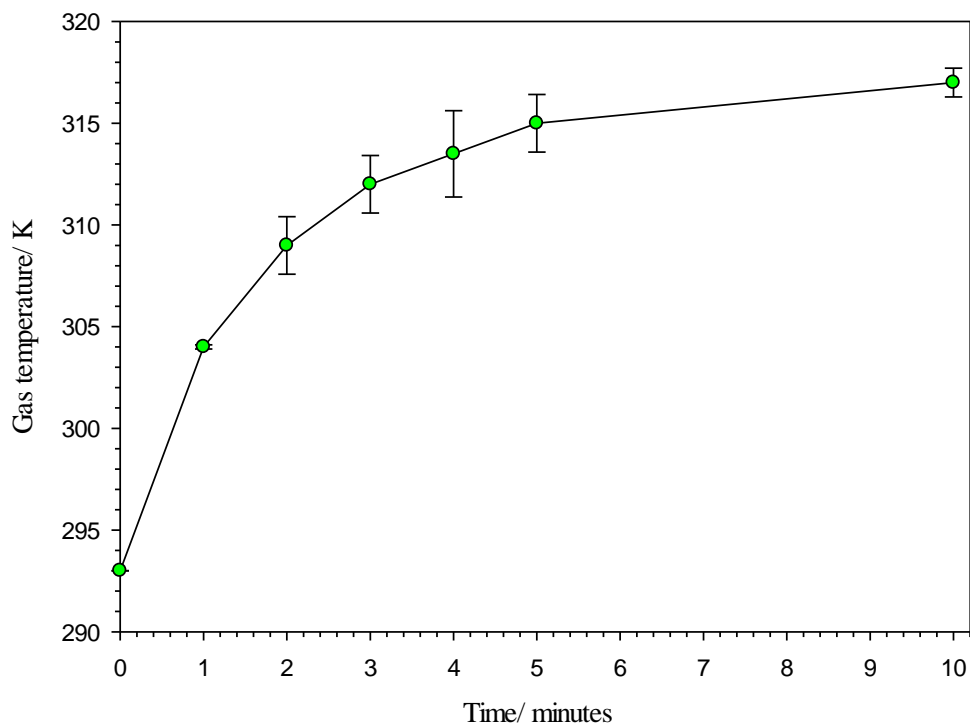


Figure 3.8. Plot of plasma jet temperature 5.0 mm from the DBD nozzle as a function of running time using ambient air. The input power was 36 W at $0.5 \text{ dm}^3 \text{ min}^{-1}$.

The marked difference in behaviour between humidified and dry artificial air may be explained in terms of the formation and decomposition reactions in each case. For instance, the reactions responsible for NO_2 formation from dry air are: (3.37), (3.73), (3.74), (3.77), (3.82), (3.86) - (3.88) and (3.96), while the direct decomposition reactions of NO_2 are: (3.23), (3.24), (3.35) and (3.36). However, in the presence of water vapour, additional formation reactions take place: (3.40), (3.42), (3.43), (3.49), (3.66), (3.72), (3.80), (3.89), (3.91-3.93) and (3.70) while the decomposition reactions are (3.48) and (3.58). Thus, the number of reactions responsible for NO_2 formation increases significantly in the presence of water vapour, in contrast to the decomposition reactions.

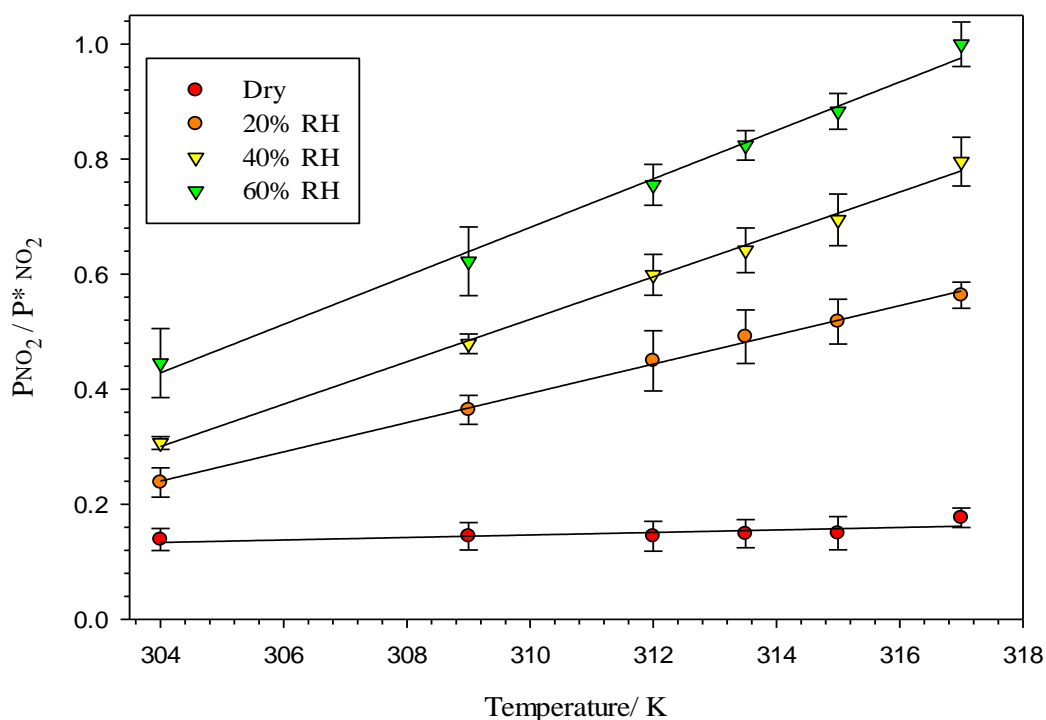


Figure 3.9. Plots of NO_2 partial pressure as a function of relative humidity and plasma jet temperature monitored *in-situ* using FTIR. The feed gas was artificial air. The input power was 36 W at $0.5 \text{ dm}^3 \text{ min}^{-1}$. Maximum NO_2 partial pressure = $P^*_{\text{NO}_2} = 7.7 \pm 0.62 \times 10^{-5} \text{ atm}$.

Figures 3.10(a) and (b) show the change in ozone partial pressure monitored *in-situ* as a function of running time (a) and gas temperature (b) at different humidities. As can be seen from the figures, the partial pressure of ozone was found to decrease significantly with relative humidity. From figures 3.10(a) & (b) it can be seen that the partial pressure of ozone using dry air decreased by 46, 64 and 70% at humidity levels of 20, 40 and 60%, respectively. As can be seen from figure 3.10(a), the ozone partial pressure was found to decrease steadily, by ca. 35%, during the first 10 minutes, regardless of the humidity of the feed gas. However, it can be clearly seen from figure 3.10(b) that ozone decomposition was more significant at high temperatures, regardless of the relative humidity. This would be expected on the basis of the fact that the primary ozone generating step (3.30) is exothermic, while the majority of its decomposition reactions are endothermic. For instance, in dry air, the main reactions responsible for ozone decomposition include: (3.33), (3.21), (3.84), (3.73) and (3.83). While the significant loss of ozone observed in the presence of water vapor in the feed gas may be attributed to the formation of ozone decomposing species such as H, OH and HO_2 through

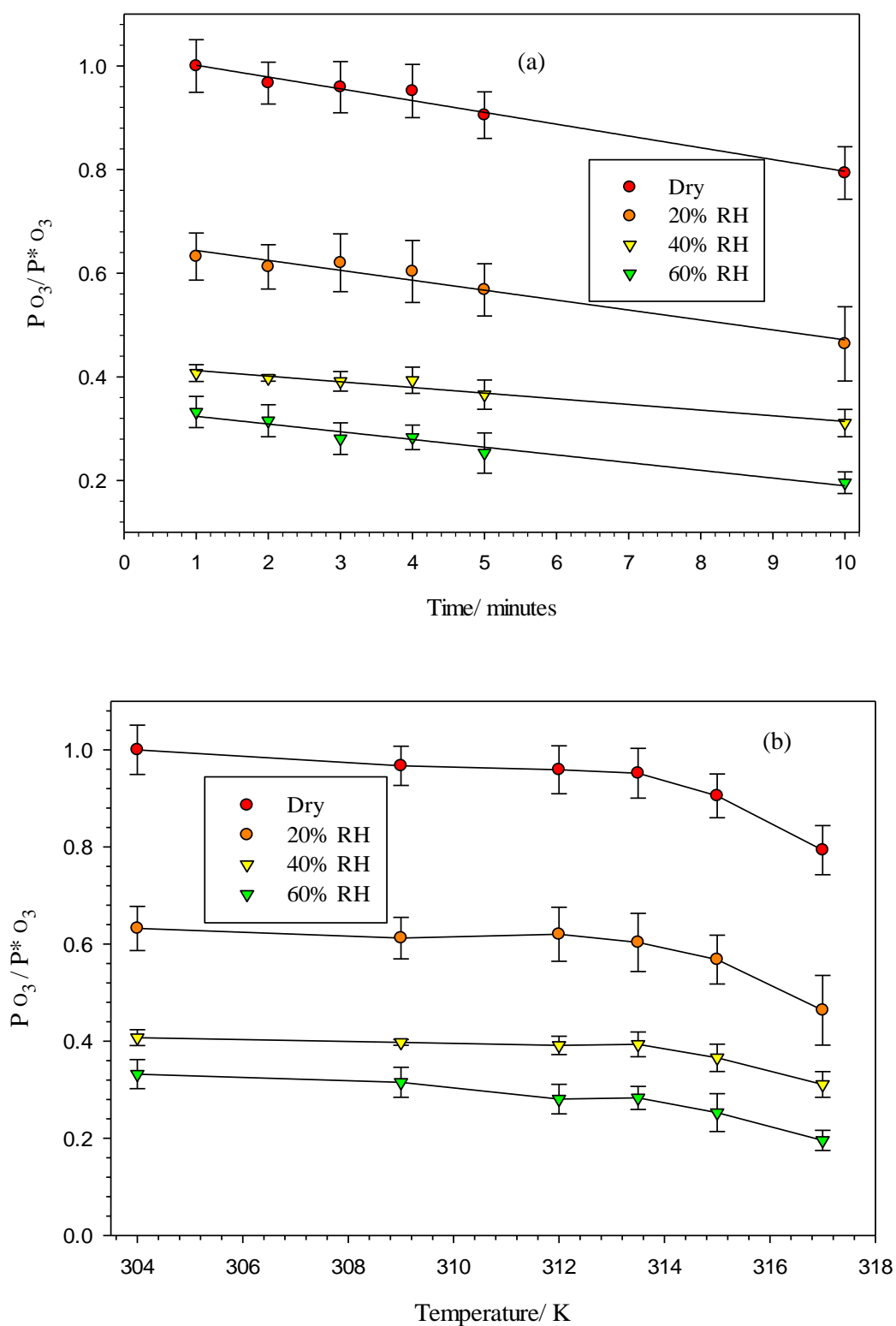
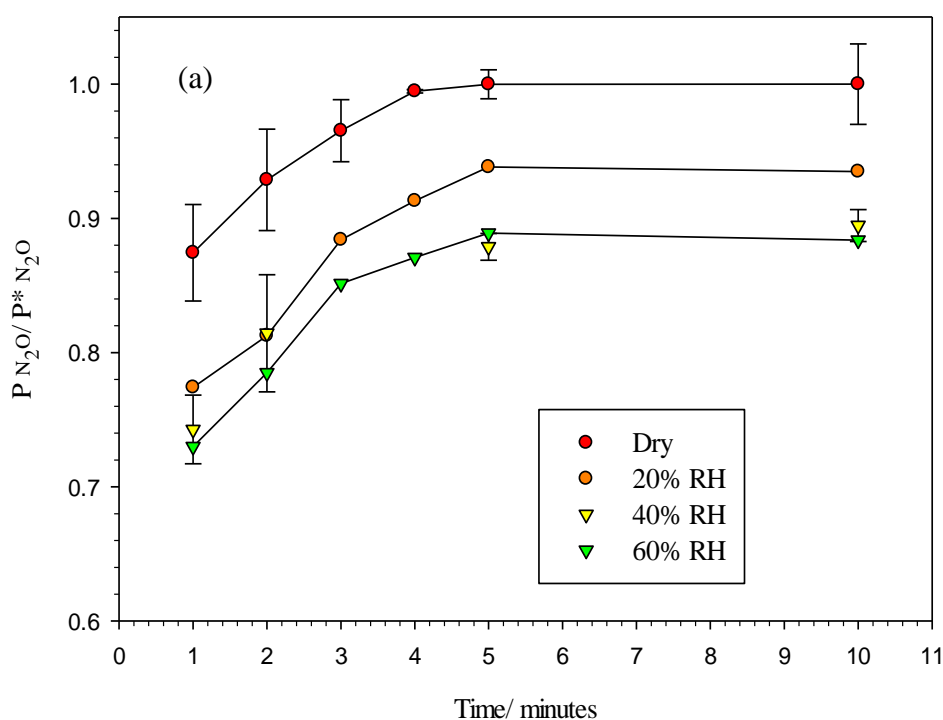


Figure 3.10. Plots of O₃ partial pressure monitored using in-situ FTIR spectroscopy as a function of relative humidity vs.: (a) running time, (b) plasma jet temperature using artificial air. The input power was 36 W at 0.5 dm³ min⁻¹. Maximum ozone partial pressure = $P^*_{O_3} = 8.9 \pm 0.08 \times 10^{-4}$ atm.

reactions (3.45), (3.57) & (3.85), respectively. In addition, the formation of additional quantities of NO_2 will increase ozone consumption via reaction (3.83), which may be considered as an indirect effect of relative humidity. Another indirect effect is the dissociation of water molecules and concomitant consumption of energetic electrons.

Figures 3.11(a) and (b) show the change in N_2O partial pressure produced from artificial air as a function of running time and gas temperature at different humidity levels. As can be seen from the figures, the partial pressure of N_2O increased gradually with running time and temperature to reach a steady state after ca. 5 minutes, regardless of the relative humidity. However, the partial pressure of N_2O decreased with increasing humidity.

The formation of N_2O from dry air may take place through reactions (3.28), (3.24) and (3.14), with the additional reactions (3.91) & (3.26) in the presence of water vapor. However, N_2O can be consumed via reactions (3.27), (3.13) and (3.41) in dry and humidified artificial air. In addition, in the presences of water vapor, N_2O may be consumed via its reactions with OH radicals (3.67) & (3.68). Furthermore, the contributions of the reactions (3.28) and (3.24) to N_2O formation may be reduced due to the consumption of atomic nitrogen by OH and HO_2 radicals through reactions (3.17) and (3.25). Hence, as in the case with the other species,



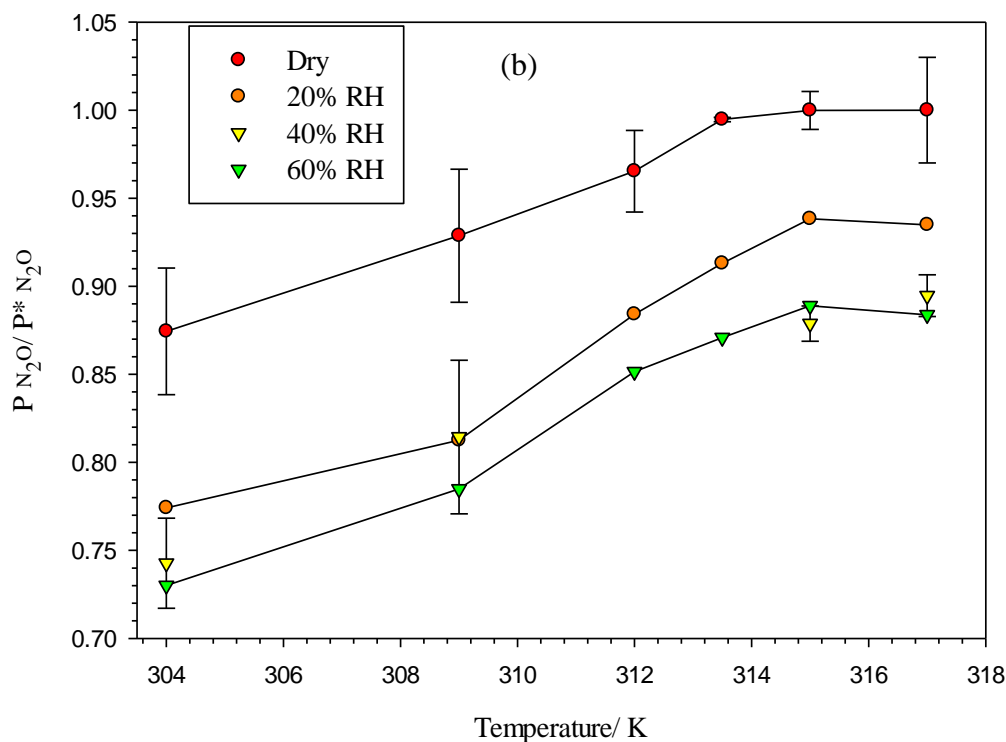


Figure 3.11. Plots of N_2O partial pressure monitored using in-situ FTIR spectroscopy as a function of relative humidity vs.: (a) running time, (b) plasma jet temperature using artificial air. The input power was 36 W at $0.5\text{ dm}^3\text{ min}^{-1}$. Maximum N_2O partial pressure = $P^*_{N_2O} = 2.07 \pm 0.1 \times 10^{-5}\text{ atm}$.

the partial pressure of N_2O at any time represents an equilibrium between the formation and decomposition reactions.

3.3. Downstream analyses

In this section, the chemical composition of the exhaust from the non-thermal plasma was analysed in downstream to establish a comparison with that monitored *in-situ*.

3.3.1. FTIR analysis

Figure 3.12 shows the spectra collected from the exhaust of the non-thermal plasma cell using FTIR spectroscopy. As can be seen from the figure, the chemical species observed downstream using dry artificial air were O_3 , N_2O_5 and N_2O . With ambient air, HNO_3 was seen in addition to these species. In contrast to the chemical composition observed *in-situ*,

neither NO_2 nor $\text{CO}_2^*(\nu)$ were seen within the downstream exhaust. Hence, it can be concluded that these species are mainly concentrated in the plasma glow region. In general, these data were in good agreement with the DBD effluent analyses carried out downstream by Eliasson et al. [50], and in the afterglow region by Sakiyama et al. [10].

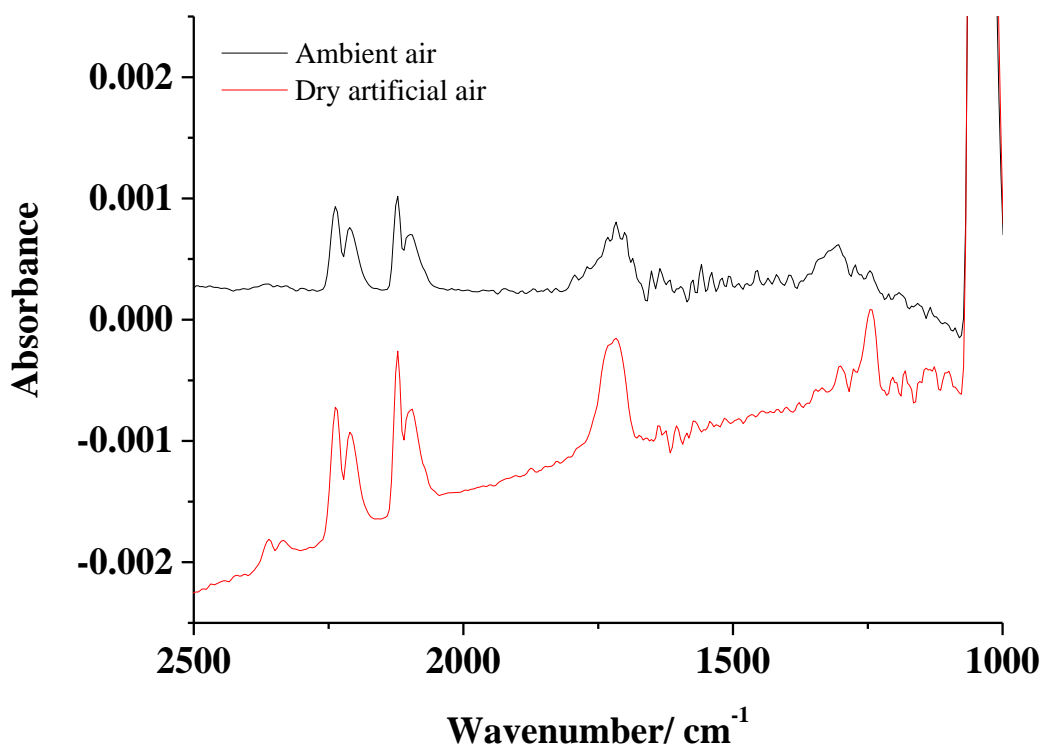


Figure 3.12. FTIR Spectra collected in downstream after 1 minute of DBD operation as a function of the feed gas composition. The input power was 36W and gas flow rate $0.5 \text{ dm}^3 \text{ min}^{-1}$.

3.3.2. Ozone analyses

The analyses of ozone in the downstream exhaust from the NTP was carried out using FTIR and UV-Vis spectroscopies to cross check these methods, using pure oxygen as the feed gas. In general, the variation between both analytical approaches measurements was found to lie within the level of uncertainty (i.e. 1.5%) based on the extinction coefficients employed [51]. However, when the feed gas was replaced with dry or humidified artificial air, a significant

variation between the UV and FTIR measurements was observed. Hence, the comparison between both techniques will be discussed below (section 3.3.4).

Figure 3.13 compares the FTIR measurements of ozone partial pressure collected from the plasma glow and downstream regions as a function of operation time using dry and humidified artificial air. From the figure, it can be seen that the highest ozone concentrations were obtained using dry air in both glow and downstream regions. In addition, regardless of the humidity of the artificial air, the ozone concentration in the downstream exhaust was found to be 30-40% lower than that in plasma glow. In fact, such a significant change suggests the occurrence of chemical reactions rather than a simple diffusion effect. In addition, the similar magnitude of ozone reduction observed in dry and humidified artificial air suggested that the effect of feed gas humidity on ozone is more significant in the plasma region. Based on the supposition that 1 mole of NO_2 reacts with one mole of O_3 , from figures 3.9 and 3.10, it would be expected that, at the highest partial pressure of NO_2 produced in artificial air and 40% RH, no more than 2.2% of the ozone present would be decomposed. The fact that a 40% reduction in the partial pressure of O_3 was observed between the plasma glow and downstream exhaust region strongly suggests that the decomposition of ozone occurs via other paths. Some of the species that would be expected to play roles in ozone decomposition post the plasma region are metastable atomic oxygen and nitrogen [11, 52-54].

Atomic nitrogen can react directly with ozone (3.21) or with oxygen (3.20) to produce NO molecules which, in turn, consume ozone via reaction (3.73) to produce NO_2 . Furthermore, atomic nitrogen can react with nitric oxide (3.19) to produce vibrationally excited N_2 with sufficient energy to induce ozone dissociation [55]. Atomic oxygen can decompose ozone through reaction (3.33) or by reacting with atomic nitrogen (3.18) to produce nitric oxide. From figure 3.13, it can be seen that the downstream measurements obtained from dry artificial air indicated a rapid decomposition of ozone during the first 5 minutes, slowing down at longer times. This behaviour was not observed using humidified artificial air which may be attributed to the lower amounts of atomic oxygen and nitrogen being available for ozone decomposition as a result of: (i) lower formation due to the consumption of energetic electrons by the dissociation of water molecules, and (ii) reaction with water dissociation products such as OH and HO_2 through reactions (3.19), (3.25), (3.31) and (3.32).

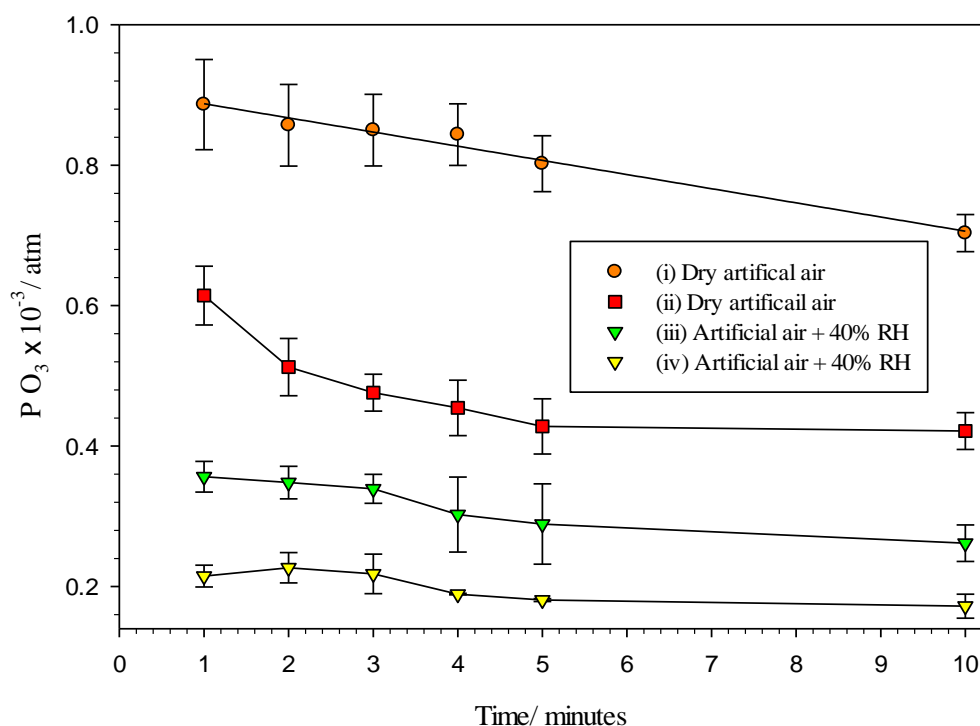


Figure 3.13. Plots of ozone partial pressure as a function of running time and feed gas composition, monitored using *in-situ* (i) + (iii) and downstream FTIR spectroscopy (ii) + (iv). The input power was 36 W at $0.5 \text{ dm}^3 \text{ min}^{-1}$.

3.3.3. N_2O analyses

Figure 3.14 shows the change in N_2O partial pressure as a function of feed gas composition and running time monitored *in-situ* in the plasma and downstream in the exhaust. As can be seen from the figure, in the case of humidified air, the partial pressure of N_2O monitored downstream was lower by ca.18% than found in the plasma. However, with dry artificial dry air, the downstream partial pressure of N_2O was found to be higher than that monitored *in-situ* and to increase significantly with the running time. After 10 minutes, the downstream partial pressure was found to be more than 30% higher than that monitored *in-situ*. Considering the fact that N_2O generation from dry air would be expected to take place through the reactions of atomic nitrogen with NO_2 (3.24) or NO (3.28), it can be concluded that some of these reactions must be taking place in afterglow region. This further indicates the major role of atomic nitrogen in the afterglow region. In the case of humidified artificial air, the negative effects of water molecules on atomic nitrogen, discussed in section 3.2.5,

may be expected to depress the formation of N_2O in the downstream region. On the other hand, atomic oxygen which has diffused from the plasma or formed in the afterglow region through ozone dissociation can facilitate N_2O decomposition through reaction (3.41).

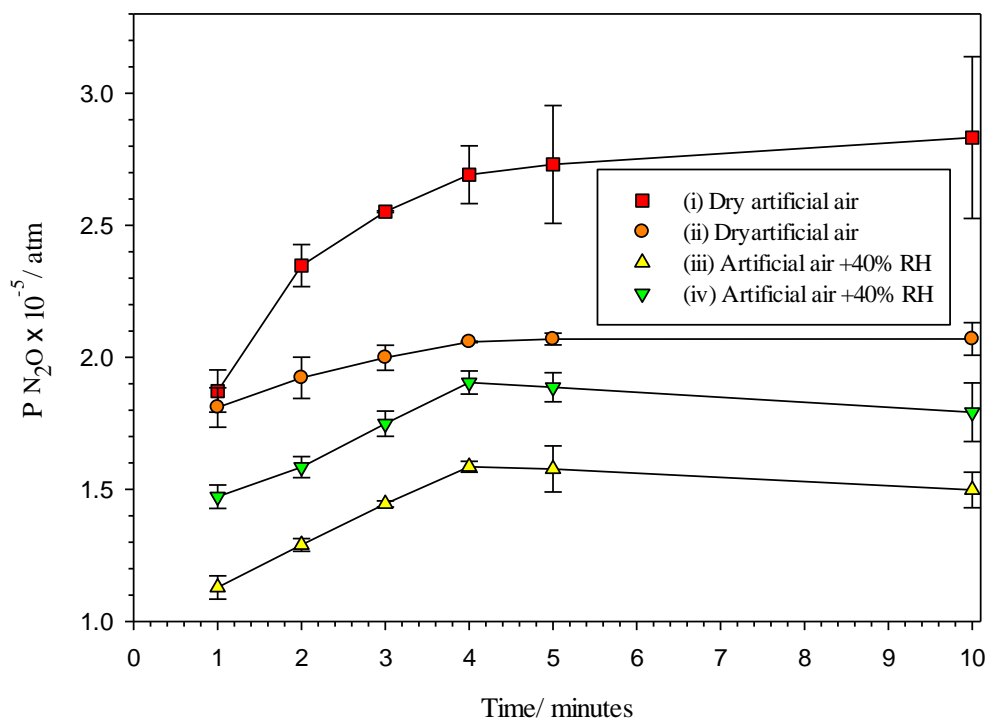


Figure 3.14. Plots of ozone partial pressure as a function of running time and feed gas composition, monitored in-situ (ii) + (iv) and downstream (ii) + (iv) using FTIR spectroscopy. The input power was 36 W at $0.5 \text{ dm}^3 \text{ min}^{-1}$.

3.3.4. The uncertainty associated with downstream UV analyses of ozone

UV spectroscopy is one of the most common methods that have been used widely for ozone monitoring [56], and a significant number of articles have employed this approach for ozone monitoring from various types of air-fed ozonisers. Recently, Moiseev and co-workers [57] have employed UV-Vis spectroscopy to monitor the change in the chemical composition of humid air in a container after being exposed to NTP for 15-120 seconds in a large gap DBD. From their work, several species were assumed to interfere with the ozone absorbance at 254 nm namely: NO_2 , N_2O_4 , N_2O_5 , H_2O_2 , HNO_2 , HNO_3 and HNO_4 , and hence they have employed three deconvolution methods to compute these interferences to evaluate the concentrations of different species. Their results suggest that the ozone concentration can be

overestimated by up to 20% in the presence of the interfering species. However, since not all of these species were observed during this work, it was decided to evaluate the level of uncertainty in UV-Vis measurements of ozone in the outputs of a DBD fed with dry and humidified artificial air.

Figure 3.15 shows a comparison between ozone partial pressure measurements carried out using FTIR and UV-Vis spectroscopies in the downstream region as a function of running time using dry and humidified artificial air. As can be seen from the figure, ozone measurements carried out using the UV spectrometer were found to be higher than those obtained using FTIR spectroscopy. Furthermore, the difference between the UV and FTIR measurements was found to increase with time from 19% to 40% and from 33% to 42% when dry and humidified artificial air were employed, respectively. The increase in the difference between the UV and FTIR measurements with time can be attributed to the increase in the concentrations of N_2O_5 and HNO_3 that can interfere with UV measurements

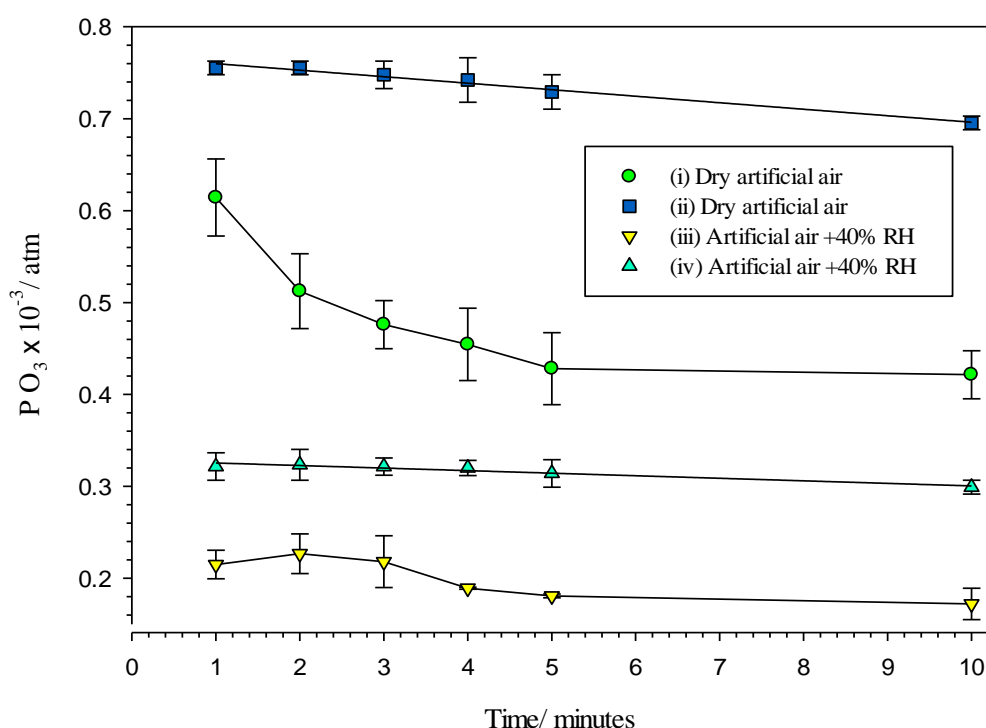


Figure 3.15. Plots of ozone partial pressure as a function of running time and feed gas composition monitored downstream using FTIR spectroscopy (i) + (iii), and UV-Vis spectroscopy (ii) + (iv). The input power was 36 W at $0.5 \text{ dm}^3 \text{ min}^{-1}$. Plots (ii) and (iv) were obtained from fig. 3.13.

of ozone in dry and humidified artificial air, respectively. Thus, the overestimation of ozone concentration obtained using UV is expected to increase with the number and concentration of interfering species. Therefore, the determination of these interfering species and the magnitude of their interference is important to maintain a reliable level of accuracy when employing UV spectroscopic analyses of ozone.

3.4. Conclusions

The chemical composition of non-thermal plasma (NTP) produced using an air-fed dielectric barrier discharge (DBD) jet was monitored in the plasma glow and downstream regions employing FTIR and UV-Vis spectroscopies. Depending on the constituents of the feed gas, N_2O , O_3 , N_2O_5 , NO_2 and HNO_3 were observed in the NTP glow region, while N_2O , O_3 , N_2O_5 and HNO_3 were detected in the downstream exhaust. However, when the feed gas included CO_2 , CO and a vibrationally excited form of CO_2 (i.e. $\text{CO}_2^*(\nu)$) were also detected. The latter has hitherto not been observed in NTP using FTIR spectroscopy.

It was postulated that the formation of $\text{CO}_2^*(\nu)$ from CO_2 may take place through direct electron collision and/or through interaction with other excited molecules. However, the relaxation to CO_2 and/or dissociation to CO and atomic oxygen were assumed to be the main pathways of $\text{CO}_2^*(\nu)$ loss. In 1% CO_2/Ar , the conversion of CO_2 to $\text{CO}_2^*(\nu)$ and CO appears to be ca. 15%. $\text{CO}_2^*(\nu)$ was found to be less stable at high energy densities.

When using dry air, the partial pressures of N_2O and O_3 increased with the specific energy density, while NO_2 decreased. However, in the presence of water vapour, the partial pressures of NO_2 , O_3 and N_2O increased. In addition, while the presence of water vapour was essential for the production of HNO_3 , the partial pressure of NO_2 increased with the relative humidity and that of O_3 , N_2O_5 and N_2O decreased.

The time-dependent behaviour of the partial pressure of NO_2 in the plasma glow region was found to correlate with the time dependence of the plasma temperature, i.e. increasing with increasing temperature. In contrast, the ozone partial pressure decreased with increasing temperature, as would be expected on the basis of thermodynamic principles. Moreover, in the presence of water vapour the effect of gas temperature on NO_2 , N_2O and O_3 was more significant, suggesting a synergetic effect of relative humidity and plasma temperature.

Unexpectedly, the spectroscopic analyses of O₃, NO₂ and N₂O in the plasma glow region and in the downstream exhaust suggested the occurrence of chemical reactions in afterglow region rather than simple diffusion. For instance, the higher partial pressure of N₂O observed in the downstream exhaust than in the plasma glow region when using dry air, suggested that active species such as atomic nitrogen play important roles in the afterglow region.

Finally, it is clear from the work presented in this chapter that the UV analyses of ozone cannot employed with any accuracy in the presence of interfering species such as N₂O₅ and/or HNO₃.

3.5. References

[1] Akitsu, T., Ohkawa, H., Tsuji, M., Kimura, H. and Kogoma, M. (2005) 'Plasma sterilization using glow discharge at atmospheric pressure', *Surface and Coatings Technology*, 193(1–3), pp. 29-34.

[2] Sladek, R.E.J., Stoffels, E., Walraven, R., Tielbeek, P.J.A. and Koolhoven, R. (2004) 'Plasma treatment of dental cavities: a feasibility study', *Plasma Science, IEEE Transactions on*, 32(4), pp. 1540-1543.

[3] Visser, R.J. (1989) 'Determination of the power and current densities in argon and oxygen plasmas by insitu temperature measurements', *Journal of Vacuum Science & Technology A*, 7(2), pp. 189-194.

[4] Koinuma, H., Ohkubo, H., Hashimoto, T., Inomata, K., Shiraishi, T., Miyanaga, A. and Hayashi, S. (1992) 'Development and application of a microbeam plasma generator', *Applied Physics Letters*, 60(7), pp. 816-817.

[5] McCaa, D.J. and Shaw, J.H. (1968) 'The infrared spectrum of ozone', *Journal of Molecular Spectroscopy*, 25(3), pp. 374-397.

[6] Schmidt-Bleker, A., Winter, J., Iseni, S., Dünnbier, M., Weltmann, K.D. and Reuter, S. (2014) 'Reactive species output of a plasma jet with a shielding gas device—combination of

FTIR absorption spectroscopy and gas phase modelling', *Journal of Physics D: Applied Physics*, 47(14), p. 145201.

[7] Nightingale, R.E., Downie, A.R., Rotenberg, D.L., Crawford, B. and Ogg, R.A. (1954) 'The preparation and infrared spectra of the oxides of nitrogen', *The Journal of Physical Chemistry*, 58(11), pp. 1047-1050.

[8] Herzberg G 1945 Molecular spectra and molecular structure. Vol. 2: Infrared and Raman spectra of polyatomic molecules *Molecular spectra and molecular structure. Vol. 2: Infrared and Raman spectra of polyatomic molecules*, by G. Herzberg. New York: Van Nostrand, Reinhold, 1945 **1**.

[9] Haridass, C., Aw-Musse, A., Misra, P. and Jordan, J. (2000) 'Fourier transform infrared (FT-IR) spectroscopy of trace molecular species of importance for the elucidation of atmospheric phenomena', *Computers & Electrical Engineering*, 26(1), pp. 47-65.

[10] Yukinori, S., David, B.G., Hung-Wen, C., Tetsuji, S. and Gregor, E.M. (2012) 'Plasma chemistry model of surface microdischarge in humid air and dynamics of reactive neutral species', *Journal of Physics D: Applied Physics*, 45(42), p. 425201.

[11] Gaens, W.V. and Bogaerts, A. (2013) 'Kinetic modelling for an atmospheric pressure argon plasma jet in humid air', *Journal of Physics D: Applied Physics*, 46(27), p. 275201.

[12] Lowke, J.J. and Morrow, R. (1995) 'Theoretical analysis of removal of oxides of sulphur and nitrogen in pulsed operation of electrostatic precipitators', *Plasma Science, IEEE Transactions on*, 23(4), pp. 661-671.

[13] Cravens, T.E., Kozyra, J.U., Nagy, A.F., Gombosi, T.I. and Kurtz, M. (1987) 'Electron impact ionization in the vicinity of comets', *Journal of Geophysical Research: Space Physics*, 92(A7), pp. 7341-7353.

[14] Piper, L.G. (1987) 'Quenching rate coefficients for N₂ (a' ¹Σ⁻_u)', *The Journal of Chemical Physics*, 87(3), pp. 1625-1629.

- [15] Mätzing H 2007 *Advances in Chemical Physics*: (John Wiley & Sons, Inc.), pp. 315-402.
- [16] Iannuzi, M.P., Jeffries, J.B. and Kaufman, F. (1982) 'Product Channels of the $N_2(A_3\Sigma^+_u)$ + O_2 interaction', *Chemical Physics Letters*, 87(6), pp. 570-574.
- [17] Atkinson, R., Baulch, D.L., Cox, R.A., Hampson Jr, R.F., Kerr, J.A., Rossi, M.J. and Troe, J. (1997) 'Evaluated kinetic, photochemical and heterogeneous data for atmospheric chemistry: Supplement V. IUPAC Subcommittee on Gas Kinetic Data Evaluation for Atmospheric Chemistry', *Journal of Physical and Chemical Reference Data*, 26(3), pp. 521-1011.
- [18] Atkinson, R., Baulch, D.L., Cox, R.A., Hampson, R.F., Kerr, J.A., Rossi, M.J. and Troe, J. (1997) 'Evaluated kinetic and photochemical data for atmospheric chemistry: supplement VI. IUPAC subcommittee on gas kinetic data evaluation for atmospheric chemistry', *Journal of Physical and Chemical Reference Data*, 26(6), pp. 1329-1499.
- [19] Atkinson, R., Baulch, D.L., Cox, R.A., Hampson, R.F., Kerr, J.A. and Troe, J. (1989) 'Evaluated kinetic and photochemical data for atmospheric chemistry: Supplement III. IUPAC Subcommittee on Gas Kinetic Data Evaluation for Atmospheric Chemistry', *Journal of Physical and Chemical Reference Data*, 18(2), pp. 881-1097.
- [20] Herron, J. and Green, D. (2001) 'Chemical kinetics database and predictive schemes for nonthermal humid air plasma chemistry. Part II. Neutral Species Reactions', *Plasma Chemistry and Plasma Processing*, 21(3), pp. 459-481.
- [21] Kossyi, I.A., Kostinsky, A.Y., Matveyev, A.A. and Silakov, V.P. (1992) 'Kinetic scheme of the non-equilibrium discharge in nitrogen-oxygen mixtures', *Plasma Sources Science and Technology*, 1(3), p. 207.
- [22] Eichwald, O., Yousfi, M., Hennad, A. and Benabdessadok, M.D. (1997) 'Coupling of chemical kinetics, gas dynamics, and charged particle kinetics models for the analysis of NO reduction from flue gases', *Journal of Applied Physics*, 82(10), pp. 4781-4794.

[23] Capitelli M, Ferreira C M, Gordiets B F and Osipov A I 2000 Plasma kinetics in atmospheric gases. (Berlin: Springer).

[24] Woodall, J., Agúndez, M., Markwick-Kemper, A.J. and Millar, T.J. (2007) 'The UMIST database for astrochemistry 2006', *A&A*, 466(3), pp. 1197-1204.

[25] National Institute of Standards and Technology NIST Chemical Kinetics Database (2011)

[26] Baulch, D.L., Cobos, C., Cox, R.A., Esser, C., Frank, P., Just, T., Kerr, J.A., Pilling, M.J., Troe, J. and Walker, R.W. (1992) 'Evaluated kinetic data for combustion modelling', *Journal of Physical and Chemical Reference Data*, 21(3), pp. 411-734.

[27] Kushner, M.J. (1993) 'Plasma chemistry of He/O₂/SiH₄ and He/N₂O/SiH₄ mixtures for remote plasma-activated chemical-vapor deposition of silicon dioxide', *Journal of Applied Physics*, 74(11), pp. 6538-6553.

[28] Mukkavilli, S., Lee, C.K., Varghese, K. and Tavlarides, L.L. (1988) 'Modeling of the electrostatic corona discharge reactor', *Plasma Science, IEEE Transactions on*, 16(6), pp. 652-660.

[29] Gordillo-Vazquez, F.J. (2008) 'Air plasma kinetics under the influence of sprites', *Journal Of Physics. D. Applied Physics*, 41(23), p. 234016.

[30] Person, J.C. and Ham, D.O. (1988) 'Removal of SO₂ and NO_x from stack gases by electron beam irradiation', *International Journal of Radiation Applications and Instrumentation. Part C. Radiation Physics and Chemistry*, 31(1), pp. 1-8.

[31] Jeong, J.Y., Park, J., Henins, I., Babayan, S.E., Tu, V.J., Selwyn, G.S., Ding, G. and Hicks, R.F. (2000) 'Reaction chemistry in the afterglow of an oxygen–helium, atmospheric-pressure plasma', *The Journal of Physical Chemistry A*, 104(34), pp. 8027-8032.

[32] Freund, H.J. and Roberts, M.W. (1996) 'Surface chemistry of carbon dioxide', *Surface Science Reports*, 25(8), pp. 225-273.

[33] Modest, M.F. and Bharadwaj, S.P. (2002) 'Medium resolution transmission measurements of CO₂ at high temperature', *Journal of Quantitative Spectroscopy and Radiative Transfer*, 73(2-5), pp. 329-338.

[34] Toselli, B.M. and Barker, J.R. (1991) 'Excitation of CO₂ by energy transfer from highly vibrationally excited benzene derivatives', *The Journal of Chemical Physics*, 95(11), pp. 8108-8119.

[35] Rond, C., Bultel, A., Boubert, P. and Chéron, B.G. (2008) 'Spectroscopic measurements of nonequilibrium CO₂ plasma in RF torch', *Chemical Physics*, 354(1), pp. 16-26.

[36] Richard, J. (2011) 'Vibrational and rotational excitation and dissociation of CO₂ Reexamined', in *49th AIAA Aerospace Sciences Meeting including the New Horizons Forum and Aerospace Exposition*. American Institute of Aeronautics and Astronautics.

[37] Fridman A 2012 Plasma Chemistry (Cambridge: Cambridge University Press), pp. 263

[38] Moore. C. E. 1949 Atomic Energy Levels, Vol. I", NBS Circular 476.

[39] Chase Jr. M.W., NIST-JANAF Thermochemical Tables, 4th edition, American Institute of Physics, New York, 1998, part 2, p. 1790

[40] Arin, L.M. and Warneck, P. (1972) 'Reaction of ozone with carbon monoxide', *The Journal of Physical Chemistry*, 76(11), pp. 1514-1516.

[41] Toby, S., Sheth, S. and Toby, F.S. (1984) 'Reaction of carbon monoxide with ozone and oxygen atoms', *International Journal of Chemical Kinetics*, 16(2), pp. 149-157.

[42] Wilde, K.A., Zwolinski, B.J. and Parlin, R.B. (1957) 'Decomposition of carbon dioxide in a radiofrequency arc1', *Journal of the American Chemical Society*, 79(6), pp. 1323-1329.

[43] Schulz, G.J. (1962) 'Cross sections and electron affinity for O⁻ ions from O₂, CO, and CO₂ by electron impact', *Physical Review*, 128(1), pp. 178-186.

[44] Savinov, S.Y., Lee, H., Song, H.K. and Na, B.-K. (1999) 'Decomposition of methane and carbon dioxide in a radio-frequency discharge', *Industrial & Engineering Chemistry Research*, 38(7), pp. 2540-2547.

[45] Stepaniuk, V.P., Ioppolo, T., Ötügen, M.V. and Sheverev, V.A. (2007) 'Measurement of gas temperature and convection velocity profiles in a dc atmospheric glow discharge', *Journal of Applied Physics*, 102(12), p. 123302.

[46] Inomata, K., Aoki, N. and Koinuma, H. (1994) 'Production of fullerenes by low temperature plasma chemical vapor deposition under atmospheric pressure', *Japanese journal of applied physics*, 33(2A), p. L197.

[47] Guohua, N., Peng, Z., Cheng, C., Ye, S., Hirotaka, T. and Yuedong, M. (2012) 'Characterization of a steam plasma jet at atmospheric pressure', *Plasma Sources Science and Technology*, 21(1), p. 015009.

[48] Colucci, D.W. and Viskanta, R. (1996) 'Effect of nozzle geometry on local convective heat transfer to a confined impinging air jet', *Experimental Thermal and Fluid Science*, 13(1), pp. 71-80.

[49] Ni, T.L., Ding, F., Zhu, X.D., Wen, X.H. and Zhou, H.Y. (2008) 'Cold microplasma plume produced by a compact and flexible generator at atmospheric pressure', *Applied Physics Letters*, 92(24), p. 241503.

[50] Eliasson B and Kogelschatz U., (1987) Nitrogen oxide formation in ozonizers. In: *Proc. 8th Int. Symp. on Plasma Chemistry (ISPC-8), Tokyo*, pp 736-41

[51] Dufour, G., Valentin, A., Henry, A., Hurtmans, D. and Camy-Peyret, C. (2004) 'Concentration measurements of ozone in the 1200–300 ppbv range: an intercomparison

between the BNM ultraviolet standard and infrared methods', *Spectrochimica Acta Part A: Molecular and Biomolecular Spectroscopy*, 60(14), pp. 3345-3352.

[52] Mozetič, M., Vesel, A., Gaillard, M. and Ricard, A. (2001) 'Atomic oxygen concentration in a flowing post-discharge reactor', *Plasmas and Polymers*, 6(1-2), pp. 71-79.

[53] Babayan, S.E., Ding, G., Nowling, G.R., Yang, X. and Hicks, R.F. (2002) 'Characterization of the active species in the afterglow of a nitrogen and helium atmospheric-pressure plasma', *Plasma Chemistry and Plasma Processing*, 22(2), pp. 255-269.

[54] Kang, W.S., Kim, H.-S. and Hong, S.H. (2010) 'Atomic oxygen generation by in-situ plasma and post-plasma in dielectric barrier discharges for surface treatment', *Thin Solid Films*, 518(22), pp. 6578-6582.

[55] Phillips, L.F. and Schiff, H.I. (1962) 'Mass spectrometric studies of atom reactions. II. vibrationally excited N₂ formed by the reaction of N atoms with NO', *The Journal of Chemical Physics*, 36(12), pp. 3283-3286.

[56] Rakness, K., Gordon, G., Langlais, B., Masschelein, W., Matsumoto, N., Richard, Y., Robson, C.M. and Somiya, I. (1996) 'Guideline for measurement of ozone concentration in the process gas from an ozone generator', *Ozone: Science & Engineering*, 18(3), pp. 209-229.

[57] Moiseev, T., Misra, N.N., Patil, S., Cullen, P.J., Bourke, P., Keener, K.M. and Mosnier, J.P. (2014) 'Post-discharge gas composition of a large-gap DBD in humid air by UV-Vis absorption spectroscopy', *Plasma Sources Science and Technology*, 23(6), p. 065033.

4. A characteristic study of a novel dielectric barrier discharge packed bed reactor (DBD-PBR) for ozone generation

4.1. Introduction

Heat rising during the operation of conventional dielectric barrier discharge packed bed reactors (DBD-PBRs) is one of the challenges that significantly depress the efficiency of these reactors towards ozone generation, see section 1.3.2. The same effect is expected to accelerate the formation of undesirable NO_x that can significantly lower the yield of ozone when air is employed to feed the DBD-PBRs as shown in section 3.2.5. Thus, the focus of this chapter will be on ozone generation from oxygen and air using a novel dielectric barrier discharge packed bed reactor DBD-PBR.

The main aim of this chapter was to design, commission and optimize a DBD-PBR with an effective cooling system. The objectives were to:

- Design and fabricate a DBD-PBR with an efficient cooling system
- Identify the optimal arrangement of the electrodes and dielectrics within the discharge cell of the DBD-PBR
- Investigate the performance of the DBD-PBR towards ozone production as a function of:
 - Feed gas flow rate, input power and coolant temperature
 - Dielectric material type, shape, size and packing gap width (PGWD)
- Identify and determine the concentrations of NO_x by-products when using air to feed DBD-PBR
- Develop and evaluate an effective ozone and NO_x catalytic destruction cell

The work was carried out employing a novel DBD-PBR designed and fabricated in-house using four arrangements of the discharge cell shown in figure 4.1, and the cross-sections of these arrangements are shown in fig. 4.2. As can be seen from the figures, the arrangements were varied in the shape and number of electrodes and dielectric layers to facilitate determining the effects of these parameters. From the figures, each of the cells was divided into two halves with each consisting of the same number of HV and supporting electrodes.

Each half of the cells A2 and A3 consists of 2 and 3 planer stainless steel electrodes, respectively, with supporting PTFE sheets at the inlet and outlet sides of the cell. The stainless steel electrodes in cells B2 and B3 were 2 and 3, respectively, semi-cylindrical in shape and were in direct contact with the inner wall of the cell. Further details can be found in section 2.3. Table 2.1 shows the dielectrics employed in this work along with some of their physical properties and is reproduced here for convenience.

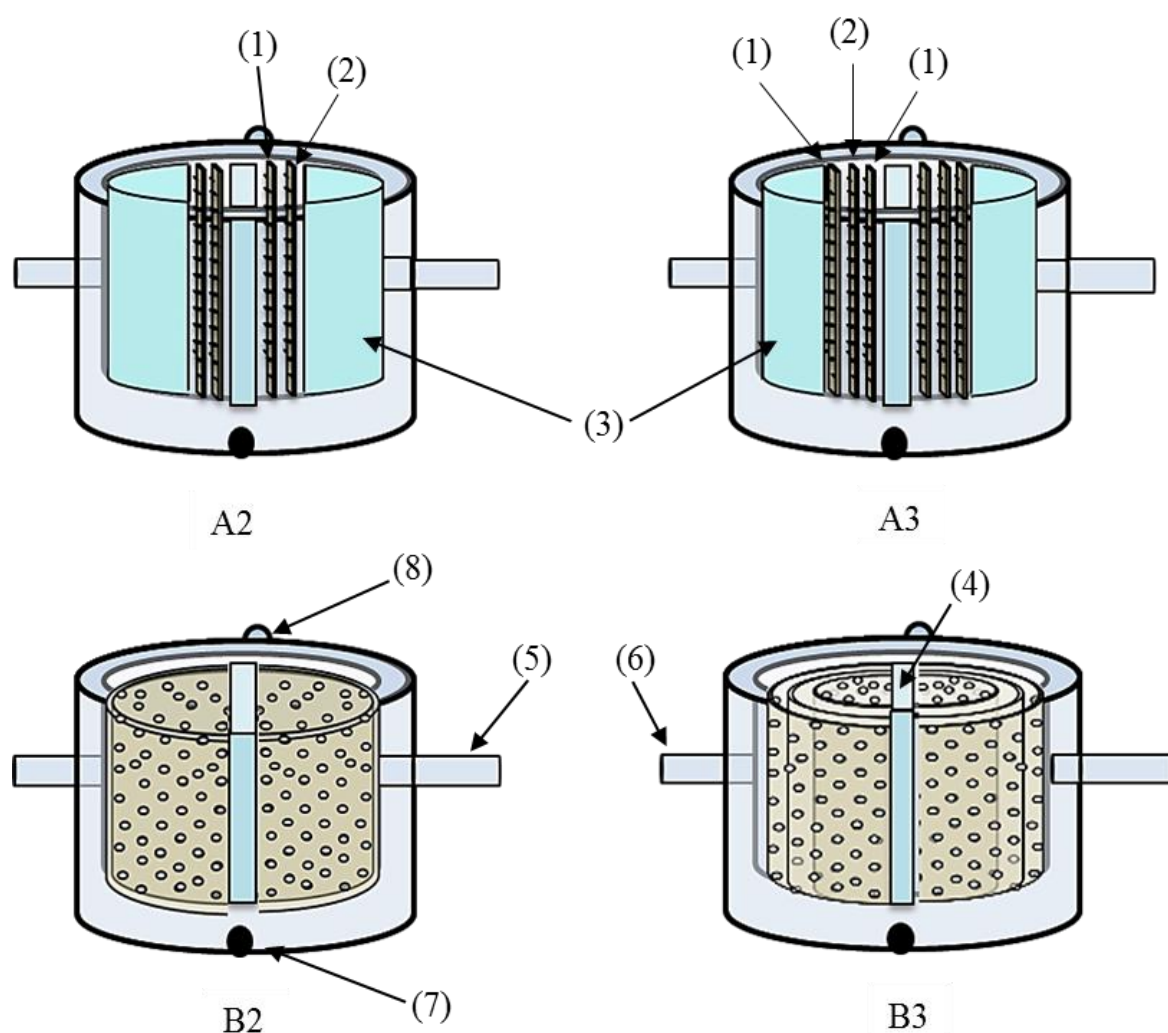


Figure 4.1. Schematic of the DBD-PBR discharge cell arrangements employed for ozone generation: (1) support electrode, (2) high voltage electrode, (3) perforated PTFE supports, (4) perforated PTFE sheet (i.e. the cell separator), (5) feed gas inlet, (6) exhaust gas outlet, (7) coolant liquid inlet and (8) coolant outlet. The cell names indicate the shape and number of electrodes in each half: planer electrodes in A and semi-cylindrical in B.

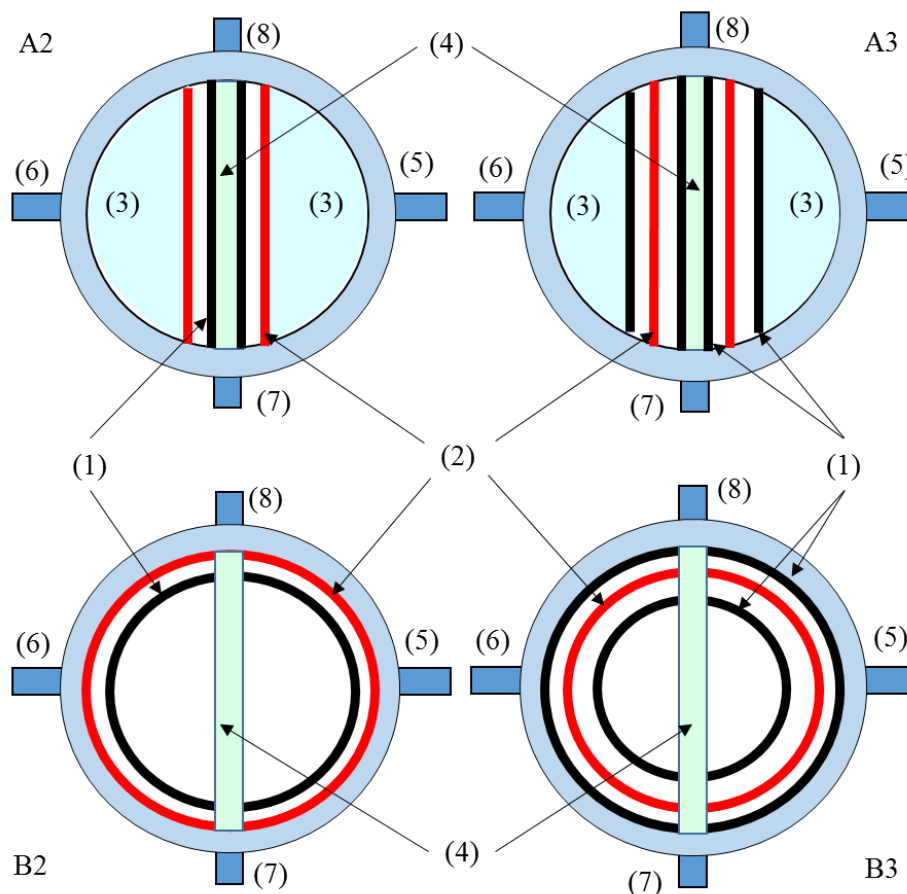


Figure 4.2. Schematic of the DBD-PBR discharge cell shows the coross-sections of arrangements shown in fig.4.1: (1) support electrode, (2) high voltage electrode, (3) perforated PTFE supports, (4) perforated PTFE sheet (i.e. the cell separator), (5) feed gas inlet, (6) exhaust gas outlet, (7) coolant liquid inlet and (8) coolant outlet.

Dielectric	Type	Diameter /mm	Dielectric constant	Thermal conductivity / $\text{W m}^{-1} \text{K}^{-1}$
D1	Alumina pellets (93%)	2	8.5 – 10	14.0 - 24.0
D2	Borosilicate glass beads	2	4 – 6	1.0 - 1.2
D3	A ₃ molecular sieve	2	N/A	0.12 - 0.14
D4	Soda-Lime glass beads	3	7.3	0.9 - 1.1
D5	Alumina pellets (93%)	3	8.5 – 10.0	14.0 - 24.0
D6	Perforated PTFE sheets	1	2.1	0.25 - 0.3

Table 2.1. Physical properties of the dielectrics employed for ozone generation using the novel dielectric barrier discharge-packed beads reactor (DBD-PBR).

4.2. Results and discussion

4.2.1. The effect of the discharge cell arrangement

The discharge cell arrangements shown in figure 4.1 were employed for determining the effect of the number and shape of electrodes and dielectric layers on the performance of the DBD-PBR towards ozone generation. Figure 4.3 shows plots of ozone concentration as a function of oxygen flow rate and the arrangement of the discharge cell at fixed conditions of input power, coolant temperature and dielectric type. The dielectric employed in these experiments was perforated sheets of PTFE (D6) placed between the HV and supporting electrodes. As can be seen from fig.4.3, regardless of the cell arrangement, the concentration of ozone was found to correlate inversely with the number of supporting electrodes and dielectric layers. This behaviour was more pronounced at low oxygen flow rates; for instance at $0.2 \text{ dm}^3 \text{ min}^{-1}$ the amount of ozone produced using the arrangements A2 and B2 was 24 and 32% higher than that using A3 and B3, respectively. Thus, it does not seem unreasonable to postulate that using more electrodes and dielectric layers may increase the heat produced in the cell [1, 2], hence decreasing ozone production. This heating effect would be expected to increase when using dielectrics of low thermal conductivity [3] such as PTFE (i.e. $0.25\text{-}0.3 \text{ W m}^{-1} \text{ K}^{-1}$ [4]), see section 1.3.2. Also, at a constant input power the discharge power characteristics were expected to be affected significantly by increasing the number of dielectric layers in contact with the HV electrodes, and this factor will be discussed in section 4.2.7.

It is clear from fig. 4.3 that, at flow rates lower than $5.0 \text{ dm}^3 \text{ min}^{-1}$, the ozone produced using cells B2 and B3 were higher than that produced by A2 and A3, respectively. This difference increased with reducing the feed gas flow rate; for instance at $0.2 \text{ dm}^3 \text{ min}^{-1}$ the concentration of ozone produced using cells B2 and B3 were 31 and 24% higher than that observed using A2 and A3, respectively. This may be attributed to the direct contact between the electrodes in B and the internal wall of the cell, and hence more effective cooling. Another possible reason could be the increased width of the HV electrodes in B (i.e. 30 %) leading to a greater active area of the discharge cell. However, the minimum input power required for initiating the non-thermal plasma (NTP) and, consequently, ozone formation (i.e. the onset power) for cells A2 and B2 were 1-2W and 13W, respectively. This behaviour was found to be relevant to the variation in the discharge power characteristics with the cell arrangement that will be discussed as well in section 4.2.7.

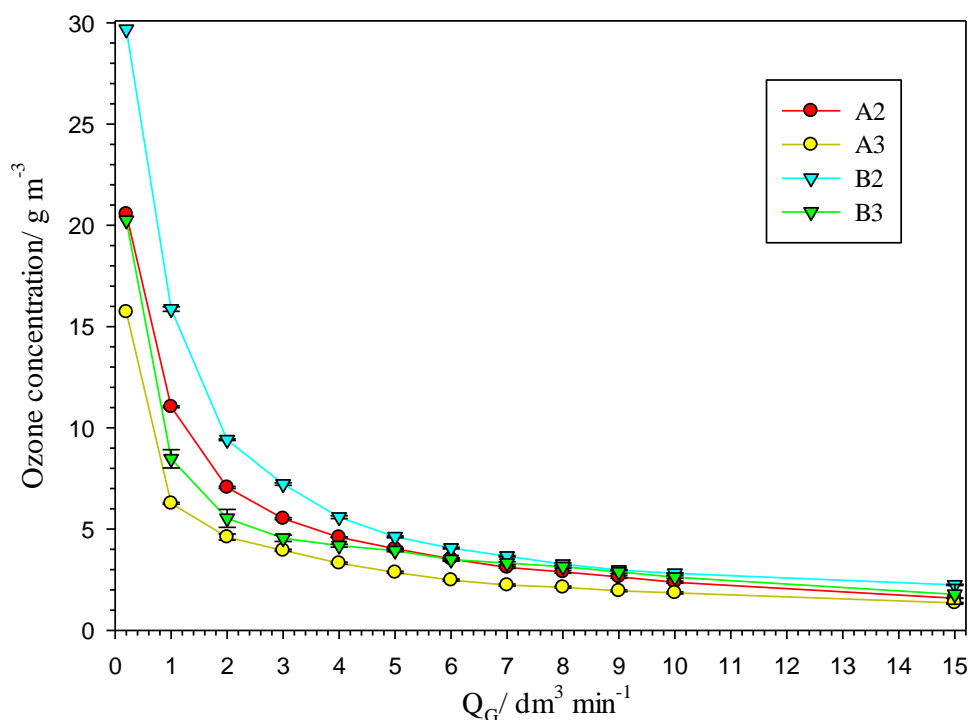


Figure 4.3. Plots of ozone concentration as a function of oxygen flow rate and discharge cell arrangement. The dielectric was 1.0 mm thick perforated sheets of PTFE (D6). The input power and the coolant temperature were 17W and 5.0 °C, respectively.

4.2.2. The effect of cell separator thickness

The effect of varying the thickness of the PTFE plate (employed to divide the discharge cell) on ozone generation was investigated using the B2 arrangement, and the results are shown in fig. 4.4. As can be seen from the figure, by changing the cell divider thickness from 10 to 3 mm the onset power decreased from 13 to 11.5W, and the rate of ozone production increased with input power. For instance, at an input power of 18W, the concentration of ozone produced from the cell using the 3 mm thick separator was ca. 27% higher than that observed using the 10 mm separator. This enhancement may be attributed to the increase in the electric field strength associated with decreasing the gap width between the HV electrodes. However, at input power higher than 18W, the cell with the thinner separator started arcing, followed by a breakdown of the electric field. Therefore, for safety reasons and to allow for a wider range of input power, the 10 mm cell divider was employed in all experiments discussed below.

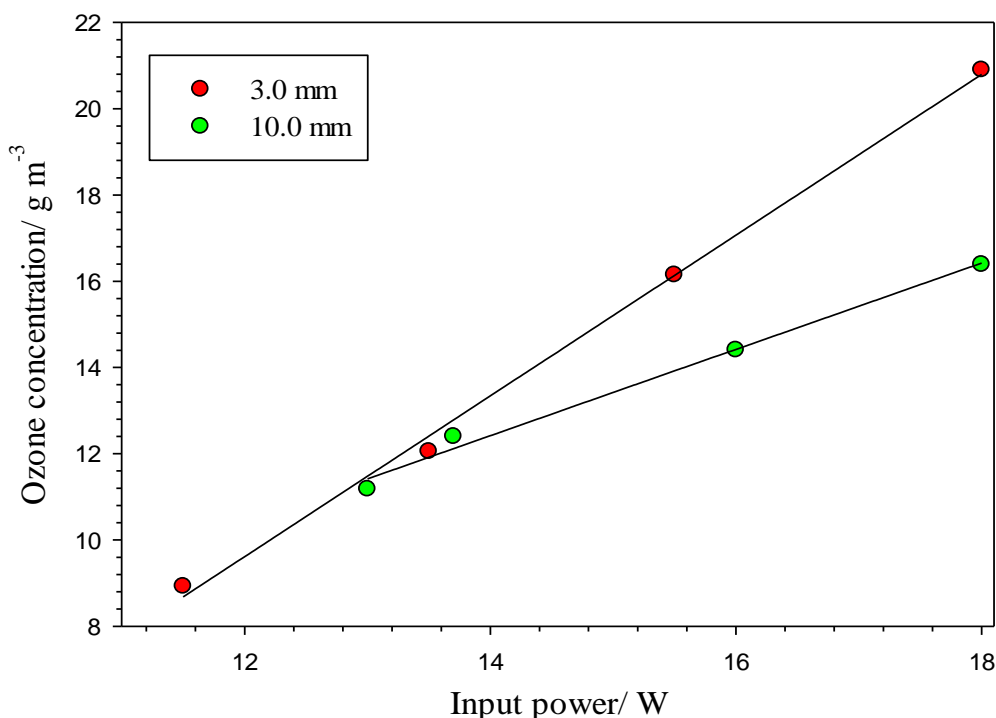


Figure 4.4. Plots of ozone concentration as a function of input power and the discharge B2 cell divider thickness. Oxygen flow rate $1.0 \text{ dm}^3 \text{ min}^{-1}$ and coolant temperature $5.0 \text{ }^\circ\text{C}$ using 1.0 mm thick perforated sheets of PTFE (D6) as the dielectric.

4.2.3. The effect of dielectric packing gap width on ozone generation

The gap widths between the HV and supporting electrodes control a number of parameters, including the thickness of filling, packing geometry, void shape and size, angles and number of contact points between the dielectrics. These parameters are expected not only to determine the plasma properties [5-9], but also the effectiveness of heat transfer [10-12] (see section 1.3.2) and consequently the overall performance of the DBD-PBR. Figure 4.5 shows the effect of varying the packing gap width for the dielectric (PGWD), i.e. the gaps between the supporting and HV electrodes in cell B2, on ozone generation using different dielectrics. As can be seen from the figure, the effect of varying the PGWD on ozone generation depends on the dielectric; for instance the highest ozone concentration using the dielectric D1 was observed at PGWDs of 2 and 3 mm, decreasing at 4 mm. However, in the case of dielectrics D2, D3 and D5, the highest ozone concentration was observed at 3 mm, while a small enhancement was observed using the 4 mm gap compared to the 3 mm gap in the case of

D4. From these results, it is clear that the optimal PGWD varied with the shape and diameter of the dielectric, and it was estimated to be $1\times$ and $1.5\times$ the dielectric diameter for the cylindrical and spherical dielectrics, respectively.

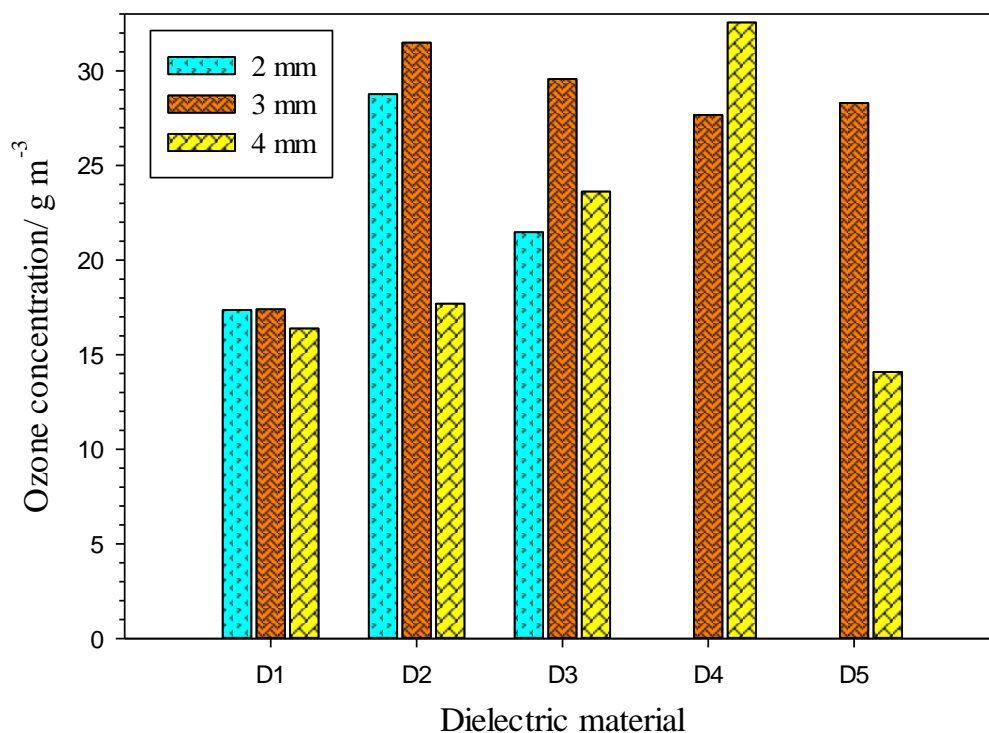


Figure 4.5. Ozone concentrations as a function of the dielectric type and packing gap width. The dielectrics employed were (D1) 2 mm alumina pellets (D2) 2 mm borosilicate glass beads, (D3) 2 mm A3 molecular sieve, (D4) 3 mm Soda-Lime glass beads and (D5) 3 mm alumina pellets. Using the B2 arrangement at an input power of 35W, coolant temperature of 5 °C and oxygen flow rate of $1.0 \text{ dm}^3 \text{ min}^{-1}$.

Other parameters that may play important roles in determining the optimal dielectric packing gap width are the electric field strength and the thermal conductivity of the dielectric. For instance, when the PGWD is equal to the dielectric diameter all of the dielectric beads or pellets would be expected to touch the HV electrode surface. Hence, the strength of the electric fields between the beads and the HV electrodes (i.e. surface discharge, SD) and within the voids between beads (i.e. volume discharge, VD) increased [13-15]. However, the increase in SD would be expected to increase the temperature of the dielectric surface [16, 17], see section 1.2.6. Therefore, the benefits obtained from enhancing the dielectric contact

with the HV electrode on ozone generation may be expected to be reduced by heat formation. Thus, it may be reasonable to assume that dielectrics with high thermal conductivity would be less affected by heat formation, and hence ozone production is mainly determined by the electric field strength. The results showed in fig. 4.5 agreed well with this assumption. From the figure, it can be seen that the highest ozone concentrations observed using D1 and D5 (i.e. the highest in thermal conductivity) were at the narrowest PGWD. Whilst, in the case of D2, D3, and D4 (i.e. low thermal conductivity) ozone production was determined by the electric field strength and heat formation, and hence the optimal PGWD was increased.

Figures 4.6 and 4.7 show plots of ozone concentration as a function of oxygen flow rate and the PGWD using 2 mm borosilicate glass beads (D2) and 3 mm alumina pellets (D5), respectively. As can be seen from fig. 4.6, the effect of varying the PGWD on ozone concentration increased with reducing oxygen flow rate from 1.0 to 0.06 dm³ min⁻¹. Within this range the concentration of ozone increased in the order: 3 mm > 2 mm > 4 mm. However, at oxygen flow rates > 1.0 dm³ min⁻¹, similar amounts of ozone were produced at PGWD of 3 mm and 2 mm while the lowest concentrations were observed at 4 mm. Therefore, it is reasonable to assume that increasing the feed gas flow rate reduced the temperature of the dielectric surface (i.e. convective cooling), and hence depress the negative effect of the low thermal conductivity of D2. As a result, similar ozone concentrations were observed at PGWD of 2 and 3 mm. However, the low ozone concentration observed at the PGWD of 4 mm may be attributed to the weaker electric field compare to those at PGWD of 2 and 3 mm, and hence was the least efficient over the oxygen flow rates investigated. From fig. 4.7 it can be seen that by reducing the packing gap from 4 mm to 3 mm, the concentration of ozone increased from 29 to 79 g m⁻³ at an oxygen flow rate of 0.06 dm³ min⁻¹. However, this enhancement decreased with increasing oxygen flow rate until it disappeared above 10 dm³ min⁻¹. This behaviour may be attributed to the high thermal conductivity of D5 which enhances the removal of heat from the dielectric and hence resulted in the ozone concentration being determined primarily by the electric field strength.

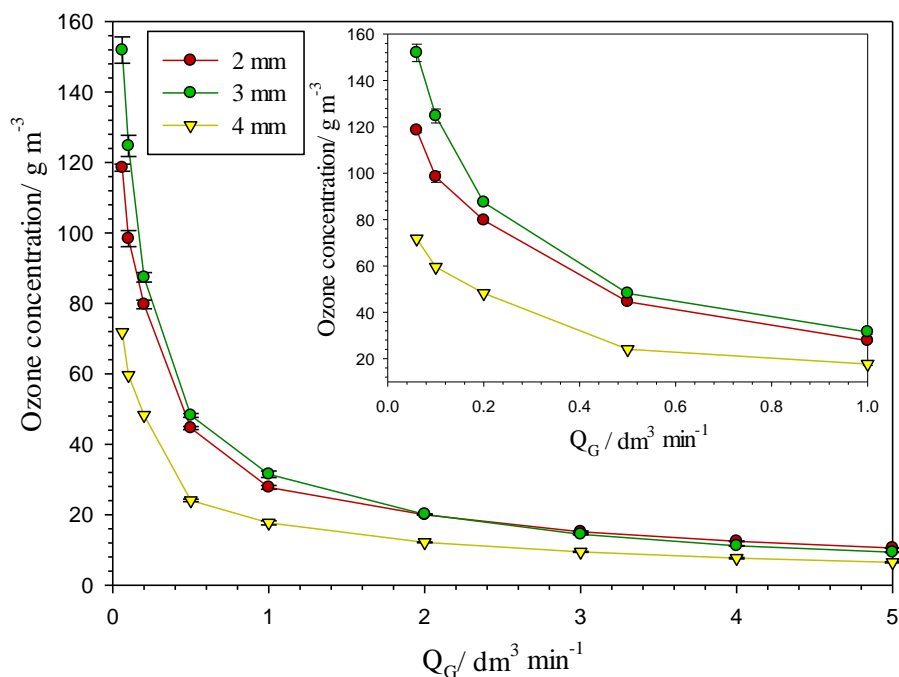


Figure 4.6. Plots of ozone concentrations as a function of oxygen flow rate and dielectric packing gap width. The dielectric employed was 2 mm borosilicate glass beads (D2), using the cell B2 at an input power of 35W and coolant temperature of 5 °C.

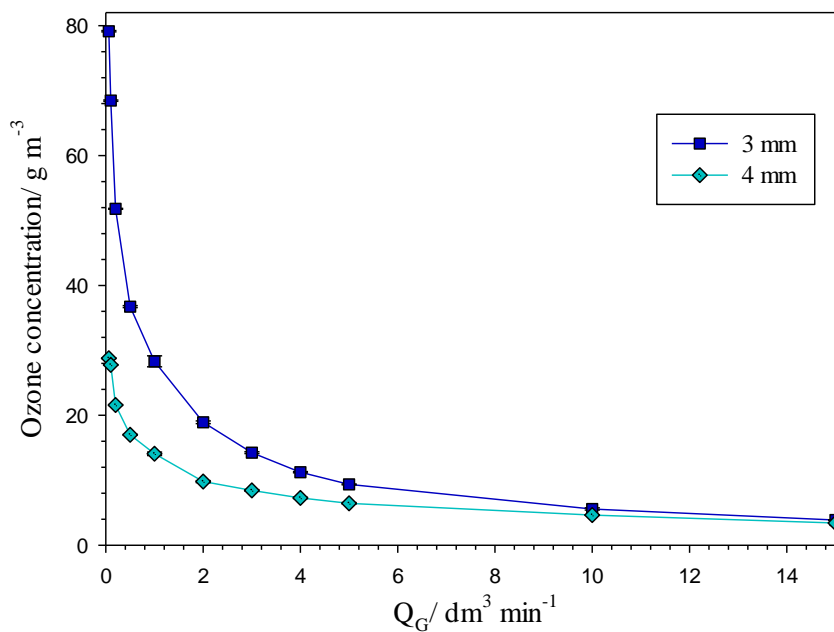


Figure 4.7. Plots of ozone concentrations as a function of oxygen flow rate and the packing gap width of the dielectric (PGWD). The dielectric employed was 3 mm alumina pellets (D5), using cell B2 at an input power of 35W and coolant temperature of 5 °C.

4.2.4. The effect of dielectric material on ozone generation

The effect of dielectric type and shape on ozone generation was investigated as a function of oxygen flow rate employing cell B2, and the results are shown in fig. 4.8. As can be seen from the figure, regardless of the dielectric employed, the concentration of ozone was found to increase as the oxygen flow rate decreased. This may be attributed to the increase in the specific energy density (SED, J cm^{-3}), see section 3.2.4. In addition, from fig. 4.8, it can be seen that the effect of dielectric type on ozone generation was more pronounced at flow rates from 0.06 to $0.5 \text{ dm}^3 \text{ min}^{-1}$ while it was less important at higher flow rates. This may be attributed to the higher residence time at low flow rates which allows better interaction between the feed gas and the surface of the dielectric. It should be noted that the experiments in fig.4.8 were carried out at the optimal packing gap width of each dielectric (PGWD) discussed in section 4.2.3.

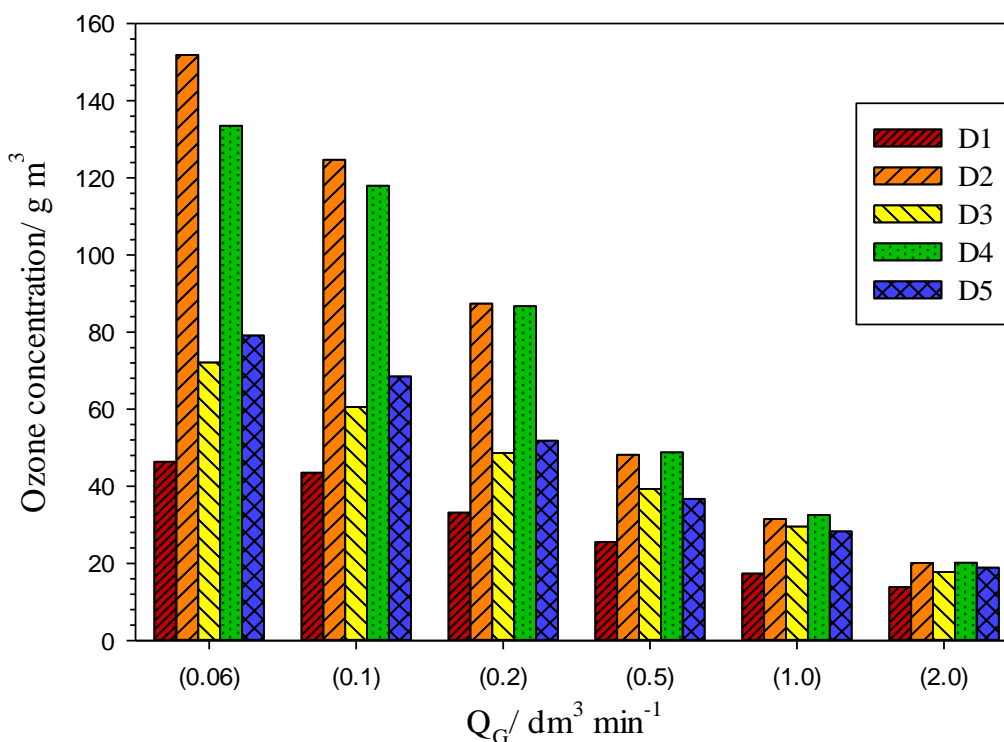


Figure 4.8. Ozone concentration as a function of oxygen flow rate using cell B2 packed with: 2 mm alumina pellets (D1), 2 mm borosilicate glass beads (D2), 2 mm A3 molecular sieve (D3), 3 mm Soda-Lime glass beads (D4) and 3 mm alumina pellets (D5). The packing gap width of the dielectric (PGWD) were 2 mm for D1, 3 mm for D2, D3 and D5, and 4 mm for D4. Using the cell B2; input power was 35W at a coolant temperature of 5.0 °C.

On the basis of the results shown in fig. 4.8, the effectiveness of the dielectrics for ozone generation from oxygen at flow rates $0.06 - 0.5 \text{ dm}^3 \text{ min}^{-1}$ increased in the order: 2.0 mm glass beads (D2) > 3.0 mm Soda-Lime glass beads (D4) > 3.0 mm Al_2O_3 pellets (D5) > 2.0 mm A3 molecular sieve (D3) > 2.0 mm Al_2O_3 pellets (D1). Thus it can be concluded that, regardless of the size of the dielectric, the spherical dielectrics were more efficient for ozone generation from oxygen than the cylindrical pellets. This in contrast to Chen et al. [5], who reported the order: 2.0 mm Al_2O_3 pellets > 3.0 mm Al_2O_3 > 3.0 mm glass beads > 2.0 mm glass beads. This disagreement may be attributed to the differences in reactor arrangements. Their reactor was a conventional DBD-PBR, consisting of a glass tube filled with dielectric beads or pellets with a 2.0 mm HV stainless steel rod electrode passed at the axis of the tube, and copper foil HV electrode wrapped around the external wall of the tube. The gap between the inner electrode and the internal surface of the glass tube was 12.0 mm, with no cooling system. Thus, it does not seem unreasonable to postulate that, in the absence of effective cooling, the thermal conductivity of the dielectric was the most important parameter determining ozone generation. Hence, the observed order of the dielectric reported by Chen et al. was in accord with the higher thermal conductivity of alumina compared to glass beads.

From fig. 4.8, the higher ozone concentration observed using smaller glass beads over the larger one may be attributed to the higher number of contact points between the beads and the beads with the HV electrodes [5, 7]. Even though the alumina pellets possessed a higher thermal conductivity than the glass beads, they were found to be less effective for ozone production from oxygen. Furthermore, the larger alumina pellets were more efficient than the smaller ones. This behaviour suggests that thermal conductivity was not the most important factor when using a cooling system, and the electrical properties of the dielectric were expected to play the major role in determining the efficiency of ozone production. In general, alumina has a higher dielectric constant (i.e. 8.5-10) than glass beads (i.e. 4-6) and on the basis of equation 1.5 discussed in section 1.3.1 (see p.14):

$$C_d = \epsilon_r \times \epsilon_0 A/d \quad (1.5)$$

where C_d is the dielectric capacitance (F), ϵ_r is the dielectric constant, ϵ_0 is vacuum permittivity ($8.854 \times 10^{-12} \text{ F m}^{-1}$), A and d were the dielectric area (m^2) and thickness (m), respectively; it is clear that the capacitance of dielectric increases with the dielectric constant and surface area and decreases with thickness. Thus, alumina pellets with smaller diameter

possessed higher capacitance than the larger ones, and hence more current would be expected to be delivered by the micro-discharges [1, 18, 19], see sections 1.3.1. As a result, the discharge voltage and the efficiency of ozone production decreased [1, 18-20].

It is important to note that the highest ozone concentration observed in this work (i.e. 152 mg dm³) was ca. 2.5 times higher than the maximum ozone concentration reported in the literature to date using the conventional DBD-PBR [5]. Therefore, it is clear that the novel DBD-PBR employed in this work was significantly more efficient for minimising the negative effects of heat on ozone generation that are normally encountered when using conventional DBD-PBRs.

4.2.5. Input power effect

Figure 4.9 shows plots of ozone concentration as a function of input power and dielectrics using the cell B2. As can be seen from the figure, regardless the type of dielectric employed, the concentration of ozone increased linearly with input power, with the possibility of still higher ozone concentrations at higher power. However, for safety reasons, the input power was not increased beyond 35W. The observed increase in ozone concentration with the input power may be attributed to the increase in the number of electrons with sufficient energy for oxygen dissociation [5-7, 18, 21]. Apart from D1 that showed the slowest rate of ozone concentration increase with input power, no significant variation was observed with the other dielectrics. This may be attributed to the lower contribution of the dielectric type and shape on ozone generation at feed gas flow rates of 1.0 dm³ min⁻¹, as discussed above.

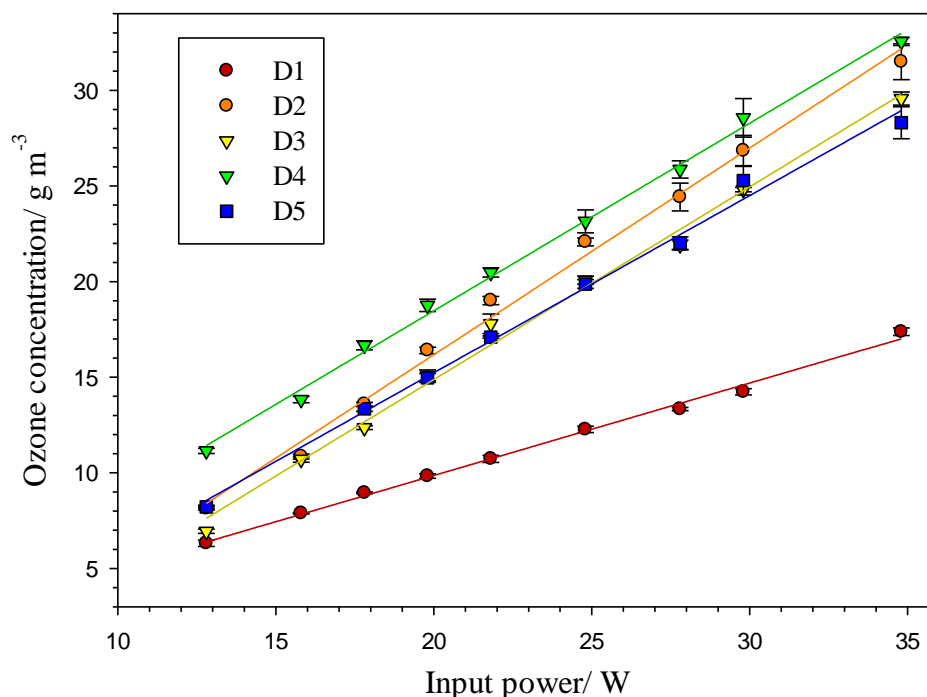


Figure 4.9. Plots of ozone concentration as a function of input power using cell B2 packed with: 2 mm alumina pellets (D1), 2 mm borosilicate glass beads (D2), 2 mm A3 molecular sieve (D3), 3 mm Soda-Lime glass beads (D4) and 3 mm alumina pellets (D5). The packing gap widths of the dielectric (PGWD) were same as those in fig. 4.8. The cell was fed with oxygen at $1.0 \text{ dm}^3 \text{ min}^{-1}$, and the coolant temperature was $5.0 \text{ }^\circ\text{C}$.

4.2.6. Ozone yield efficiency

The yield efficiency (η , g/kWh) of ozone was determined using equation 1.2 (see section 1.2.6, p.12):

$$\eta = C Q / P \quad (1.2)$$

where C is the ozone concentration (g dm^{-3}), Q is flow rate ($\text{dm}^3 \text{ h}^{-1}$), and P is input power (kW). Figure 4.10 shows the ozone yield efficiency as a function of input power and dielectric from the data shown in fig. 4.9. As can be seen from the figure, the yield efficiency increased with the input power up to ca. 22 - 25 W, depending on the type of the dielectric. At higher input power, the yield efficiency remained almost constant along the input power range investigated and regardless of the dielectric type. This behaviour may be understood on the basis that these experiments were carried out at a fixed oxygen flow rate, and the

change in yield efficiency was primarily determined by the change in ozone concentration. Thus, the observation of a steady state in yield efficiency suggests that the rate of ozone production with the input power was constant. This is not in agreement with the behaviour normally observed using conventional DBD-PBRs in which the yield efficiency decreases with increasing input power as a result of heat formation [22, 23].

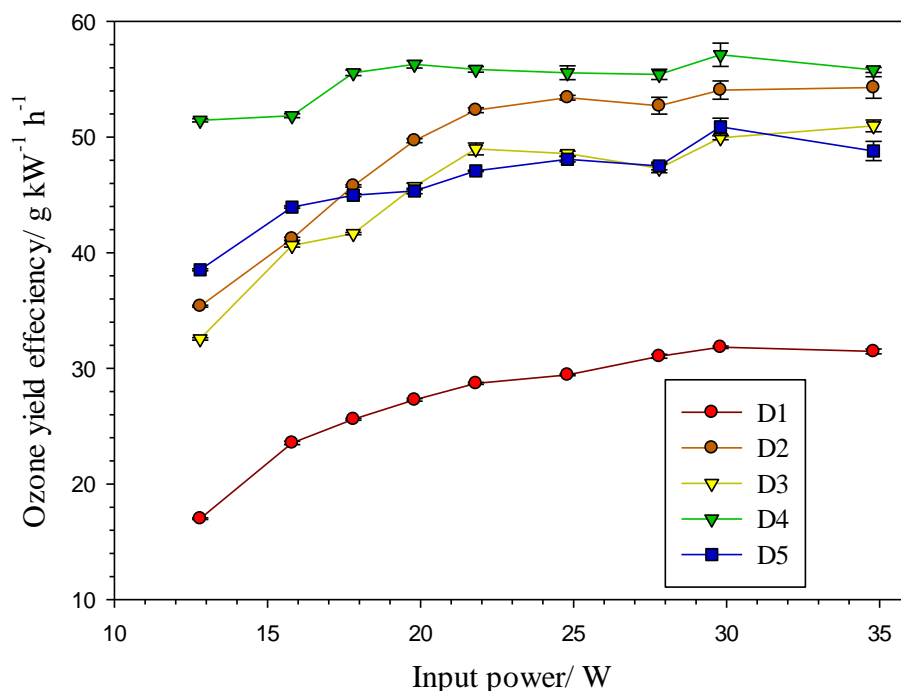


Figure 4.10. Plot of ozone yield efficiency as a function of input power and dielectric from the data in fig. 4.9. Cell B2 was packed with: 2 mm alumina pellets (D1), 2 mm borosilicate glass beads (D2), 2 mm A3 molecular sieve (D3), 3 mm Soda-Lime glass beads (D4) and 3 mm alumina pellets (D5). The packing gap widths of the dielectric were same as those in fig. 4.8. The cell was fed with oxygen at $1.0 \text{ dm}^3 \text{ min}^{-1}$, and the coolant temperature was $5.0 \text{ }^\circ\text{C}$.

Figure 4.11 shows plots of the yield efficiency as a function of oxygen flow rate and dielectric at a constant input power. As can be seen from the figure, the yield efficiency increased with increasing oxygen flow rate from 0.06 to $15.0 \text{ dm}^3 \text{ min}^{-1}$, and no steady state was observed. In addition, apart from D1, the effect of the type of dielectric on ozone yield efficiency decreased with increasing the flow rate from 0.06 to $2.0 \text{ dm}^3 \text{ min}^{-1}$, and became negligible at $3 \text{ dm}^3 \text{ min}^{-1}$ or higher. This behaviour can be attributed to the lower dependence

of ozone generation on the type of dielectric at high flow rates as discussed in section 4.2.4. The highest ozone yield efficiencies were obtained at $15 \text{ dm}^3 \text{ min}^{-1}$, of: 86, 98, 97, 94 and 100 g kW h^{-1} using D1, D2, D3, D4 and D5, respectively. The increase in yield efficiency with the feed gas flow rate is normally observed with DBDs [23-25]. Some authors attribute this behaviour to the reduction of heat-induced ozone decomposition by lowering the residence time of ozone within the discharge region [23, 24]. Others consider the same behaviour to be induced by lowering the discharge energy density, and hence the rate of ozone decomposition through collisions with electrons [26] or interaction with atomic oxygen radicals [21, 22].

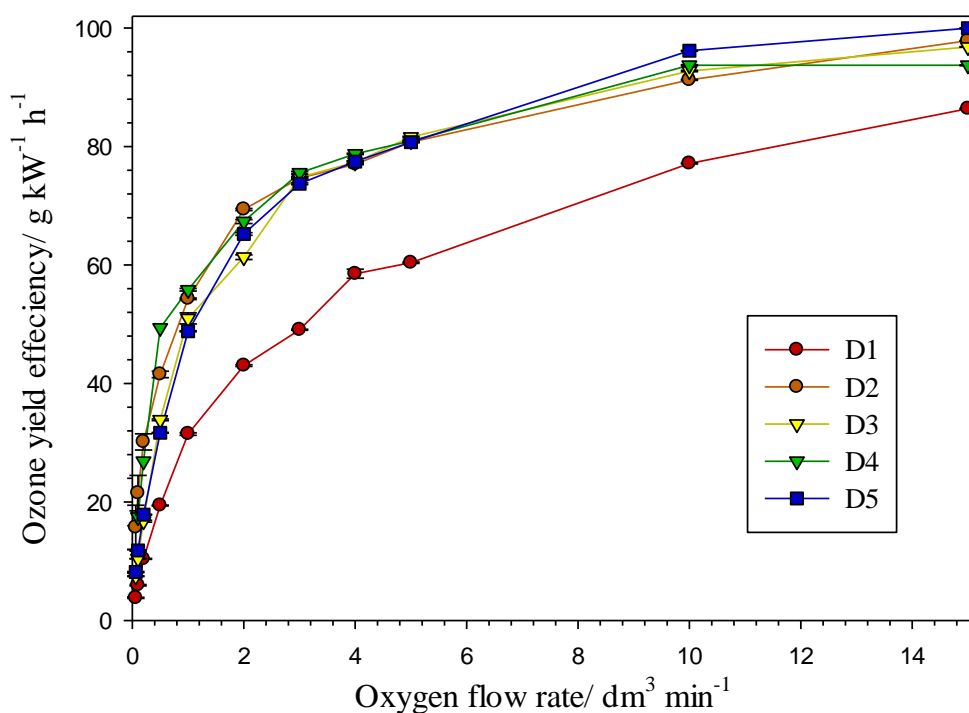


Figure 4.11. Plots of ozone yield efficiency as a function of oxygen flow rate and dielectric material using cell B with 2 electrode configuration and a dielectric thickness of 3.0 mm. The input power was 35W and coolant temperature was 5.0 °C.

During this work it was observed that increasing the feed gas flow rate enhanced ozone production from air by cooling down the DBD-PBR, as will be discussed in section 4.2.9. From figs. 4.8, 4.9, 4.10 and 4.11 it is clear that the highest ozone yield efficiencies and

ozone concentration cannot be maintained under the same experimental conditions of input power and feed gas flow rate. In fact, this behaviour is generally observed [5, 25-27]. In addition, the discharge cell arrangement [24, 25, 27, 28,] and dielectric type [5, 6, 23, 29] play important roles on determining the discharge power characteristics, and hence the yield efficiency. Figure 4.12 shows plots of ozone concentration as a function of SED observed using cells A2 and B2 at oxygen flow rates of 10, 15 and 20 dm³ min⁻¹. The ranges of the input power for the cells A2 and B2 were 2 - 20W and 13 - 30 W, respectively. As can be seen from the figure, regardless of the cell arrangement and oxygen flow rate, there were clear linear relationships between ozone concentration and specific energy density (SED). The regression coefficients and slopes of the plots are summarized in table 4.1. From table 4.1, it can be seen that the slopes of ozone concentration vs. SED obtained from the cell A2 were, on average, ca. 29% lower than those from B2. In fact, this value agrees well with the

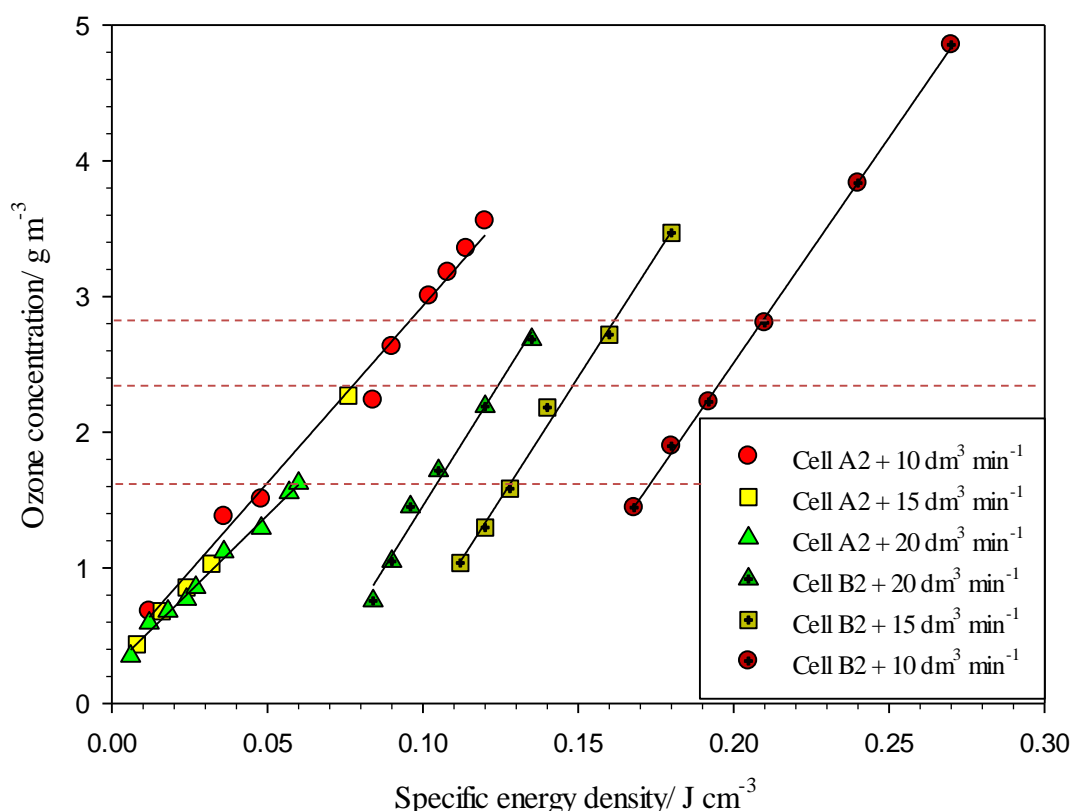


Figure 4.12. Plots of ozone concentration as a function of specific energy density, cell arrangement and oxygen flow rate. All experiments were carried out using 2 mm glass beads (D2) and a fixed packing gap width of 2 mm. The coolant temperature was 5.0 °C. The dashed red lines were added for comparison purposes, see text for more details.

Plot	R ²	Slope/ g cm ³ J ⁻¹ m ⁻³
(i)	0.986	26.1
(ii)	0.998	26.8
(iii)	0.992	22.5
(iv)	0.983	36.7
(v)	0.994	35.8
(vi)	0.999	33.2

Table 4.1. R² coefficients and slopes of the plots in fig. 4.12.

results discussed in section 4.2.1. The dashed red lines in fig. 4.12 were added to show the SED required for each cell to reach a fixed ozone concentration. From the figure, it is clear that the SED required for producing a specific concentration of ozone using cell A2 was much lower than that required using B2. In addition, as the flow rate of oxygen increased, the SED required for producing a particular ozone concentration decreased when cell B2 was employed and this effect was not observed with cell A2.

Figure 4.13 shows plots of ozone yield efficiency vs. SED obtained from the data in fig. 4.12. As can be seen from the figure, the yield efficiency varied with the SED depending on the cell employed. With cell A2, the highest yield efficiencies at flow rates of 10, 15 and 20 dm³ min⁻¹ were 204, 196 and 209 g kW⁻¹ h⁻¹, respectively. These efficiencies were observed at specific energy densities of 0.012, 0.008 and 0.006 J cm⁻³ and flow rates 10, 15 and 20 dm³ min⁻¹, respectively. Interestingly, the average of these yield efficiencies was ca. 15% higher than the best efficiency attained using the conventional DBD-PBRs (i.e. 173 g kW⁻¹ h⁻¹) reported by Chen et al. 2006 [5]. On the other hand, the highest yield efficiencies obtained using cell B2 at flow rates of 10, 15 and 20 dm³ min⁻¹ were 98, 105 and 108 g kW⁻¹ h⁻¹, respectively. It should be noted that the input power measurements account for the total power consumed by the whole system, and hence higher yield efficiencies may be expected if the only discharge power is considered.

From fig. 4.13 it can be seen that the yield efficiencies attained using cell A2 were ca. 2 × higher than that using B2 under similar conditions of oxygen flow rate and coolant temperature. In fact, this difference in yield efficiency between A2 and B2 was more than the 30% variation in ozone concentration discussed in section 4.2.1. Thus, it does not seem

unreasonable to postulate that, in addition to the variation in ozone concentration, there were one or more factors that caused the lower efficiency of B2 than A2. One possible factor was the variation in the discharge voltage that may be affected by the cell arrangement [19]. Therefore, monitoring the discharge voltage was expected to allow a better understanding of the discharge environments developed in A2 and B2, and hence the variation in the yield efficiency.

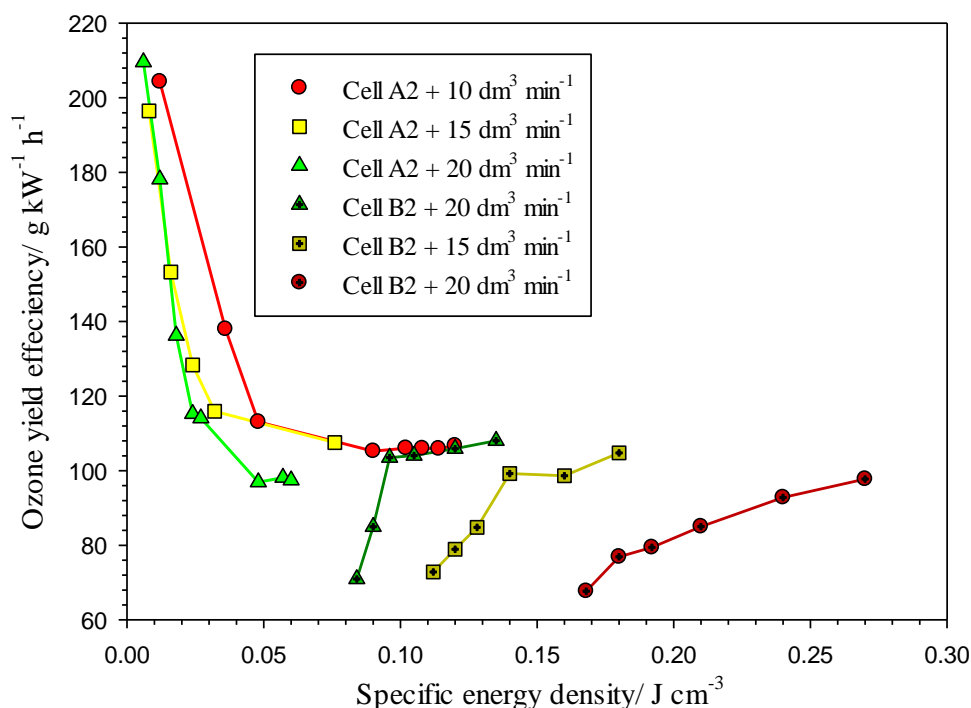


Figure 4.13. Plots of ozone yield efficiency as a function of specific energy density, cell arrangement and oxygen flow rate. Using 2 mm glass beads (D2). The coolant temperature was 5.0 °C.

4.2.7. Cell arrangement and discharge power characteristics

Figure 4.14 shows plots of discharge voltage profiles obtained from the cells A2 and B2 at different input power from the onset levels. As can be seen from the figure, the discharge voltage profile varied with the cell arrangement. With cell A2, the discharge voltage increased linearly with input power from the onset to the maximum output of the HV transformer of 10kV at 20 W after which the discharge V did not change. In the case of B2,

the discharge voltage profile revealed two linear regions: (I) increasing from 8.6 to 9.5 kV with input power from 13 to 24 W and (II) increasing from 9.5 to 10kV with input power from 24 to 35 W, but with a lower slope than (I). From the figure, it can be seen that the onset discharge voltage and input power for the cell A2 were ca. 1.0 kV (i.e. 13%) and 10 W lower than B2, respectively. In addition, the slope of the discharge voltage vs. the input power obtained from the cell A2 in region (I) was ca. 83% higher than that from B2. Therefore, it does not seem unreasonable to postulate that the higher efficiency observed with cell A2 is associated with effective power conversion to the discharge voltage compared to B2. This variation in the discharge voltage may be understood on the basis of Manley's equation discussed in section 1.3.1 (see eq.1.3, p.14). According to the equation, at a constant input power and frequency, increasing the capacitance of the dielectric increases the current and lowers the voltage of the discharge power. Therefore, the lower discharge voltage observed in the case of B2 may be attributed to the larger area of the dielectric surface (i.e. 30%) than in A2.

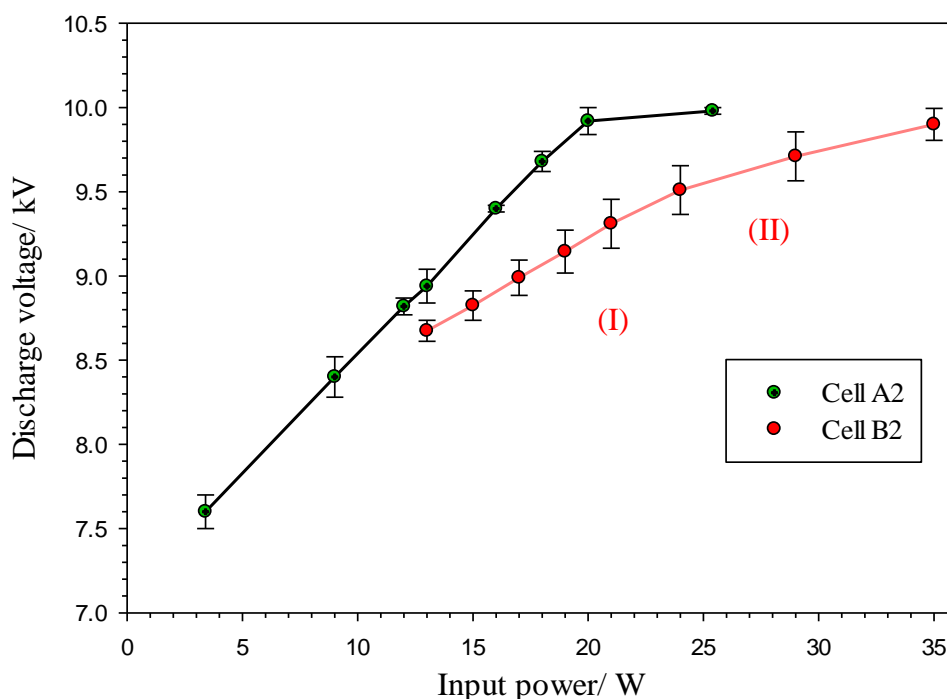


Figure 4.14. Plots of discharge voltage as a function of input power and cell arrangement. The oxygen flow rate was $1.0 \text{ dm}^3 \text{ min}^{-1}$, using 2 mm glass beads for packing with PGWD of 2.0 mm, and coolant temperature $5.0 \text{ }^\circ\text{C}$. The uncertainty in the discharge voltage measurement was $\pm 0.2 \text{ kV}$.

It is important to highlight that plasma glow was observed between the HV electrodes and the internal wall of the cell B2 when it was operated using air as a feed. This may be taken as evidence of the involvement of the surface of the internal wall of the cell in plasma formation as a dielectric, and hence the total capacitance of the cell B2 would be expected to be higher than that from the packing dielectric. However, in the case of the cell A2 the HV electrodes were separated from the cell wall by sheets of PTFE as shown in figs. 4.1 and 4.2. Therefore, considering the higher dielectric constant of the cell wall (i.e. borosilicate = 4 - 6) and the 30% excess in the HV electrodes surface in the case of B2 compared to the PTFE sheets in A2 (ca. 2.1), the total dielectric capacitance of B2 was estimated to be 90% higher than A2. Therefore, it is possible that the lower yield efficiency obtained using B2 compared to A2 was due to the higher dielectric capacitance of the former.

4.2.8. Ozone generation from air

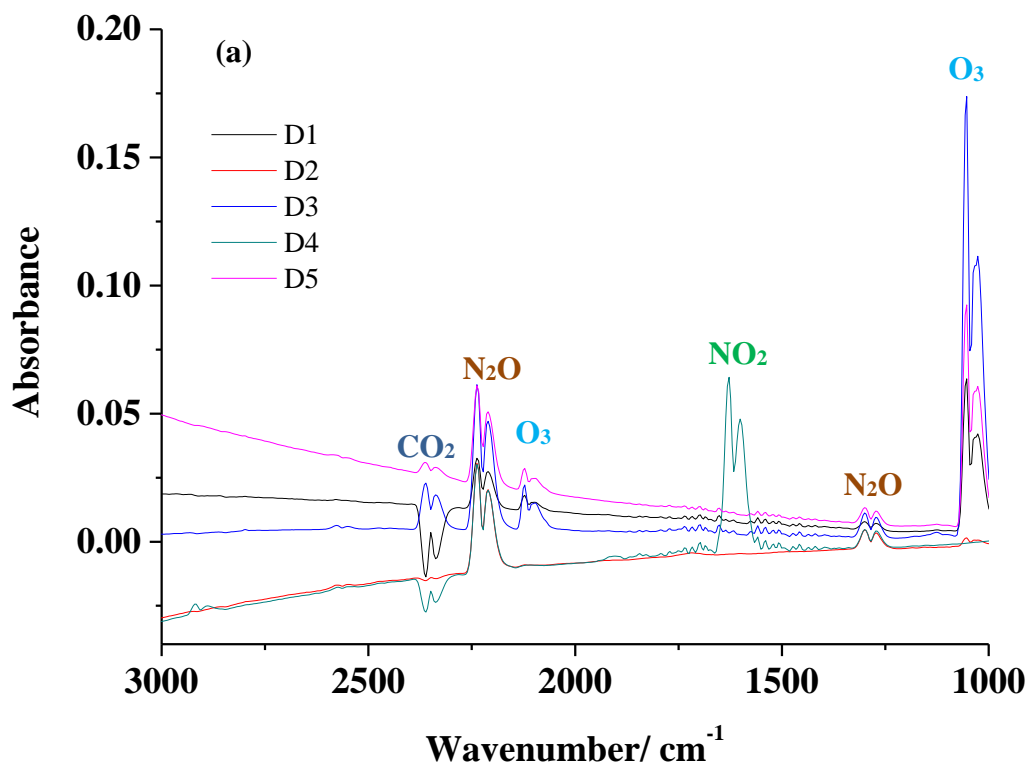
Ozone generation from air may be favoured in some applications from an economical point of view simply because air is freely available. However, several challenges are always encountered during this process such as the low ozone concentration and the formation of NO_x by-products. It was shown in sections 3.2.5 and 3.3.2 that the formation of NO_x can affect ozone generation in three different ways: (i) compete with oxygen for energetic electrons which lowers the rate of oxygen dissociation and, subsequently, ozone generation, (ii) accelerate the decomposition of ozone through its reactions with N, NO and NO₂, and (iii) consume atomic oxygen required for ozone generation in NO_x formative reactions.

From the experimental results reported in section 3.2.5, it was concluded that the formation of HNO₃ and HNO₂ from air can be avoided using dry air, while the formation of other NO_x by-products can be controlled by effective cooling of the ozone generator. In this section ozone generation from air was investigated using cell B2. Ambient air was passed through freshly activated silica gel to maintain the relative humidity $\leq 0.6\%$. The concentrations of ozone and other by-products were monitored using FTIR spectroscopy to ensure the accuracy of ozone measurements, see section 3.3.4.

Figures 4.15(a) and (b) show FTIR spectra collected from the exhausts of the cell B2 fed with dried ambient air at 0.06 dm³ min⁻¹, input power of 35W and coolant temperature of 5 °C using dielectrics D1-D5. As can be seen from the figure, the chemical composition of the exhaust varied with the dielectric employed. Under these experimental conditions, the 2.0

mm Al_2O_3 pellets (D1), 2.0 mm spherical A_3 molecular sieve (D3) and 3.0 mm Al_2O_3 (D5) were more efficient for ozone production than the 2.0 mm glass beads (D2) and 3.0 mm Soda-Lime glass beads (D4). In addition, while the only products observed using D1, D2, D3, and D5 were N_2O and ozone, significant amounts of NO_2 and N_2O , some NO and very small amount of ozone were observed using D4. Table 4.2 shows the concentrations of O_3 , N_2O and NO_2 as a function of dielectric determined from the data shown in figs. 4.15(a) and (b). As can be seen from the table, the concentration of ozone increase in the order: $\text{D3} > \text{D5} > \text{D1} > \text{D4} > \text{D2}$. The highest ozone concentrations were observed using D3 with a maximum of 15.6 g m^{-3} at $0.06 - 0.1 \text{ dm}^3 \text{ min}^{-1}$.

Apart from D3, it was clear from the dielectric order that alumina dielectrics were more efficient than glass beads, and this may be attributed to the higher thermal conductivity of the former. In addition, regardless the type of the dielectric, the dielectrics with higher diameters were more efficient than the small ones. Therefore, it can be concluded that the production of ozone from air at low flow rates correlates proportionally with the thermal conductivity and inversely with the capacitance of the dielectric. This behaviour agrees with the positive effect of the dielectric thermal conductivity proposed by Teranishi and co-



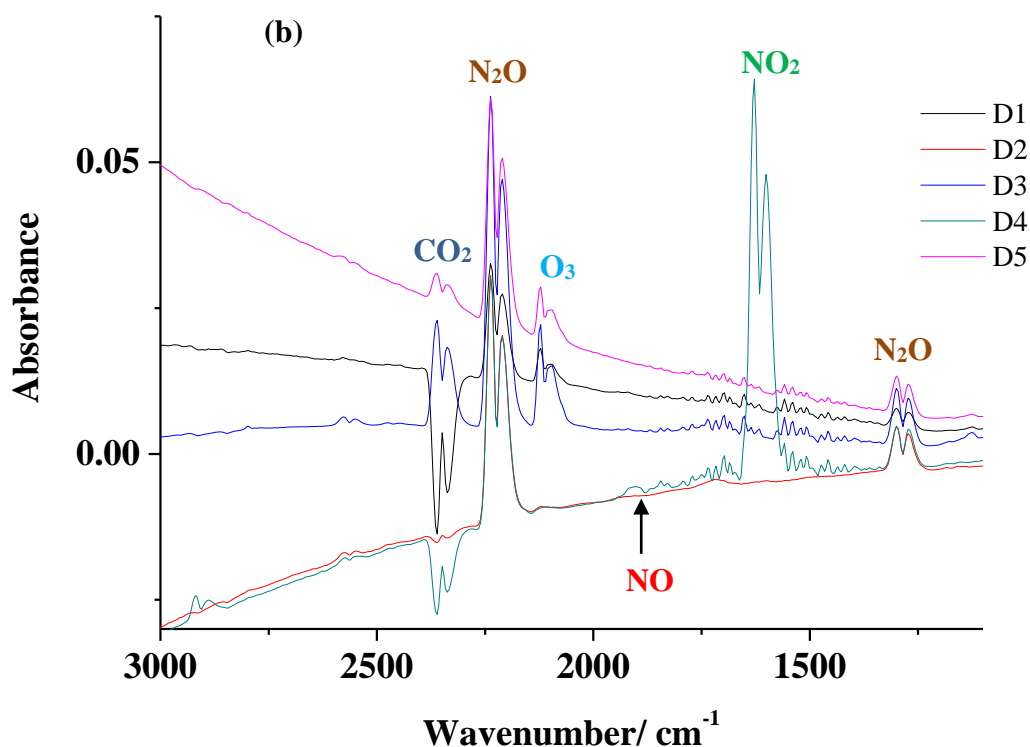


Figure 4.15. (a) FTIR spectra collected of the exhaust from cell B2 after running the DBD-PBR for 30 minutes as a function of dielectric type. (b) The spectra in (a) replotted to show the gain features more clearly. Each spectrum was ratioed to its reference spectrum collected with no input power. The feed gas was dried ambient air at $RH \leq 0.6\%$, input power 35W, gas flow rate $0.06 \text{ dm}^3 \text{ min}^{-1}$ and coolant temperature $5.0 \text{ }^\circ\text{C}$.

Dielectric	[NO ₂]/ mg dm ⁻³	[N ₂ O]/ mg dm ⁻³	[O ₃]/ mg dm ⁻³
D1	BDL	0.6	4.9
D2	BDL	1.4	0.5
D3	BDL	1.9	15.6
D4	3.6	1.4	0.8
D5	BDL	1.2	7.8

Table 4.2. The concentrations of O₃, N₂O and NO₂ as a function of dielectric calculated from the data shown in figs. 4.15(a) and (b). BDL = below detection limit.

workers [3] and the negative effect of the dielectric constant of the dielectric observed by Sung and Sakoda [27].

Figure 4.16 shows a chart of ozone concentration as a function of air flow rate and dielectric type at a fixed input power of 35W and coolant temperature of 5.0 °C. As can be seen from the figure, the effectiveness of the dielectric toward ozone production varied with the flow rate, eg. at flow rates of 0.06 and 0.1 dm³ min⁻¹ the order was: D3 > D5 > D1 > D4 > D2. As the flow rate increased from 0.1 dm³ min⁻¹ to 1.0 dm³ min⁻¹, the effectiveness of D2 and D4 increased rapidly, changing the order to D3 > D4 > D5 > D2 > D1. However, at higher flow rates the effectiveness of all dielectrics became similar and agreed with the behaviour observed using oxygen and discussed in section 4.2.4. Therefore, it is clear that the effects of thermal conductivity and the dielectric capacitance of the dielectric on ozone production from air decreased with increasing the feed gas flow rate. This behaviour agrees well with

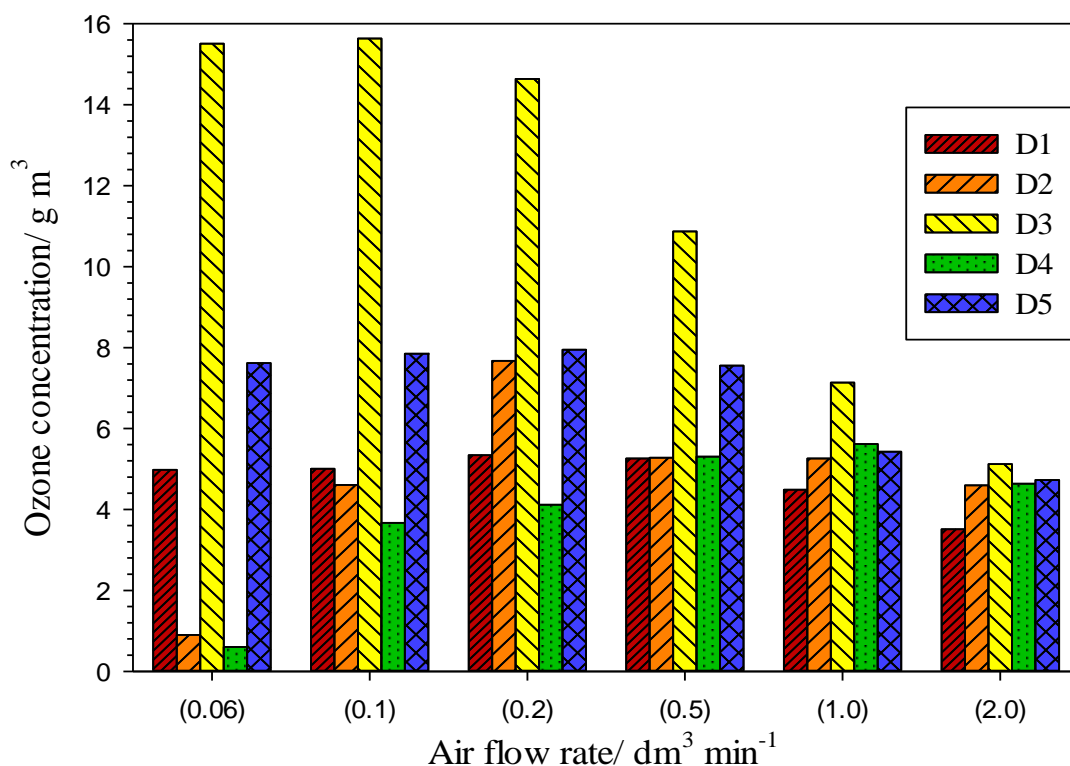


Figure 4.16. Ozone concentration as a function of air flow rate using the dielectrics: 2 mm alumina pellets (D1), 2 mm borosilicate glass beads (D2), 2 mm A3 molecular sieve (D3), 3 mm Soda-Lime glass beads (D4) and 3 mm alumina pellets. The packing gap width of the dielectric (PGWD) were 2 mm for D1, 3 mm for D2, D3 and D5, and 4 mm for D4, input power of 35W at coolant temperature of 5.0 °C, monitored using FTIR spectroscopy.

that observed by Teranishi and co-workers [3], who showed that the effect of thermal conductivity on ozone generation decreased with the flow rate from $0.3 \text{ dm}^3 \text{ min}^{-1}$, becoming negligible at $1.5 \text{ dm}^3 \text{ min}^{-1}$. The same authors have attributed this behaviour to lower heat formation at high flow rates due to the reduction of the discharge SED. Further details on the system employed by Teranishi et al. [3] were presented in section 1.3.3. The difference in the order of dielectric performance observed during ozone generation from air and oxygen may be attributed to the significant effects of heat formation on air plasma chemistry, discussed in sections 3.2.5 and 3.3.2.

4.2.9. Coolant temperature effect

It is well known that the rate of ozone decomposition increases with temperature. Hence, the effects of the coolant temperature and feed gas flow rate (i.e. convective heat transfer) on ozone generation from oxygen and air were investigated to evaluate the contribution of these two parameters on the performance of cell B2. Figure 4.17 shows plots of ozone concentration as a function of dielectric and coolant temperature using oxygen as a feed gas. As can be seen from the figure, the concentration of ozone declined as the coolant temperature increased. In general, the concentration of ozone decreased by 12-27% and 33-48% as the coolant temperature increased from 5 to 20 and 50 °C, respectively. Even though, these results were obtained at a fairly high oxygen flow rate of $1.0 \text{ dm}^3 \text{ min}^{-1}$, the effect of the coolant temperature on ozone production was clearly significant.

Figures 4.18(a), (b), (c) and (d) show FTIR spectra collected from the exhaust of cell B2 packed with D2 and fed with dried ambient air at an input power of 35W as a function of feed gas flow rate and at a coolant temperature of 50, 30, 10 and 5 °C, respectively. The concentrations of NO_2 , N_2O and O_3 were obtained from the spectra shown in figs. 4.18(a), (b), (c) and (d) and are summarised in table 4.3. As can be seen from fig. 4.18(a) and table 4.3, at the highest coolant temperature of 50 °C and an air flow rate of $0.06 \text{ dm}^3 \text{ min}^{-1}$, no ozone was produced, and significant amounts of NO_2 and some NO and N_2O were observed. From the same figure and table, it can be seen that, as the flow rate increased to $0.1 \text{ dm}^3 \text{ min}^{-1}$, the NO disappeared, there was a significant reduction in NO_2 and N_2O , some N_2O_5 was formed and no ozone was observed. However, increasing the flow rate to 0.5 and $1.0 \text{ dm}^3 \text{ min}^{-1}$ ozone was observed, the N_2O and N_2O_5 concentrations decreased, and no other species was observed. From these observations, it is very clear that the feed gas flow rate plays an important role in enhancing the heat removal from the cell. This role may be

achieved through direct cooling by means of convective heat transfer (see section 1.3.2) or indirectly through reducing the SED [3]. Similar behaviour was observed at 30, 10 and 5 °C.

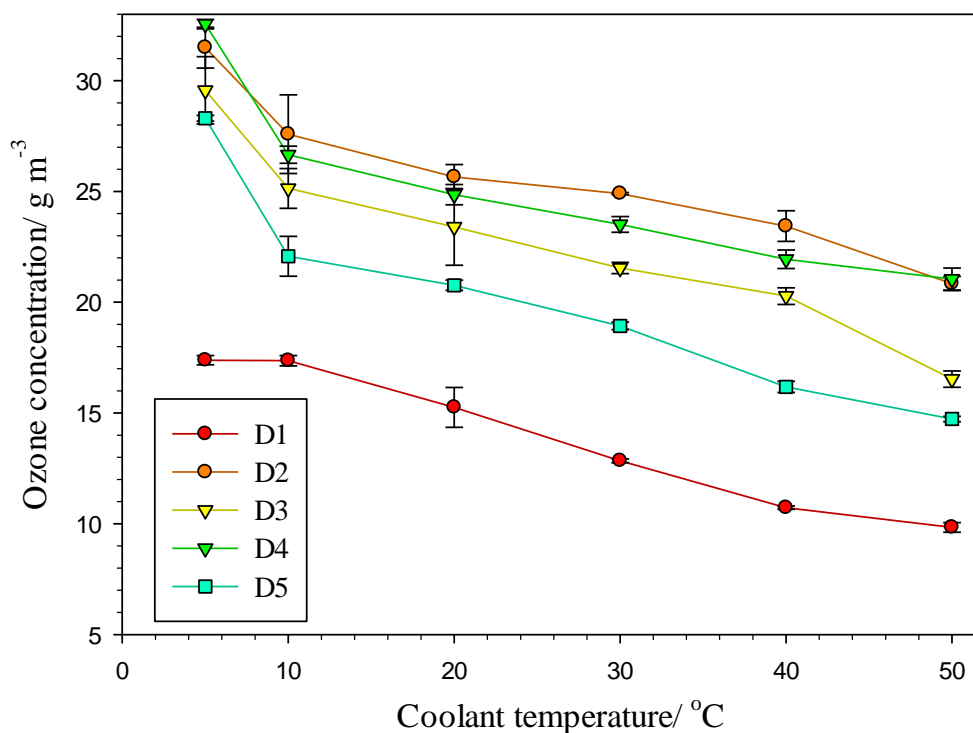
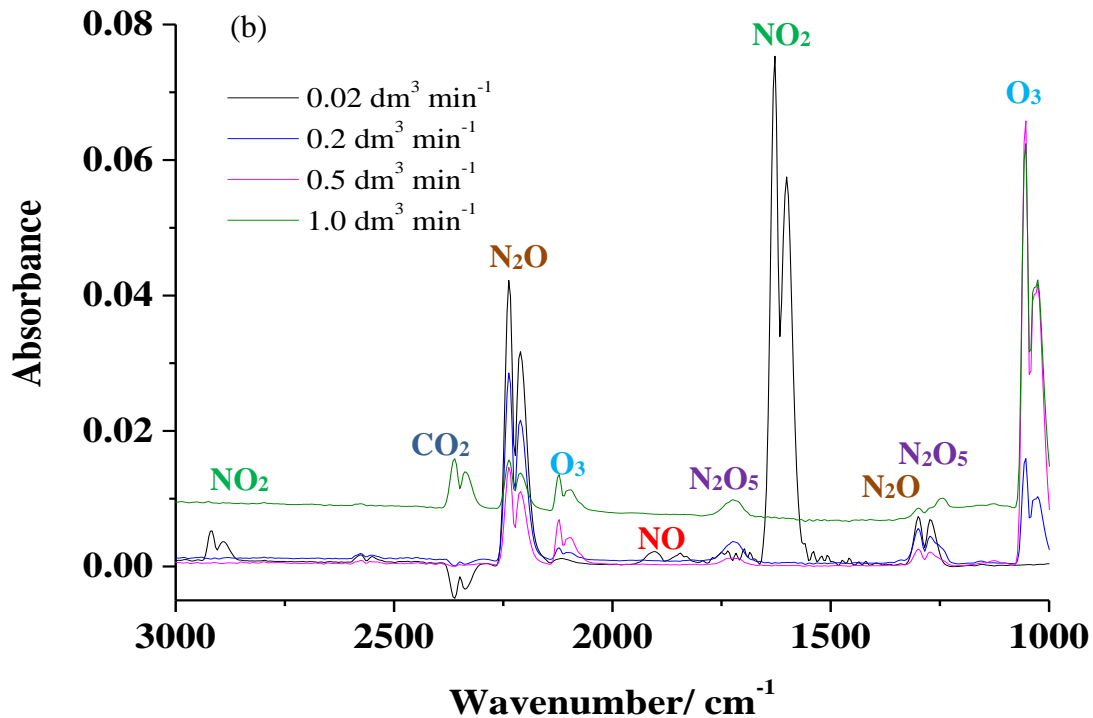
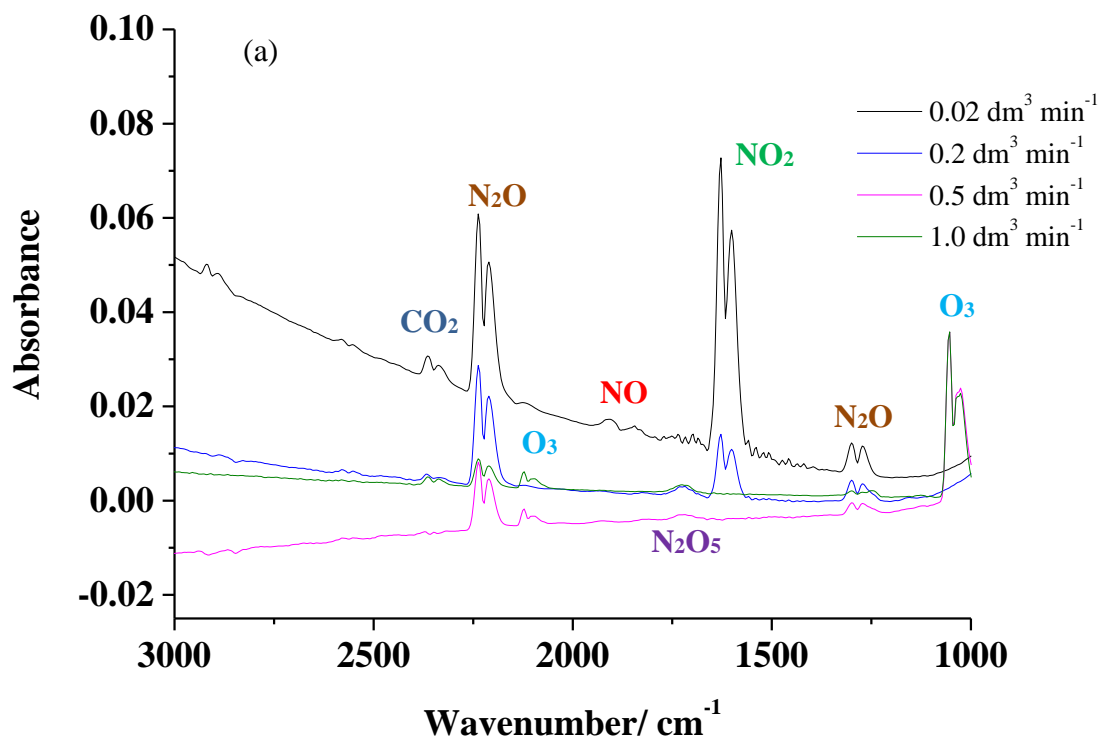


Figure 4.17. Plots of ozone concentration as a function of coolant temperature using dielectrics: 2 mm alumina pellets (D1), 2 mm borosilicate glass beads (D2), 2 mm A3 molecular sieve (D3), 3 mm Soda-Lime glass beads (D4) and 3 mm alumina pellets (D5). The PGWDs were the same as in fig.4.16. The input power was 35W and oxygen flow rate was $1.0 \text{ dm}^3 \text{ min}^{-1}$.

From figs. 4.18(a) - (d) and table 4.3 it can be seen that at the dried ambient air flow rates of 0.06 and $0.1 \text{ dm}^3 \text{ min}^{-1}$ the coolant temperature plays an important role in determining not only the concentration of ozone, but also the nature and amount of other by-products. As the coolant temperature was reduced from 50 °C to 30 and 10 °C at a dried ambient air flow rate of $1.0 \text{ dm}^3 \text{ min}^{-1}$, the concentration of ozone increased by ca. 33% and 43% respectively, with no further enhancement observed at 5.0 °C . These values agree with those observed using oxygen under the same conditions of flow rate, dielectric and coolant temperature shown in fig. 4.17. However, it is clear from table 4.3 that the contribution of the coolant



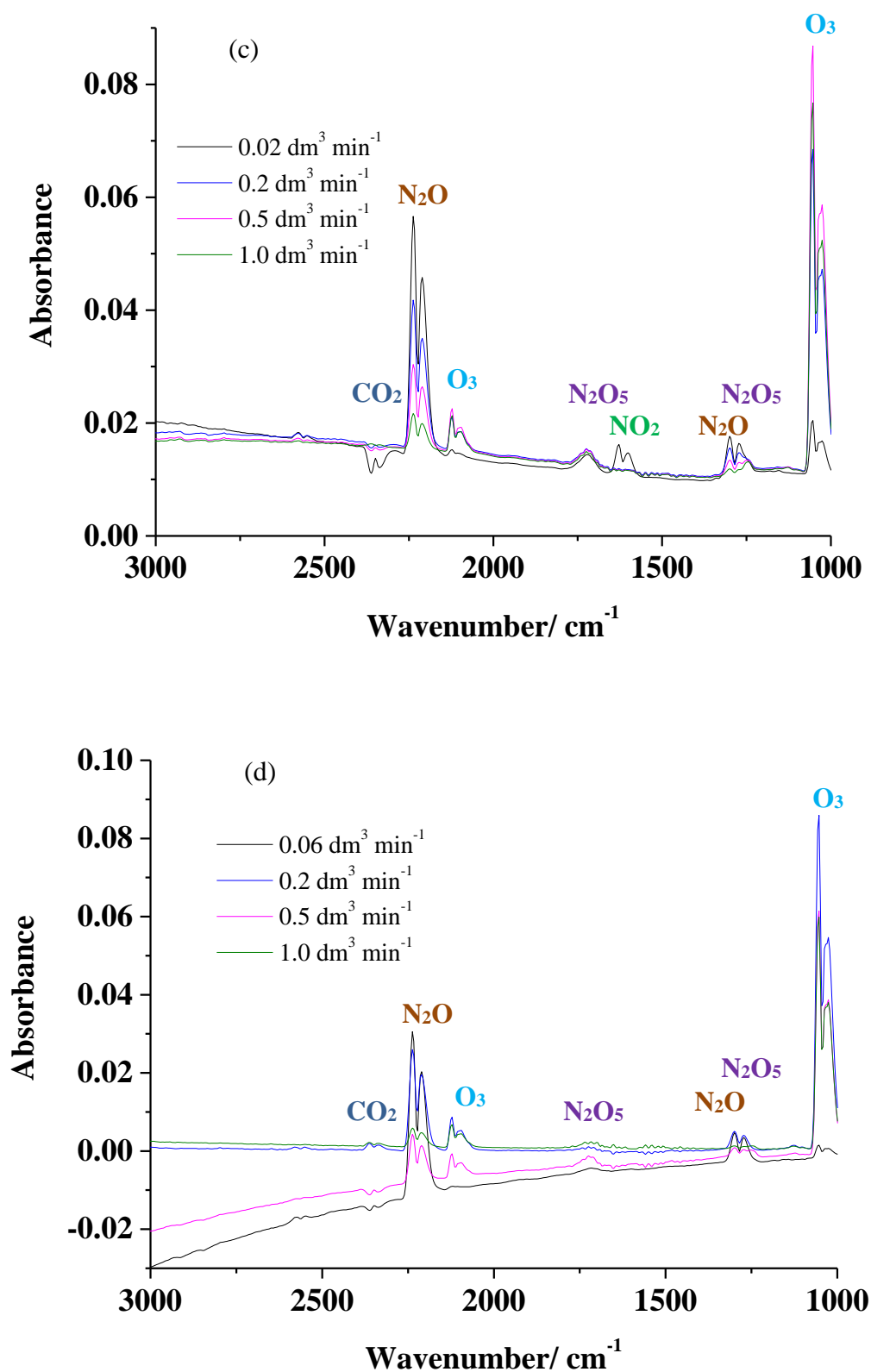


Figure 4.18. FTIR spectra collected from the exhaust of cell B after running the DBD-PBR for 30 minutes at different temperatures: (a) 50, (b) 30, (c) 10 and (d) 5 °C. Using dried ambient air at different flow rate. $\text{RH} \leq 0.6\%$, input power 35W, using 2.0 mm glass beads (D2).

Temperature /°C	Flow rate /dm ³ min ⁻¹	[NO ₂] /mg dm ⁻³	[N ₂ O] /mg dm ⁻³	[O ₃] /mg dm ⁻³
50	0.06	3.8	1.2	BDL
50	0.1	0.8	0.8	BDL
50	0.5	BDL	0.4	2.8
50	1.0	BDL	0.2	3.1
30	0.06	4.6	1.4	0.4
30	0.1	BDL	0.9	1.4
30	0.5	BDL	0.5	5.8
30	1.0	BDL	0.2	4.6
10	0.06	0.3	1.1	1.3
10	0.1	BDL	1.4	1.6
10	0.5	BDL	0.5	6.5
10	1.0	BDL	0.2	5.6
5	0.06	BDL	1.4	0.9
5	0.1	BDL	0.8	4.5
5	0.5	BDL	0.4	5.3
5	1.0	BDL	0.2	5.3

Table 4.3. The concentrations of NO₂, O₃ and N₂O as a function of dielectric calculated from the data shown in figs. 4.18(a), (b), (c) and (d). DBL = below detection limit.

temperature to ozone production was more significant at flow rates of 0.06 and 0.1 than 1.0 dm³ min⁻¹. This may be attributed to the cooling effect of the feed gas at 1.0 dm³ min⁻¹ that reduced the dependence of the system on the coolant temperature. In addition, the low thermal conductivity of the dielectric D2 (i.e. 2.0 mm glass beads) may be expected to reduce the effect of the coolant temperature. This behaviour agrees well with that observed by Teranishi et al. [3] as discussed in section 4.2.8.

4.2.10. Ozone and NO_x control

For safety purposes, the exhaust of the DBD-PBR was passed through an ozone catalytic destruction cell, discussed in section 2.3.4. The cell contained a MnO₂ catalyst to facilitate the conversion of ozone to oxygen before it was released safely to the atmosphere, see section 1.4. The cell was tested and was found to be extremely efficient for removing ozone from air or oxygen regardless of the flow rate and ozone concentration. In addition, the cell was observed to be efficient for removing most of the NO_x species when the DBD-PBR was fed with dried ambient air. Figures 4.19(a) and (b) show FTIR spectra collected from the

exhaust of cell B2 fed with dried ambient air before and after interaction with the ozone catalytic destruction cell, respectively. These experiments were carried out at 35W input power, coolant temperature of 50 °C, and dried ambient air flow rates of 0.6 and 1.0 dm³ min⁻¹. These two flow rates were employed to evaluate the effect of varying the contents and flow rate of the NO_x within the exhaust of the cell B2 on the performance of catalyst cell towards ozone and NO_x removal.

As can be seen from figs. 4.19(a) and (b), at a flow rate of 0.06 dm³ min⁻¹, ozone and most of the NO_x species were removed from the exhaust, including ca. 70 % of N₂O. However, at a flow rate of 1.0 dm³ min⁻¹, the catalyst efficiency towards ozone and other NO_x was similar to that observed at 0.06 dm³ min⁻¹, but with ca. 25% reduction in N₂O. Therefore, for maintaining a high efficiency of NO_x removal, the contact time between NO_x and the catalyst must be taken into account. From figs. 4.19(a) and (b) it can be seen that a significant loss of CO₂ was observed after passing the exhaust through the catalyst cell, and was confirmed not to be due to a reaction with plasma or its products as can be clearly seen from runs (i) in the figures, which was carried out under no discharge conditions. Thus, the loss of CO₂ may be attributed to possible adsorption on the catalyst surface.

In general, these results agree with the work recently carried out by Ge and co-workers [30], who observed a high activity of MnO₂ catalyst towards the simultaneous removal of O₃ and NO₂ from the exhaust of a cold corona discharge (CCD) fed with air. The authors attributed the removal of ca.89% of NO₂ to its oxidation to NO₃ by atomic oxygen developed on the surface of the MnO₂ catalyst during ozone decomposition, see section 1.4. However, on the basis of the results shown in figs. 4.19(a) and (b) it can be concluded not only NO₂ and O₃ can be removed using MnO₂ catalyst but also N₂O₅, NO and N₂O.

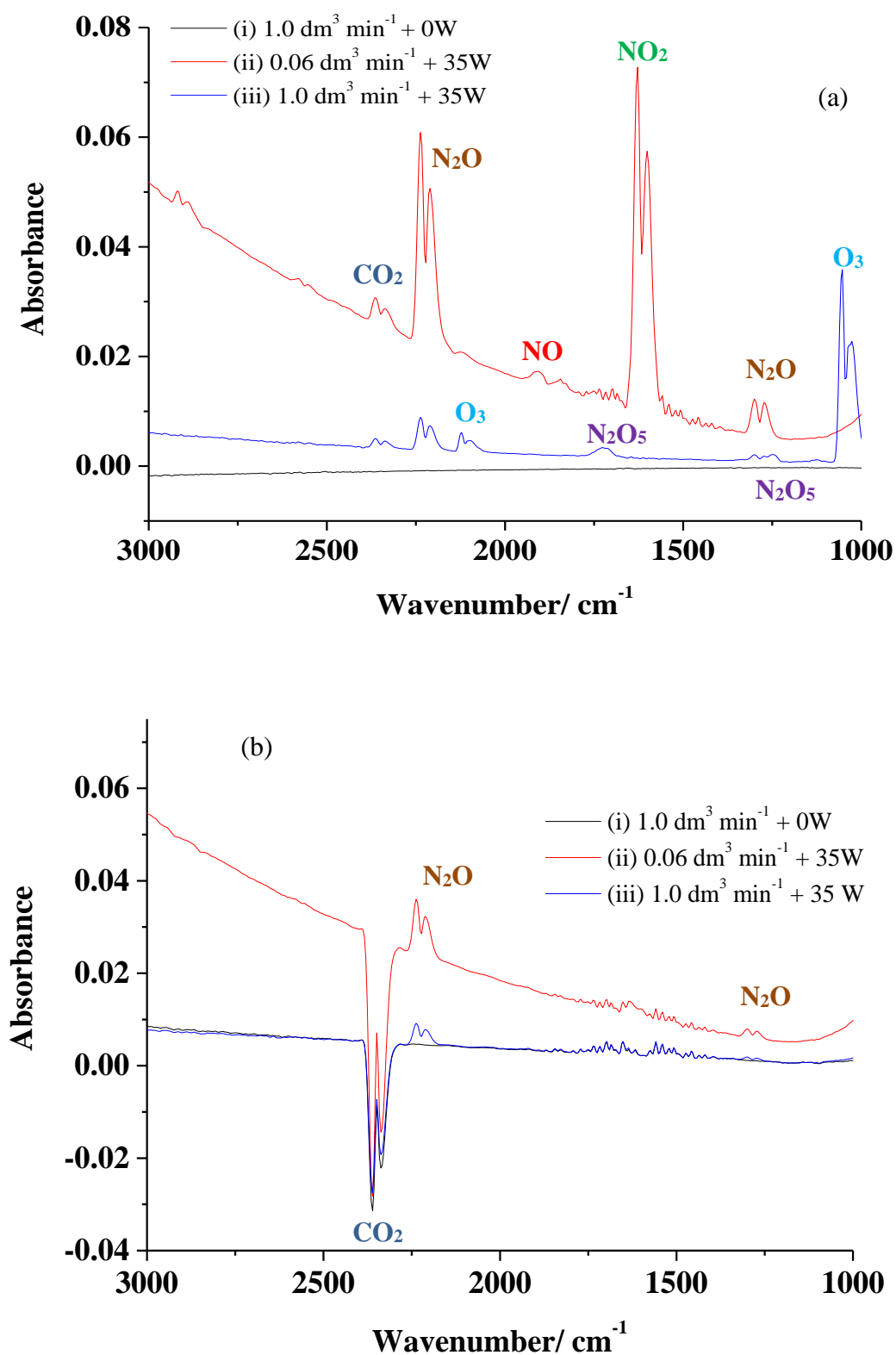


Figure 4.19. FTIR spectra collected from cell B exhaust after running the DBD-PBR for 30 minutes monitored (a) before and (b) after the interaction with the MnO_2 catalyst. Using the cell B at 50°C , 2.0 mm glass beads (D2) and fed with dried ambient air.

4.3. Conclusions

Ozone generation from oxygen and air was investigated using a novel dielectric barrier discharge packed bed reactor (DBD-PBR) supplied with a cooling system. The DBD-PBR was designed, commissioned, characterized and optimized using 4 arrangements of discharge cell. The results have shown that the DBD-PBR performance towards ozone production from oxygen and air was significantly affected by the reactor arrangement, dielectric material, coolant temperature, gas flow rate and discharge voltage.

Ozone concentration and yield efficiency decreased with the number of dielectric layers in contact with the HV electrodes, which was attributed to heat formation and the reduction in the discharge voltage. In addition, reducing gap between the HV electrodes (i.e. the cell divider) from 10 mm to 3 mm decreased the input power required for initiating the plasma by 11.5% and increased the yield efficiency by 27%.

Regardless of the feed gas, the effect of dielectric type, shape, thermal conductivity, dielectric constant and thickness were found to play important roles in ozone generation at flow rates $\leq 1.0 \text{ dm}^3 \text{ min}^{-1}$, and become less important at higher flow rates. This behaviour was attributed to the decrease in contact time between the feed gas and the dielectric, and to the decrease in specific energy density (SED, J cm^{-3}).

In general, ozone generation was enhanced by using dielectrics with high thermal conductivity and low dielectric constant. However, the priority of each of these parameters over others varied with the experimental conditions. For instance, dielectrics with low dielectric constant were found to be more efficient for ozone production from oxygen, while those with high thermal conductivity were more effective when air was employed.

The highest ozone concentrations produced from oxygen or air were observed at high input power and low coolant temperature and feed gas flow rate. The highest ozone concentration produced from oxygen was 152 g m^{-3} at $0.06 \text{ dm}^3 \text{ min}^{-1}$, input power of 35W and coolant temperature of $5 \text{ }^\circ\text{C}$ using 2 mm borosilicate glass beads (D2). This concentration was ca. $2.5\times$ higher than the maximum ozone concentration reported in the literature to date using the conventional DBD-PBR. Under the same experimental conditions, the highest ozone concentration produced from air was 15.6 g m^{-3} using 2 mm A3 molecular sieve (D3).

The yield efficiency decreased with the capacitance of the dielectric, and increased with the feed gas flow rate and ozone concentration. While the effect of input power on the yield efficiency was found to vary with the discharge cell arrangement. The highest yield efficiency of ozone from oxygen was $209 \text{ g kW}^{-1} \text{ h}^{-1}$ attained at $20 \text{ dm}^3 \text{ min}^{-1}$ and SED of 6.0 J dm^{-3} using A2. Whilst the highest efficiency obtained using the cell B2 was $108 \text{ g kW}^{-1} \text{ h}^{-1}$ at $20 \text{ dm}^3 \text{ min}^{-1}$ and SED of 135 J dm^{-3} .

Decreasing the coolant temperature was found to increase ozone production from oxygen and air and to lower the number and concentrations of NO_x from air.

An ozone catalytic destruction cell was designed, commissioned for ozone control and it was found to be extremely efficient not only for ozone removal but also for most of the NO_x species. However, the performance of the cell towards NO_x was highly dependent on the contact time between the NO_x and the catalyst.

4.4. References

- [1] Pietsch, G.J. and Gibalov, V.I. (1998) 'Dielectric barrier discharges and ozone synthesis', *Pure and Applied Chemistry*, 70(6), pp. 1169-1174.
- [2] Ogata, A., Shintani, N., Mizuno, K., Kushiya, S. and Yamamoto, T. (1999) 'Decomposition of benzene using a nonthermal plasma reactor packed with ferroelectric pellets', *Industry Applications, IEEE Transactions on*, 35(4), pp. 753-759.
- [3] Teranishi, K., Shimomura, N., Suzuki, S. and Itoh, H. (2009) 'Development of dielectric barrier discharge-type ozone generator constructed with piezoelectric transformers: effect of dielectric electrode materials on ozone generation', *Plasma Sources Science and Technology*, 18(4), p. 045011.
- [4] Price, D.M. and Jarratt, M. (2002) 'Thermal conductivity of PTFE and PTFE composites', *Thermochimica Acta*, 392–393(0), pp. 231-236.
- [5] Liang Chen, H., Ming Lee, H. and Been Chang, M. (2006) 'Enhancement of energy yield for ozone production via packed-bed reactors', *Ozone: Science and Engineering*, 28(2), pp. 111-118.

[6] Schmidt-Szalowski, K. and Borucka, A. (1989) 'Heterogeneous effects in the process of ozone synthesis in electrical discharges', *Plasma Chemistry and Plasma Processing*, 9(2), pp. 235-255.

[7] Chen, H.L., Lee, H.M. and Chen, S.H. (2008) 'Review of packed-bed plasma reactor for ozone generation and air pollution control', *Industrial & Engineering Chemistry Research*, 47(7), pp. 2122-2130.

[8] Takuma, T. (1991) 'Field behaviour at a triple junction in composite dielectric arrangements', *Electrical Insulation, IEEE Transactions on*, 26(3), pp. 500-509.

[9] Techaumnat, B. and Takuma, T. (2005) *Electrical Insulating Materials, 2005. (ISEIM 2005). Proceedings of 2005 International Symposium on. 5-9 June 2005.*

[10] Löf, G.O.G. and Hawley, R.W. (1948) 'Unsteady-State heat transfer between air and loose solids', *Industrial & Engineering Chemistry*, 40(6), pp. 1061-1070.

[11] Yagi, S. and Kunii, D. (1957) 'Studies on effective thermal conductivities in packed beds', *AIChE Journal*, 3(3), pp. 373-381.

[12] Balakrishnan, A.R. and Pei, D.C.T. (1979) 'Heat transfer in gas-solid packed bed systems. 2. The conduction mode', *Industrial & Engineering Chemistry Process Design and Development*, 18(1), pp. 40-46.

[13] Fang, Z., Qiu, Y., Sun, Y., Wang, H. and Edmund, K. (2008) 'Experimental study on discharge characteristics and ozone generation of dielectric barrier discharge in a cylinder-cylinder reactor and a wire-cylinder reactor', *Journal of Electrostatics*, 66(7-8), pp. 421-426.

[14] Jung, J.-S. and Moon, J.-D. (2008) 'Corona discharge and ozone generation characteristics of a wire-plate discharge system with a glass-fiber layer', *Journal of Electrostatics*, 66(5-6), pp. 335-341.

- [15] Chang, J., x, Shih, Kostov, K.G., Urashima, K., Yamamoto, T., Okayasu, Y., Kato, T., Iwaizumi, T. and Yoshimura, K. (2000) 'Removal of NF_3 from semiconductor-process flue gases by tandem packed-bed plasma and adsorbent hybrid systems', *Industry Applications, IEEE Transactions on*, 36(5), pp. 1251-1259.
- [16] Haacke, M., Humpert, C. and Pietsch, G.J. (2002) 'Influence of field strength and energy distribution of different barrier discharge arrangements on ozone generation', *Ozone: Science & Engineering*, 24(3), pp. 193-201.
- [17] Nomoto, Y., Ohkubo, T., Kanazawa, S. and Adachi, T. (1995) 'Improvement of ozone yield by a silent-surface hybrid discharge ozonizer', *Industry Applications, IEEE Transactions on*, 31(6), pp. 1458-1462.
- [18] Gibalov, V.I. and Pietsch, G.J. (2006) 'On the performance of ozone generators working with dielectric barrier discharges', *Ozone: Science & Engineering*, 28(2), pp. 119-124.
- [19] Manley, T.C. (1943) 'The electric characteristics of the ozonator discharge', *Transactions of The Electrochemical Society*, 84(1), pp. 83-96.
- [20] Chen, M.-G., Mihalcioiu, A., Takashima, K. and Mizuno, A. (2009) 'Catalyst size impact on non-thermal plasma catalyst assisted deNO_x reactors', in Yan, K. (ed.) *Electrostatic Precipitation*. Springer Berlin Heidelberg, pp. 681-684.
- [21] Eliasson, B. and Kogelschatz, U. (1991) 'Nonequilibrium volume plasma chemical processing', *Plasma Science, IEEE Transactions on*, 19(6), pp. 1063-1077.
- [22] Eliasson, B., Hirth, M. and Kogelschatz, U. (1987) 'Ozone synthesis from oxygen in dielectric barrier discharges', *Journal of Physics D: Applied Physics*, 20(11), p. 1421.
- [23] Jodzis, S. (2003) 'Effect of silica packing on ozone synthesis from oxygen-nitrogen mixtures', *Ozone: Science & Engineering*, 25(1), pp. 63-72.
- [24] Jodzis, S. (2012) 'Effective ozone generation in oxygen using a mesh electrode in an ozonizer with variable linear velocity', *Ozone: Science & Engineering*, 34(5), pp. 378-386.

[25] Samaranayake, W.J.M., Namihira, T., Katsuki, S., Miyahara, Y., Sakugawa, T., Hackam, R. and Akiyama, H. (2001) 'Pulsed power production of ozone using nonthermal gas discharges'.

[26] Atkinson, R., Baulch, D L., Cox, R A., Hampson, R F., Kerr, J A. and Troe, J. (1989) 'Evaluated kinetic and photochemical data for atmospheric chemistry: Supplement III', IUPAC Subcommittee on Gas Kinetic Data Evaluation for Atmospheric Chemistry *Journal of Physical and Chemical Reference Data* **18** 881-1097

[27] Sung, Y.-M. and Sakoda, T. (2005) 'Optimum conditions for ozone formation in a micro dielectric barrier discharge', *Surface and Coatings Technology*, 197(2), pp. 148-153.

[28] Samaranayake, W.J.M., Miyahara, Y., Namihira, T., Katsuki, S., Hackam, R. and Akiyama, H. (2001) 'Ozone generation in dry air using pulsed discharges with and without a solid dielectric layer', *Dielectrics and Electrical Insulation, IEEE Transactions on*, 8(4), pp. 687-697.

[29] Kenji, T., Naoyuki, S., Susumu, S. and Haruo, I. (2009) 'Development of dielectric barrier discharge-type ozone generator constructed with piezoelectric transformers: effect of dielectric electrode materials on ozone generation', *Plasma Sources Science and Technology*, 18(4), p. 045011.

[30] Ge, H., Hu, D., Li, X., Tian, Y., Chen, Z. and Zhu, Y. (2015) 'Removal of low-concentration benzene in indoor air with plasma-MnO₂ catalysis system', *Journal of Electrostatics*, 76, pp. 216-221.

5. Characterization and optimization of an oscillatory baffled reactor (OBR) for ozone-water mass transfer

5.1. Introduction

From the discussion in section 1.5.1 it is clear that enhancing the rate of ozone-to-water mass transfer is the key process for reducing the capital and operational costs of water and wastewater treatments. Oscillatory baffled reactors (OBRs) have shown a promise in oxygen dissolution in water [1-4], and hence were assumed to enhance the solubility of ozone in water. Through the literature review carried out during this work it was found that: (i) the performance of OBRs towards ozone-water mass transfer has not been investigated and (ii) no information was found on how the performance of OBRs varies between semi-batch to continuous flow conditions. Therefore, the main aim of this chapter was to characterize and optimize an oscillatory baffled reactor (OBR) for ozone-water mass transfer under semi-batch and continuous flow conditions. The objectives were to:

- Design and commission an OBR supplied with a sufficient monitoring system for instantaneous determination of the dissolved ozone concentration.
- Assess the accuracy and reliability of the monitoring system through determining the Henry's law constant for ozone solubility in water and comparison to literature.
- Operate the reactor as a bubble column (without baffles or oscillation), baffled reactor (without oscillation), and as an OBR (with baffles and oscillation) to determine the effect of varying the reactor arrangement on ozone dissolution and to establish a base of comparison with literature.
- Investigate the effects of input ozone concentration, mixing conditions, type of gas diffuser, feed gas and water flow rates on ozone-to-water volumetric mass transfer coefficient (k_La) and mass transfer efficiency (MTE).

It should be noted that all the experiments discussed in this chapter were carried out at room temperature under atmospheric pressure with no pH adjustment, using deionised water. Hence the presence of ozone-scavenging species were avoided [5, 6]. Tables 2.3 and 2.4 summarise the range of experimental conditions in terms of the input gas and liquid flow

rates, ozone concentrations and oscillation amplitude and frequency in the semi-batch and in continuous flow experiments. These tables are reproduced from chapter 2 for convenience.

Parameter	Semi-batch	Continuous
$Q_G/\text{dm}^3 \text{ min}^{-1}$	0.1 - 2.0	0.1 - 1.0
$U_G/\text{cm s}^{-1}$	0.3 - 6.8	0.3 - 3.4
$Q_L/\text{dm}^3 \text{ min}^{-1}$	0.0	0.1 - 1.0
$U_L/\text{cm s}^{-1}$	0.0	0.3 - 3.4
$[\text{O}_3]_G/\text{mg dm}^{-3}$	11.3 - 64.5	11.3 - 64.5
Sampling rate $/\text{dm}^3 \text{ min}^{-1}$	0.18	= Q_L

Table 2.3. Summary of the experimental conditions employed in the ozone- water mass transfer study.

Parameter	Semi-batch	Continuous
Frequency /Hz	1.2 - 5.0	5.0
Amplitude /mm	1.0 - 6.0	6.0
Re_o	178 - 4600	4600
St	1.99 - 0.33	0.33

Table 2.4. The oscillation conditions employed for the work reported in this chapter.

5.2. Ozone-water mass transfer under semi-batch conditions

5.2.1. The effect of ozone concentration on ozone-water solubility

The effect of varying the input ozone concentration on the dissolved ozone concentration was investigated using the baffled reactor with no oscillation or water throughput to determine the unperturbed, dissolved ozone concentration. Figure 5.1 shows plots of the

dissolved ozone concentration as a function of time and input gas phase ozone concentration. As can be seen from the figure, the steady-state dissolved ozone concentration increased as the gas phase ozone concentration increased. In all cases, the dissolved ozone concentration increased rapidly during the first minute, reaching steady-state after ca. 2.5 minutes. The steady-state dissolved ozone concentration, k_{LA} and the Henry's Law constant were determined from fig. 5.1, and these are presented in table 5.1. The k_{LA} (s^{-1}) was obtained from equation (5.1) [2], Henry's Law constant (H_o , $atm\ dm^3\ mol^{-1}$) was evaluated from equation (5.2) and the ozone partial pressure (P_{O_3} , atm) in the feed gas was determined using equation (5.3):

$$\ln ([O_3]_s - [O_3]_t) = -k_{LA} t + constant \quad (5.1)$$

$$P_{O_3} = H_o [O_3]_s / 48000 \quad (5.2)$$

$$P_{O_3} = [O_3]_G \times T \times R / 48000 \quad (5.3)$$

where $[O_3]_s$ is the steady state dissolved ozone concentration ($mg\ dm^{-3}$), $[O_3]_t$ is the dissolved ozone concentration ($mg\ dm^{-3}$) at time t (min), $[O_3]_G$ is ozone concentration in feed gas ($mg\ dm^{-3}$), T is the temperature (K), R is the ideal gas constant ($dm^3\ atm\ K^{-1}\ mol^{-1}$) and the factor 48000 ($mg\ mol^{-1}$) was added to convert ozone concentration from $mg\ dm^{-3}$ to $mol\ dm^{-3}$.

From table 5.1, the steady state dissolved ozone concentration was found to increase linearly with the input ozone concentration. However, the H_o and k_{LA} values so obtained were almost constant and independent of the input ozone concentration. This does not seem unreasonable considering the consistency of these experiments in terms of temperature, pH and ionic strength which are the only parameters that determine the Henry's Law constant [7-9]. The average Henry's Law constant for ozone-water dissolution determined in this work, i.e. $80.1 \pm 5\ atm\ dm^3\ mol^{-1}$, was in good agreement with the $79.4\ atm\ dm^3\ mol^{-1}$ determined by Kuosa et al. [7] and within the range of $78.0\ atm\ dm^3\ mol^{-1}$ at $20\ ^\circ C$ and $87.5\ atm\ dm^3\ mole^{-1}$ at $25\ ^\circ C$ reported by Kosak-Channing and Helz [9]. Therefore, it was assumed that the monitoring system employed for the estimation of the dissolved ozone concentration in this work was reasonably accurate.

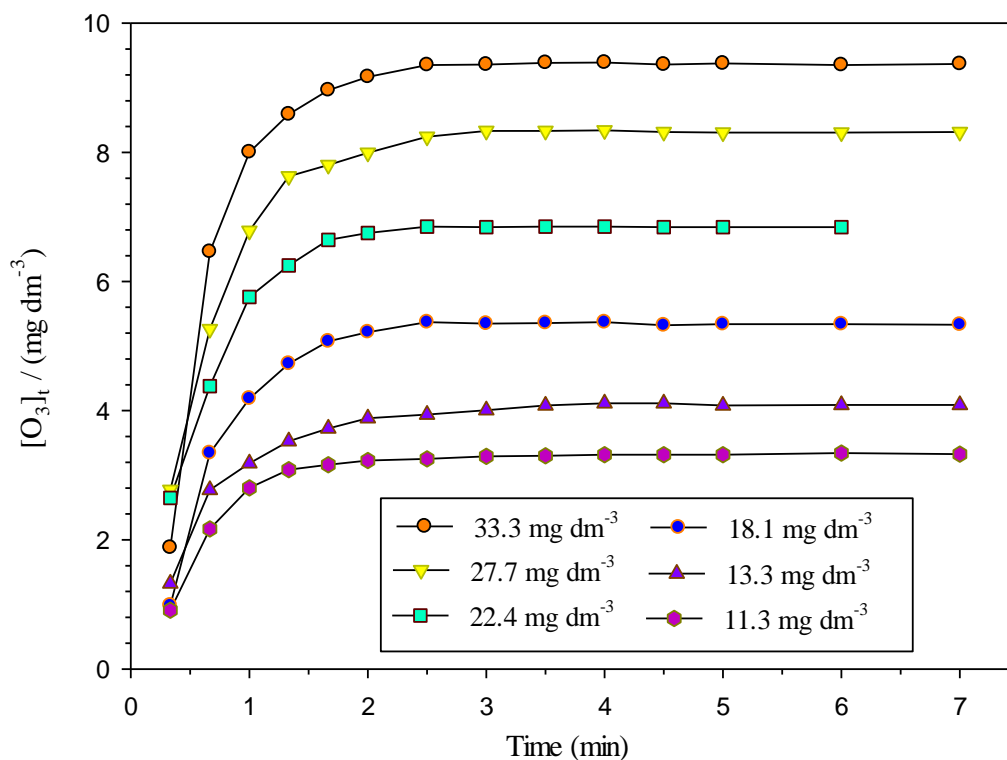


Figure 5.1. Plots of dissolved ozone concentration with time as a function of the input gas phase ozone concentration using the baffled reactor. The input gas flow rate (Q_G) was $1.0 \text{ dm}^3 \text{ min}^{-1}$.

$[\text{O}_3]_G / \text{mg dm}^{-3}$	$[\text{O}_3]_S / \text{mg dm}^{-3}$	k_{LA} / min^{-1}	k_{LA} / s^{-1}	Henry's constant / $\text{atm dm}^3 \text{ mol}^{-1}$
11.3	3.34	1.99	0.033	81.4
13.3	4.29	1.99	0.033	74.6
18.1	5.37	1.94	0.032	81.1
22.4	6.85	1.93	0.032	78.7
27.7	8.33	1.91	0.032	80.0
33.3	9.39	2.00	0.033	85.3

Table 5.1. Summary of k_{LA} values, Henry's law constant and steady state dissolved ozone concentrations at different input ozone concentrations from the data in fig.5.1.

5.2.2. The effect of oscillation conditions on ozone-water mass transfer

In order to identify the optimal mixing conditions for ozone mass transfer, the OBR was operated at various oscillation amplitudes and frequencies, and the k_{LA} values were recorded. Figures 5.2(a) and (b) show plots of ozone-water k_{LA} as a function of oscillation amplitude and frequency, respectively. The results in fig. 5.2(a) were obtained at 5 Hz and various amplitudes, while those in (b) were at an oscillation amplitude of 6.0 mm and various frequencies. The zero level in both figures was obtained using the same reactor without oscillation. As can be seen from figs. 5.2(a) and (b), the ozone-water volumetric mass transfer coefficient increased with both oscillation amplitude and frequency in a similar fashion showing an almost exponential increase. This pattern agreed well with those observed in previous studies using OBRs for oxygen-to-water and air-to-water dissolution by Oliveira and Ni [4] and Ni and Gao [10], respectively. It is interesting to note that the internal diameters of the OBRs employed by Oliveira and Ni [4] and Ni and Gao [10] were 2 and 4 times, respectively, larger than the one employed in this work (i.e. 25 mm) while maintaining the same effective height of water within the OBR ca. 1 m. Therefore, it can be concluded that the scale-up of OBRs does not reduce their performance towards gas-to-liquid mass transfer in agreement with the work carried out by Ni and Gao [10].

From figs 5.2(a) and (b) the highest k_{LA} (i.e. 0.048 s^{-1}) was observed at an oscillation amplitude and frequency of 6.0 mm and 5.0 Hz, respectively. Further enhancement may be expected on increasing the oscillation frequency and amplitude beyond the maximum values in figs. 5.2(a) and (b); however, this was not possible due to instrumental limitations. According to Oliveira and Ni [4] at an oscillation amplitude of 4 mm and frequencies from 0 – 3 Hz a small enhancement in oxygen k_{LA} was observed, while a significant increase in the latter was observed from 3 to 5 Hz. This behaviour was assumed to be due to the combined effect of the oscillation frequency and amplitude [4]. It should be noted that whilst the oscillation amplitude controls the length of eddies produced between each pair of baffles [10] the bubble break-up rates increased with frequency through intensive collisions with the baffles of the OBR [11]. Hence, the enhancement observed with increasing oscillation amplitude and frequency may be attributed to increased bubble breakup induced by increasing the speed and strength of the interaction between the oscillating liquid and the sharp edges of the baffles [1-4, 10, 11]. As a consequence, the contact area and time between the bubbles and the liquid increased [10, 11]. According to the work carried out by Oliveira

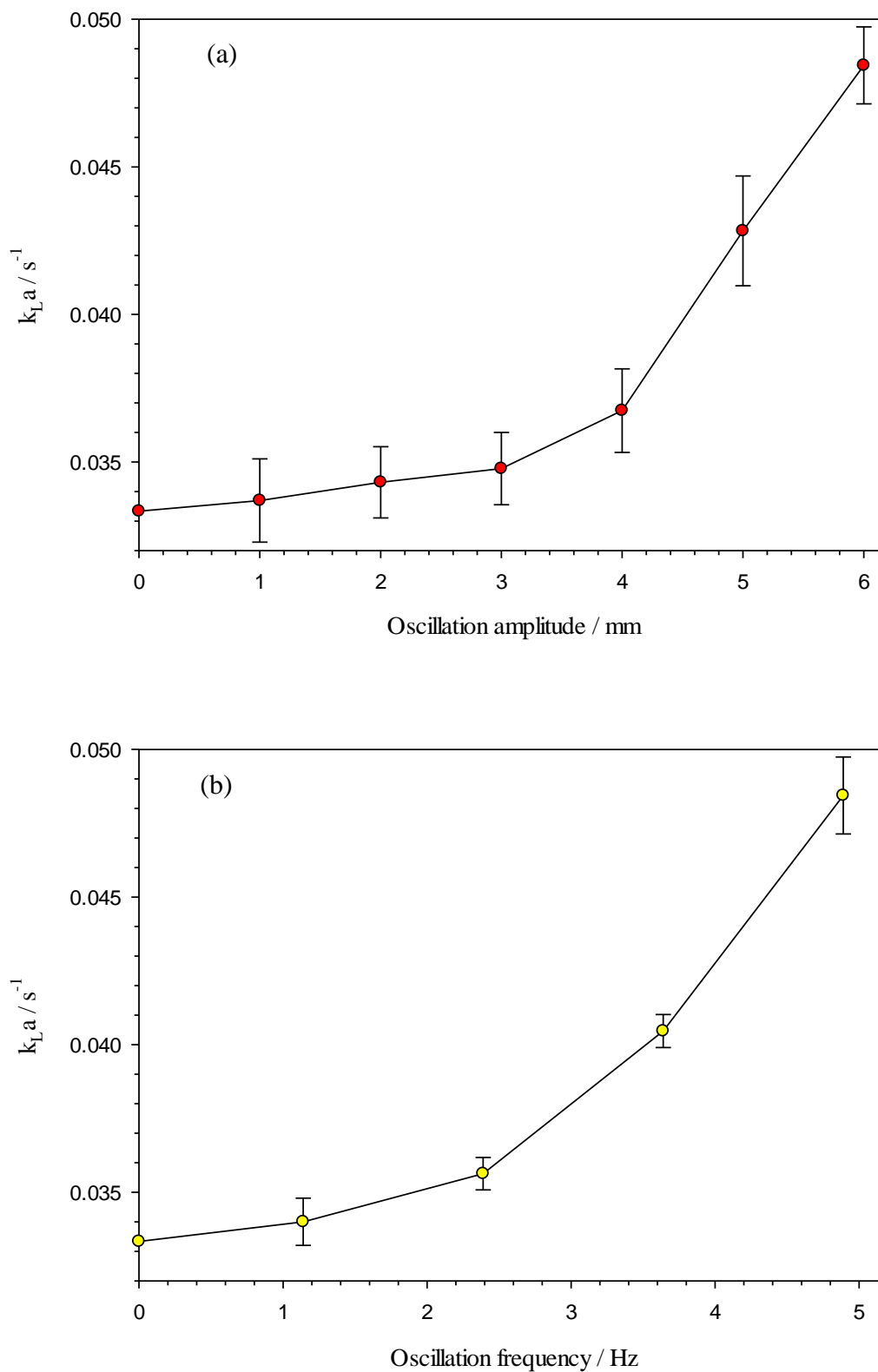


Figure 5.2. Plots of ozone volumetric mass transfer coefficient ($k_L a$) as a function of (a) oscillation amplitude at 5.0 Hz and (b) oscillation frequency at 6.0 mm, using the OBR. The ozone concentration in oxygen was 62.0 mg dm^{-3} at a flow rate of $1.0 \text{ dm}^3 \text{ min}^{-1}$.

et al. [11], regardless of the bubble size, increasing the oscillation frequency from 0 to 2 Hz at a constant amplitude of 4 mm doubled the residence time of bubbles within the OBR, in contrast to bubble column (without baffles or oscillation) or baffled column reactor (without oscillation) [11]. This effect was attributed to bubble trapping by eddies [11].

Figure 5.3 shows a plot of the volumetric mass transfer coefficient as a function of the oscillatory Reynolds number (Re_o) calculated from the data in figs. 5.2(a) and (b). The oscillatory Reynolds number (Re_o) which is normally used to describe the mixing condition in OBRs is an important characteristic because it correlates the applied mechanical conditions (i.e. amplitude and frequency) with the physical properties of the liquid and the geometry of the reactor. Re_o was calculated using the equation 1.32 (see section 1.5.6, p. 33) [2, 12, 13]:

$$Re_o = \frac{2\pi f X_o \rho D}{\mu} \quad (1.32)$$

where f is the oscillation frequency (Hz), x_o the oscillation amplitude centre to peak (m), ρ is the liquid density (kg m^{-3}), μ is the liquid viscosity ($\text{kg m}^{-1} \text{s}^{-1}$) and D is the column inner diameter (m). As can be seen from fig. 5.3 the volumetric mass transfer coefficient (k_{LA}) increased slightly as Re_o increased from 0 to 1000, however the most important enhancement was observed at Re_o above 3000. This behaviour was in agreement with the individual effects of the oscillation amplitude and frequency on k_{LA} shown in figs. 5.2(a) and (b), respectively.

According to Oliveira et al. [11] who carried out a comparison between a bubble column and an OBR (50 cm height and 5 cm internal diameter) in term of the rising velocity of a single bubble of oxygen in water. From their results, and regardless of the bubble size, operating the OBR at Re_o from 0 to 1250 the bubble rise velocity was similar to that observed using the bubble column. However, as the oscillation intensity of the OBR increased to Re_o of 2500 the bubble rise velocity reduced to half that observed using the bubble column, a dramatic change. Thus, the significant improvement in ozone-water volumetric mass transfer coefficient observed at Re_o above 3000 may be attributed to the significant enhancements in the contact area and time of the bubbles with water. In addition, from the data reported by Oliveira and Ni [1] the change in oxygen-water mass transfer coefficient with Re_o was similar to that observed in fig. 5.3 using an OBR 150 cm in height and 5 cm internal diameter.

However, from their results the most important enhancement in k_{LA} was obtained at $Re_o > 5000$ at a superficial air velocity of $1.06 \times 10^{-3} \text{ m s}^{-1}$, decreasing to $Re_o > 4000$ at $4.24 \times 10^{-3} \text{ m s}^{-1}$. Therefore, considering the higher range of superficial gas velocity employed in this work (i.e. $3.4 \times 10^{-2} \text{ m s}^{-1}$) compared to that employed by Oliveira and Ni [1], the lower range of Re_o for effective mass transfer observed here (i.e. > 3000) is not unreasonable.

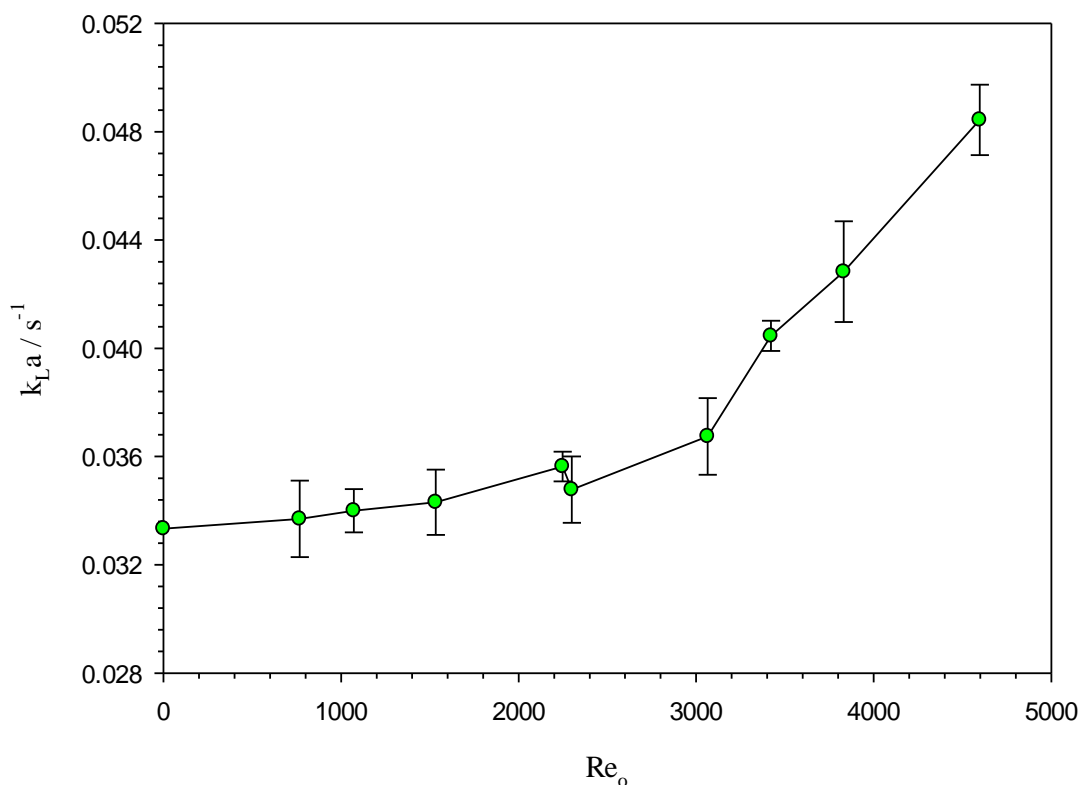


Figure 5.3. Plot of ozone-water mass transfer coefficient as a function of Re_o for the data in figs. 5.2 (a) and (b).

5.2.3 The effect of the reactor arrangement on ozone-water mass transfer

The effect of the reactor arrangement on the ozone-water dissolution rate is shown in fig. 5.4. Figure 5.4 shows the change in dissolved ozone concentration as a function of ozonation time and reactor arrangement, and the inset figure shows the plots obtained using equation (5.1) to determine the changes in k_{LA} for the same data points. As can be seen from the figure, the time required for the dissolved ozone concentration to reach steady-state varied with the reactor arrangement, and decreased in the order: OBR < baffled reactor < bubble column. In addition,

linear relationships were observed between $\ln ([O_3]_s - [O_3]_t)$ and time with slopes (i.e. k_{LA}) increasing in the order: OBR > baffled column > bubble column. The value of k_{LA} observed using the OBR at gas flow rate (Q_G) of $0.1 \text{ dm}^3 \text{ min}^{-1}$, superficial velocity (U_G) of $1.58 \times 10^{-3} \text{ ms}^{-1}$ and Re_o of 4600 was found to be 5 and 3 times greater than those observed using the bubble and baffled reactors, respectively.

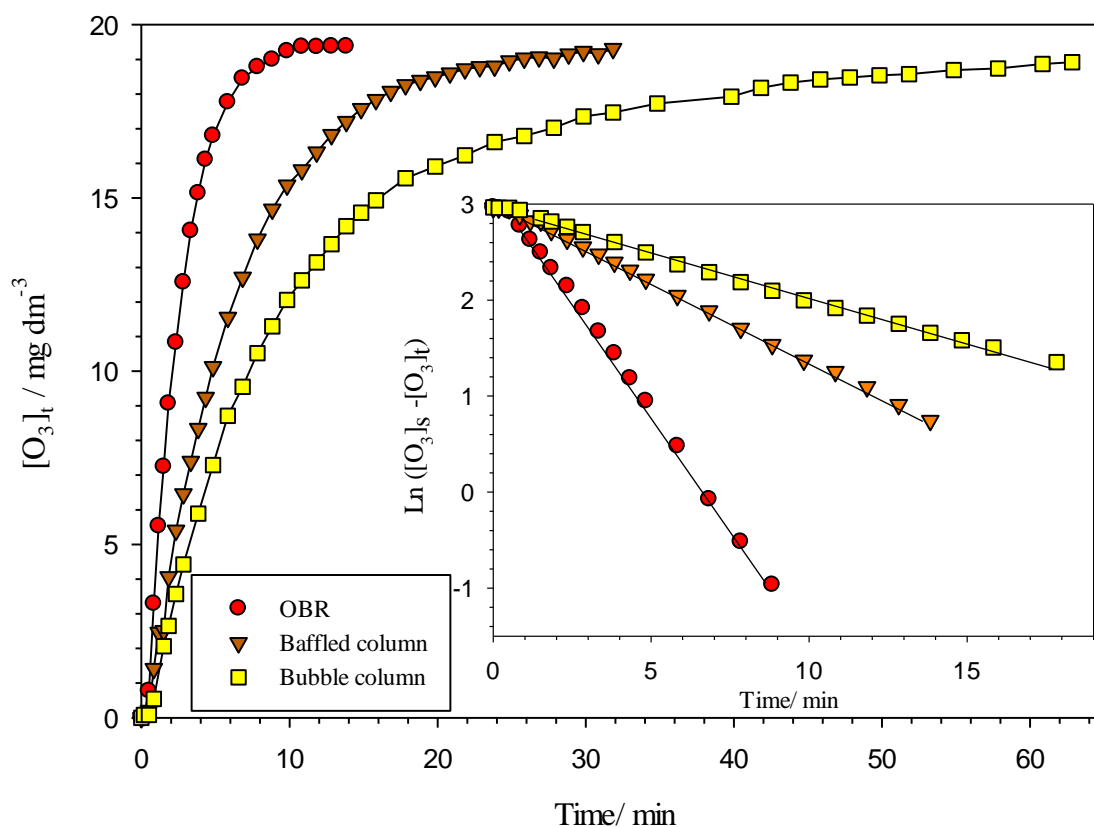


Figure 5.4. Plots of ozone-water dissolution as a function of running time and reactor arrangement. $[O_3]_G$ was 65 mg dm^{-3} at an input gas flow rate (Q_G) of $0.1 \text{ dm}^3 \text{ min}^{-1}$. Re_o was fixed at 4600 in the case of the OBR. The inset plots of $\ln ([O_3]_s - [O_3]_t)$ vs. time used for the determination of k_{LA} (see text for further details).

The enhancement in ozone-water mass transfer coefficient attained using OBR over the bubble column may be expected due to the enhancement in mixing and residence time of the bubble within the water in the former. In fact, this improvement was found to be in good agreement with the work carried out by Hewgill et al. [2] using an OBR for oxygen-to-water dissolution.

The OBR employed in their work (i.e. 100 cm height and 2.6 cm internal diameter) was similar in dimensions to the one employed in this work. According to their results at a feed gas superficial velocity (U_G) of $7.4 \times 10^{-4} \text{ m s}^{-1}$ and oscillatory Reynolds number (Re_o) of 5200 the oxygen-to-water k_{LA} was 6 times higher than that obtained using the same column without baffles or oscillation.

It is interesting to note that the enhancement in ozone-water mass transfer coefficient using the baffled reactor over the bubble column was not observed in previous studies. For instance, the work carried out by Oliveira et al. [11] have shown that the rising velocity of a single bubble in a bubble column was not affected by adding baffles to the same column. Furthermore, the results observed here are in disagreement with those observed by Hewgill and co-workers who found that the baffled reactor was less efficient than bubble column for oxygen-water dissolution [2]. This disagreement may be attributed to the lower input gas superficial velocities (i.e. from 0.042 to 0.24 cm s^{-1}) employed during their investigation compared with those investigated here (i.e. 0.34 – 6.8 cm s^{-1}).

Figure 5.5 shows a chart of ozone-water volumetric mass transfer coefficient as a function of the feed gas flow rate (Q_G) and reactor arrangement. As can be seen from the figure, k_{LA} increased with input gas flow rate regardless of the reactor arrangement. This behaviour is generally observed in most of ozone-water contactors, as discussed in section 1.5.5, and was attributed to the increase in gas hold up (ϵ_G) as will be shown in section 5.2.4. In general, the k_{LA} values obtained using the bubble column at different feed gas flow rates were found to agree well with data reported in the literature [14, 15]. In addition, equation (5.4) which was proposed by Watanabe et al. [16] for the estimation of ozone –water volumetric mass transfer coefficient (k_{LA} , s^{-1}) in bubble columns reproduced well the data obtained in this work as can be seen in table 5.2.

$$k_{LA} = 0.67 U_G^{1.15} \quad (5.4)$$

where U_G is the superficial gas velocity in m s^{-1} . Therefore, this agreement may be taken as an indicator of the validity of the comparisons shown in figs. 5.4 and 5.5.

From fig. 5.5, it can be seen that the enhancement in ozone dissolution obtained using the baffled reactor over the bubble column was found to increase from 1.8 to 2.3 times as the input

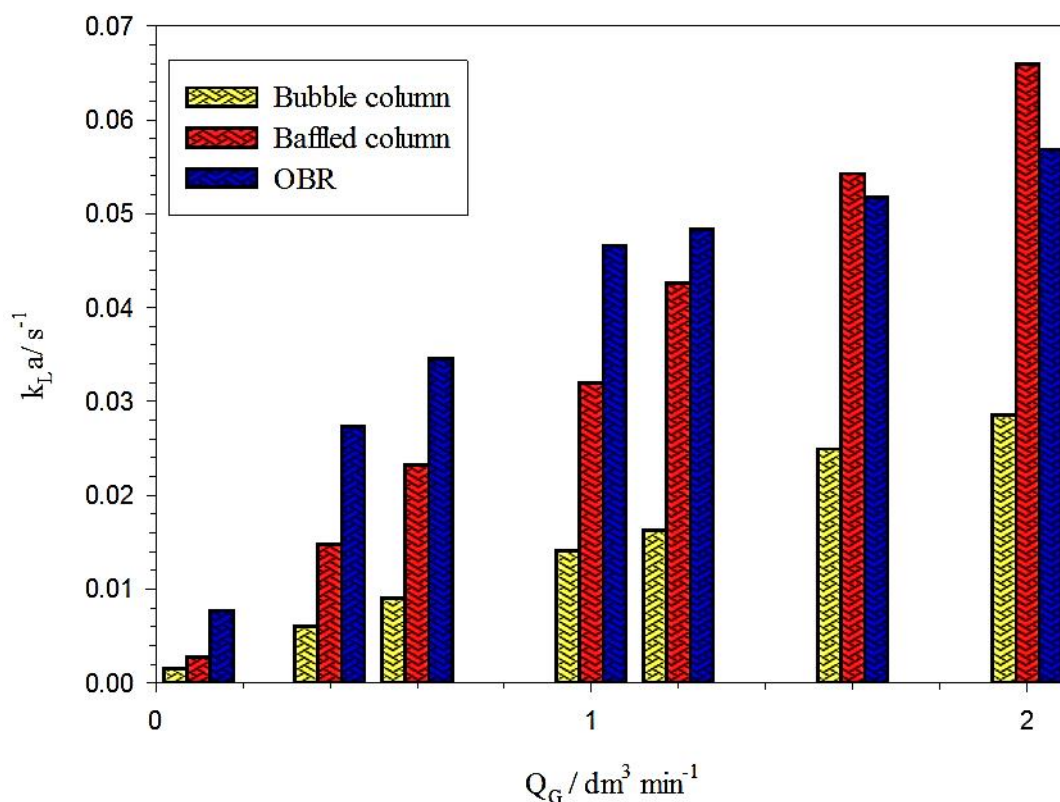


Figure 5.5. Chart of ozone-water mass transfer coefficients as a function of the reactor arrangement and input gas flow rate. Re_o was kept at 4600 in the case of the OBR.

Flow rate (Q_G) / $\text{dm}^3 \text{ min}^{-1}$	$(U_G) / \text{cm s}^{-1}$	k_{La} / s^{-1}	
		This work	$0.67 U_G^{1.15}$ [16]
0.1	3.39	0.002	0.001
0.4	13.58	0.006	0.005
0.6	20.37	0.009	0.008
1.0	33.95	0.014	0.014
1.2	40.74	0.016	0.017
1.6	54.32	0.025	0.024
2.0	67.91	0.029	0.030

Table 5.2. A comparison of ozone-water mass transfer coefficient (k_{La}, s^{-1}) determined in this work using the bubble column with the correlation proposed by Watanabe et al. [16] for bubble columns.

gas flow rate increased from 0.1 to 2.0 dm³ min⁻¹. This suggested that the performance of the baffled reactor towards ozone-water mass transfer increased with the feed gas flow rate. In general, the enhancement obtained using the baffled reactor may be attributed to the continuous collisions of bubble with the baffles, which reduces the rise velocity of the bubbles within the reactor and increases their break-up, as can be seen in fig. 5.6(a). These two factors become more significant as the gas flow rate increases, hence increasing the k_{LA} . In addition, from fig. 5.5 it can be seen that the enhancement in k_{LA} obtained with the OBR at input gas flow rates of 0.1 - 1.0 dm³ min⁻¹ was more significant than that observed at the higher input gas flow rates of 1.2 - 2.0 dm³ min⁻¹. However, as the flow rate increased from 1.6 to 2.0 dm³ min⁻¹, the k_{LA} values observed with the OBR were lower than those obtained using the baffled reactor. This behaviour may be interpreted by considering the variation of gas flow patterns at high and low flow rates, as shown in figs. 5.6(b) and (c).

Figures 5.6(a) – (c) show images of various gas flow patterns observed using the baffled reactor (a) and the OBR operated at low (b) and high (c) input gas flow rates, respectively. As can be seen from fig. 5.6(a), heterogeneous bubble sizes were observed between each pair of baffles along the reactor. Through the visualization of the bubble rise within the reactor at input gas flow rate of 0.4 dm³ min⁻¹, it was observed that they split at the edges of the baffles to smaller sizes, see fig. 5.6(a). Some of these bubbles nested at the underside of the baffles before they increased in size and returned to the main flow to the next baffle at which the same behaviour occurred again. This phenomenon increased the interfacial area and the residence times of the bubbles, and hence this may be the reason for the higher efficiency of the baffled reactor than the bubble column.

In the OBR, small and homogeneously distributed bubbles were observed at input gas flow rate of 0.4 dm³ min⁻¹ as can be seen in fig. 5.6(b), and most of these bubbles were trapped by high speed, circulating vortices, shown by the dashed lines on the figure. Thus, higher residence times and increased interfacial areas between the ozone bubbles and water would be expected compared to baffled and bubble columns. Nevertheless, larger bubbles were observed at the edges of each vortex. This may result from the coalescence of bubbles at the centre of each vortex before they were swept to the external wall of the vortex. Increasing the feed gas flow rate to 1.6 dm³ min⁻¹ caused a significant increase in the average bubble size and

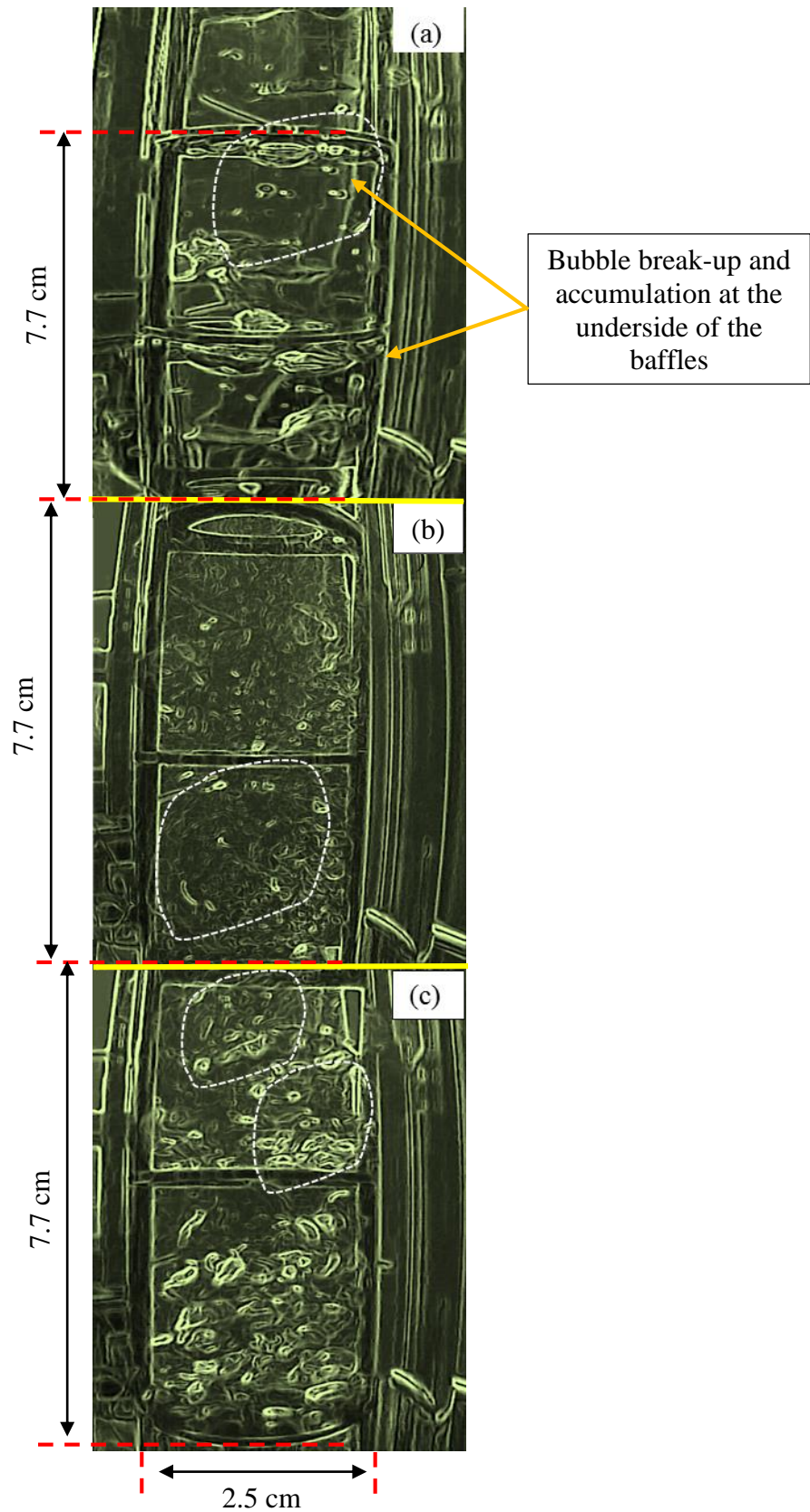


Figure 5.6. Images of various gas flow patterns observed using the baffled reactor at an input gas flow rate of $0.4 \text{ dm}^3 \text{ min}^{-1}$ (a) and the OBR at $0.4 \text{ dm}^3 \text{ min}^{-1}$ (b) and $1.6 \text{ dm}^3 \text{ min}^{-1}$ (c). The Re_o was fixed at 4600 in both (b) and (c).

vortices were not observed as can be seen in fig. 5.6(c), in contrast to that observed at $0.4 \text{ dm}^3 \text{ min}^{-1}$ as seen in (b). This behaviour was thought to be caused by increasing the number of bubbles and hence the rate of bubble collisions at the vortex centers, which led to vortex disturbance and, eventually, reduced the residence time. This behaviour was assumed to be the cause for the lower performance of the OBR than the baffled reactor observed in fig 5.5 at high flow rates.

5.2.4. Gas hold-up and k_{LA}

The gas hold-up (ϵ_G), which determines the volumetric fraction of gas within the liquid, is generally accepted as an important hydrodynamic parameter which describes the effectiveness of a gas-liquid contactor with respect to mass transfer [4, 17]. Oliveira et al. [4] have shown that the type of gas diffuser had no effect on mass transfer coefficient in an oscillatory baffled reactor, and this was attributed to the high turbulence caused by liquid oscillation. In this work, the effect of gas diffuser type on gas hold-up and k_{LA} was investigated in the absence of oscillation using the baffled reactor. The gas hold-up (ϵ_G) was measured at different input ozone flow rates according to [4]:

$$\epsilon_G = (h - h_0)/h \quad (5.5)$$

where h and h_0 were the liquid heights (cm) during and before aeration, respectively. Two gas diffusers were employed for this experiment: a perforated PTFE diffuser (A) 12 mm high and 10 mm in diameter with a 1.0 mm pore diameter which produced large bubbles ca. 8.0 mm in diameter, and a stone diffuser (B) with a small pore size producing small bubbles of diameter 1.0 - 3.0 mm. Figure 5.7 shows the effect of superficial gas velocity on gas hold-up observed using the two diffusers. As can be seen from the figure, a slight and almost constant enhancement of gas hold-up was observed using the diffuser (A) over (B). However, the diffuser type had no apparent effect on the volumetric mass transfer coefficient, as shown in fig. 5.8. Therefore, it can be concluded that the independence of the gas-liquid mass transfer coefficient of OBRs on the diffuser type observed by Oliveira et al. [4] can be extended to include the baffled reactors. This may be due to the continuous change in bubble size during their rise through the baffled column, as discussed above, which significantly reduced the importance of the initial size of the bubbles released from the diffuser.

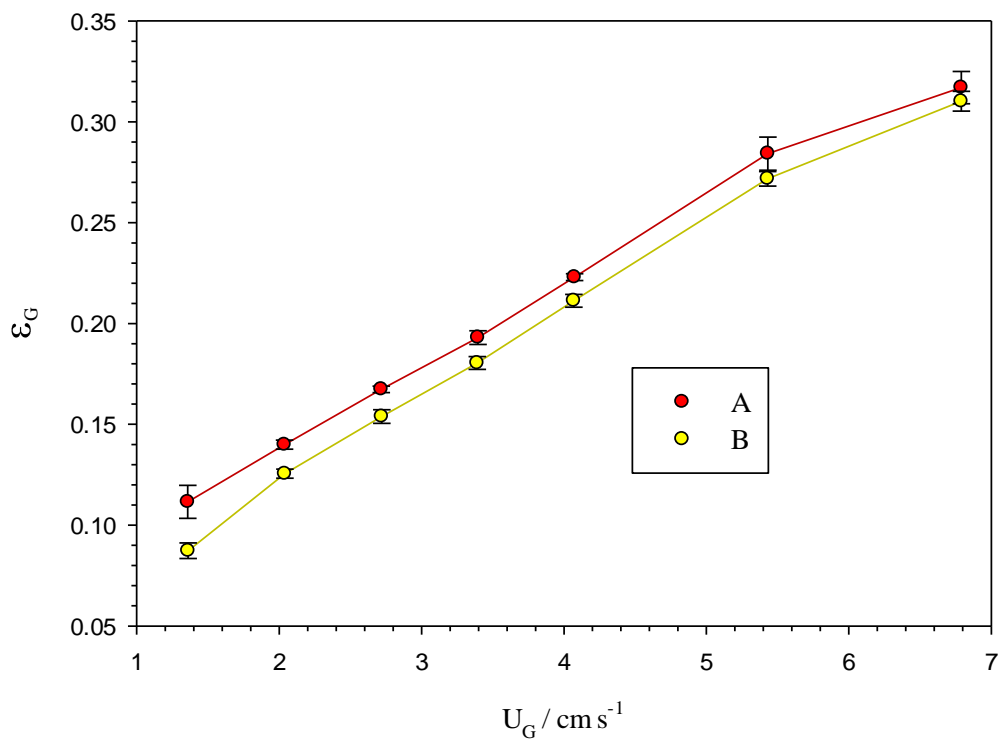


Figure 5.7. Plot of gas hold-up as a function of the gas superficial velocity obtained using gas diffusers A and B in the baffled reactor. See text for details.

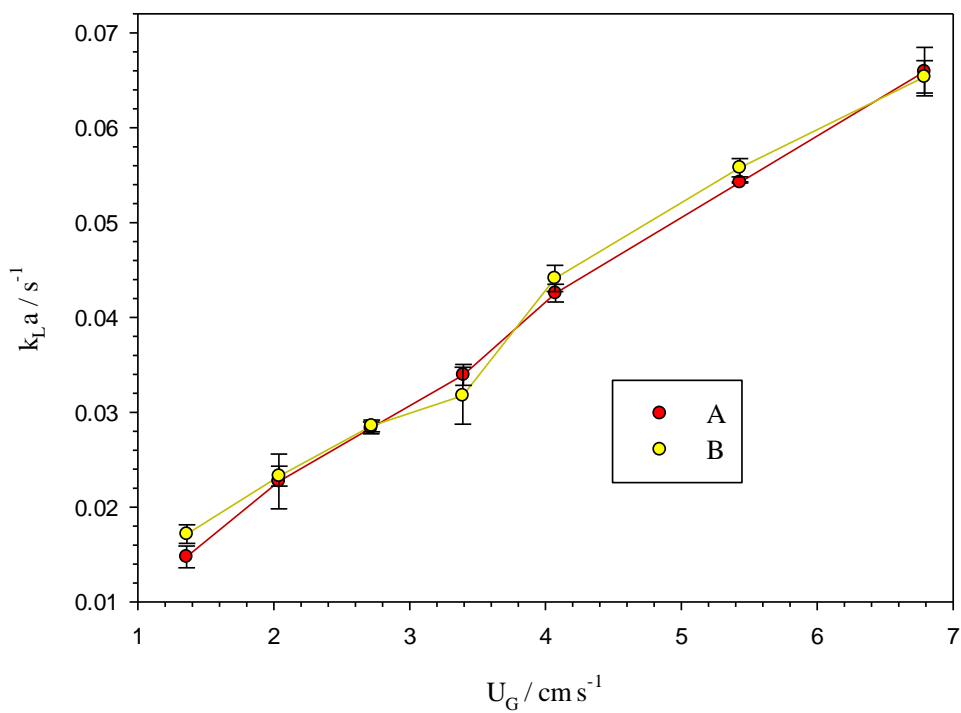


Figure 5.8. Plot of k_{La} as a function of gas superficial velocity obtained using gas diffusers A and B in the baffled reactor.

Figure 5.9 shows a plot of volumetric mass transfer coefficient as a function of gas hold-up obtained under different operational conditions of reactor arrangement, oscillation condition, diffuser type and input gas flow rates. As may be seen from the figure, there is a linear relationship between gas hold-up and mass transfer coefficient. Considering the variety of the operational conditions and bubble size, it does not seem unreasonable to postulate that gas hold-up is the most important factor that controls the ozone-water mass transfer coefficient irrespective of reactor type. This assumption is in agreement with the work carried out by Oliveira et al. [4] who have shown that in OBRs the contribution of gas hold-up on mass transfer coefficient is more significant than bubble size.

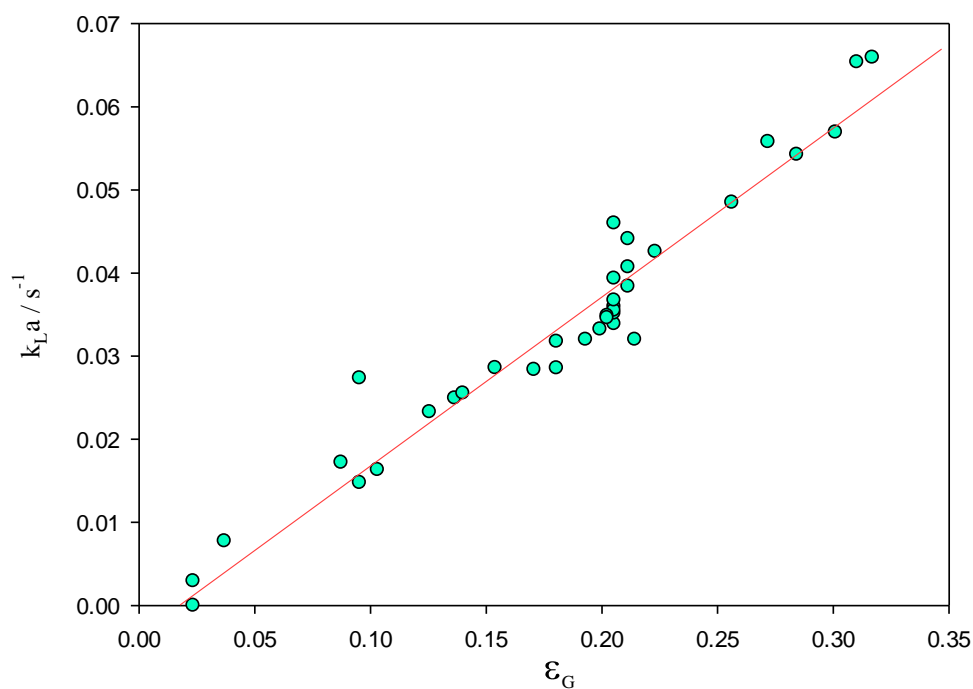


Figure 5.9. Plot of ozone-water mass transfer coefficients as a function of gas hold-up obtained using the three reactor arrangements, under various input gas flow rates and oscillation conditions.

5.3. Ozone-water mass transfer under continuous flow conditions

5.3.1. The effect of the input gas and water flow rates on k_{La}

The baffled reactor was operated as a co-current, up flow contactor to assess its performance with respect to ozone-water mass transfer. The ozone-water mass transfer coefficient was

determined at gas and liquid flow rates of 0.1 to 1.0 $\text{dm}^3 \text{min}^{-1}$, and the results are shown in fig. 5.10. As can be seen from the figure, k_{LA} increased significantly with the input gas and water flow rates, and the highest k_{LA} of 0.134 s^{-1} was observed at the maximum flow rates employed. Interestingly, this value is 2 times greater than that achieved with the same reactor operated at the same input gas flow rate and without water throughput as was shown in fig. 5.5. This may be attributed to the additional turbulence induced by water flow and to the potential acceleration of liquid film renewal at the interface, based on thin film renewal theory (TFRT) [18] discussed in section 1.5.2.3.

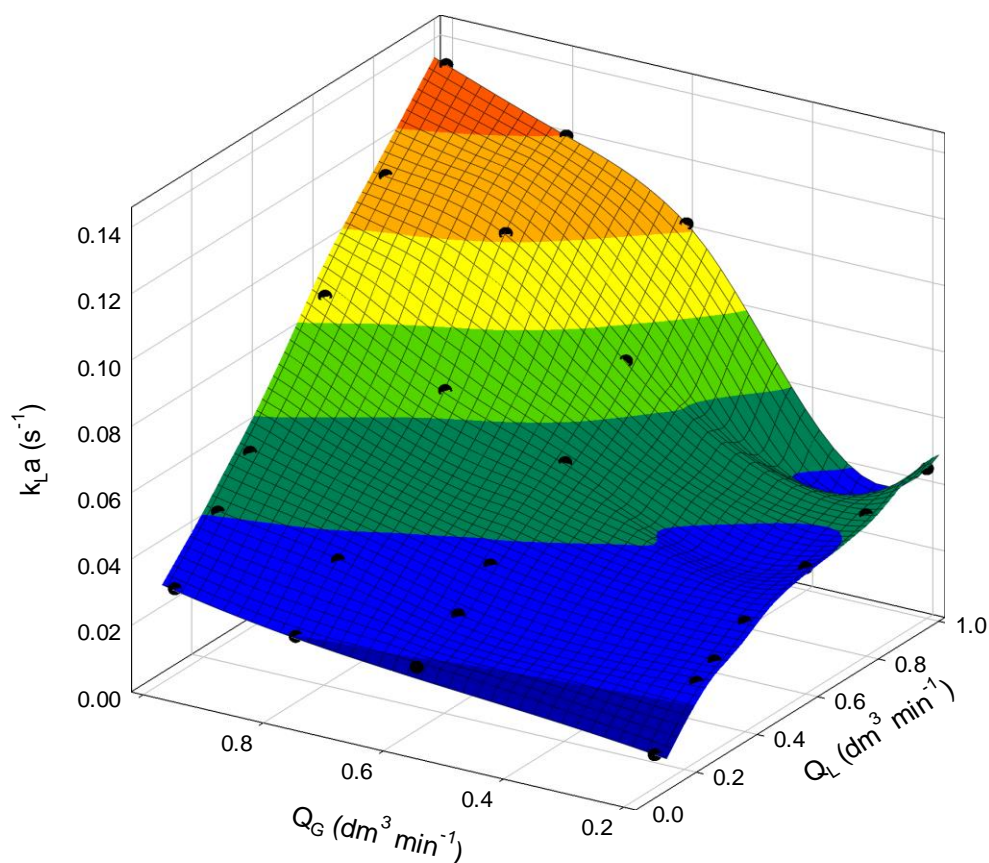


Figure 5.10. A surface plot of the variation in ozone-water mass transfer coefficient as a function of the input gas (Q_G) and water flow rates (Q_L) using the baffled reactor.

Figure 5.11 shows plots of ozone-water k_{LA} as a function of input water flow rate obtained using the baffled reactor and OBR operated at Re_o of 4600 and at a fixed input gas flow rate

of $0.2 \text{ dm}^3 \text{ min}^{-1}$. As can be seen from the figure, regardless of the reactor arrangement, k_{La} increased rapidly with water flow rate from 0.1 to $0.4 \text{ dm}^3 \text{ min}^{-1}$ before it slows down at higher flow rates. In addition, oscillation enhanced ozone-water dissolution, and the enhancement was almost constant at ca. 38-43% irrespective of water flow rate. Further increase in k_{La} with the feed flow rate may be expected, but due to the limited size of the reactor and significant rise of water within the OBR, due to the gas hold-up, higher flow rates were not investigated.

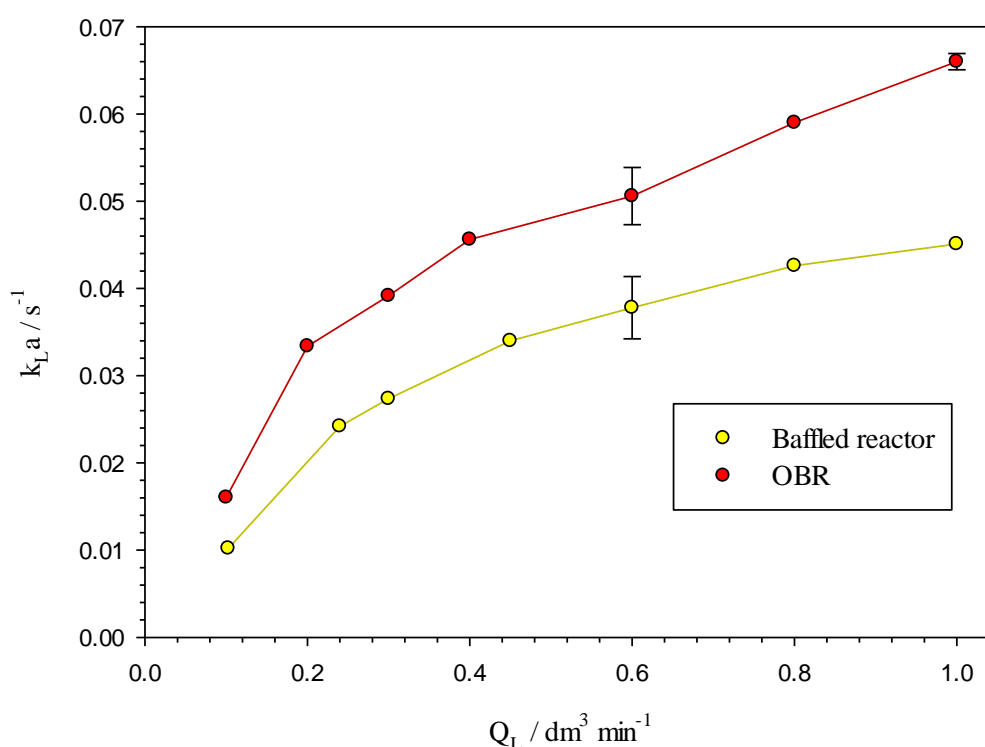


Figure 5.11. Plots of ozone-water mass transfer coefficient (k_{La}) obtained using the baffled reactor without oscillation and the OBR at Re_o of 4600 as a function of input water flow rate. At $Q_G = 0.2 \text{ dm}^3 \text{ min}^{-1}$ and $[O_3]_G = 29.8 \text{ mg dm}^{-3}$.

5.3.2 The effect of the input gas and liquid flow rates on mass transfer efficiency (MTE)

The mass transfer efficiency (MTE), is the ratio of the mass of dissolved ozone to that dissipated via gas bubbling, and was determined according to:

$$\text{MTE \%} = ((Q_L \times [O_3]_s) / (Q_G \times [O_3]_G)) \times 100 \quad (5.6)$$

where Q_L and Q_G are the input water and gas flow rates ($\text{dm}^3 \text{min}^{-1}$), and $[\text{O}_3]_s$ and $[\text{O}_3]_G$ are the steady state dissolved ozone concentrations in liquid and gaseous phases (mg dm^{-3}), respectively. The effect of the input gas and water flow rates upon MTE was determined using the baffled reactor, and the data is shown in fig. 5.12. From the figure, it can be seen that the mass transfer efficiency increased proportionally with water flow rate and inversely to the gas flow rate. The highest mass transfer efficiency of 57% was obtained at the lowest input gas flow rate, $0.1 \text{ dm}^3 \text{min}^{-1}$, and highest input water flow rate, $1.0 \text{ dm}^3 \text{min}^{-1}$. In addition to the high efficiency, operation of the baffled reactor at low input gas flow rate is beneficial because of the lower cost of gas pumping and the reduction in the waste of valuable gases such as ozone. Furthermore, operation under such conditions facilitates the production of high ozone concentrations through the DBD-PBR as discussed in sections 4.2.4 and 4.2.8.

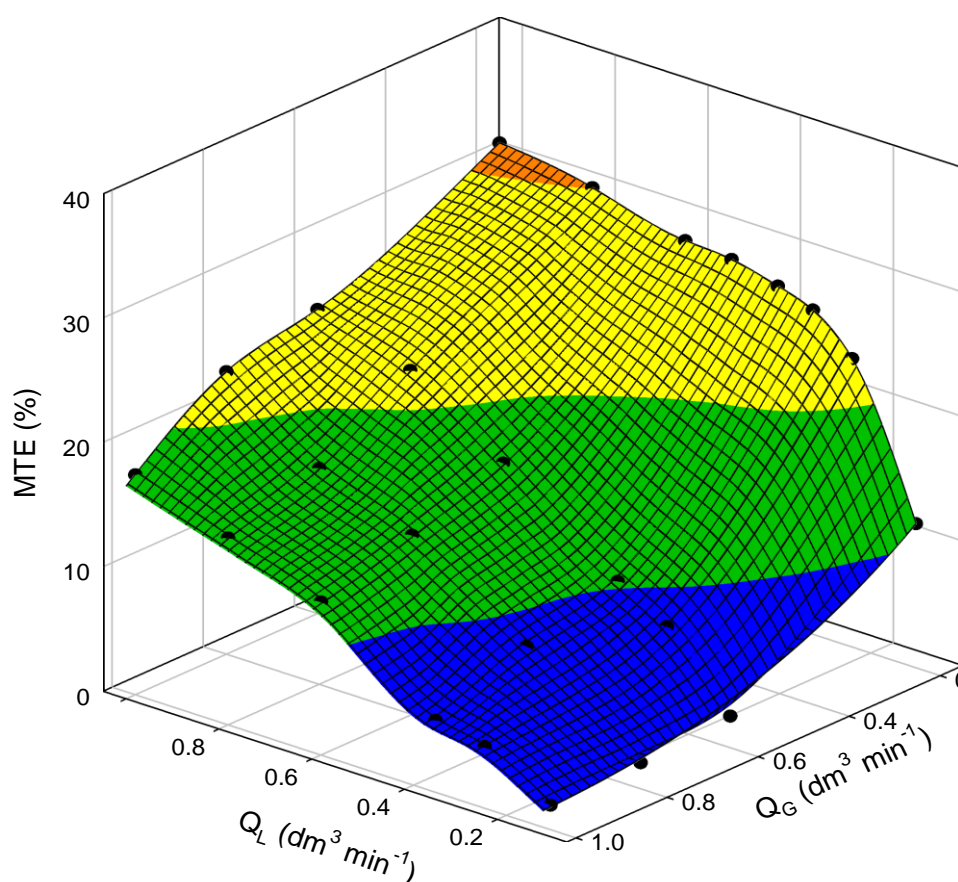


Figure 5.12. A surface plot of ozone-water mass transfer efficiency as a function of the input gas and water flow rates obtained using the baffled reactor.

The effect of oscillation on MTE was extracted from fig. 5.11 and the results so obtained are shown in fig. 5.13. As can be seen from the figure, the effect of oscillation on MTE was found to be more important at water flow rates $> 0.6 \text{ dm}^3 \text{ min}^{-1}$. This may be attributed to the larger difference between the k_{LA} values at high water flow rates as was seen in fig. 5.12. The highest MTE, of a ca. 92%, was observed using the OBR at gas and water flow rates of 0.1 and $1.0 \text{ dm}^3 \text{ min}^{-1}$. Table 5.3 shows the variation of MTE and steady state dissolved ozone concentrations at low input gas flow rate using the baffled reactor and OBR. The enhancement so obtained at low superficial gas velocity may be attributed to the longer contacting time between the phases, and to the lower bubble collisions, as discussed in section 5.2.4.

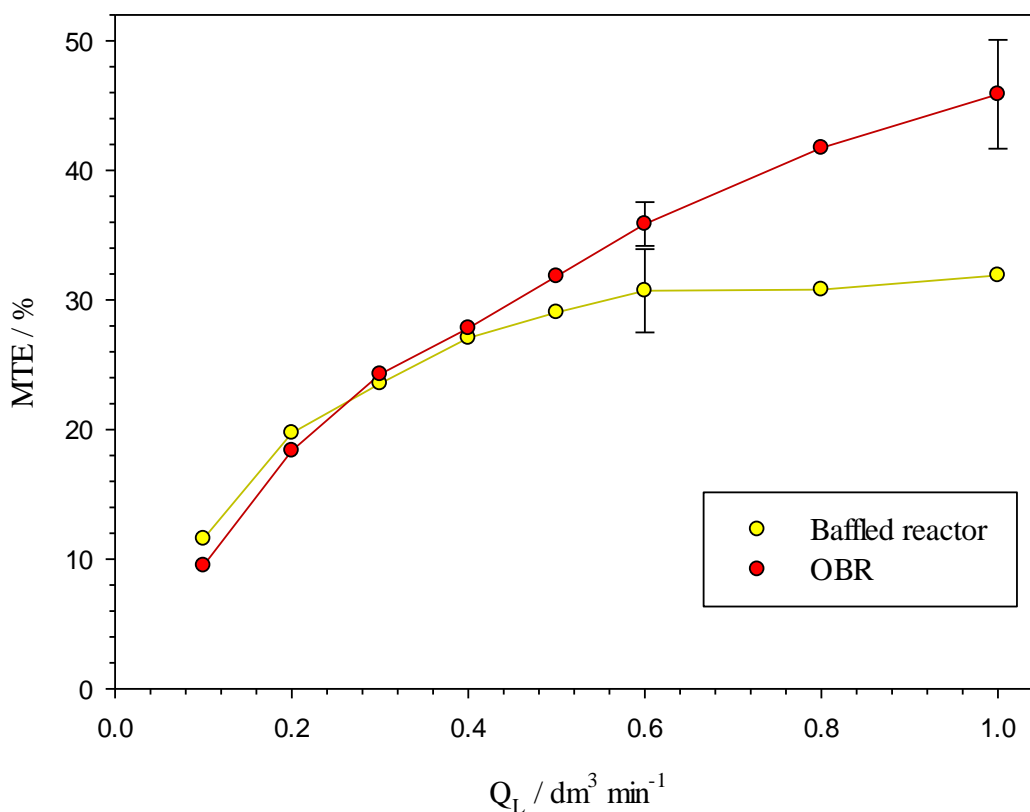


Figure 5.13. Plots of MTE obtained using the baffled reactor and the OBR as a function of input water flow rate; the conditions as for fig. 5.11.

Reactor arrangement	$Q_G / \text{dm}^3 \text{min}^{-1}$	$Q_L / \text{dm}^3 \text{min}^{-1}$	$[\text{O}_3]_G / \text{mg dm}^{-3}$	$[\text{O}_3]_s / \text{mg dm}^{-3}$	MTE / %
Baffled reactor	0.1	0.6	42.1	2.5	35.3
	0.1	1.0	31.5	1.8	57
OBR	0.1	0.6	42.1	4.8	67.8
	0.1	1.0	31.2	2.7	91.6

Table 5.3. The effect of the reactor arrangement and input gas (Q_G) and liquid flow rates (Q_L) on the dissolved ozone concentration and MTE. The Re_o was 4600 in the case of the OBR.

5.4. Conclusions

Ozone-water mass transfer was investigated under semi-batch conditions in a bubble column, a baffled column and an oscillatory baffled reactor. The OBR was demonstrated to be up to five and three times more efficient for ozone-water mass transfer than bubble and baffled column reactors, respectively. The results obtained using the bubble column were found to agree well with literature. For the first time, it was found that the baffled reactor was more efficient than bubble column for ozone-water mass, and its performance increased with the feed gas flow rate. The effect of varying the gas diffuser type (i.e. initial bubble size) was found to not affect the performance of the baffled reactor towards ozone-water mass transfer due to the continuous change in the bubble size during their rise within the reactor. The enhancement obtained with OBR over the baffled column reactor for ozone-water mass transfer was found to decline with gas flow rate due to the growth in bubble size which reduces the residence time of the feed gas bubbles within water and depress the mixing efficiency.

Under continuous flow conditions, the performance of the baffled reactor and the OBR were found to increase with water and gas flow rates, probably due to increasing liquid turbulence and liquid film renewal. However, the mass transfer efficiency in both reactors was found to increase proportionally with water flow rate and inversely to the gas flow rates due to the decrease in contact time between the phases and to the acceleration of bubble collisions. The significant enhancements on k_{La} and MTE attained using OBR under atmospheric pressure, using a short reactor length, and low gas/liquid volumetric ratios make this type of reactor one of the most effective contactors for ozone-water mass transfer.

5.5. References

- [1] Oliveira, M.S.N. and Ni, X. (2001) 'Gas hold-up and bubble diameters in a gassed oscillatory baffled column', *Chemical Engineering Science*, 56(21-22), pp. 6143-6148.
- [2] Hewgill, M.R., Mackley, M.R., Pandit, A.B. and Pannu, S.S. (1993) 'Enhancement of gas-liquid mass-transfer using oscillatory flow in a baffled tube', *Chemical Engineering Science*, 48(4), pp. 799-809.
- [3] Ni, X., Gao, S., Cumming, R.H. and Pritchard, D.W. (1995) 'A comparative study of mass transfer in yeast for a batch pulsed baffled bioreactor and a stirred tank fermenter', *Chem Eng Sci*, 50, pp. 2127-2136.
- [4] Oliveira, M.S.N. and Ni, X.W. (2004) 'Effect of hydrodynamics on mass transfer in a gas-liquid oscillatory baffled column', *Chemical Engineering Journal*, 99(1), pp. 59-68.
- [5] Hoigné, J., Bader, H., Haag, W.R. and Staehelin, J. (1985) 'Rate constants of reactions of ozone with organic and inorganic compounds in water-III. Inorganic compounds and radicals', *Water Research*, 19(8), pp. 993-1004.
- [6] Zhou, H. and Smith, D.W. (2000) 'Ozone mass transfer in water and wastewater treatment: experimental observations using a 2D laser particle dynamics analyzer', *Water Research*, 34(3), pp. 909-921.
- [7] Kuosa, M., Laari, A. and Kallas, J. (2004) 'Determination of the Henry's coefficient and mass transfer for ozone in a bubble column at different pH values of water', *Ozone-Science & Engineering*, 26(3), pp. 277-286.
- [8] Beltran, F.J., Garcia-Araya, J.F. and Encinar, J.M. (1997) 'Henry and mass transfer coefficients in the ozonation of wastewaters'.
- [9] Kosak-Channing, L.F. and Helz, G.R. (1983) 'Solubility of ozone in aqueous solutions of 0-0.6 M ionic strength at 5-30 °C', *Environmental Science & Technology*, 17(3), pp. 145-149.

[10] Ni, X. and Gao, S. (1996) 'Scale-up correlation for mass transfer coefficients in pulsed baffled reactors', *The Chemical Engineering Journal and the Biochemical Engineering Journal*, 63(3), pp. 157-166.

[11] Oliveira, M.S.N., Fitch, A.W. and Ni, X. (2003) 'A study of bubble velocity and bubble residence time in a gassed oscillatory baffled column: effect of oscillation frequency', *Chemical Engineering Research and Design*, 81(2), pp. 233-242.

[12] Harvey, A.P., Mackley, M.R. and Stonestreet, P. (2001) 'Operation and optimization of an oscillatory flow continuous reactor', *Industrial & Engineering Chemistry Research*, 40(23), pp. 5371-5377.

[13] Ni, X. and Gough, P. (1997) 'On the discussion of the dimensionless groups governing oscillatory flow in a baffled tube', *Chemical Engineering Science*, 52(18), pp. 3209-3212.

[14] Bin, A.K., Duczmal, B. and Machniewski, P. (2001) 'Hydrodynamics and ozone mass transfer in a tall bubble column', *Chemical Engineering Science*, 56(21-22), pp. 6233-6240.

[15] Mizuno, T. and Tsuno, H. (2010) 'Evaluation of solubility and the gas-liquid equilibrium coefficient of high concentration gaseous ozone to water', *Ozone: Science & Engineering*, 32(1), pp. 3-15.

[16] Watanab, K., Kinugasa, I. and Higaki, K. (1991) 'Ozone absorption in bubble column', *Memoir of Niihama College of Technology*, 27, pp. 48-52.

[17] Krishna, R. and van Baten, J.M. (2003) 'Mass transfer in bubble columns', *Catalysis Today*, 79 (1-4), pp. 67-75.

[18] Danckwerts, P. V. (1951) 'Significance of Liquid-Film Coefficients in Gas Absorption', *Ind Eng Chem Res*, 43, pp. 1460-1467.

6. The remediation of water containing Cu(II)-EDTA or Fe(III)-EDTA by ozonation, and ozonation followed by UV irradiation

6.1. Introduction

As was discussed in section 1.6, the chelating reagent EDTA has been employed extensively in a wide range of applications due to its high efficiency in forming very stable metallorganic complexes. However, because most of the M-EDTA complexes are highly resistive towards remediation via conventional biological or thermal methods [1-6] the risks of surface and ground water contamination is increased. Ozonation alone, or in combination with UV irradiation, has been shown to be promising with respect to the degradation of free or complexed EDTA into smaller fragments [7-12] that can be removed readily by conventional biotreatments [9, 13]. However, the efficiency of M-EDTA treatment via ozonation is highly dependent on the amount and rate of ozone being transferred to the water during treatment [7, 11]. Thus, the aim of this chapter was to evaluate to what extent the intensification of ozone-to-water mass transfer using the system DBD-PBR/OBR/UVR can increase the removal efficiency of the most recalcitrant complexes Cu(II)-EDTA and Fe(III)-EDTA [3, 4] from water. The objectives were to:

- Commission the system DBD-PBR/ OBR coupled with a UV irradiation reactor (UVR) for water treatment.
- Determine the effect of input water flow rate and the ozonation reactor arrangement on performance.
- Evaluate the benefit of following ozonation treatment with UV irradiation in the removal of the EDTA complexes from water.
- Identify the optimal operational conditions for treatment by ozonation and ozonation followed by UV irradiation.
- Monitor the products of EDTA treatment using ion chromatography (IC), electron spray ionization mass spectroscopic (ESI-MS) and total organic carbon (TOC) analyses, and to estimate the potential decomposition pathways on the basis of these analyses.

Water treatment was carried out in two stages: in which the water was first passed through the DBD-PBR/ OBR system before being directed to the UVR for irradiation. In all experiments reported below, ozone was fed to the system at a constant concentration and flow rate of $60.4 \pm 0.7 \text{ g m}^{-3}$ and $0.4 \text{ dm}^3 \text{ min}^{-1}$, respectively. Table 2.5 summarises the water flow rates investigated and the corresponding residence times at the different stages of the treatment. It should be noted that the shorter residence times observed using the OBR compared to the baffled reactor at the same input water flow rates was due to the variation in the gas holdup (ϵ_G) between the reactors. ϵ_G was higher in the case of the OBR and caused the mixture of water and gas bubbles to reach the sampling port faster than in the baffled reactor, see section 5.2.4 for a detailed discussion of ϵ_G . Table 2.5 is reproduced from chapter 2 for convenience.

Water sample flow rate/ $\text{cm}^3 \text{ min}^{-1}$	Baffled reactor residence time/ min	OBR residence time/ min	UVR-photolysis residence time/ min
20.0	18.16	16.69	15.10
30.0	11.42	10.50	9.50
40.0	9.08	8.25	7.55
60.0	6.05	5.57	5.03
80.0	4.54	4.09	3.78
100.0	3.63	3.3	3.02

Table 2.5. Summary of the operational conditions employed for water remediation.

6.2. Cu(II)-EDTA analysis and treatment

6.2.1. Cu(II)-EDTA analysis by ion chromatography

Ion chromatography (IC) was employed for monitoring the concentration of Cu(II)-EDTA in aqueous samples as described in section 2.5.3. Figure 6.1 shows a typical example of an IC chromatogram of a pure sample of Cu(II)-EDTA in deionised water. As can be seen from the figure, a distinctive peak was observed at a retention time of 13.4 min. By plotting the peak height for a range of Cu(II)-EDTA concentrations from 5 to 250 mg dm^{-3} , a calibration

curve was produced as can be seen in fig. 6.2. This calibration curve was employed to estimate the residual Cu(II)-EDTA after treatment.

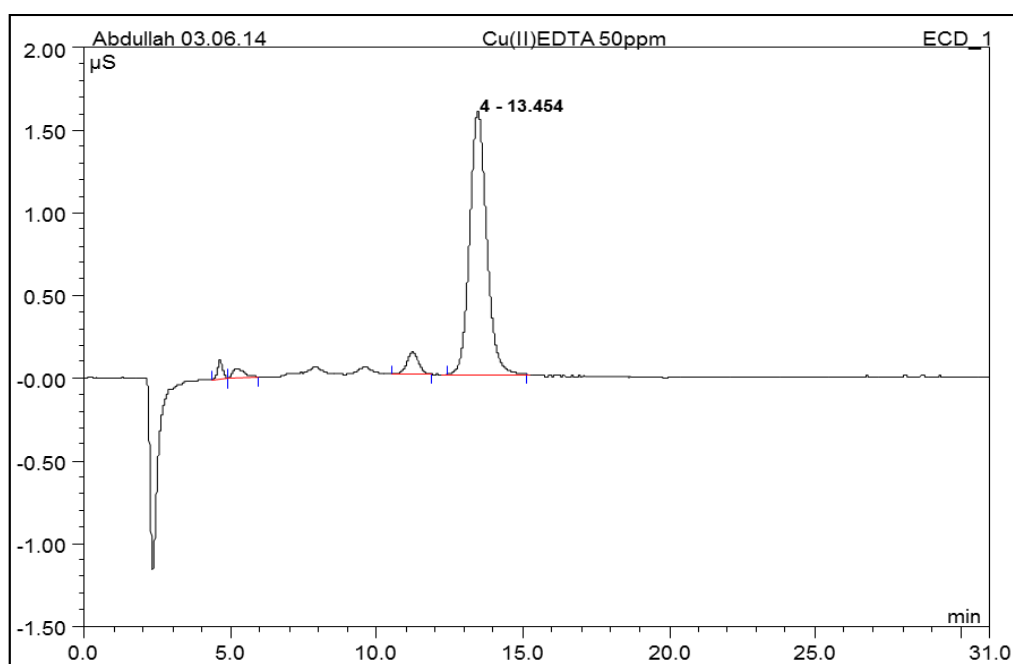


Figure 6.1. A typical chromatogram of 50 mg dm^{-3} of Cu(II)-EDTA in water obtained using ion chromatography.

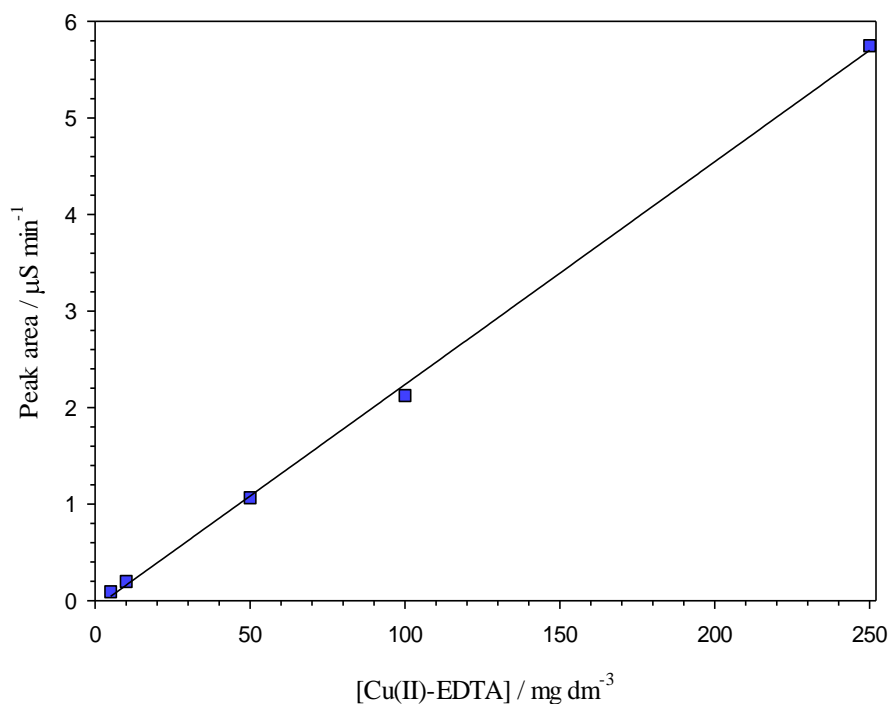


Figure 6.2. Calibration curve of Cu(II)-EDTA in water obtained using ion chromatography for the peak observed at the retention time of 13.4 minutes. $R^2 = 0.999$.

6.2.2. *Cu(II)-EDTA treatment by ozone*

Figure 6.3 shows the removal of Cu(II)-EDTA from water using the baffled reactor or OBR as a function of water residence time within the reactor. As can be seen from the figure, 81% and 95% of Cu(II)-EDTA was removed after 3.6 and 9.0 minutes, respectively, using the baffled reactor. When the baffled reactor was replaced with the OBR the removal increased to 86% and 96% after 3.3 and 9.0 minutes, respectively. By increasing the residence time, complete removal of Cu(II)-EDTA was observed within 17 and 18 minutes using the OBR and the baffled reactor, respectively. From fig. 6.3 it can be seen that similar Cu(II)-EDTA removal behaviour with the residence time was observed with the baffled reactor and the OBR. In both reactors, the % removal increased with residence time, following (apparently) first-order kinetics. This behaviour was generally observed during the treatment of EDTA and its metal complexes with ozone [8-11]. Hence, by plotting $\ln e([\text{Cu(II)-EDTA}]_t / [\text{Cu(II)-EDTA}]_0)$ vs. the residence time, linear plots were obtained as can be seen from the

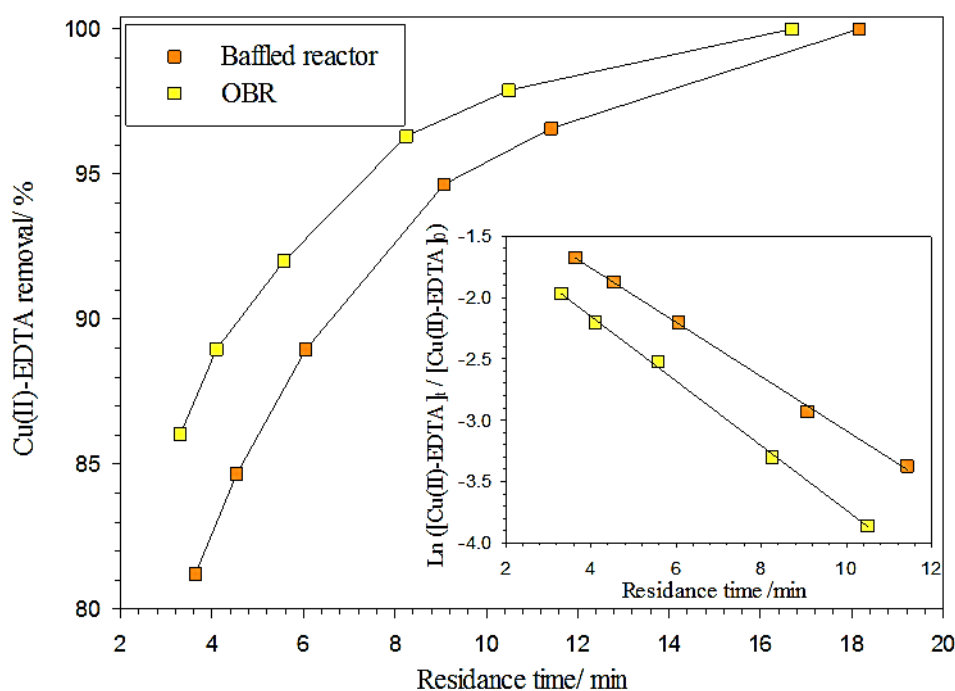


Figure 6.3. Plots of % removal of Cu(II)-EDTA by ozonation as a function of the reactor arrangement and water residence time. The input water flow rate was varied from 0.02 to $0.1 \text{ dm}^3 \text{ min}^{-1}$. The experiments were carried out at room temperature with no pH adjustment. The Cu(II)-EDTA initial concentration was 250 mg dm^{-3} . Ozone flow rate and concentration were $0.4 \text{ dm}^3 \text{ min}^{-1}$ and $60.4 \pm 0.7 \text{ g m}^{-3}$, respectively. The oscillatory Reynolds number (Re_o) was fixed at 4600 in the case of the OBR. The inset shows plots of $\ln ([\text{Cu(II)-EDTA}]_t / [\text{Cu(II)-EDTA}]_0)$ vs. time.

inset of fig. 6.3. The slopes of these plots are the rate constants for Cu(II)-EDTA decomposition: $2.22 \times 10^{-1} \pm 4.8 \times 10^{-3}$ and $2.64 \times 10^{-1} \pm 5.4 \times 10^{-3} \text{ min}^{-1}$ using the baffled reactor and the OBR, respectively. From these rate constants, it is clear that the removal of Cu(II)-EDTA using OBR was ca. 17% faster than the baffled reactor, and this does not seem unreasonable considering the higher efficiency of the former toward ozone-water mass transfer, see section 5.3.1. It should be noted that these rate constants are affected by several factors such as the ratio of $[\text{O}_3] / [\text{M-EDTA}]$, EDTA complex, reaction temperature, pH, reactor type and operational conditions [10]. Thus, establishing a valid comparison of the Cu(II)-EDTA decomposition rate constants observed here with those in limited number of studies in the literature was found to be difficult.

Figures 6.4(a) and (b) show photographs of the changes in the Cu(II)-EDTA solution observed before and after the ozonation treatment using the baffled reactor and the OBR. As can be seen from fig. 6.4(a), the blue colour of the Cu(II)-EDTA solution faded after treatment, with a precipitate of pale blue particles, possibly $\text{Cu}(\text{OH})_2$ [8]. Figure 6.4(b) shows photos of Cu(II)-EDTA solutions after ozonation using the baffled reactor and OBR. As can be seen from the figure, the treated solutions were similar in colour and both contained $\text{Cu}(\text{OH})_2$ particles. Therefore, it can be concluded that the ozonation treatment alone is sufficient for metal removal from Cu(II)-EDTA.

Table 6.1 shows a comparison of the experimental conditions employed in this work to obtain 95% removal of Cu(II)-EDTA by ozonation using the baffled reactor and the OBR to those employed by Yang et al. [7] using a bubble column reactor. From the table it may be seen that the replacement of the bubble column with a baffled column or an OBR enhanced significantly the efficiency of Cu(II)-EDTA: (i) the treatment was carried out under continuous water flow conditions, (ii) the time of the treatment was $2.2 \times$ and $2.6 \times$ faster in the cases of the baffled and the OBR, respectively, (iii) the ratio of $[\text{O}_3]_{\text{G}} / [\text{Cu(II)-EDTA}]_0$ was reduced by 61% compared to the bubble column reactor, (iv) the feed gas flow rate was ca. $4 \times$ lower than that employed in the bubble column reactor and (v) the reactor height in the case of the OBR and the baffled reactor was $2 \times$ shorter than that of the bubble column reactor.

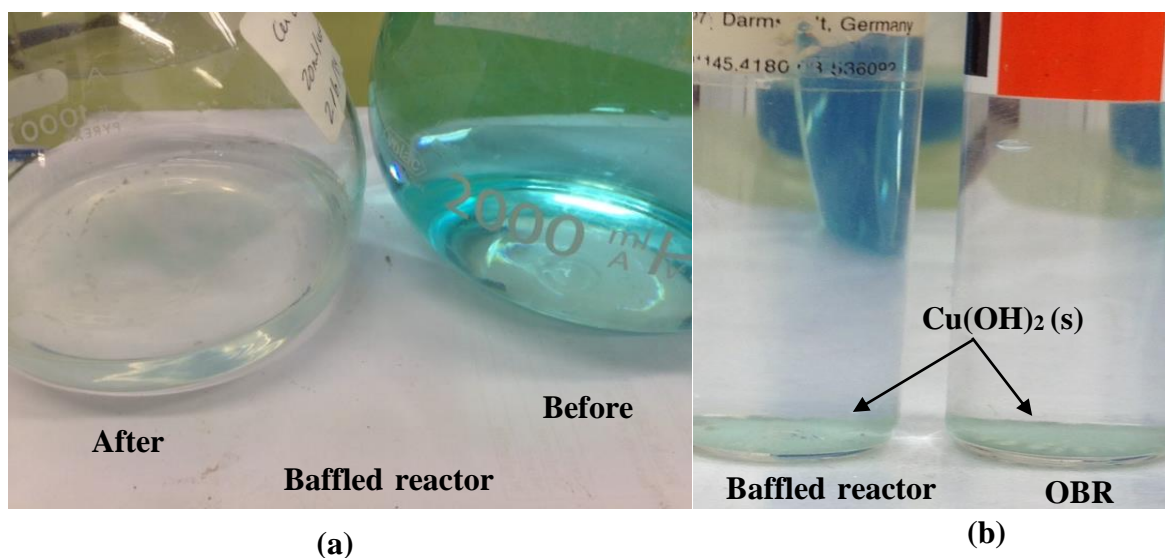


Figure 6.4. Photographs of Cu(II)-EDTA solution before and after ozonation treatment using the baffled reactor (a), and (b) the effluent collected from the baffled reactor and OBR after treatment. The input ozone concentration was $60.4 \pm 0.7 \text{ g m}^{-3}$ at $0.4 \text{ dm}^3 \text{ min}^{-1}$. The Cu(II)-EDTA initial concentration was 250 mg dm^{-3} and the water flow rate was $0.02 \text{ dm}^3 \text{ min}^{-1}$.

Reference	This work	This work	Yang et al. [7]
Reactor type	Baffled reactor	OBR	Bubble column
Dimensions/ H (cm) \times ID (cm)	104 \times 2.5	104 \times 2.5	200 \times 2.9
Water volume/ dm^3	0.5	0.5	1.0
Operation mode	continuous	continuous	semi-batch
$Q_G/\text{dm}^3 \text{ min}^{-1}$	0.4	0.4	1.7
$[\text{O}_3]_G/\text{mg dm}^{-3}$	60.4	60.4	20
$[\text{Cu(II)-EDTA}]_0/\text{mg dm}^{-3}$	250	250	32
Treatment time for 95% removal /min	13.5*	11.3*	30

Table 6.1. A comparison of the experimental conditions and results of Cu(II)-EDTA treatment with ozone obtained in this work to those obtained by Yang et al. [7] using a bubble column reactor. * Estimated using the decomposition rates $2.22 \times 10^{-1} \pm 4.8 \times 10^{-3}$ and $2.64 \times 10^{-1} \pm 5.4 \times 10^{-3} \text{ min}^{-1}$ obtained from fig. 6.3 using the baffled reactor and the OBR, respectively.

6.2.3. *Cu(II)-EDTA treatment by ozonation followed by UV irradiation*

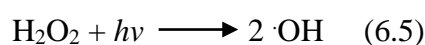
In order to evaluate the feasibility of following the ozonation treatment by UV irradiation on the removal of Cu(II)-EDTA, the effluents of the baffled reactor and OBR were passed through the UVR. Table 6.2 shows a comparison between the % removal of Cu(II)-EDTA so obtained by ozonation and ozonation followed by UV irradiation as a function of the ozonation reactor arrangement and total residence time. As can be seen from the table, following the ozonation treatment by UV irradiation doubled the treatment time. In addition, the % removal of Cu(II)-EDTA enhanced by ca. 3.5% after UV irradiation of water samples ozonated for 3.6 or 3.3 minutes using the baffled reactor or OBR, respectively. However, this enhancement decreased with increasing the ozonation time, regardless of the reactor arrangement.

Ozonation				Ozonation followed by UV irradiation			
Baffled reactor		OBR		Baffled reactor + UVR		OBR + UVR	
time/ min	Removal/ %	time/ min	Removal/ %	time/ min	Removal/ %	time/ min	Removal/ %
18.2	100	16.7	100	33.2	100	31.8	100
11.4	96.6	10.5	98	26.5	98.2	20	98.8
9.1	94.7	8.2	96.3	16.6	96.5	15.8	97.5
6.0	89.0	5.6	92	11.1	92.4	10.6	93.2
4.5	84.7	4.1	89	8.3	89.3	7.9	91.5
3.6	81.2	3.3	86	6.7	84.7	6.3	89.4

Table 6.2. A comparison of Cu(II)-EDTA % removal by ozonation and ozonation followed by UV irradiation as a function of reactor arrangement and total residence time. The experimental conditions were similar to those showed in figure 6.3.

The enhancement in Cu(II)-EDTA removal so obtained by passing the effluents of the ozonation reactors through the UVR may be attributed to the formation of highly reactive

$\cdot\text{OH}$ radicals (i.e. 3 - 5 orders of magnitude more reactive than ozone [14]). Several mechanisms have been proposed for $\cdot\text{OH}$ formation in O_3/UV systems including direct photolysis of ozone or dissociation of H_2O_2 [12, 15, 16]:



From these reactions it is clear that the amount of dissolved ozone in water is a critical parameter in determining the concentration of OH radicals [11, 12]. Therefore, the limited effect of UV irradiation in Cu(II)-EDTA removal may be attributed to the consumption of $\cdot\text{OH}$ radicals by other products formed during the ozonation treatment, and this assumption was supported by the TOC analyses as will be discussed below.

6.2.4. TOC analysis of Cu(II) -samples after treatments

Figure 6.5 shows plots of TOC removal as a function of residence time, treatment method and reactor arrangement. As can be seen from the figure, the reduction of TOC was found to increase with the residence time regardless of the treatment method or reactor arrangement. However, at residence times higher than 6 minutes, the effect of reactor type and treatment method on the TOC were more pronounced. From fig. 6.5, it can be seen that the highest enhancement in TOC reduction obtained using OBR over the baffled reactor with no UV treatment was ca. 3% at the highest residence times in both reactors. Following the ozonation by UV irradiation enhanced the reduction in TOC by 11 and 13% for the samples treated at the highest residence times using the baffled reactor and the OBR, respectively. Therefore, it can be concluded that the TOC reduction was determined not only by the decomposition of Cu(II)-EDTA but also by the stability of the degradation products. The highest reduction in TOC observed by following the ozonation with UV irradiation using the baffled reactor and OBR were 44 and 49%, respectively. These results were 50% and 67% higher than those obtained by Yang et al. [7] after treating Cu(II)-EDTA by ozonation

and UV irradiation for 30 minutes using the bubble column reactor described above connected to a UV reactor.

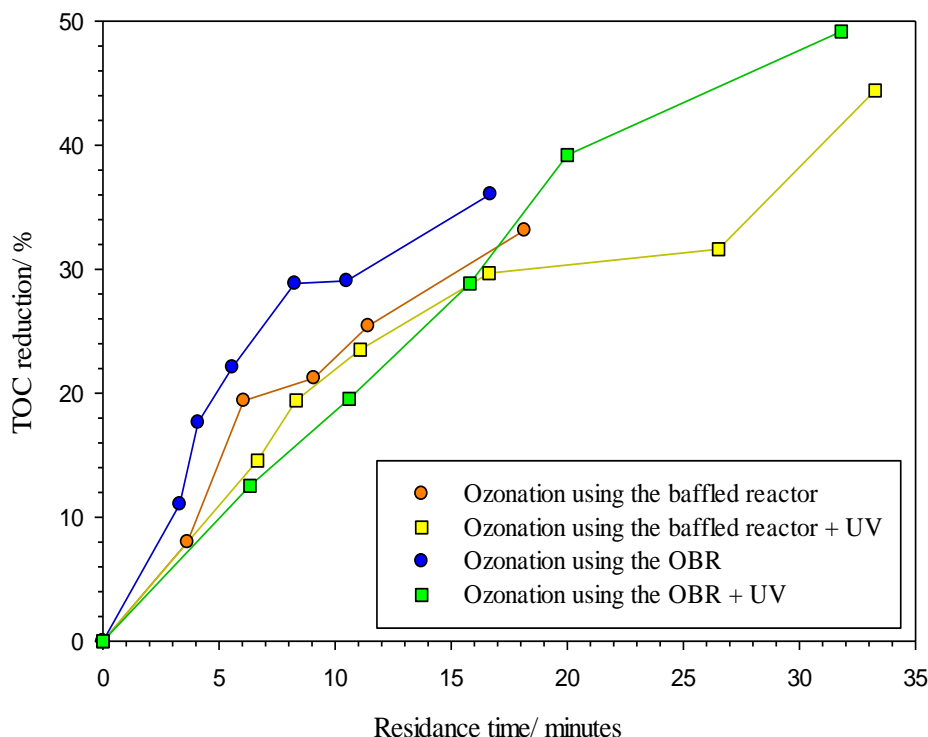


Figure 6.5. Plots of % reduction in the total organic carbon (TOC) content of the Cu(II)-EDTA solutions as a function of total residence time and reactor arrangement. The initial TOC concentration was $86.0 \pm 1.0 \text{ mg dm}^{-3}$. The experimental conditions were the same as those in fig. 6.3.

6.3. Fe(III)-EDTA analysis and treatment

6.3.1. Fe(III)-EDTA analysis by ion chromatography

Figure 6.6 shows a typical IC chromatogram of 50 mg dm^{-3} Fe(III)-EDTA in Millipore water. As can be seen from the figure, the separation of Fe(III)-EDTA was carried out successfully and resulted in a broad peak having a retention time from a ca. 6.5 to 14 minutes. However, due to the fact that the majority of the EDTA by-products appear within the same region, as will be shown below, it was found to be extremely difficult to monitor the changes in Fe(III)-EDTA concentration after treatment using the IC approach. Instead, TOC and mass spectroscopic analyses were employed.

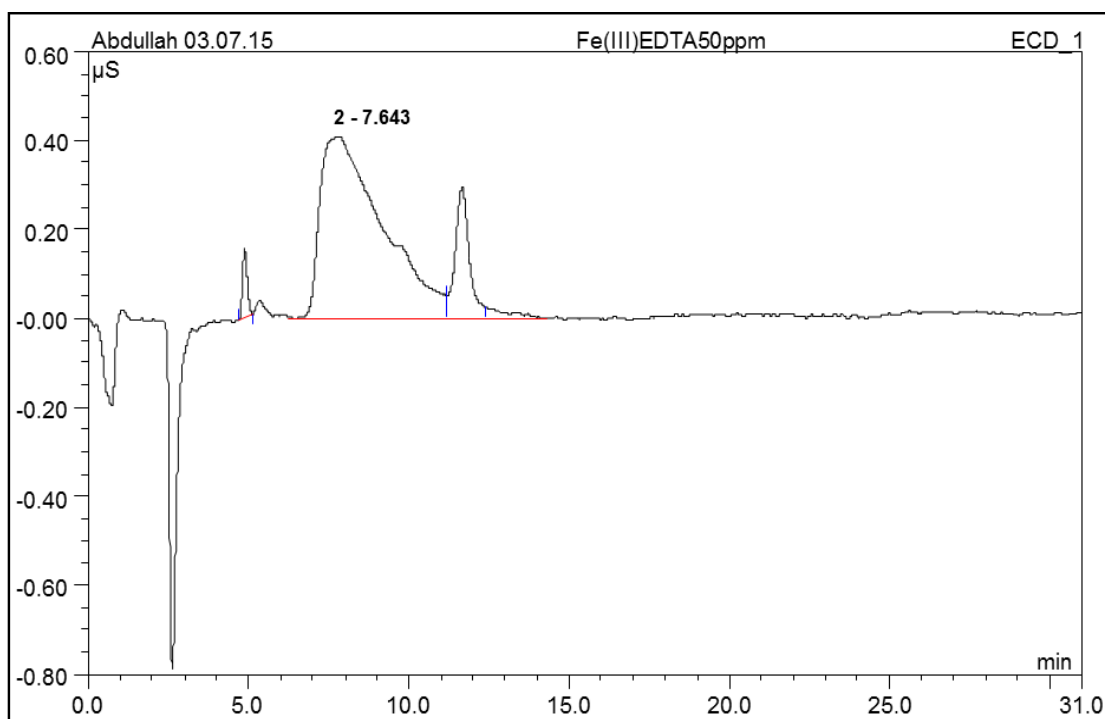


Figure 6.6. A typical IC chromatogram of 50 mg dm^{-3} of Fe(III)-EDTA in water.

6.3.2. TOC analyses of Fe(III)-EDTA after treatments

The treatment of the Fe(III)-EDTA samples was carried out under similar conditions to those employed for Cu(II)-EDTA, and the change in TOC was monitored as a function of residence time, treatment method and reactor type, see fig. 6.7. As can be seen from the figure, regardless of the treatment method and reactor type, the TOC decreased with the ozonation time of the Fe(III)-EDTA in agreement with results observed with Cu(II)-EDTA. In addition, it can be seen from fig. 6.7 that the OBR was twice as effective as the baffled reactor for reducing the TOC by ozonation of the Fe(III)-EDTA. This enhancement agreed well with the higher performance of the OBR toward ozone dissolution in water. From section 5.2.3, at feed gas flow rate of $0.4 \text{ dm}^3 \text{ min}^{-1}$ the ozone-water volumetric mass transfer coefficient using the OBR (i.e. 0.027 s^{-1}) was twice greater than that obtained using the baffled reactor. However, no such behaviour was observed in the case Cu(II)-EDTA as shown in fig. 6.5, and this may be understood considering the variation between the reactivity of Cu(II)-EDTA and Fe(III)-EDTA with ozone and the subsequent increase in ozone-consuming species formation as intermediates [9] or final products (e.g. oxalate [17]) with treatment time. The reaction rate of ozone with Cu(II)-EDTA (i.e. $1.5 \times 10^{-3} \text{ M}^{-1} \text{ s}^{-1}$ [8])

is significantly lower than that of Fe(III)-EDTA (i.e. $3.3 \times 10^2 \text{ M}^{-1} \text{ s}^{-1}$ [18]), and hence the decomposition of Fe(III)-EDTA with ozone would be expected to be much faster than that of Cu(II)-EDTA [7]. Hence, the reduction in TOC caused by the decomposition of intermediates and final products would be expected to be more dependent on ozone concentration in the case of Fe(III)-EDTA. Another likely reason is the higher stability of these intermediates and final products towards ozone than those produced from the ozonation of Cu(II)-EDTA. These reasons may explain the significant reduction in TOC from 22 to 43% (ca. 2 \times) when the ozonation treatment was followed by UV irradiation for the samples treated using the baffled reactor, and from 46 to 48% for those treated using the OBR, as can be seen from fig. 6.7.

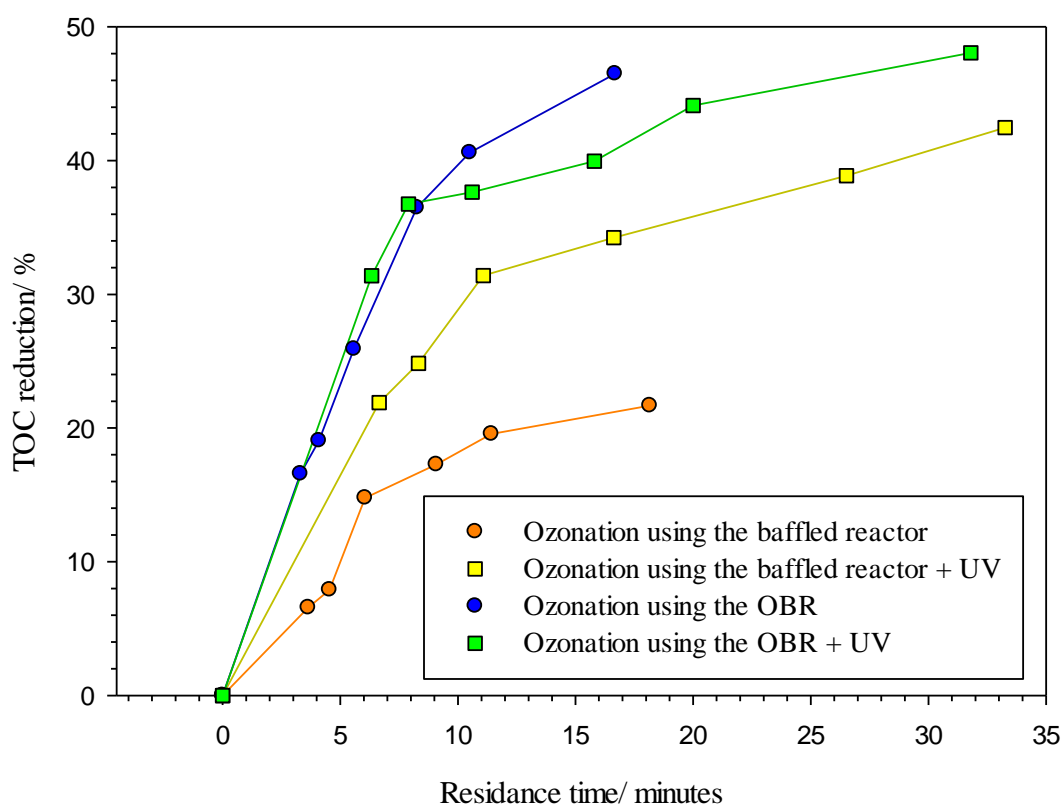


Figure 6.7. Plots of the reduction in total organic carbon (TOC) of the Fe(III)-EDTA solutions as a function of total residence time, treatment type and reactor arrangement. TOC at 0% reduction = $45.0 \pm 1.0 \text{ mg dm}^{-3}$. The experimental conditions were the same as in fig. 6.3.

Figure 6.8 shows photos of the Fe(III)-EDTA samples taken after treatment by ozonation and ozonation followed by UV irradiation for ca. 17 and 18 minutes using the OBR and baffled reactors, respectively. As can be seen from the figure, regardless of the reactor arrangement, for the samples treated with ozone alone, clear solutions were observed, while those treated by UV irradiation after ozonation gave yellowish precipitate, possibly Fe(III) oxide(s) [19]. Therefore, it is clear from this observation and the TOC analysis that some of the products formed during the treatment of Fe(III)-EDTA with ozone alone were capable of making stable complexes with iron, and this was confirmed by mass spectroscopic analyses.

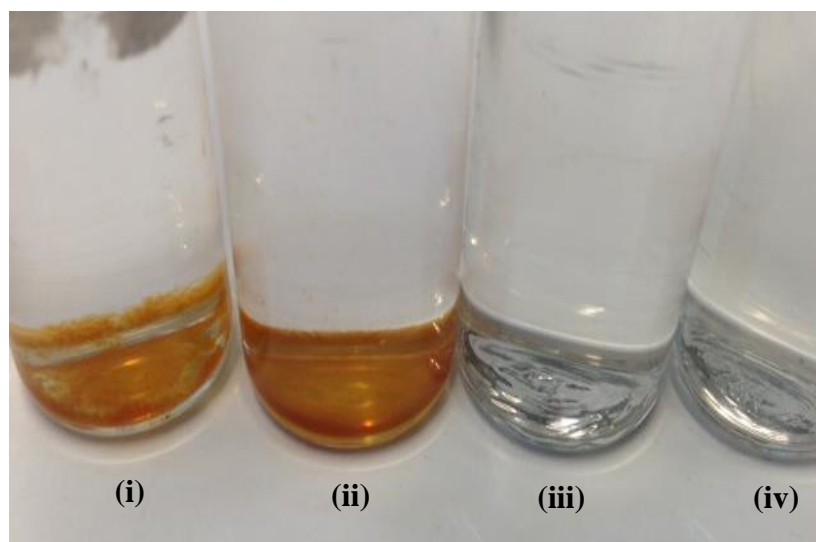


Figure 6.8. Photos of Fe(III)-EDTA solution after ozonation and UV treatment (i) and (ii), and after ozonation (iii) and (iv) using baffled reactor (i) and (iii) and OBR (ii) and (iv) treatment (a) and (b) the effluents characteristic collected from baffled reactor and OBR after treatment. The experimental conditions were the same as in 6.9.

Figures 6.9(a) and (b) show examples of electrospray ionization mass spectroscopic (ESI-MS) analysis of Fe(III)-EDTA samples after ozonation for 8 and 17 minutes, respectively, using the OBR. As can be seen from figs. 6.9(a) and (b), unreacted Fe(III)-EDTA was observed after ozonation for 8 and 17 minutes using the OBR. In addition, Fe(III)-ED3A (i.e. ethylenediaminetriacetic acid) along with other by-products such as N-MED3A (i.e. N-methyltriacetylenediamine), Fe(III)-IDA (i.e. iminodiacetate) and unidentified species

having molecular weights of 214 and 260 g mol⁻¹ were also observed. The relative intensities of these by-products were higher after 17 minutes ozonation than after 8 minutes. From these results it is clear that the formation of the complexes Fe(III)-ED3A and Fe(III)-IDA prevent the precipitation of Fe(III) oxide(s) during the ozonation of Fe(III)-EDTA. In fact, Fe(III)-ED3A was identified as one of the most stable by-products during the UV irradiation of Fe(III)-EDTA [20], ozonation of Fe(III)-DTPA (Diethylenetriaminepentaactate) [21] and aerobic photolysis of Fe(III)-EDTA [2]. The IDA and ED3A ligands were identified during the treatment of EDTA by ozonation [8, 9], biotreatment [22], UV or gamma irradiation [11] and UV + H₂O₂ [23]. Hence Fe(III)-ED3A, Fe(III)-IDA and other products are expected to compete with the parent molecule Fe(III)-EDTA for ozone, and thus increase the amount of ozone required for the remediation of the Fe(III)-EDTA.

Figures 6.10(a) and (b) show mass spectra collected from Fe(III)-EDTA samples ozonated for 8 and 17 minutes, respectively, using the OBR with subsequent UV irradiation. As can be seen from fig. 6.10(a) following the ozonation by UV irradiation enhanced significantly the removal of Fe(III)-EDTA. Figure 6.10(b) shows that Fe(III)-EDTA and Fe(III)-ED3A were completely removed from the solution, whilst the amount of Fe(III)-IDA increased and smaller molecular fragments were formed. However, according to Gilbert and Hoffmann-Glewe [9] and Thomas et al. [13], the biodegradability of these products were significantly enhanced compared to Fe(III)-EDTA or other M-EDTA complexes.

Figure 6.11 shows a typical example of the product analysis carried out using ion chromatography of a Cu(II)-EDTA sample treated using ozone and UV. As can be seen from the figure, the major products of Cu(II)-EDTA degradation were NO₃⁻, NO₂⁻, glycolic, formic and oxalic acids and other (unidentified) products. It should be highlighted that the IC analysis of the Fe(III)-EDTA was not carried out due to the interference discussed above. According to Gilbert and Hoffmann-Glewe [9] the formation of nitrate indicates the complete mineralization of the EDTA complex and most of its intermediates, and this agrees with the mass spectroscopic results discussed above. The same by-products were observed using ozonation alone, but at lower concentrations.

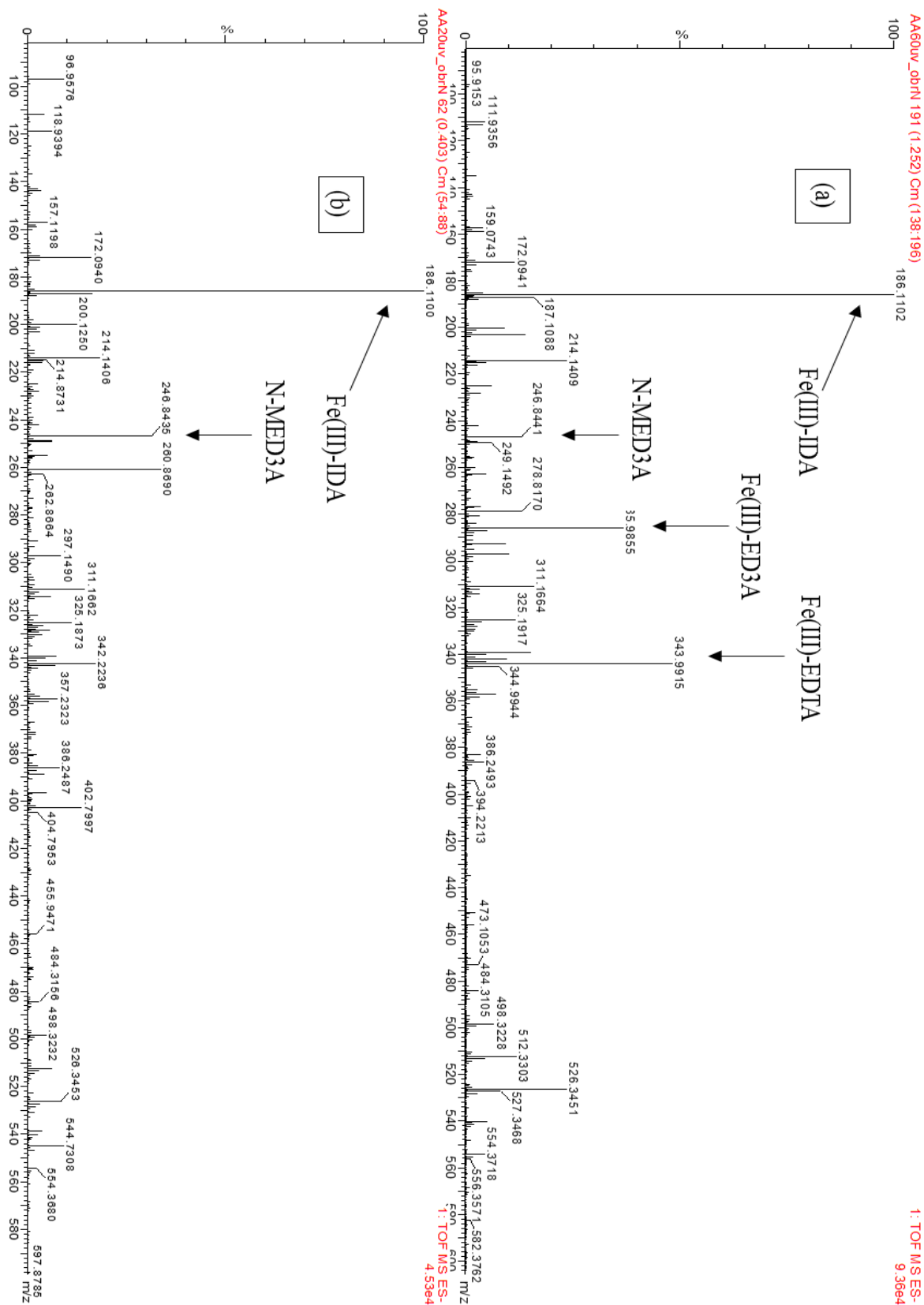


Figure 6.10. Electrospray Ionization Mass Spectroscopy (ESI-MS) spectra of Fe(III) EDTA samples after ozonation for: (a) 8 and (b) 17 minutes using the OBR followed by UV irradiation. The experimental conditions were the same as in fig. 6.7.

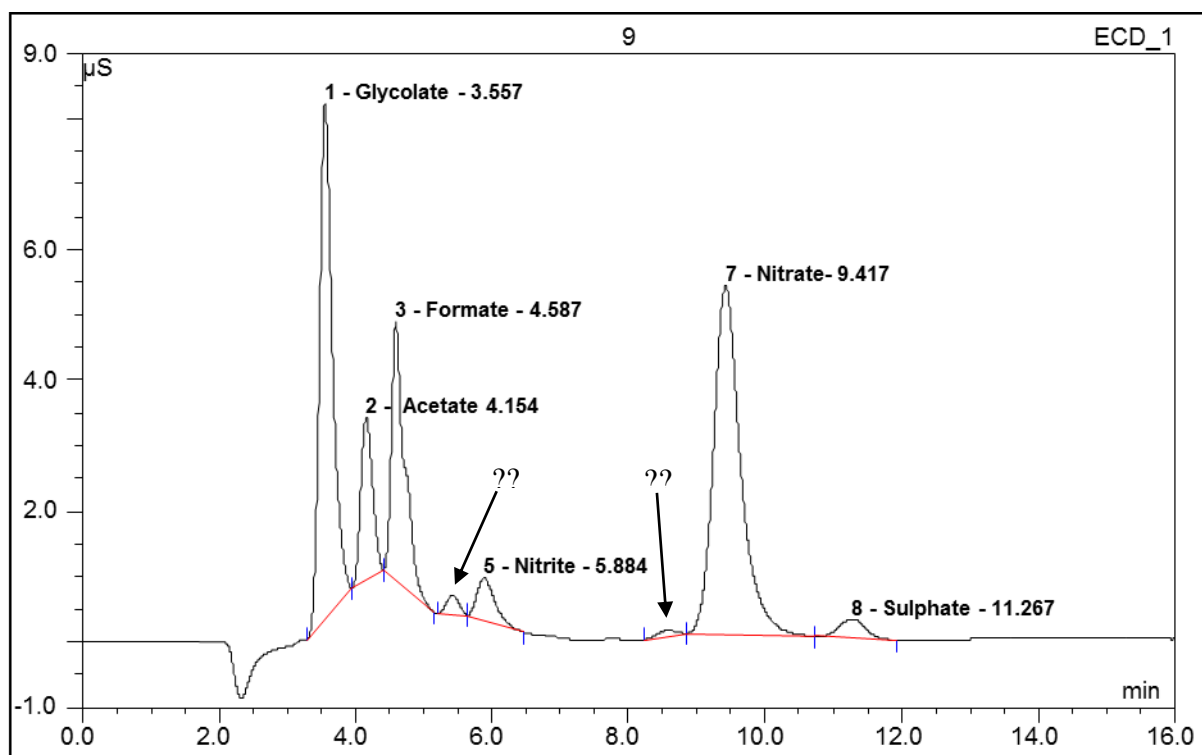


Figure 6.11. Typical IC chromatogram of Cu(II)-EDTA degradation by-products after ozonation and UV irradiation. The input ozone concentration was $60.4 \pm 0.7 \text{ mg dm}^{-3}$ at $0.4 \text{ dm}^3 \text{ min}^{-1}$. The initial concentration of Cu(II)-EDTA was 250 mg dm^{-3} , and the input water flow rate was $0.2 \text{ dm}^3 \text{ min}^{-1}$ using the baffled reactor for ozonation.

On the basis of the results obtained from the ESI-MS and IC analyses and the data available in literature, the potential degradation pathways of M-EDTA by ozonation and ozonation followed by UV are shown in fig. 6.12. The degradation scheme presented in fig. 6.12 was suggested by Gilbert and Hoffmann-Glewe [9]. In addition, routes A and B in the same figure were proposed by Sorensen et al. [23] for EDTA decomposition by UV/ H_2O_2 . In addition, from the ESI-MS analyses shown in figs 6.9 and 6.10 it may be observed that the formation of Fe(III)-IDA was higher when ozonation treatment was followed by UV irradiation, which agrees with the route B proposed by Sorensen et al. [23]. Interestingly, the intermediate N-MED3A observed in figs 6.9 and 6.10 was not identified in the previous works carried out by Gilbert and Hoffmann-Glewe [9] or Sorensen et al. [23] and the reason for this disagreement was not clear at the present time. However, based on the chemical structure of MED3A it was assumed to be produced through the decomposition route A (shown in fig. 6.12) prior to the formation of ED3A as can be seen from fig. 6. 13.

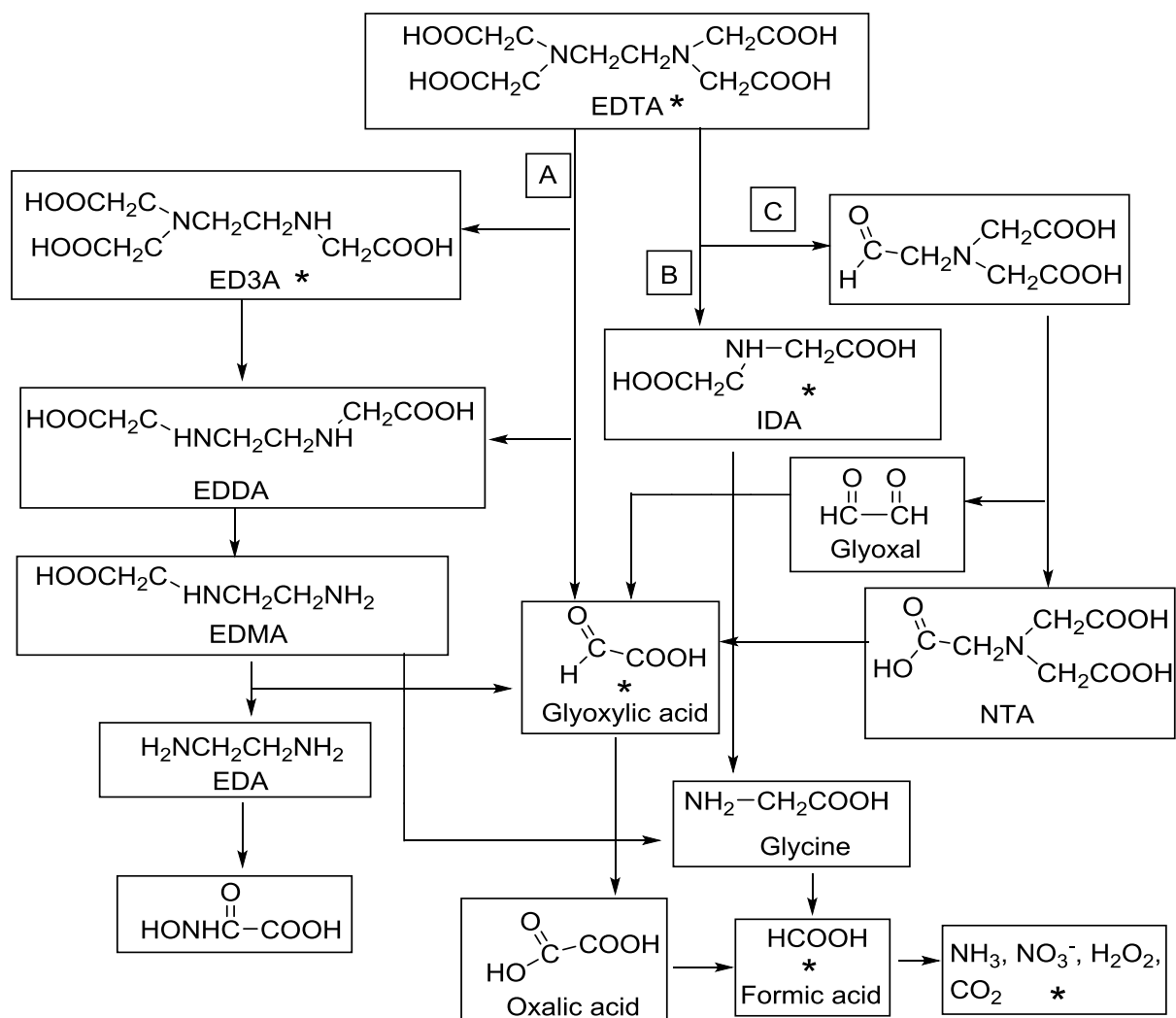


Figure 6.12. Degradation pathways of EDTA: A, B and C by ozonation, A and B by UV irradiation. Reproduced after Gilbert and Hoffmann-Glewe [9] and Sorensen et al. [23]. (*) identified during this work.

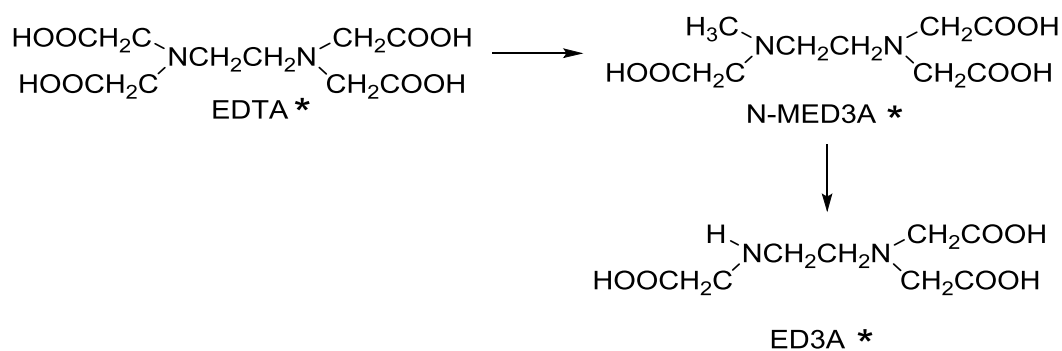


Figure 6.13. Possible mechanism for the formation and decomposition of N-MED3A.

6.4. Conclusions

The effects of ozonation and ozonation followed by UV on Cu(II)-EDTA and Fe(III)-EDTA were investigated using the baffled reactor and the OBR under continuous flow conditions. The degradation of these complexes was observed to increase with treatment time, and following the ozonation treatment with UV irradiation was found to enhance the reduction of TOC. The complete removal of Cu(II)-EDTA was attained by ozonation after 17 and 18 minutes using the OBR and the baffled reactor, respectively. In general, the OBR and the baffled reactors have shown high performance towards the treatment of EDTA complexes than the conventional bubble column reactors.

In the case of Fe(III)-EDTA, ozonation alone was not sufficient for complete degradation, and hence subsequent UV irradiation was essential for the decomposition of this complex and its intermediates. The effect of ozone dissolution rate was found to be more significant in the case of Fe(III)-EDTA mineralization. This behaviour was attributed to: (i) the higher reactivity of Fe(III)-EDTA with ozone than that of Cu(II)-EDTA, which reduces the dissolved ozone concentration available for the degradation by-products; and (ii) to the high stability of these by-products towards ozone. Fe(III)-ED3A, Fe(III)-IDA and N-MED3A were identified by mass spectroscopic analysis as the main intermediates and products during the treatment of Fe(III)-EDTA. Other products were identified using ion chromatography, and included: glycolic, acetic and formic acids, nitrite and nitrate. From the by-product analyses carried out during this work, and the data available in literature, the degradation pathways of EDTA complexes were proposed. The intermediate N-MED3A was determined during this work but not in the previous studies on EDTA treatment by O₃/UV and the reason for this disagreement was not clear at the present time. However, on the basis of the chemical structure of MED3A the routes of its formation and decomposition were proposed.

6.5. References

[1] Park, E.-H., Jung, J. and Chung, H.-H. (2006) 'Simultaneous oxidation of EDTA and reduction of metal ions in mixed Cu(II)/Fe(III)-EDTA system by TiO₂ photocatalysis', *Chemosphere*, 64(3), pp. 432-436.

[2] Lockhart, H.B. and Blakeley, R.V. (1975) 'Aerobic photodegradation of iron(III)-(ethylenedinitrilo)tetraacetate (ferric EDTA). Implications for natural waters', *Environmental Science & Technology*, 9(12), pp. 1035-1038.

[3] Satroutdinov, A.D., Dedyukhina, E.G., Chistyakova, T.y.I., Witschel, M., Minkevich, I.G., Eroshin, V.K. and Egli, T. (2000) 'Degradation of Metal-EDTA Complexes by Resting Cells of the Bacterial Strain DSM 9103', *Environmental Science & Technology*, 34(9), pp. 1715-1720.

[4] Nörtemann, B. (1999) 'Biodegradation of EDTA', *Applied Microbiology and Biotechnology*, 51(6), pp. 751-759.

[5] Belly, R.T., Lauff, J.J. and Goodhue, C.T. (1975) 'Degradation of ethylenediaminetetraacetic acid by microbial populations from an aerated lagoon', *Applied microbiology*, 29(6), pp. 787-794.

[6] Motekaitis, R.J., Cox Iii, X.B., Taylor, P., Martell, A.E., Miles, B. and Tvedt Jr, T.J. (1982) 'Thermal degradation of EDTA chelates in aqueous solution', *Canadian Journal of Chemistry*, 60(10), pp. 1207-1213.

[7] Yang, C., Xu, Y.R., Teo, K.C., Goh, N.K., Chia, L.S. and Xie, R.J. (2005) 'Destruction of organic pollutants in reusable wastewater using advanced oxidation technology', *Chemosphere*, 59(3), pp. 441-445.

[8] Morooka, S., Ikemizu, K., Kamano, H. and Kato, Y. (1986) 'Ozonation rate of water-soluble chelates and related compounds', *Journal of Chemical Engineering of Japan*, 19(4), pp. 294-299.

[9] Gilbert, E. and Hoffmann-Glewe, S. (1990) 'Ozonation of ethylenediaminetetraacetic acid (edta) in aqueous solution, influence of pH value and metal ions', *Water Research*, 24(1), pp. 39-44.

[10] Wang, J., Wang, X., Li, G., Guo, P., Luo, Z. (2010) 'Degradation of EDTA in aqueous solution by using ozonolysis and ozonolysis combined with sonolysis', *Journal of Hazardous Materials*, 176, pp. 333-338.

[11] Krapfenbauer, K., Getoff, N. (1999) 'Comparative studies of photo- and radiation-induced degradation of aqueous EDTA. Synergistic effects of oxygen, ozone and TiO₂' (acronym: CoPhoRaDe/EDTA), *Radiation Physics and Chemistry*, 55, pp. 385-393.

[12] Sillanpää, M.E.T., Agustiono Kurniawan, Lo, T., W. h. (2011) 'Degradation of chelating agents in aqueous solution using advanced oxidation process (AOP) ', *Chemosphere*, 83, pp. 1443-1460.

[13] Thomas, R.A.P., Lawlor, K., Bailey, M., Macaskie, L.E. (1998) 'Biodegradation of metal-EDTA complexes by an enriched microbial population', *Applied and Environmental Microbiology*, 64, pp. 1319-1322.

[14] Lee, Y., von Gunten, U. (2010) 'Oxidative transformation of micropollutants during municipal wastewater treatment: Comparison of kinetic aspects of selective (chlorine, chlorine dioxide, ferrate VI, and ozone) and non-selective oxidants (hydroxyl radical)', *Water Res*, 44, pp. 555-566.

[15] Andreozzi, R., Caprio, V., Insola, Marotta, A., R. (1999) 'Advanced oxidation processes (AOP) for water purification and recovery', *Catal Today*, 53, pp. 51-59.

[16] Li, X., Cubbage, J.W., Tetzlaff, T.A., Jenks, W.S. (1999) 'Photocatalytic degradation of 4-chlorophenol. 1. The hydroquinone pathway', *The Journal of Organic Chemistry*, 64, pp. 8509-8524.

[17] Emilio, C.A., Jardim, W.F., Litter, M.I. and Mansilla, H.D. (2002) 'EDTA destruction using the solar ferrioxalate advanced oxidation technology (AOT): Comparison with solar photo-Fenton treatment', *Journal of Photochemistry and Photobiology A: Chemistry*, 151(1-3), pp. 121-127.

[18] Munoz, F. and von Sonntag, C. (2000) 'The reactions of ozone with tertiary amines including the complexing agents nitrilotriacetic acid (NTA) and ethylenediaminetetraacetic acid (EDTA) in aqueous solution', *Journal of the Chemical Society, Perkin Transactions 2*, (10), pp. 2029-2033.

[19] Sunda, W. and Huntsman, S. (2003) 'Effect of pH, light, and temperature on Fe–EDTA chelation and Fe hydrolysis in seawater', *Marine Chemistry*, 84(1–2), pp. 35-47.

[20] Kocot, P., Karocki, A. and Stasicka, Z. (2006) 'Photochemistry of the Fe(III)–EDTA complexes: A mechanistic study', *Journal of Photochemistry and Photobiology A: Chemistry*, 179(1–2), pp. 176-183.

[21] Stemmler, K., Glod, G. and von Gunten, U. (2001) 'Oxidation of metal–diethylenetriamine-pentaacetate (DTPA) – complexes during drinking water ozonation', *Water Research*, 35(8), pp. 1877-1886.

[22] Belly, R.T., Lauff, J.J. and Goodhue, C.T. (1975) 'Degradation of ethylenediaminetetraacetic acid by microbial populations from an aerated lagoon', *Applied microbiology*, 29(6), pp. 787-794.

[23] Sørensen, M., Zurell, S., Frimmel, F.H. (1998) 'Degradation pathway of the photochemical oxidation of ethylenediaminetetraacetate (EDTA) in the UV/H₂O₂-process', *Acta hydrochimica et hydrobiologica*, 26, pp. 109-115.

7. Conclusions and future work

The FTIR studies on the glow of the atmospheric plasma jet fed with CO₂ and various combinations of humidity and N₂, as well as with air, detected O₃, N₂O₅, N₂O, HNO₃, CO₂, CO and, for the first time, a vibrationally excited form of CO₂ (i.e. CO₂^{*}(*v*)), while O₃, N₂O₅, HNO₃ and N₂O were detected in the downstream exhaust. It is clear from this work that the feed gas composition, input power, gas temperature and relative humidity have a significant effect upon the NTP chemistry in the glow and post the glow regions. In addition, synergic effects were observed, e.g. in the presence of water vapour the effect of gas temperature on NO₂, N₂O and O₃ was more significant than the sum of their individual effects. In addition, there are significant differences between the plasma glow and downstream exhaust regions with respect to the type and concentration of neutral and metastable detectable species. This variation suggested, unexpectedly, the occurrence of chemical reactions in afterglow region, and this was confirmed by the spectroscopic analyses of O₃, NO₂ and N₂O in the plasma glow region and the downstream exhaust. This behaviour rules out the general assumption that reactive chemistry is confined to the glow region. It was postulated that some of the reactions that take place in post plasma region include free radicals, metastable and neutral species. The observation of the higher partial pressure of N₂O in the downstream exhaust compared to the plasma glow region when using dry air suggested that active species such as atomic nitrogen play important roles in the afterglow region.

The efficiency of ozone generation via DBD-PBRs enhanced significantly by reducing the amount of discharge current during the generation of NTP by decreasing the capacitance of the dielectric and by effective heat removal. It was found that ozone concentration and yield efficiency decreased with the number of dielectric layers in contact with the HV electrodes, and this was attributed to heat formation due to an increase in the discharge current and the reduction in the discharge voltage. From these results and those presented in chapter 3 it is clear that some of the input power was dissipated as heat and gas ionization, and hence monitoring the discharge power (i.e. working power) is essential to assess accurately the yield efficiency of the DBD-PBR towards ozone production. This can be achieved by monitoring the discharge voltage and current. Even though the discharge frequency is one of the most important parameters that affect the discharge power characteristics significantly, it was, unfortunately, not possible to investigate the effect of this parameter on

ozone generation during this work due to the limited capability of the power supply available. Therefore, it would be interesting to investigate the effect of this parameter on the performance of the DBD-PBR. Another important observation during this work was the high efficiency of the MnO₂-based catalyst towards simultaneous ozone and NO_x removal from the exhausts of the DBD-PBR at room temperature. However, it is important to understand the mechanism of NO_x removal (the mechanism of ozone decomposition on MnO₂ was discussed in section 1.4) in the presence of ozone, e.g. by using *in-situ* FTIR reflectance spectroscopy.

From the results presented in the Chapters 5 and 6 it is clear that OBR and baffled reactor are promising approaches for enhancing ozone-water mass transfer and its application in water treatment. With a mass transfer efficiency of up to 92% being observed under continuous flow conditions, the OBR was demonstrated to be one of the most efficient ozone-water contactors. This performance was reflected by the high efficiency of Cu(II)-EDTA and Fe(III)-EDTA remediation by ozonation over bubble column reactors. It is clear from Chapter 6 that following the ozonation treatment with UV irradiation is essential for complete degradation of Fe(III)-EDTA and TOC reduction due to the formation of highly reactive free radicals (e.g. OH, HO₂). Further studies would be required to determine if and to what extent is carrying out simultaneous ozonation and UV irradiation can enhance the remediation of M-EDTA complexes.

At the moment, studies of plasma reactors are at an early stage and efficiencies are low, and much of the work has been empirical. The introduction of different ceramics as possible catalysts is of considerable potential interest, since it appears to be possible to direct the reacting plasma to yield different products with different catalysts, but there is little *molecular* information available on which a chemical understanding can be built. An additional complexity is that the plasma itself is driven by a succession of micro-discharges each with a lifetime of a few tens of nanoseconds. The importance of this is that the lifetime of many of the species formed is only of this magnitude. Therefore, the main challenges in providing a molecular framework for plasma reactors are essentially twofold: (i) the identity and reactivity of intermediates generated in the plasma need to be understood in more detail. Given the very rapid decay of such species, this can only be done by using a rapid spectroscopic technique. (ii) The development of catalysts for plasma reactors. Hence the

next step in the research should be to employ fast, Time Resolved Step Scan Fourier Transform InfraRed Spectroscopy to study plasma-driven chemical processes of topical interest on time scales from ca. 10 – 50 ns up to s. Infrared spectroscopy allows unambiguous assignments of chemical species in the plasma and by collecting spectra at set time delays after the potential pulse will be able to establish the kinetics of these species. In addition, reflection /absorption IR spectroscopy (i.e. by using a surface discharge cell) should be employed to study the surface of the electrodes and catalysts again obtaining kinetic information on the species observed.